APPLIED
COMPUTATIONAL
ELECTROMAGNETICS
SOCIETY
JOURNAL

SPECIAL ISSUE
on
THE NUMERICAL COMPUTATION
of
LOW FREQUENCY
ELECTROMAGNETIC FIELDS

GUEST EDITORS
A. KONRAD
J.D. LAVERS

1994
Vol. 9 No. 2

ISSN 1054-4887

GENERAL PURPOSE AND SCOPE. The Applied Computational Electromagnetics Society Journal hereinafter known as the ACES Journal is devoted to the exchange of information in computational electromagnetics, to the advancement of the state-of-the-art, and to the promotion of related technical activities. A primary objective of the information exchange is the elimination of the need to "re-invent the wheel" to solve a previously-solved computational problem in electrical engineering, physics, or related fields of study. The technical activities promoted by this publication include code validation, performance analysis, and input/output standardization; code or technique optimization and error minimization; innovations in solution technique or in data input/output; identification of new applications for electromagnetics modeling codes and techniques; integration of computational electromagnetics techniques with new computer architectures; and correlation of computational parameters with physical mechanisms.

SUBMISSIONS CONTENT. The ACES Journal welcomes original, previously unpublished papers, relating to applied computational electromagnetics.

Typical papers will represent the computational electromagnetics aspects of research in electrical engineering, physics, or related disciplines. However, papers which represent research in applied computational electromagnetics itself are equally acceptable.

For additional details, see "Information for Authors", elsewhere in this issue.

SUBSCRIPTIONS. All members of the Applied Computational Electromagnetics Society (ACES) who have paid their subscription fees are entitled to receive the ACES Journal with a minimum of two issues per calendar year. Current annual subscription fees are subject to change every 1 April. Current fees are:

AREAS: U.S. and Canada: SURFACE/AIRMAIL: $65 Individual, $115 Organizational ; Mexico, Central & So. America: AIRMAIL: $70 Individual, $115 Organizational, SURFACE MAIL: $68; Europe, Former USSR, Turkey, Scandinavia, AIRMAIL: $78 Individual, $115 Organizational, SURFACE MAIL: $68; Asia, Africa, Middle East and Pacific Rim: AIRMAIL: $85 Individual, $115 Organizational, SURFACE MAIL: $68. FULL-TIME STUDENTS: $25.00. REMIT BY: (1) BANK DRAFTS (MUST BE DRAWN ON U.S. BANK with US ADDRESS); (2) INTERNATIONAL MONEY ORDER, (3) TRAVELER'S CHECKS IN U.S. DOLLARS. **Prices are subject to change each 1 April.**

Back issues, when available, are $15.00 each. Subscriptions to ACES, orders for back issues of the ACES Journal and changes of addresses should be sent to:

Dr. Richard Adler
ACES Executive Officer
ECE Department, Code ECAB
Naval Postgraduate School
833 Dyer Road, Room 437
Monterey, CA 93943-5121 USA

Allow four week's advance notice for change of address. Claims for missing issues will not be honored because of insufficient notice or address change or loss in mail unless the secretary is notified within 60 days for USA and Canadian subscribers or 90 days for subscribers in other countries, from the last day of the month of publication. For information regarding reprints of individual papers or other materials, see "Information for Authors".

LIABILITY. Neither ACES or the ACES Journal editors are responsible for any consequence of misinformation or claims, express or implied, in any published material in an ACES Journal issue. This also applies to advertising, for which only camera-ready copies are accepted. Authors are responsible for information contained in their papers. If any material submitted for publication includes material which has already been published elsewhere, it is the author's responsibility to obtain written permission to reproduce such material.

APPLIED COMPUTATIONAL ELECTROMAGNETICS SOCIETY Journal

July 1994
Vol. 9 No. 2

ISSN 1054-4887

The ACES Journal is abstracted in INSPEC, in Engineering Index, and in DTIC.

The second, third, fourth, and fifth illustrations on the front cover have been obtained from Lawrence Livermore National laboratory.

The first illustration on the front cover has been obtained from FLUX2D software, CEDRAT S.S. France, MAGSOFT Corporation, New York.

THE APPLIED COMPUTATIONAL ELECTROMAGNETICS SOCIETY JOURNAL

SPECIAL ISSUE
on
THE NUMERICAL COMPUTATION OF LOW FREQUENCY

ELECTROMAGNETIC FIELDS

SPECIAL GUEST EDITORS

A. Konrad
J.D. Lavers
Department of Electrical and Computer Engineering
University of Toronto
10 King's College Road
Toronto, Ontario
CANADA M5S 1A4

REVIEWERS

S. Baronijan
University of Toronto
Toronto, Ont. CANADA

G. Bendzsak
Hatch Associates Ltd.
Mississauga, Ont. CANADA

O. Biro
IGTE
Graz, AUSTRIA

A. Bossavit
Electricite de France
Clamart, FRANCE

J.R. Brauer
The MacNeal-Swendler Corp.
Milwaukee, WI USA

A.C. Cangellaris
University of Arizona
Tucson, AZ USA

M.V.K. Chari
General Electric Co.
Schenectady, NY USA

Q. Chen
University of Toronto
Toronto, Ont. CANADA

J. Chilo
INPG/ENSIEG
Grenoble, FRANCE

G. Costache
University of Ottawa
Ottawa, Ont. CANADA

E. Della Torre
George Washington University
Washington, DC USA

M. Gyimesi
University of Toronto
Toronto, Ont. CANADA

R.F. Harrington
Syracuse University
Syracuse, NY USA

S.R.H. Hoole
Harvey Mudd College
Claremont, CA USA

N. Ida
University of Akron
Akron, OH USA

W. Janischewskyj
University of Toronto
Toronto, Ont. CANADA

S.J. Kubina
Concordia University
Montreal, Que. CANADA

R.J. Luebbers
Pennsylvania State Univ.
University Park, PA USA

D. Lynch
Dartmouth College
Hanover, NH USA

G. Meunier
INPG/ENSIEG
Grenoble, FRANCE

G. Molinari
University of Genova
Genova, ITALY

REVIEWERS (cont)

T.W. Preston
GEC Alsthom Engr. Res. Ctr
Stafford, ENGLAND

R.R. Saldanha
UFMG
Belo Horizonte, MG BRASIL

S.J. Salon
Rensselaer Polytechnic Institute
Troy, NY USA

A. Semlyen
University of Toronto
Toronto, Ont. CANADA

I.A. Tsukerman
University of Toronto
Toronto, Ont. CANADA

T.E. van Deventer
University of Toronto
Toronto, Ont. CANADA

J.C. Verite
Electricite de France
Clamart, FRANCE

J.P. Webb
McGill University
Montreal, Que. CANADA

THE APPLIED COMPUTATIONAL ELECTROMAGNETICS SOCIETY JOURNAL

EDITORS

EDITORS (Continued)

THE APPLIED COMPUTATIONAL ELECTROMAGNETICS

SPECIAL ISSUE OF THE JOURNAL

on

THE NUMERICAL COMPUTATION OF LOW FREQUENCY ELECTROMAGNETIC FIELDS

Vol. 9 No. 2 July 1994

TABLE OF CONTENTS

THE APPLIED COMPUTATIONAL ELECTROMAGNETICS

SPECIAL ISSUE OF THE JOURNAL

on

THE NUMERICAL COMPUTATION OF LOW FREQUENCY ELECTROMAGNETIC FIELDS

REGULAR PAPERS

Vol. 9 No. 2 July 1994

EDITORIAL

A. Konrad & J.D. Lavers
Guest Editors

We are very pleased to present a special issue of the ACES Journal that focuses on recent advances in the numerical computation of low frequency electromagnetic fields. At the outset, the goals of this special issue were threefold: (1) to inform those researchers who normally work in the area of high frequency computational electromagnetics of advances in the computation of static and low frequency field problems; (2) to provide examples where methods used in high frequency areas have been successfully adapted to low frequency problems; and (3) to focus attention on the need for educational tools for the computation of low frequency electromagnetic fields. The papers that have been selected for this special issue address the first two of these goals.

A total of 12 papers, two of which have been invited, appear in this special issue. These papers have been submitted by authors from Canada, the United States, England, Croatia, Yugoslavia, the Netherlands, Australia, Japan and China, thus making the issue truly international. Furthermore, there is a relatively even balance between papers coming from researchers who normally work on low frequency problems and those whose focus is on high frequency fields. We are particularly pleased that Professor Peter Silvester accepted our invitation to co-author the lead paper in this issue. It was 25 years ago that pioneering work on the application of the Finite Element Method to electric machine problems was initiated by Professor Silvester and his colleagues. Since that time, the Finite Element Method has been developed to the point where it is the method of choice for many low frequency applications.

To date, there have been relatively few forums where researchers in the low and high frequency areas of computational electromagnetics could interact with one another. In terms of conferences, the biennial Conference on Electromagnetic Field Computation (CEFC), sponsored by the Magnetics Society of the IEEE, was the first international conference to promote this linkage. The aim of bringing together researchers from the low and high frequency communities has remained a central aim of the CEFC. More recently, the COMPUMAG Conference has also begun to include high frequency sessions. This special issue of the ACES Journal is a further, important step in this direction. As editors, we are both strongly of the opinion that both sides of the computational electromagnetics community should work to establish mutual linkages since there is a considerable common ground to our research efforts. We hope that the present special issue is the first of many that will continue this trend.

BIOGRAPHY OF ADALBERT KONRAD

Adalbert Konrad received his B.Eng., M.Eng. and Ph.D. degrees in Electrical Engineering from McGill University, Montreal, Canada in 1970, 1971 and 1975, respectively. In 1975 he was visiting researcher at the Polytechnic Institute of Grenoble in France. Following that he worked at the Canadian National Research Council in Ottawa until 1979. In 1979 he joined the Electromagnetics Program at the GE R&D Centre in Schenectady, NY where he was involved in the development of numerical methods and codes for the solution of electromagnetic field problems with applications to transformers, motors, ceramic electronic packaging, microwave integrated circuits and rf scattering. In 1990 he became Associate Professor in the Electrical Engineering Department of the University of Toronto. His current technical interests are in the area of eddy currents, coupled magnetic field and electric circuit problems, and time domain finite element field analysis. Dr. Konrad has over 100 publications. He has been an enthusiastic promoter of computational electromagnetics by organizing and participating in workshops and conferences. He is a member of the Steering Committees of the COMPUMAG and CEFC conferences, a founding member of the International Compumag Society, the editorial boards of the ACES Journal and the IEEE Transactions on Microwave Theory and Techniques. He is currently Associate Editor-In-Chief of the ACES Journal.

BIOGRAPHY OF J. DOUGLAS LAVERS

J. Douglas Lavers received the B. Sc. degree in Engineering Physics from Dalhousie University, Halifax, Nova Scotia in 1963, and the M.A.Sc. and Ph.D. degrees in Electrical Engineering from the University of Toronto in 1966 and 1970, respectively. Following graduation, he worked from 1971 until 1973 for Brown Boveri in Dortmund, West Germany as a Development Engineer where he was involved in the design of induction heating and melting equipment. Since 1974, he has been on staff of the Department of Electrical and Computer Engineering, University of Toronto, where he presently holds the position of Professor. Dr. Lavers is Past Chairman of the Power Devices and Systems Research Group within the Department of Electrical and Computer Engineering and is Past President of Electrical Engineering Consociates, a consulting company offering research and design services. In 1990, he served as General Chairman of the IEEE Conference on Electromagnetic Field Computation (CEFC), held in Toronto, and presently serves as the Chairman of the Advisory Committee for that conference. He has also acted as one of the Editors of the INTERMAG issue of the IEEE Transactions on Magnetics during 1993 and 1994. His research interests include the application of Finite and Boundary Element methods for power frequency electromagnetic field problems, particularly those that involve electrometallurgical processes, and the development of CAD tools for the analysis and design of power electronic circuits and systems. He has published widely on these topics in the technical literature and has acted as consultant to companies in North America, Europe and Australia. In recognition for his contributions to the field of electrometallurgy, Dr. Lavers has been made a Fellow of the IEEE.

Finite elements in electromagnetics: A jubilee review

J. Brian Davies
University College London

Peter P. Silvester
McGill University, Montreal

Abstract: *This review describes the historical origins and the present state of the finite element method in electromagnetics. The foundation principles of finite elements are briefly reviewed. Applications are mainly to two and three dimensional problems of microwave and optical structures. The major types of scalar element are noted, and edge-interpolative vector elements are reviewed, firstly for the waveguide problem and then in three dimensions. An extensive bibliography is given, particularly stressing review papers.*

1. The Beginnings

When Courant prepared the text of his winter address to the American Mathematical Society for publication in 1943, he added a two-page Appendix to illustrate how the variational methods first described by Lord Rayleigh could be put to wider use in potential theory [1]. Choosing piecewise-linear approximants on a set of triangles which he called "elements", he dashed off a couple of two-dimensional examples and the finite element method was born.

Finite element methods remained dormant, perhaps waiting for computers to be invented, for more than a decade. They next appeared in the work of Duffin [2,3] in a form similar to that given by Courant but relying also on the mathematical ideas of Synge [4]. A variational approach was retained in this work, making it relatively hard of access to engineers, for whom variational methods were not then a part of the normal mathematical toolkit. Where variational methods were used at all by applied field analysts, they were viewed as ways of generating finite difference formulae [5].

Finite element activity in electrical engineering began in earnest about 1968–1969. A paper on waveguide analysis [6] was published in *Alta Frequenza* in early 1969, giving the details of a finite element formulation of the classical hollow waveguide problem. It was followed by a rapid succession of papers on magnetic fields in saturable materials [7], dielectric loaded waveguides [8], and other well-known boundary value problems of electromagnetics. The method was quickly applied to integral operators as well, both in electrostatics [9] and wire antenna problems [10].

In the decade of the eighties, finite element methods spread quickly. In several technical areas, they assumed a dominant role in field problems. An assessment of the finite element literature, and of its growth rate, may be obtained by examining the INSPEC bibliographic data base over the 1968–1992 period. In 1968 the number of extant finite element papers with electrical engineering content amounted to a mere handful. By 1993 the total had reached about 6000, with 600 or more additional papers published annually. The number of papers added to the literature each year, as recorded by INSPEC, is shown in Fig. 1.

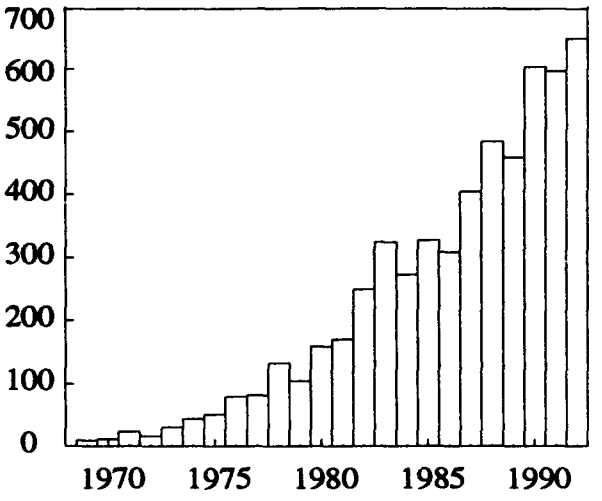

Fig. 1. Production of finite element papers in electrical engineering, 1968–1992.

Having initiated the method, mathematicians at first failed to grasp the significance of finite elements to practical analysis. Serious attention began to be paid to this technique about the same time as it gained a foothold in electrical engineering. Zlámal [11] published the first mathematical paper

explicitly devoted to the finite element method about the same time as electrical engineers began to use it seriously. He and Whiteman [12] recognized the value of this technique at an early date. Other able mathematicians, such as Ciarlet [13], quickly followed.

2. Theoretical Basis

Over the past 30 years the mathematics of finite elements has developed into a distinctive field of study, mainly based on projective and variational methods. This survey is directed to electromagnetics so a detailed treatment of the mathematics would be inappropriate. However, a brief overview may clarify what is special about electromagnetics problems.

2.1. Strong and weak solutions

The finite element method as used in electromagnetics is a special case of a general mathematical method [14] in which the differential or integral equation to be solved

$$\mathcal{P}u = v \tag{1}$$

is first replaced by an equivalent *weak form*, and this weak-form equation is subsequently solved by numerical approximation. The operator $\mathcal{P}$ may represent a boundary value problem (differential equations plus boundary conditions) or an integral operator, or a mixed (integrodifferential) operator.

The quantity u is said to be a *strong solution* of the operator equation (1). A *weak solution* $\bar{u}$ is obtained if the left and right sides of (1) have equal inner product projections onto all functions $w \in \mathbf{W}$, where $\mathbf{W}$ is some function space whose closure is the range of the operator $\mathcal{P}$,

$$\langle \mathcal{P}\bar{u}, w\rangle = \langle v, w\rangle, \qquad (\text{all } w \in \mathbf{W}). \tag{2}$$

The space $\mathbf{W}$ is open to choice so the weak reformulation permits a variety of approximate solutions. The general principle is to choose a finite-dimensional subspace $\mathbf{W}_N \subset \mathbf{W}$ and to solve the finite-dimensional (subspace) version of (2) in $\mathbf{W}_N$, a subspace which actually cannot contain the range of $\mathcal{P}$, and might not even intersect it! Such approximations are particularly attractive if the inner product $\langle a, b\rangle$ is an energy product [15] or a product integral, as illustrated by the following example.

2.2. Boundary-value problems.

The finite element method was first applied to boundary-value problems of differential equations, of a class illustrated by the mixed boundary value problem of Fig. 2. Here

$$\nabla^2 u = v \quad \text{in } \Omega, \quad \text{with } u = 0 \quad \text{on } \partial_D, \qquad \frac{\partial u}{\partial n} = 0 \quad \text{on } \partial_N. \tag{3}$$

The solution u of (3) lies in a Hilbert space whose inner product is conveniently defined by the simple product integral

$$\langle a, b\rangle = \int_\Omega ab\, d\Omega. \tag{4}$$

Taking inner products on both sides with every possible $w \in \mathbf{W}$ in turn,

$$\int_\Omega w\nabla^2 u\, d\Omega = \int_\Omega wv\, d\Omega, \quad (\text{all } w \in \mathbf{W}), \tag{5}$$

and applying Green's second identity to the left-hand member, there results

$$\int_\Omega \operatorname{grad} w \cdot \operatorname{grad} \bar{u}\, d\Omega + \int_\Omega wv\, d\Omega - \oint_{\partial\Omega} w \operatorname{grad} \bar{u} \cdot \mathbf{dS} = 0. \tag{6}$$

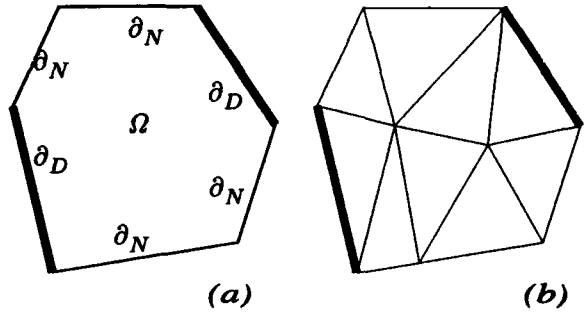

Fig. 2. (a) Simply connected two-dimensional region Ω. (b) One possible subdivision of Ω into triangular finite elements.

A key point to note is that $\langle \mathcal{P}\bar{u}, w\rangle$ is well defined by (6) even if $\bar{u}$ is only once differentiable, while $\nabla^2\bar{u}$ is not defined! This permits great freedom in choosing approximations for $\bar{u}$. However, to ensure the boundary conditions are satisfied it is still necessary to restrict the space $\mathbf{W}$ by requiring the boundary and bulk integrals in (6) to vanish independently,

$$\int_\Omega \operatorname{grad} w \cdot \operatorname{grad} \bar{u}\, d\Omega = -\int_\Omega wv\, d\Omega \tag{7}$$

(for all w)

$$\oint_{\partial\Omega} w \operatorname{grad} \bar{u} \cdot \mathbf{dS} = 0, \qquad \partial\Omega = \partial_N \cup \partial_D. \tag{8}$$

Nothing in Green's second identity enforces the Dirichlet boundary condition $u = 0$; consequently, this condition must be explicitly imposed on the approximate solution. However, the surface integral (8) corresponding to the Neumann boundary condition appears naturally in the weak formulation. Consequently the Neumann boundary condition of eqn. (3) is termed a *natural* boundary condition, while the Dirichlet boundary condition is termed *principal* or *essential*.

Reformulation through Green's second identity weakens the continuity requirements on $\bar{u}$ but places stronger demands on w than on v: w must be once differentiable while v in the original boundary value problem (3) need not even be continuous. In fact the differentiability required by (6) is precisely equal for $\bar{u}$ and w. This suggests the weak solution may be sought in the space $\mathbf{W}$ itself. To summarize, $\mathbf{W}$ has three key properties in this problem: (1) its member functions are once differentiable, (2) they vanish on ∂_D, (3) the closure of $\mathbf{W}$ includes the range of $\mathcal{P}$. This weakened continuity requirement on u (which incidentally accounts for the strange name *weak form*) thus allows twice-differentiable solutions to be approximated by functions which do not themselves possess his property.

2.3. Finite element methods.

To obtain an approximate weak solution $\tilde{u} \simeq \bar{u}$, the problem region Ω is partitioned into nonoverlapping, simply connected *finite elements* Ω_i,

$$\Omega = \bigcup_i \Omega_i. \tag{9}$$

A finite set $\{\alpha_k \mid k = 1, \ \ldots, \ N\}$ of approximating functions is defined to span $\mathbf{W}_N$, a finite subspace of $\mathbf{W}$. These functions must possess as high a degree of continuity as the weak form requires, and must satisfy all the principal boundary conditions. (In the example, $\alpha_k \in \mathbf{C}^0$, and $\alpha_k = 0$ on ∂_D, suffices). A large part of the literature of finite elements deals with systematic methods for partitioning Ω into elements and generating approximating functions on them. One popular method is to construct interpolation functions on an element-by-element basis so that the function values along the boundaries of each element will match the function values along the edges of its adjoining elements. Ensuring function continuity turns out to be quite easy, but it is surprisingly difficult to construct approximating functions with continuous derivatives.

Once the finite element function space $\mathbf{W}_N$ has been constructed, the weak solution is approximated by the finite summation

$$\tilde{u} = \sum_k^N u_k \alpha_k. \tag{10}$$

Equation (7) then yields

$$-\sum_k^N \int_\Omega \operatorname{grad} \alpha_j \cdot \operatorname{grad} \alpha_k \, d\Omega \, u_k = \int_\Omega \alpha_j v \, d\Omega. \tag{11}$$

Since the integrals can be evaluated immediately, this may be regarded as a matrix equation and solved by the usual methods of numerical linear algebra. More generally, boundary-value problems in the scalar Helmholtz equation

$$(\nabla^2 + k^2)u = v \tag{12}$$

take the matrix form

$$(\mathbf{S} + k^2\mathbf{T})\,\mathbf{u} = \mathbf{v} \tag{13}$$

where

$$\begin{aligned} S_{jk} &= -\int_\Omega \operatorname{grad} \alpha_j \cdot \operatorname{grad} \alpha_k \, d\Omega, \\ T_{jk} &= \int_\Omega \alpha_j \alpha_k \, d\Omega, \\ v_k &= \int_\Omega v \alpha_k \, d\Omega. \end{aligned} \tag{14}$$

Most of the computing time is usually expended in solving the matrix equation, so a good deal of effort has been devoted to the development of methods able to exploit the algebraic and topological peculiarities of $\mathbf{S}$ and $\mathbf{T}$. These depend both on the physical problem class, and on the type of finite elements used.

3. Element Types

Finite elements used for electromagnetics initially resembled those used in structural mechanics, but differences in the underlying physical problems rapidly led to development of distinctive element types. It is probably fair to say that almost all work in electromagnetics has used distinctive elements since about 1970. The basic differences between scalar and vector problems, as well as between those of spatially infinite or finite extent, have led to

several families of fundamentally different elements.

3.1. Scalar Lagrangian simplexes

Scalar potential or wave problems have traditionally been solved using approximating functions based on Lagrangian interpolation polynomials. A family of interpolation polynomials ψ_i on some finite element Ω is associated with a point set $\mathbf{P}: \{P_i \mid P_i \in \Omega, i = 1, \ldots, K\}$ such that $\psi_i(P_j) = \delta_i^j$ (Kronecker delta). Aside from their computational advantages, interpolation polynomials are esthetically pleasing because all computed numbers represent physically significant quantities, e.g., local potential values. On the finite element Ω of Fig. 3(a), for example, the function ϕ is modeled by

$$\phi = \sum_i \phi(P_i)\psi_i, \tag{15}$$

so the coefficient that accompanies ψ_i is the value of ϕ at point P_i.

Interpolative finite element approximating functions are defined on an element-by-element basis so as to satisfy the principal continuity requirements at element boundaries. Suppose an interelement boundary is shared by two distinct elements Ω_i and Ω_j used to model some scalar function ϕ. Function continuity is assured if the function value at every interface point is determined entirely by the nodal values on that interface. For example, along the (one-dimensional) edge between two-dimensional elements of Fig. 3(b), the approximated function ϕ is a cubic polynomial in the distance s along the edge; the four coefficients of this cubic function are determined by the four nodal potential values associated with the edge.

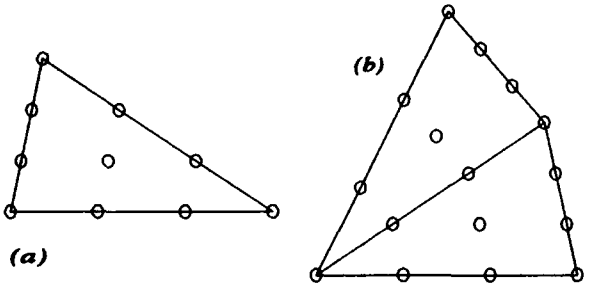

Fig. 3. (a) Triangular finite element with cubic interpolation node set. (b) Shared nodes of two cubic elements allow cubic interpolation on the interelement boundary.

Interpolation functions for simplex elements (lines, triangles, and tetrahedra) are readily derived by an extension into d dimensions of the classical Lagrangian interpolation theory [16]. Interpolation nodes are placed on the element in a regular array, as in Fig. 3(a). This procedure is best carried out in homogeneous coordinates $\zeta_1, \zeta_2, \ldots, \zeta_{d+1}$ attached to the simplex. These span the range $0 \leq \zeta_i \leq 1$ in any simplex and allow producing "universal" matrices that only need to be multiplied by a few geometric properties to produce the complete matrix representation of any simplicial finite element.

Establishing finite element matrices involves extensive algebraic manipulation of polynomials, an almost embarrassingly obvious application of computer algebra, which has indeed been used since the days of the Formac language [17]. By the late 1980s MACSYMA was routinely used for element generation in applied mechanics but electrical engineers rarely took any interest in this approach. Early developments in mechanics were reviewed by Noor and Andersen [18], and the state of the art in electromagnetics is covered by a more recent review paper [19]. Symbolic algebra will probably have a major impact on finite elements for electrical engineering applications in years to come.

3.2. Flexible elements

Although simplicial elements permit modeling of quite complicated geometric shapes, they are necessarily restricted to rectilinear interfaces and do not represent curved surfaces very well. The conventional solution to this problem, due to Ergatoudis, Irons and Zienkiewicz [20], is based on the simple observation that any Cartesian space coordinate, or indeed any linear measure of distance s, is (trivially) a linear function of the Cartesian coordinates x, y, z. It may therefore be expressed in terms of the finite element interpolation functions,

$$s(P) = \sum_i s(P_i)\,\psi_i(x_P, y_P, z_P), \tag{16}$$

where x_P, y_P, z_P are the coordinates of the point P. If the functions ψ_i are quadratic or higher polynomials, then (16) can express coordinate transformations which allow derivation of curvilinear elements from rectilinear ones. For example, the triangular element of Fig. 4(a) is mapped into the curved triangle of Fig. 4(b) by such a transformation. These elements are known as *isoparametric* because the *same* approximating functions are used to model the geometric shape and the fields to be determined. Isoparametric elements were used in magnetic field problems at an early date [21], and have remained in use by several working groups.

Their element matrices are obtained by the same process as previously. However, their evaluation is computationally more demanding because the integrations must be carried out numerically.

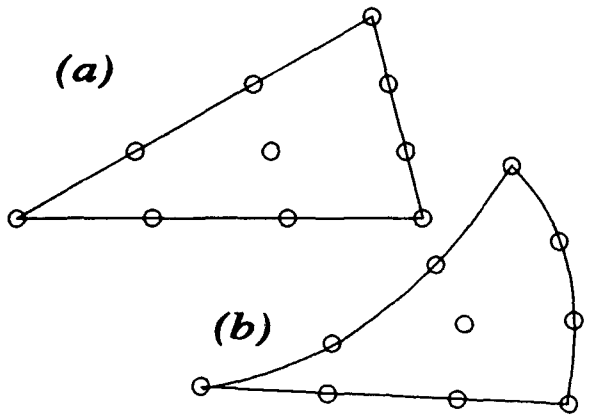

Fig. 4. Isoparametric element generation. (a) Rectilinear (simplicial) parent element. (b) Isoparametric triangle derived by coordinate mapping.

Accuracy improvement in finite element analysis may be sought by refining the mesh. Alternatively, the analysis may be repeated using elements of higher order. In this *hierarchal* elements are valuable. Their approximating functions ψ_i are constructed in nested families, so that the functions of polynomial order n are a proper subset of the functions of order $n+1$. Such functions were first pioneered by Rossow and Katz [22] and have developed considerably since [23]. Because the approximating functions form nested families, programs can be organized to compute only the projection of the weak solution onto the newly added functions, not to repeat the entire calculation, when moving to a higher-order approximation.

3.3. Geometrically infinite elements

Electromagnetic fields often extend over infinite geometric regions. Even static field problems often lack clearly defined finite boundaries, while an infinite region is the very essence of radiation and propagation problems. Several methods have accordingly been developed for handling what might be called "infinite finite elements", i.e., elements that encompass finite energy or power in a geometrically infinite space. These, and related methods from civil engineering practice, were reviewed by Emson [24].

Consider the ribbon transmission line of Fig. 5(a). To find the fields surrounding it, all the infinite-element methods encase the line in an artificial delimiting surface that subdivides all space into a finite interior and an infinite exterior region. The interior is handled by conventional finite element techniques. For the exterior region several techniques are available, of which at least four are properly convergent: (1) hybrid representations, (2) recursive growth, (3) inversion mapping, (4) special boundary conditions. All may be viewed as ways to find *boundary elements* which correctly (but implicitly) represent the effect of the exterior field on values in the interior region.

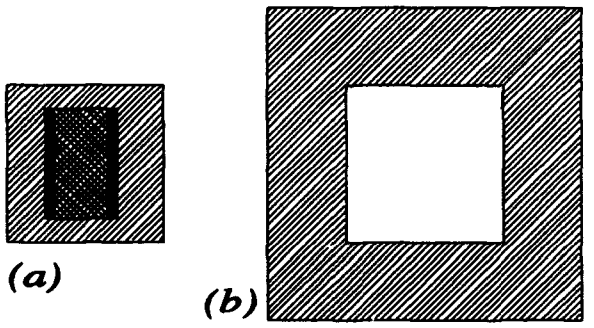

Fig. 5. (a) An artificial boundary encases the region of interest. (b) Space exterior to the artificial boundary is represented as an infinitely-extending element.

The hybrid technique describes the field by differential equations in the interior portion, integral equations in the exterior. This means choosing a set of approximating functions $\{\beta_i \mid i = 1, \ldots, M\}$ to satisfy the field equations exactly in the exterior and to match the interior element functions α_j along the exterior-interior interface. This procedure [25] was introduced and implemented around 1970 and has been extended variously since. For example, the exterior functions may be chosen to satisfy the field equations exactly, but match the interior elements only at the element nodes, not everywhere on the interface [26]; in this case, they may be expressed as orthogonal series expansions [27] or (in two dimensions) circular harmonics. The major difficulty in element formation is the evaluation of integrals containing Green's function singularities. These may be dealt with by geometric transformations [28] or by generating special weighted quadrature formulae [29]; or alternatively, by an ingenious scheme of using double boundaries [30].

Recursive growth algorithms model the exterior as a nested sequence of convex shells or annuli. They alternately add a shell and eliminate unwanted exterior variables, so that the memory required during construction of the exterior element with N_b boundary nodes never exceeds $9N_b^2$. The result is an extremely large, though still finite, exterior region [31]. Its growth rate in recursion can be doubly exponential, so that only a few recursion steps suffice to achieve immensely large exterior regions. The method is applicable to propagating-wave problems, provided an approximate radiation condition is attached to the outermost boundary and the growth of element size is controlled according to certain stability rules [32]. It has been used to solve waveguide problems [33,34] as well as two or three dimensional propagation.

Inversion mappings first appeared in Maxwell's *Treatise*. A circular or spherical boundary of radius R is drawn around the interior region and the exterior is mapped into a finite region by inverting all radial distances r with respect to this radius:

$$r' = \frac{R^2}{r}. \tag{17}$$

The differential equation governing the exterior region is transformed accordingly, and finite elements are constructed for this transformed equation. Two coupled boundary-value problems of the interior type thus result [35]. The restriction on boundary shape can be removed; non-circular boundary shapes have been proposed by Imhoff *et al.* [36], and a fairly complete theory of alternative shapes was developed by Stochniol [37].

In propagating-wave problems, the method of *absorbing boundary conditions* has recently gained great popularity. This method was initially developed by Bayliss and his associates [38,39], and augmented by other workers [40]. A review of the available variants of this method was given by Cooray and Costache [41]. Here a boundary element is created on which the wave function and its first derivatives are so related as to minimize the local reflection coefficient. A normally-directed outgoing wave is then *absorbed* by the boundary, much as a wave is absorbed by dissipative material in an anechoic room.

3.4. Vector operators and elements

A difficulty encountered with weak-form equivalents to boundary-value problems, and apparently peculiar to electromagnetic field problems, is the existence of *spurious modes*. These physically impossible solutions arise because weak solutions of the Helmholtz equation need not satisfy all four Maxwell equations even though the corresponding strong solutions do. Koshiba, Hayata and Suzuki [42] reviewed the literature and methodology of this problem in the context of waveguides, where this problem was first observed in the 1960s. It has been pointed out more recently that deterministic problems can suffer from the non-physical modes equally well [43]. This should not be surprising, given that the matrix representations of the eigenvalue problem of guided waves, and the deterministic problem of forced fields, involve the same finite element matrices and therefore have the same eigenfunction spectra. The spurious mode problem and its solutions will be dealt with in detail further below.

4. Applications to Magnetics

Finite elements have been applied to problems of applied magnetics, to waveguides and resonators, to antennas and scatterers; there is also a substantial literature in the area of semiconductor process modeling. This review concentrates mainly on the popular area of microwave and optical devices, but it must include certain parts of magnetics — most notably the eddy current problem — because they involve the same mathematical difficulties.

The early papers of Chari and Silvester [9,44] that dealt with finite element applications to magnetic field analysis were followed up by other workers fairly quickly. By 1990 this had become the dominant numerical method for magnetics problems, and now accounts for nearly half the finite element literature in electromagnetics. The central problem here is to solve the magnetic vector potential equation

$$\mathrm{curl}\left(\frac{1}{\mu_r}\mathrm{curl}\,\mathbf{A}\right) - \mu_0 g\frac{\partial \mathbf{A}}{\partial t} = \mu_0 \mathbf{J}, \tag{18}$$

subject to appropriate boundary conditions. Konrad [45] has reviewed this field well, though in view of recent rapid growth, that review has now become dated.

Although the magnetic flux density **B** due to a given set of currents is clearly unique, the accompanying vector potential **A** is open to choice of gauge and therefore not unique. Gauge transformations are introduced by specifying the divergence of **A**. Because the curl of **A** must always equal the flux density **B**, these two specifications define **A** unequivocally. A typical choice is

$$\operatorname{div} \mathbf{A} = -\mu g V - \mu\epsilon \frac{\partial V}{\partial t}, \tag{19}$$

where V is the electric scalar potential. Numerous other choices are possible. However, they all have the same form in classical two-dimensional magnetostatics, where **A** is time-invariant and possesses only one component. This situation characterizes a large class of useful problems in electromechanics and the electric machines community in particular adopted the finite element method at an early date. It was widely assumed that three-dimensional problems would be solvable by straightforward extensions of the techniques that worked so well in two dimensions, and that it was merely a matter of waiting for computing machines to grow large and powerful enough to handle three-dimensional problems. This supposition, however, proved false. Initial attempts to solve three-dimensional problems largely ignored the question of gauge [46]; in other words, they allowed the computer to choose the gauge through arithmetic chance and roundoff error. The resulting values of **A**, of course, are irreproducible, though **B** is well defined. The gauge problem and the associated choice of potential formulation may now be regarded as solved [47,48] — so far as any problem in technology is ever solved — but it has taken almost a decade to establish what methods are actually useful and correct.

This area has produced a large number of software packages for general use by design engineers and analysts, experts in magnetics with little knowledge of finite element methods. A recent survey of the available techniques was given by Tsukerman, Konrad, Bedrosian and Chari [49] while both the methods and the available software packages were comprehensively reviewed by Tseng [50].

5. Microwave and Optical Components

Optical and microwave applications of finite elements are now considered in detail. Microwave devices were indeed the first class of electromagnetic field problem solved by finite element methods [6]. Daly [51] analyzed wave propagation in microstrip lines at an early date, and the hollow waveguide problem attracted sufficient analysis to merit a review paper [52] shortly thereafter. Stone [53] extended the methodology to acoustic guided waves and Konrad determined the fields in cavity resonators [54]. Antenna analysis by finite elements lay dormant after an early start [55], but has recently blossomed. The review by Glisson [56] indicates much valuable material, though unfortunately it is already becoming dated. More recently, finite elements have had particularly strong impact in the analysis of optical waveguides [57] and related devices. Recent texts on finite elements applied to microwave and optical frequencies are by Davies [58] and a comprehensive treatment by Koshiba [59].

The microwave and optical component problems [60] addressed here include *(a)* waveguide that is uniform in z, where a modal approach is appropriate, *(b)* resonators and *(c)* closed scattering problems (e.g., finding the scattering matrix for a transmission filter). Problem *(a)* is quasi-two-dimensional while *(b)* and *(c)* are very closely related and genuinely 3-D in nature.

5.1. Uniform waveguide

To consider item *(a)* of the list above, the following four examples will be examined:

(i) hollow conducting waveguide (e.g. hollow ridged waveguide)
(ii) conductors coexisting with $\epsilon(x,y)$ (e.g. microstrip and coplanar waveguide)
(iii) optical waveguide $\epsilon(x,y)$ (e.g. rib or channel waveguide)
(iv) nonlinear optical guide $\epsilon(x,y,|\mathbf{E}|)$ where permittivity ϵ depends on optical power level.

Firstly to clarify the problem being considered [61,62]: it is a uniform optical or microwave guide, where the structure is strictly uniform in z (as declared in (i) to (iv) above), and modes are being looked for, defined by

$$\begin{aligned} \mathbf{E}(x,y,z,t) &= \mathbf{e}(x,y) \exp j(\omega t - \beta z) \\ \mathbf{H}(x,y,z,t) &= \mathbf{h}(x,y) \exp j(\omega t - \beta z) \end{aligned} \tag{20}$$

Finite elements have been applied mostly by using a variational approach and many formulations have been used [61], generally in terms of one of the six: **H**; **E**; **H** and **E**; H_z and E_z; $\mathbf{H}_t$; $\mathbf{E}_t$; or $\mathbf{H}_t$ and $\mathbf{E}_t$. There is no best choice, but the most common is the following variational form (with *s.v.* denoting "stationary value of") [63]:

$$\omega^2 = s.v. \frac{\iiint (\operatorname{curl} \mathbf{H})^* \| \epsilon \|^{-1} (\operatorname{curl} \mathbf{H})\, d\Omega}{\iiint \mathbf{H}^* \| \mu \| \mathbf{H}\, d\Omega}. \tag{21}$$

A feature of this formula for optics is that, although ϵ is inhomogeneous, μ is invariably constant, so that physically **H** is continuous everywhere. This eases the finite element representation, as all three components of **H** are now continuous. As the permittivity enters as a simple multiplying factor in the numerator, quite arbitrary $\epsilon(x,y)$ can be included with negligible additional computing cost. Anisotropic dielectric has commonly to be modeled in optics, and this gives no problem with formulation (21) providing only that the material is everywhere lossless. To use formulation (21) one chooses a propagation constant β which gives the z-dependence of all fields. Applying finite elements across the waveguide cross-section with the Rayleigh-Rits method gives the following matrix equation:

$$\mathbf{A}\mathbf{v} = \omega^2 \mathbf{B}\mathbf{v} \tag{22}$$

B is real, symmetric and positive-definite, while **A** is Hermitian but can usually be reduced to real, symmetric. One then has a range of quite excellent matrix algorithms for numerical solution.

By far the most serious difficulty with a finite element (or almost any other) procedure based on (21) is the occurrence of many spurious modes which come from the numerical procedure. These have already been referred to, and we will return later to this difficulty, but the chief trouble is with non-physical solutions which do not satisfy the divergence condition [64]. (Another class of 'spurious modes' cluster around zero frequency, but these are less troublesome, and again will be referred to later.) Unfortunately the number of spurious modes increases with finite element mesh density and matrix order, so that any desire for high accuracy is accompanied by persistent difficulties. For many years this failure has been rectified by adding a *penalty term* [65] to give [66,67]

$$\omega^2 = s.v.\left\{ \frac{\iiint (\mathrm{curl}\,\mathbf{H})^* \| \epsilon \|^{-1} (\mathrm{curl}\,\mathbf{H})\, d\Omega}{\iiint \mathbf{H}^* \| \mu \| \mathbf{H}\, d\Omega} + \frac{p\epsilon_0^{-1} \iiint (\mathrm{div}\,\mathbf{H})^* (\mathrm{div}\,\mathbf{H})\, d\Omega}{\iiint \mathbf{H}^* \| \mu \| \mathbf{H}\, d\Omega} \right\} \tag{23}$$

The penalty parameter p shifts the spectrum of all modes, but most strongly the spurious modes. The user can therefore 'filter out' the unwanted modes. Theoretically all now seems respectable — the required constraint has been added in a classic least-squares sense, with little additional computational effort. Although the penalty function is widely used in finite element work, in this context the whole procedure is neither numerically robust nor mathematically elegant.

Much effort has gone into the proper removal of spurious modes from the accurate approaches over the last decade. One method that retains sparsity, maintains reasonable computational economy and preserves a canonical matrix form such as eqn. (22) is to accept the original variational form of eqn. (21) but apply a more appropriate choice of basis vector functions from the armory of finite elements. This is by taking advantage of the recent introduction of edge elements [68], tangential vector finite elements (TVFE's) [69,70,71] and Whitney forms in general [72,73,74], which have transformed many applications of finite elements.

The method seems to have more relevance, and to be more comfortable, in three dimensions, as treated in section 6, rather than in two. Briefly, tangential vector finite elements (of which edge elements are the simplest subset) are a radical alternative to the nodal shape functions commonly used in finite elements. They represent the vector, not via three separate components, but as a vector which is arranged to have prescribed *tangential*, but not normal, values at the edges of the elements. Lee [72], Koshiba [75] and Hano [76] have in fact used tangential vector elements, a family of vector basis functions of which edge elements are the simplest and lowest order. It can be seen that their choice results in much more involved algebra and calculus (for evaluation of the usual element matrices) than nodal elements. Also a considerably more complicated matrix eigenvalue equation emerges, which arises from their introduction of a field transformation to obtain a canonical eigenvalue form in β^2. Some of these complications arise because of the disparity between *three*-dimensional vectors and *two*-dimensional fields.

In 1984 Hano [76] introduced a special set of finite elements. By using simple Cartesian rectangular elements, he was able to choose separate shape functions for the x, y and z components that achieved the basic aim of tangential vector elements. This was, in essence, a precursor of the edge element approach, but limited strictly to rectangular elements. Covariant projection elements were applied

to 3-D problems in 1988 [77] and applied to the waveguide problem in 1991 [78]. All eliminate the troublesome spurious modes, but leave a countable cluster of (strictly) spurious modes around zero frequency.

5.2. Uniform waveguide with nonlinear material

To illustrate the almost limitless versatility of finite elements, a more complicated problem is now taken up. In all of the above, it has been presumed that there can be a transversely varying permittivity $\epsilon(x,y)$. But *nonlinear* material, as described by $\epsilon(x,y,|\mathbf{E}|)$, is of considerable interest [79] and can similarly be solved [80,81] by using the above methods within an iterative loop, which seeks consistency between the linear solver and the specified nonlinear law for ϵ. A typical structure would have constant (with respect to field) ϵ over part of the cross-section, but a finite region would have a law such as [82]

$$\epsilon = \epsilon_{lin} + \Delta\epsilon_{sat}\left\{1 - \exp\left(-\frac{a\,|\mathbf{E}|^2}{\Delta\epsilon_{sat}}\right)\right\}. \qquad (24)$$

Clearly for any two specified values of ω, β and total power in the mode, the third parameter is an unknown eigenvalue, necessitating some iterative scheme for its solution. Finite element solutions are now being routinely produced for fairly arbitrary nonlinear laws as well as two-dimensional profiles of permittivity.

6. Three-Dimensional Structures

We now consider resonators and closed scattering problems. If we focus discussion here on the resonator, it is with the understanding that most of the aspects of finite element implementation are identical for the two classes of problem [60,83]. For any solution approach to the resonator, an analogous approach exists for the scattering problem. The main difference is that part of the resonator walls have to be removed and replaced by resistive boundary conditions (simulating a matched port) and/or by reactive impedances and/or by stipulating at the removed walls (say) the magnetic field and evaluating the consistent electric field — and so evaluating the scattering matrix. Though these considerations are not trivial, we by-pass them to consider the more fundamental issues of the finite element formulation and choice of basis functions.

The other major difference between the resonator and the evaluation of a scattering matrix is that the former leads inevitably to an eigenvalue problem — best couched into a canonical matrix equation with relevant eigenvalues. The scattering problem is essentially a deterministic, rather than eigenvalue, problem and so inevitably leads, instead of eqn. (22), to a matrix for solution of the usual deterministic form $\mathbf{Ax} = \mathbf{y}$. This is, of course, a fundamentally easier matrix equation to solve than the eigenvalue equation (22).

We therefore concentrate on solution of the typical resonator which consists of an enclosing conducting wall, with an interior of permittivity $\|\epsilon\|(x,y,z)$ and possibly (most likely at microwaves) permeability $\|\mu\|(x,y,z)$. Optical resonators can similarly be studied without metal walls, but some mathematical artifact (such as a magnetic or electric wall, if physically realistic, or an 'evanescent' infinite element [57]), is best used to avoid treatment of a lossy resonator, which loses the Hermitian formulation. As with the waveguide problem of section 5.1, finite elements have been implemented by generalized Galerkin [84,85] and variational [86,87] approaches. Unless some special requirement forces the issue, it is generally possible and advisable to use a variational approach. The same variational form of eqn. (21) can be used, or its dual form, with $\mathbf{H}$ replaced by $\mathbf{E}$, and ϵ and μ exchanged.

Again if inhomogeneity of material is purely dielectric, then the form in terms of $\mathbf{H}$ is easier by orthodox nodal elements, as the 3-vector $\mathbf{H}$ is continuous everywhere. By contrast any form using $\mathbf{E}$ would need extra care for continuity of appropriate fields and flux densities between elements However, separate use of each formulation has the advantage of bounding the true solution [70,87] and/or providing information for error signatures, relevant to the important matter of adaptive mesh generation [70].

Resonators have been studied for many years using 3-D versions of the traditional nodal elements. Just as in 2-D, where the simplest first degree elements are popular for their ultimate simplicity and ultimate sparsity of resulting matrix, so can first degree tetrahedral elements be used. Again, whether in 2-D or 3-D, first order elements fit very conveniently into a Delaunay-generated mesh of elements, especially with adaptive mesh-generators [70]. Higher order elements are also used [88], including their attractive subset, hierarchal elements, where extra nodes are added to elements, as one proceeds to higher order, without abandoning any nodes from the low orders.

Spurious modes have commonly been reported [64,89,90] with 3-D resonators just as with (quasi-)2-D problems. Clearly less work has been reported on 3-D numerical work than on 2-D, because of the heavier computing demands of the former. Spurious solutions can be avoided or alleviated by the use of edge elements, which will be briefly described next.

6.1. Edge and tangential vs. nodal elements

So far in the vast majority of finite element work, nodal or scalar shape functions have been used [85], as already described. For a vector field, whether **H**, **E**, **B**, **D**, **A** or **J**, the conventional scheme has been to represent the vector as three separate scalars in the standard nodal manner. Analytically exact and conventional as this procedure is, it grates — it is uneasy in this context. In contrast, there are alternative schemes for directly expanding vectors in terms of vector forms.

Whitney forms [70,74,75] span the relevant possibilities of continuity between elements related to the grad, curl and div operators. W^0 forms are spaces of scalar basis functions that are continuous, without continuous derivatives, between elements. W^1 forms are spaces of vector functions that have continuity of tangential components, but not normal components, between elements. W^2 forms are vector functions having continuity of their normal components only between elements. W^3 forms are of scalar functions without continuity between elements. Working with tetrahedral elements, as we progress through the forms W^0, W^1, W^2, W^3 we go through W^0 which is nodal-based, W^1 which is edge-based, W^2 which is facet-based, and W^3 which is volume-based. Their intimate connection also comes from the fact that the gradient of a 0-Whitney form is a (combination of) 1-Whitney forms, the curl of a W^1 form is a W^2 form, and the divergence of a W^2 form is a W^3 form.

We illustrate with just one particular Whitney form W^1 called the *edge element*. It is a first degree polynomial form. The objective is to develop a vector representation that assures that across any face between adjacent finite elements, the tangential part (only) of the vector is continuous. This will be perfectly appropriate for representing **H** or **E**.

Consider a tetrahedron as in Fig. 6 with vertices 1 to 4 and edges 1 to 6. For node i, we first use the so-called barycentric coordinate ζ_i which has value 1 at node i, is zero over all tetrahedra not containing node i, and varies linearly over tetrahedra that contain node i. These are the local or 'volume' coordinates within the tetrahedron, so that ζ_i has unit value at node i, and varies linearly to zero at the three other vertices. To introduce the edge elements, we focus on edge 1, denoted as e_1, which joins vertices 1 and 2; associated with e_1 we introduce the vector basis function $\mathbf{w}_1$ defined over the tetrahedron by:

$$\mathbf{w}_1 = \zeta_1 \operatorname{grad} \zeta_2 - \zeta_2 \operatorname{grad} \zeta_1 \tag{25}$$

$\mathbf{w}_2$, $\mathbf{w}_3$, $\mathbf{w}_4$, $\mathbf{w}_5$ and $\mathbf{w}_6$, are similarly defined, each associated with one of the other five edges. Although $\mathbf{w}_1$ is a first degree polynomial vector field, it turns out that at all points *along* edge 1, the projection onto edge e_1 of vector $\mathbf{w}_1$ has constant value. The projections onto e_1 of vectors $\mathbf{w}_2$, $\mathbf{w}_3$, $\mathbf{w}_4$, $\mathbf{w}_5$ and $\mathbf{w}_6$ are all zero. Equation (25) therefore gives a vector substitute for the interpolatory shape functions of nodal elements,

$$\mathbf{V}(\zeta_1,\zeta_2,\zeta_3,\zeta_4) = \sum_i v_i \mathbf{w}_i \tag{26}$$

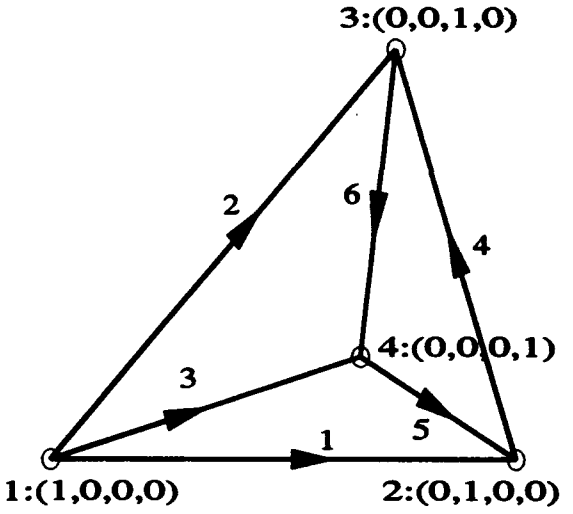

Fig. 6. Tetrahedron vertices (with local coordinates $\zeta_1,\zeta_2,\zeta_3,\zeta_4$) and directed edges.

On any edge e_i **V** will assume a value that varies; but the component (or projection) along e_i will remain constant and equal to $v_i \mathbf{u}_i$, where $\mathbf{u}_i$ is the unit vector directed along edge i with the sense of the arrow in Fig. 6. Clearly if we use the same specifications of the v_i (called the *edge values*) of eqn. (26) for different tetrahedra sharing the same edge, the overall vector field will have a continuous tangential component of vector across edges, and similarly across faces. The normal components will

have no such enforced continuity. A special property of edge elements is that their divergence is identically zero within the tetrahedra, though not across inter-element faces.

In this section we have concentrated on edge elements in 3-D. Their extension to 2-D is straightforward, although the fact that the physical quantities are fundamentally 3-vectors makes the situation less comfortable in 2-D than 3-D. For instance it is commonly found necessary [77] to use both edge and nodal elements because of the lack of parity between transverse and longitudinal components of field. Readers are referred to the literature [71,73,77,89,90,91] for details of these Whitney and related forms.

6.2. Tangential, edge and nodal elements for resonators

A number of workers have reported successful use of edge elements for the solution of resonators [84–89]. Motives have included belief in their superiority to nodal elements because of their lack of divergence-free related spurious modes, and their more efficient representation, via their fewer free variables and/or sparsity of global matrices. If one compares edge elements (with their built-in divergence-free vector) with nodal representation of the three Cartesian components of field, there can surely, be no arguing that the component version has a fundamental redundancy and therefore inefficiency. If they also give solutions free of a serious class of spurious modes, then the edge elements have very much in their favor. Recent evidence supports their fundamental advantage.

In electromagnetics, the use of edge elements was firstly with low frequency applications, especially concerning eddy currents [92]. With resonators, use with magnetic vector field formulations, eqn. (21) or its dual form in terms of **E**, has recently led to more satisfactory results [84–89]. Universally it is reported that the spurious modes associated with non-zero divergence are totally removed. However, as mentioned earlier with the waveguide problem, when the formulation used has frequency as the resulting spectrum (as in eqn. (21) and its matrix version (22)), other spurious modes appear clustered around zero frequency. Curiously, these non-physical solutions are ignored by many workers as not being serious — as not being worthy of the title of "spurious"! They are indeed less troublesome, as their location in the spectrum is very confined and away from the usual region of interest.

7. Conclusions

Finite elements in electrical engineering have had a varied and interesting history. At an early stage of development, several difficult problems were encountered, such as the determination of gauge in vector potential problems and the appearance of spurious modes in solutions of the Helmholtz equation. It has taken nearly twenty years to master these difficulties, and their solutions point the way for other, still more valuable, methods.

Incompletely solved problems of considerable importance now include general methods for (1) orthospectral elements, (2) field singularities, (3) boundary integrals, including absorbing boundaries. Several particular element types free of spurious modes are known and used, but the generation of families of such elements has still eluded analysts. Much the same can be said for singular elements. In the formation of boundary integrals, similar difficulties of integration are encountered as with field singularities. All three areas should prove fertile ground for the application of symbolic algebra. Given the current near-ubiquity of computer algebra systems, there appears to be every reason for optimism for their further development for finite element methods in electromagnetics.

In the use of finite elements for computation of high-frequency waveguides and 3-D structures there have been both major achievements and serious difficulties. As computing power has increased it has made more important the *robustness* of methods used, so that human intervention is eliminated from the inner shells of the computation. In this context it is believed that the introduction of vector finite element forms (or allied forms) will improve the performance of many codes when, as in electromagnetics, vector fields are inevitably involved. The case is more powerful in three dimensions than in two-dimensional problems. There are eloquent arguments for Whitney or equivalent vector forms with their basis in differential forms. Computational results have only appeared in the last three years or so, but hopefully the practical impact will soon be assessed, then these issues will be clarified or simplified, as were similar issues with nodal finite elements when they first appeared.

8. References

[1] R.L. Courant: 'Variational methods for the solution of problems of equilibrium and vibration.' *Bulletin of the American*

Mathematical Society, vol. **49**, pp. 1–23, 1943.

[2] R.J. Duffin: 'Distributed and lumped networks.' *Journal of Mathematics and Mechanics*, vol. **8**, pp. 793–826, 1959.

[3] R.J. Duffin and T.A. Porsching: 'Bounds for the conductance of a leaky plate via network models.' *Proceedings, Symposium on Generalized Networks.* Brooklyn: Polytechnic Press, 1959. Pp. 417–442.

[4] J.L. Synge: *The Hypercircle in Mathematical Physics.* Cambridge: Cambridge University Press, 1957.

[5] A.M. Winslow: 'Numerical solution of the quasilinear Poisson equation on a nonuniform triangle mesh.' *Journal of Computational Physics*, vol. **2**, pp. 149–172, 1967.

[6] P. Silvester: 'Finite-element solution of homogeneous waveguide problems.' *Alta Frequenza*, vol. **38**, pp. 313–317, 1969.

[7] P. Silvester and M.V.K. Chari: 'Finite element solution of saturable magnetic field problems.' *IEEE Transactions on Power Apparatus and Systems*, vol. **PAS-89**, pp. 1642–1651, 1970.

[8] Z.J. Csendes and P. Silvester: 'Numerical solution of dielectric loaded waveguides. I — Finite-element analysis.' *IEEE Transactions on Microwave Theory and Techniques*, vol. **MTT-19**, pp. 504–509, 1971.

[9] P. Benedek and P. Silvester: 'Capacitance of parallel rectangular plates separated by a dielectric sheet.' *IEEE Transactions on Microwave Theory and Techniques* vol. **MTT-20**, pp. 504–510, 1972.

[10] P. Silvester and K.K. Chan: 'Bubnov-Galerkin solutions to wire-antenna problems.' *Proceedings IEE*, vol. **119**, pp. 1095–1099, 1972.

[11] M. Zlámal: 'On the finite element method.' *Numerische Mathematik*, vol. **12**, pp. 394–409, 1968.

[12] J.R. Whiteman [ed.]: *The mathematics of finite elements and applications.* London: Academic Press, 1973.

[13] P.C. Ciarlet: *The finite element method for elliptic problems.* Amsterdam: North Holland, 1978.

[14] M.A. Krasnosel'skii, G.M. Vainikko, P.P. Zabreiko, Ya.B. Rutitskii and V.Ya. Stetsenko: *Approximate solution of operator equations.* Groningen: Noordhoff, 1972.

[15] S.G. Mikhlin and K.L. Smolitskiy: *Approximate methods for solution of differential and integral equations.* New York: Elsevier, 1967.

[16] P. Silvester: 'High-order polynomial triangular finite elements for potential problems.' *International Journal of Engineering Science*, vol. **7**, pp. 849–861, 1969.

[17] A. Konrad and P. Silvester: 'Triangular finite elements for the generalized Bessel equation of order *m*.' *International Journal for Numerical Methods in Engineering*, vol. **7**, pp. 43–55, 1973.

[18] A.K. Noor and C.M. Andersen: 'Computerized symbolic manipulation in nonlinear finite element analysis.' *Computers and Structures*, vol. **13**, pp. 379–403, 1981.

[19] P.P. Silvester: 'Computer algebra in finite element software construction.' *International Journal for Applied Electromagnetics in Materials*, vol. **3**, 1992 [in press].

[20] I. Ergatoudis, B.M. Irons and O.C. Zienkiewicz: 'Curved isoparametric 'quadrilateral' elements for finite element analysis.' *International Journal of Solids and Structures*, vol. **4**, pp. 31–42, 1968.

[21] P. Silvester and P. Rafinejad: 'Curvilinear finite elements for two-dimensional saturable magnetic fields. *IEEE Transactions on Power Apparatus and Systems*, vol. **PAS-93**, pp. 1861–1870, 1974.

[22] M.P. Rossow and I.N. Katz: 'Hierarchal finite elements and precomputed arrays.' *International Journal for Numerical Methods in Engineering*, vol. **12**, pp. 977–999, 1978.

[23] J.P. Webb and S. McFee: 'The use of hierarchal triangles in finite-element analysis of microwave and optical devices.' *IEEE Transactions on Magnetics*, vol. **27**, pp. 4040–4043, 1991.

[24] C.R.I. Emson: 'Methods for the solution of open-boundary electromagnetic-field problems.' *IEE Proceedings*, part A, vol. **135**, pp. 151-158, 1988.

[25] P. Silvester and M.-S. Hsieh: 'Finite-element solution of 2-dimensional exterior-field problems.' *Proceedings IEE*, vol. **118**, pp. 1743–1747, 1971.

[26] K.K. Mei: 'Unimoment method of solving antenna and scattering problems.' *IEEE Transactions on Antennas and Propagation*, vol. **AP-22**, pp. 760–766, 1974.

[27] J.B. Davies and M. Patwari, 'Scattering by infinite cylinders of arbitrary cross-section by the method of finite differences.' *Electronics Letters*, vol. **1**, pp. 60–61, May 1965.

[28] P. Silvester and M.-S. Hsieh: 'Projective solution of integral equations arising in electric and magnetic field problems.' *Journal of Computational Physics*, vol. **8**, pp. 73–82, 1971.

[29] P.P. Silvester: 'Weighted Gaussian quadratures for singular and near-singular integrands.' *International Journal of Numerical Modelling*, vol. **2**, pp. 131–142, 1989.

[30] B.H. McDonald and A. Wexler: 'Finite element solution of unbounded field problems.' *IEEE Transactions on Microwave Theory and Techniques*, vol. **MTT-20**, pp. 841–847, 1972.

[31] P.P. Silvester, D.A. Lowther, C.J. Carpenter and E.A. Wyatt: 'Exterior finite elements for two-dimensional field problems with open boundaries.' *Proceedings IEE*, vol. **124**, pp. 1267–1270, 1977.

[32] C.I. Goldstein: 'The finite element method with non-uniform mesh sizes applied to the exterior Helmholtz problem.' *Numerische Mathematik*, vol. **38**, pp. 61–82, 1981.

[33] C.I. Goldstein: 'Finite element methods applied to nearly one-way wave propagation.' *Journal of Computational Physics*, vol. **64**, pp. 56–81, 1986.

[34] S.L Foo and P.P. Silvester: 'Boundary-marching method for discontinuity analysis in waveguides of arbitrary cross section.' *IEEE Transactions on Microwave Theory and Techniques*, vol. **40**, pp. 1889–1993, Oct. 1992.

[35] I.R. Ciric and S.H. Wong: 'Inversion transformation for the finite-element solution of three-dimensional exterior-field problems.' *COMPEL*, vol. **5**, pp. 109-119, 1986.

[36] J.F. Imhoff, G. Meunier, X. Brunotte and J.C. Sabonnadiere: 'An original solution for unbounded electromagnetic 2-D and 3-D problems throughout the finite element method.' *IEEE Transactions on Magnetics*, vol. **25**, pp. 4135–4137, 1989.

[37] A. Stochniol: 'An efficient open boundary finite element method for electromagnetic problems.' *COMPEL*, vol. **11**, pp. 53–56, 1991.

[38] A. Bayliss and E. Turkel: 'Boundary conditions for exterior acoustic problems.' *Advances in Computer Methods for Partial Differential Equations III.* [R. Vichnevetsky and R.S. Stepelman, eds.] Pp. 127–131. New Brunswick, NJ: IMACS, 1979.

[39] A. Bayliss, M. Gunzburger and E. Turkel: 'Boundary conditions for the numerical solution of elliptic equations in exterior regions.' *SIAM Journal on Applied Mathematics*, vol. **42**, pp. 430–451, 1982.

[40] J.E. Santos, J. Douglas, Jr., M. Morley and O.M. Lovera: 'Finite element methods for a model for full waveform acoustic logging.' *IMA Journal of Numerical Analysis*, vol. **8**, pp. 415–433, 1988.

[41] F.R. Cooray and G.I. Costache: 'An overview of the absorbing boundary conditions.' *Journal of Electromagnetic Waves and their Applications*, vol. **5**, pp. 1041–1054, 1991.

[42] M. Koshiba, K. Hayata and M. Suzuki: 'Finite-element method analysis of microwave and optical waveguides — trends in countermeasures to spurious solutions.' *Electronics and Communications in Japan, 2, Electronics*, vol. **70**, no 9, pp. 96-108, 1986. [Translation of article in *Trans. Inst. Electron. & Commun. Eng. Japan*, Part C, vol. **J69C**, pp. 1477–1486, 1986.]

[43] A.R. Pinchuk, C.W. Crowley and P.P. Silvester: 'Spurious solutions to vector diffusion and wave field problems.' *IEEE Transactions on Magnetics*, vol. **MAG-24**, pp. 158–161, 1988.

[44] M.V.K. Chari and P. Silvester: 'Finite-element analysis of magnetically saturated d-c machines'. *IEEE Transactions on Power Apparatus and Systems*, vol. **PAS-90**, pp. 2362–2372, 1971.

[45] A. Konrad: 'Electromagnetic devices and the application of computational techniques in their design.' *IEEE Transactions on Magnetics*, vol. **MAG-21**, pp. 2382-2387, 1985.

[46] M.V.K. Chari, A. Konrad, J. D'Angelo and M. Palmo: 'Finite element computation of three-dimensional electrostatic and magnetostatic field problems.' *IEEE Transactions on Magnetics*, vol. **MAG-19**, pp. 2321–2324, 1983.

[47] O. Biró and K. Preis: 'Finite element analysis of 3-D eddy currents.' *IEEE Transactions on Magnetics*, vol. **26**, pp. 418–423, 1990.

[48] T. Morisue: 'The gauge and topology problem in using the magnetic vector potential.' *COMPEL*, vol. **9**, Supplement A, pp. 1–6, 1990.

[49] I.A. Tsukerman, A. Konrad, G. Bedrosian and M.V.K. Chari: 'A survey of numerical methods for transient eddy current problems.' *IEEE Transactions on Magnetics*, vol. **29**, (to appear), 1993.

[50] A.A. Tseng: 'Electroheating modeling in metal processing: a review.' *Advances in Engineering Software*, vol. **10**, pp. 58-71, 1988.

[51] P. Daly: 'Hybrid-mode analysis of microstrip by finite element methods.' *IEEE Transactions on Microwave Theory and Techniques*, vol. **MTT-19**, pp. 19–25, 1971.

[52] F.L. Ng: 'Tabulation of methods for the numerical solution of the hollow waveguide problem.' *IEEE Transactions on Microwave Theory and Techniques*, vol. **MTT-22**, pp. 322–329, 1974.

[53] G.O. Stone: 'High-order finite elements for inhomogeneous acoustic guiding structures.'

IEEE Transactions on Microwave Theory and Techniques, vol. **MTT-21**, pp. 538–542, 1973.

[54] A. Konrad: 'A linear accelerator cavity code based on the finite element method.' *Computer Physics Communications*, vol. **13**, pp. 349–362, 1978.

[55] M.A. Hassan, P. Silvester, B.A. Howarth and N. Nasu, 'Solution to the interconnected wire-scatterer problem'. *Proceedings IEE*, vol. **123**, pp. 509–514, 1976.

[56] A.W. Glisson: 'Recent advances in frequency domain techniques for electromagnetic scattering problems.' *IEEE Transactions on Magnetics*, vol. **25**, pp. 2867-2871, 1989.

[57] B.M.A. Rahman and J.B. Davies: 'Finite-element analysis of optical and microwave waveguide problems.' *IEEE Transactions on Microwave Theory and Techniques*, vol. **MTT-32**, pp. 20–28, 1984.

[58] J.B. Davies: 'Finite element method.' In: *Numerical techniques for microwave and millimeter wave passive devices* [ed. T. Itoh], Chapter 2. New York: John Wiley, 1989.

[59] M. Koshiba: *Optical waveguide theory by the finite element method.* Tokyo: KTK Scientific Publishers, 1992.

[60] R.E. Collin, *Field Theory of Guided Waves.* 2nd ed. New York: IEEE Press, 1991.

[61] B.M.A. Rahman, F.A. Fernandez and J.B. Davies: 'Review of finite element methods for microwave and optical waveguides' *Proceedings IEEE* (Special Issue on Electromagnetics), vol. **79**, pp. 1442–1448, 1991.

[62] N. Mabaya, P.E. Lagasse and P. Vandenbulcke: 'Finite element analysis of optical waveguides'. *IEEE Transactions on Microwave Theory and Techniques*, vol. **MTT-29**, pp. 600–605, June 1981.

[63] A.D. Berk: 'Variational principles for electromagnetic resonators and waveguides'. *IRE Transactions on Antennas and Propagation*, vol. **AP-4**, pp. 104–111, 1956.

[64] J.B. Davies, F.A. Fernandez and G.Y. Philippou: 'Finite element analysis of all modes in cavities with circular symmetry'. *IEEE Transactions on Microwave Theory and Techniques*, vol. **MTT-30**, pp. 1975–1980, Nov. 1982.

[65] O.C. Zienkiewicz: *The finite element method.* Chichester: McGraw-Hill, 1977.

[66] B.M.A. Rahman and J.B. Davies: 'Penalty function improvement of waveguide solution by finite elements'. *IEEE Transactions on Microwave Theory and Techniques*, vol. **MTT-32**, pp. 922–928, Aug. 1984.

[67] M. Koshiba, K. Hayata and M. Suzuki: 'Improved finite-element formulation in terms of the magnetic field vector for dielectric waveguides.' *IEEE Transactions on Microwave Theory and Techniques*, vol. **MTT-33**, pp. 227–233, Mar. 1985.

[68] A. Bossavit and I. Mayergoyz: 'Edge-elements for scattering problems' *IEEE Transactions on Magnetics*, vol. **25**, pp. 2816–2821, 1989.

[69] S.H. Wong and Z.J. Cendes: 'Combined finite element modal solution of three-dimensional eddy current problems'. *IEEE Transactions on Magnetics*, vol. **MAG-24**, pp. 2685–2687, 1988.

[70] J-F. Lee, D-K. Sun and Z.J. Cendes: 'Full-wave analysis of dielectric waveguides using tangential vector finite elements'. *IEEE Transactions on Microwave Theory and Techniques*, vol. **39**, pp. 1262–1271, Aug. 1991.

[71] Z.J. Cendes: 'Vector finite elements for electromagnetic field computation'. *IEEE Transactions on Magnetics*, vol. **27**, pp. 3958–3966, Sept. 1991.

[72] H. Whitney: *Geometric integration theory.* Princeton, NJ: Princeton University Press, 1957.

[73] A. Bossavit: 'Whitney forms: a class of finite elements for three-dimensional computations in electromagnetism'. *Proceedings IEE*, vol. **135A**, pp. 493–500, 1988.

[74] A. Bossavit: 'Solving Maxwell equations in a closed cavity and the question of spurious modes'. *IEEE Transactions on Magnetics*, vol. **26**, pp. 702–705, 1990.

[75] M. Koshiba and K. Inoue: 'Simple and efficient finite-element analysis of microwave and optical waveguides'. *IEEE Transactions on Microwave Theory and Techniques*, vol. **40**, pp. 371–377, Aug. 1991.

[76] M. Hano: 'Finite-element analysis of dielectric-loaded waveguides'. *IEEE Transactions on Microwave Theory and Techniques*, vol. **MTT-32**, pp. 1275–1279, Oct. 1984.

[77] C.W. Crowley, P.P. Silvester and H. Hurwitz: 'Covariant projection elements for 3-D vector field problems'. *IEEE Transactions on Magnetics.*, vol. **MAG-24**, pp. 397–400, Jan. 1988.

[78] R. Miniowitz and J.P. Webb: 'Covariant-projection quadrilateral elements for the analysis of waveguides with sharp edges'. *IEEE Transactions on Microwave Theory and Techniques*, vol. **39**, pp. 501–505, Mar. 1991.

[79] G.I. Stegeman and E.M. Wright: 'All-optical waveguide switching'. *Optical and Quantum*

Electronics, vol. **25**, pp. 95–122, 1990.

[80] K. Hayata and M. Koshiba: 'Full vectorial analysis of non-linear optical waveguides'. *Journal of the Optical Society of America*, pt. **A**, vol. **5**, pp. 2494–2501, Dec. 1988.

[81] R.D. Ettinger, F.A. Fernandez, B.M.A. Rahman and J.B. Davies: 'Vector finite element solution of saturable nonlinear strip-loaded optical waveguides'. *IEEE Photonics Technology Letters*, vol. **3**, pp. 147-149, Feb. 1991.

[82] R.D. Ettinger, F.A. Fernandez and J.B. Davies: 'Application of adaptive remeshing techniques to the finite element analysis of nonlinear optical waveguides'. *Directions in Electromagnetic Wave Modeling* [H.L. Bertoni and L.B. Felsen, eds.]. New York: Plenum Press, 1991.

[83] P.P. Silvester and R.L. Ferrari, *Finite Elements for Electrical Engineers*. 2nd ed. Cambridge: Cambridge University Press, 1990.

[84] J.-S. Wang and N. Ida: 'Eigenvalue analysis in anisotropically loaded EM cavities using divergence free finite elements'. *IEEE Transactions on Magnetics*, vol. **28**, pp. 1438–1441, 1993.

[85] L. Pichon and A. Razek: 'Three dimensional mode analysis using edge elements'. *IEEE Transactions on Magnetics*, vol. **28**, pp. 1493–1496, 1993.

[86] G. Mur: 'The finite element modelling of three-dimensional time-domain electromagnetic fields in strongly inhomogeneous media'. *IEEE Transactions on Magnetics*, vol. **27**, pp. 1019–1022, Mar. 1992.

[87] I. Bardi, O. Biró, K. Preis, G. Vrisk and K.R. Richter: 'Nodal and edge element analysis of inhomogeneously loaded 3-D cavities'. *IEEE Transactions on Magnetics*, vol. **27**, pp. 1031–1034, Mar. 1992.

[88] J.P. Webb: 'The finite-element method for finding modes of dielectric-loaded cavities'. *IEEE Transactions on Microwave Theory and Techniques*, vol. **MTT-33**, pp. 635–639, July 1985.

[89] Zhou Le-Zhu, J.B. Davies and F.A. Fernandez: '3-D edge element analysis of dielectric loaded resonant cavities'. *International Journal of Numerical Modelling*, [in press].

[90] G.A. Deschamps: 'Electromagnetics and differential forms'. *Proceedings IEEE*, vol. **69**, pp. 676–696, June 1981.

[91] J.F. Lee, D.K. Sun and Z.J. Cendes: 'Tangential vector finite elements for electromagnetic field computation'. *IEEE Transactions on Magnetics*, vol. **27**, pp. 4032–4035, Sept. 1991.

[92] A. Bossavit and J.C. Verite: 'A mixed FEM-BIEM method to solve 3-D eddy current problem'. *IEEE Transactions on Magnetics*, vol. **MAG-18**, pp. 431–435, 1982.

Compatibility Relations for Time-Domain and Static Electromagnetic Field Problems

Ioan E. Lager and Gerrit Mur
Faculty of Electrical Engineering
Delft University of Technology
P.O. Box 5031, 2600GA Delft, The Netherlands

Abstract - **When computing an electromagnetic field using a numerical method, e. g. the finite element method, it is possible that, although Maxwell's equations are discretised accurately, highly inaccurate computational results are obtained. In those cases it can easily be shown that (some of) the electromagnetic compatibility relations (field properties that follow from Maxwell's equations) are not satisfied. The divergence condition on the fluxes, for instance, follows directly from the field equations but not necessarily from their discretised counterparts. This necessitates inclusion of the compatibility relations in the finite-element formulation of the field problem. First a survey is given of all electromagnetic compatibility relations for the time-domain electromagnetic field equations. Subsequently the compatibility relations for the static field equations are discussed.**

I. Introduction

Because of its flexibility, the finite-element method seems to be the most suitable method for computing electromagnetic fields in inhomogeneous media and/or complicated geometries. In the finite-element formulation of an electromagnetic field problem the field equations can only be satisfied approximately. As a consequence of this, field properties that follow from Maxwell's electromagnetic field equations, the electromagnetic compatibility relations [1], may not be reflected accurately in a numerical solution. In earlier papers [2, 3] Mur presented methods for computing the electric and/or the magnetic field directly, using a combination of linear edge and linear nodal expansion functions for obtaining optimum computational efficiency. In these papers the importance of including the divergence condition, which is one of the compatibility relations, in the formulation of the problem was discussed. The equations applying to the divergence of the electric and magnetic flux densities follow directly from the electromagnetic field equations. They are satisfied whenever the field equations are satisfied exactly.

In the present paper the use of the divergence condition will be generalised to the use of the compatibility relations for electromagnetic fields. It will also be shown that the use of divergence-free edge elements, which is advocated by some authors (see [4] and the references contained in it) for satisfying some of these compatibility relations, as well as the use of face elements, introduces the possibility of violating additional relations of the compatibility type. The importance of including the electromagnetic compatibility relations explicitly in the finite-element formulation of the problem is stressed.

The analysis of the compatibility relations is carried out first for methods for computing time-domain (transient) electromagnetic fields. The analysis of methods for time-harmonic electromagnetic field problems runs along similar lines and leads to similar conclusions. It can be shown (and verified experimentally) that the importance of the compatibility relations increases with decreasing frequencies (slower variations of the solution in time) and, consequently, the compatibility relations are of the utmost importance for the numerical computation of static electric and magnetic fields. These cases will be discussed separately showing the connections between the compatibility relations for transient fields and those for static fields.

II. The Basic Equations

As the point of departure for our analysis we use the time-domain electromagnetic field equations

$$\partial_t \boldsymbol{D} \quad +\boldsymbol{J} \quad -\nabla \times \boldsymbol{H} = -\boldsymbol{J}^{\text{ext}}, \tag{1}$$

$$\partial_t \boldsymbol{B} \qquad +\nabla \times \boldsymbol{E} = -\boldsymbol{K}^{\text{ext}}, \tag{2}$$

where $\boldsymbol{J}^{\text{ext}}$ and $\boldsymbol{K}^{\text{ext}}$ are sources of electric and magnetic current that are known, throughout the domain of computation $\mathcal{D}$ (see Fig. 1), as a function of the time coordinate t. In (2) we have included the magnetic current $\boldsymbol{K}^{\text{ext}}$ for symmetry reasons. $\boldsymbol{J}^{\text{ext}}$ and $\boldsymbol{K}^{\text{ext}}$ may also represent contrast sources used in a contrast-source formulation that replaces a transparent obstacle in a known

external field by equivalent sources. The field equations are supplemented by the interface conditions

$$\nu \times \boldsymbol{E} \text{ continuous across sourcefree interfaces,} \quad (3)$$

$$\nu \times \boldsymbol{H} \text{ continuous across sourcefree interfaces,} \quad (4)$$

and the boundary conditions

$$\nu \times \boldsymbol{E} = \nu \times \boldsymbol{E}^{\text{ext}} \text{ on } \partial\mathcal{D}_{\text{E}}, \quad (5)$$

$$\nu \times \boldsymbol{H} = \nu \times \boldsymbol{H}^{\text{ext}} \text{ on } \partial\mathcal{D}_{\text{H}}, \quad (6)$$

where ν is the unit vector along the normal to either the interface $\mathcal{I}$ or the outer boundary $\partial\mathcal{D} = \partial\mathcal{D}_{\text{E}} \cup \partial\mathcal{D}_{\text{H}}$ (with $\partial\mathcal{D}_{\text{E}} \cap \partial\mathcal{D}_{\text{H}} = \emptyset$) of the domain of computation $\mathcal{D}$, and where $\nu \times \boldsymbol{E}^{\text{ext}}$ and $\nu \times \boldsymbol{H}^{\text{ext}}$ are known, along the relevant parts of this outer boundary, as a function of t.

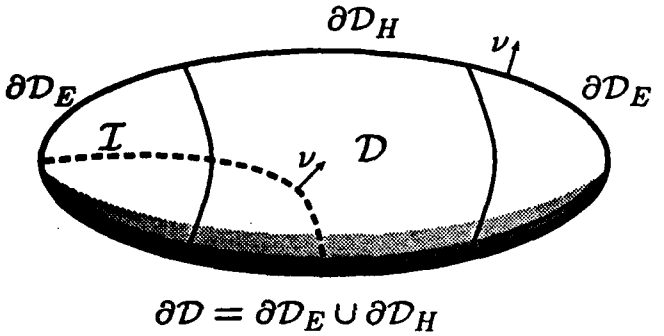

Fig. 1. The domain of computation $\mathcal{D}$.

Together with the constitutive equations and the initial conditions at $t = t_0$, (1)-(6) define an electromagnetic-field problem with a unique solution [5]. Note that the source terms in (1) and (2) are not related to the boundary conditions in (5) and (6).

III. The Compatibility Relations

Compatibility relations [1] are properties of a field that are direct consequences of the field equations and that must be satisfied to allow them to have a solution. For the electromagnetic field equations they are discussed below.

A. Interior

Applying the divergence operator $\nabla\cdot$ to (1) and (2) it follows that

$$\nabla \cdot (\partial_t \boldsymbol{D} + \boldsymbol{J}) = -\nabla \cdot \boldsymbol{J}^{\text{ext}}, \quad (7)$$

$$\partial_t \nabla \cdot \boldsymbol{B} = -\nabla \cdot \boldsymbol{K}^{\text{ext}}. \quad (8)$$

The electromagnetic compatibility (divergence) relations (7) and (8) apply to subdomains of the domain of computation in which the electromagnetic field vectors are continuously differentiable functions of the spatial coordinates.

B. Interfaces

The field vectors are not differentiable with respect to the spatial coordinates at the interfaces between regions with different medium properties. In that case (7) and (8) are replaced by

$$\nu \cdot (\partial_t \boldsymbol{D} + \boldsymbol{J}) + \nu \cdot \boldsymbol{J}^{\text{ext}} \text{ continuous across interface,} \quad (9)$$

$$\nu \cdot \partial_t \boldsymbol{B} + \nu \cdot \boldsymbol{K}^{\text{ext}} \text{ continuous across interface,} \quad (10)$$

where ν is the unit vector normal to the interface.

Note that (9) and (10) express the continuity condition applying to the normal components of the electric and the magnetic flux densities across an interface between different media.

C. Outer boundary

A third type of compatibility relation is found when studying the behavior of the field near the outer boundary of the domain of computation. Applying the operator $\nu\cdot$, where ν denotes the unit vector along the normal to the outer boundary, to (1) and (2) we obtain, using (5) and (6), the relations

$$\nu \cdot (\partial_t \boldsymbol{D} + \boldsymbol{J}) = \nu \cdot (\nabla \times \boldsymbol{H}^{\text{ext}} - \boldsymbol{J}^{\text{ext}}) \text{ on } \partial\mathcal{D}_{\text{H}}, \quad (11)$$

$$\nu \cdot \partial_t \boldsymbol{B} = -\nu \cdot (\nabla \times \boldsymbol{E}^{\text{ext}} + \boldsymbol{K}^{\text{ext}}) \text{ on } \partial\mathcal{D}_{\text{E}}. \quad (12)$$

These equations express the fact that prescribing the tangential components of the electric (magnetic) field strength at a given part $\partial\mathcal{D}_{\text{E}}$ ($\partial\mathcal{D}_{\text{H}}$) of the outer boundary $\partial\mathcal{D}$ implies a related behavior of the normal components of the magnetic (electric) flux densities at that part of the boundary.

Note that these equations have the form of additional boundary conditions applying at the outer boundary of the domain of computation. They follow, however, directly from the fact that the field inside the domain of computation should satisfy Maxwell's equations.

D. Compatibility relations and edge elements

Some authors use divergence-free edge elements (e.g. Whitney 1) for imposing the divergence conditions exactly. Edge elements cause the tangential components of

the fields to be continuous, they leave the normal components free to jump. Apart from the fact that divergence-free edge elements can only be used in the simple case where the compatibility relations (7) and (8) reduce to $\nabla \cdot \boldsymbol{D} = 0$ (or $\nabla \cdot \boldsymbol{J} = 0$) and $\nabla \cdot \boldsymbol{B} = 0$, respectively, the resulting freedom of the normal component of the field at the interface between two adjoining tetrahedra to jump, even when it should be continuous, is unwanted. Consequently, the continuity of the normal flux has to be added to our list of compatibility relations to be imposed upon the solution. Failing to do so may be the cause of undesired surface charge distributions in between edge elements. When adjoining finite elements contain identical materials, and assuming that the external sources of current are continuous between those finite elements, the following relations hold

$$\boldsymbol{\nu} \cdot \boldsymbol{E} \text{ continuous between edge elements,} \tag{13}$$

$$\boldsymbol{\nu} \cdot \boldsymbol{H} \text{ continuous between edge elements.} \tag{14}$$

In the alternative cases, (9) and (10) still apply. Imposing these relations results in an increase of the connectivity of the system matrices. Note that the need for imposing the continuity relations (13) and (14) is caused solely by the use of edge expansion functions and not by the electromagnetic field problem or the finite-element formulation used.

E. Compatibility relations and face elements

Some authors propose the use of face (also called facet) elements for modeling flux distributions. Face elements cause the normal fluxes between tetrahedra to be continuous, they have the disadvantage of leaving tangential components free to jump, even when they should be continuous. Assuming that no surface sources of current are present at the interface between those finite elements, the following continuity relations should hold

$$\boldsymbol{\nu} \times \boldsymbol{E} \text{ continuous between face elements,} \tag{15}$$

$$\boldsymbol{\nu} \times \boldsymbol{H} \text{ continuous between face elements,} \tag{16}$$

otherwise the proper jump condition should be implemented. Imposing these relations results in an increase of the connectivity of the system matrix (matrices). Note that the need for imposing the continuity relations (15) and (16) is caused solely by the use of face expansion functions that do not automatically satisfy the continuity conditions (3) and (4).

F. In summary

Equations (7)-(12) are a set of six electromagnetic compatibility relations that are direct consequences of Maxwell's equations. In exact methods for solving the electromagnetic field equations they are automatically accounted for. In numerical methods, for instance in the finite-element method, for solving the electromagnetic field equations they should be taken into account explicitly whenever the method used does not automatically account for them.

Equations (13)-(16) are additional compatibility relations the need for which is caused by the use of either edge or face elements in homogeneous domains. In those domains edge and face elements allow unphysical discontinuities in the solution and compatibility relations have to be added to the formulation of the field problem for restricting those discontinuities to acceptable values.

Note that (7)-(16) do not contain any extra information that is not contained in the field equations. However, failing to include them in the finite-element formulation of an electromagnetic-field problem, either exactly or numerically, may be the cause of highly inaccurate results. Errors of this type are often referred to as "spurious solutions" or "vector parasites".

IV. Application to Static Electric Fields

For static electric fields the basic equations (1) - (6) reduce to

$$\nabla \times \boldsymbol{E} = -\boldsymbol{K}^{\text{ext}}, \tag{17}$$

together with the interface condition

$$\boldsymbol{\nu} \times \boldsymbol{E} \text{ continuous across sourcefree interfaces,} \tag{18}$$

and the boundary condition

$$\boldsymbol{\nu} \times \boldsymbol{E} = \boldsymbol{\nu} \times \boldsymbol{E}^{\text{ext}} \text{ on } \partial\mathcal{D}_{\text{E}}. \tag{19}$$

Note that we have lost the boundary condition on $\partial\mathcal{D}_{\text{H}}$ which has to be replaced by the compatibility relation applying to this part of the outer boundary.

A. Interior compatibility

In case of a conducting medium (7) reduces to

$$\nabla \cdot \boldsymbol{J} = -\nabla \cdot \boldsymbol{J}^{\text{ext}}, \tag{20}$$

In case of a non-conducting (dielectric) medium (7) reduces to

$$\nabla \cdot \boldsymbol{D} = \rho^{\mathrm{e,ext}}, \tag{21}$$

where $\rho^{\mathrm{e,ext}}$ denotes the known external electric volume charge density.

B. Interface compatibility

In case of a conducting medium (9) reduces to

$$\boldsymbol{\nu} \cdot \boldsymbol{J} + \boldsymbol{\nu} \cdot \boldsymbol{J}^{\mathrm{ext}} \text{ continuous across interface,} \tag{22}$$

in case of a non-conducting (dielectric) medium (9) reduces to

$$\boldsymbol{\nu} \cdot \boldsymbol{D}|_1^2 = \sigma^{\mathrm{e,ext}}, \tag{23}$$

where $\boldsymbol{D}|_1^2$ denotes the jump in $\boldsymbol{D}$ across the interface and where $\sigma^{\mathrm{e,ext}}$ denotes the known external electric surface charge density. In case of an interface between a conducting and a non-conducting (dielectric) medium (9) reduces to

$$\boldsymbol{\nu} \cdot \boldsymbol{J} = \boldsymbol{\nu} \cdot \boldsymbol{J}^{\mathrm{e,ext}}|_1^2 \tag{24}$$

at the conducting side of the interface.

C. Outer boundary compatibility

In case of a conducting medium (11) reduces to

$$\boldsymbol{\nu} \cdot \boldsymbol{J} = \boldsymbol{\nu} \cdot (\nabla \times \boldsymbol{H}^{\mathrm{ext}} - \boldsymbol{J}^{\mathrm{ext}}) \text{ on } \partial\mathcal{D}_{\mathrm{H}}. \tag{25}$$

Recall that $\boldsymbol{H}^{\mathrm{ext}}$ and $\boldsymbol{J}^{\mathrm{ext}}$ are not related. In case of a non-conducting (dielectric) medium (11) reduces to

$$\boldsymbol{\nu} \cdot \boldsymbol{D} = \sigma^{\mathrm{e,ext}} \text{ on } \partial\mathcal{D}_{\mathrm{H}}, \tag{26}$$

where $\sigma^{\mathrm{e,ext}}$ denotes the known external electric surface charge density at the outer boundary.

D. Compatibility relations and edge elements

In case adjoining tetrahedra contain identical materials as regards their electric properties (13) applies, otherwise (22)-(24) apply.

E. Compatibility relations and face elements

In case no surface souces of magnetic current are present at the interface between adjoining face elements (15) applies, otherwise the proper jump condition should be implemented.

V. Application to Static Magnetic Fields

For static magnetic fields the basic equations (1) - (6) reduce to

$$\nabla \times \boldsymbol{H} = \boldsymbol{J}^{\mathrm{ext}}, \tag{27}$$

together with the interface condition

$$\boldsymbol{\nu} \times \boldsymbol{H} \text{ continuous across sourcefree interfaces,} \tag{28}$$

and the boundary condition

$$\boldsymbol{\nu} \times \boldsymbol{H} = \boldsymbol{\nu} \times \boldsymbol{H}^{\mathrm{ext}} \text{ on } \partial\mathcal{D}_{\mathrm{H}}. \tag{29}$$

Note that we have lost the boundary condition on $\partial\mathcal{D}_{\mathrm{E}}$ which has to be replaced by the compatibility relation applying to this part of the outer boundary.

A. Interior compatibility

For static magnetic fields equation (8) reduces to

$$\nabla \cdot \boldsymbol{B} = \rho^{\mathrm{m,ext}}. \tag{30}$$

where $\rho^{\mathrm{m,ext}}$ denotes the known external magnetic volume charge density.

B. Interface compatibility

For static magnetic fields equation (10) reduces to

$$\boldsymbol{\nu} \cdot \boldsymbol{B}|_1^2 = \sigma^{\mathrm{m,ext}}, \tag{31}$$

where $\sigma^{\mathrm{m,ext}}$ denotes the known external magnetic surface charge density at the interface.

C. Outer boundary compatibility

For static magnetic fields the continuity of the normal flux (12) reduces to

$$\boldsymbol{\nu} \cdot \boldsymbol{B} = -\sigma^{\mathrm{m,ext}} \text{ on } \partial\mathcal{D}_{\mathrm{E}}. \tag{32}$$

where $\sigma^{\mathrm{m,ext}}$ denotes the known external magnetic surface charge density at the outer boundary.

D. Compatibility relations and edge elements

In case adjoining tetrahedra contain identical materials as regards their magnetic properties (14) applies, otherwise (31) applies.

E. Compatibility relations and face elements

In case no surface sources of electric current are present at the interface between adjoining face elements (16) applies, otherwise the proper jump condition should be implemented.

VI. Conclusions

When the electromagnetic field equations are solved numerically using expansions that do not themselves exactly satisfy these equations, which is the case in the finite-element method, it is necessary to include the compatibility relations in the formulation in order to obtain correct results. Attempts to solve this difficulty by using edge elements merely complicate the situation by introducing the need to impose additional compatibility relations. In our analysis we have first presented the compatibility relations applying to time-domain (transient) fields and, subsequently, those for static fields. In doing so, the relation between those two cases is clarified and a better understanding is obtained of the function of the compatibility relations and their application in the entire range from static to high frequency applications.

In summary, we conclude that we have presented the electromagnetic field compatibility relations. To obtain reliable computational results from finite-element methods for solving the electromagnetic field equations, these relations should be made a part of the formulation of the problem.

Acknowledgment

The research reported in this paper has been financially supported through Research Grants from the Stichting Fund for Science, Technology and Research (a companion organisation to the Schlumberger Foundation in the U.S.A.), from Schlumberger-Doll Research, Ridgefield, CT, U.S.A., from Etudes et Productions Schlumberger, Clamart, France, and from Schlumberger Cambridge Research Limited, Cambridge, England. This support is gratefully acknowledged.

References

[1] A. E. H. Love, *A Treatise on the Mathematical Theory of Elasticity*, The Syndics of the Cambridge University Press, London, 1959, p. 49.

[2] G. Mur, "The Finite-Element Modeling of Three-Dimensional Time Harmonic Electromagnetic Fields in Inhomogeneous Media," *Radio Science*, Vol. 26, No. 1, January-February 1991, pp. 275-280.

[3] G. Mur, "The Finite-Element Modeling of Three-Dimensional Time-Domain Electromagnetic Fields in Strongly Inhomogeneous Media," *IEEE Transactions on Magnetics*, Vol. MAG-28, No. 2, pp. 1130-1133, March 1992.

[4] J. P. Webb, "Edge Elements and What They can do for You," *IEEE Transactions on Magnetics*, Vol. MAG-29, Nr. 2, pp. 1460-1465, March, 1993.

[5] J. A. Stratton, *Electromagnetic Theory*, McGraw-Hill Book Company, New York, 1941, p. 486.

[6] G. Mur, "Edge elements, their Advantages and their Disadvantages," Submitted for Publication in the IEEE Trans. on Magnetics. Also: Report nr. Et/EM 1993-35, Laboratory of Electromagnetic Research, Faculty of Electrical Engieering, Delft University of Technology, Delft, the Netherlands.

THE APPLICATION OF THE FINITE ELEMENT METHOD IN DESIGN OF ELECTRIC MOTORS

Z.Haznadar, Ž.Štih, S.Berberović, G.Manenica
Faculty of Electrical Engineering, University of Zagreb,
Unska 3, 41000 Zagreb
Croatia

ABSTRACT. The classical approach to design of electric motors is based on the concept of simplified magnetic circuit analysis. This approach fails in today's design situation due to utilization of new materials and new designs. Application of sophisticated numerical methods becomes inevitable. Some problems arising in the application of the finite element method in design of electric motors are discussed in this paper.

Electric motors are always part of a system and their behaviour within the system, which is characterized by integral parameters (torques and reactances), should be known at the design stage. Computation of these parameters from a finite element magnetic field solution is described here.

The computation of torque/angle characteristics from finite element field solution by application of two basic approaches:

- *global virtual work method and cubic spline interpolation technique,*
- *Maxwell stress tensor integration,*

is described. The applicability of both approaches is illustrated by computation of the torque in a switched reluctance motor and the advantages of virtual work approach are emphasised.

The main problem in application of the finite element method to computation of magnetic fields in electric motors is that the field sources (currents) and load angle are unknown. External environment (terminal voltage and mechanical load) are known, and the magnetic field solution is iterated until the external constraints are satisfied. To avoid finite element mesh rotation an iterative process was implemented in which only the fundamental harmonic of the lumped stator winding distribution is taken into consideration instead of the three-phase winding excitation. The direct and quadrature reactances are computed from the finite element magnetic field solution utilizing flux linkage and stored energy approaches. The procedure is illustrated by computation of the reactances of a permanent magnet synchronous electric motor.

1. INTRODUCTION

Design of electric motors is a process of synthesis based on geometrical modelling and analysis. The traditional approach to analysis in the design of electric motors was based on the concept of magnetic circuit analysis resulting with simple analytical models. These models incorporate equivalent circuits postulated on the basis of experience and intuition. Results of such an approach are qualitatively correct but quantitatively inaccurate and have to be corrected with empirically introduced correction parameters based on previous experience and measurements on prototypes. These parameters are usually valid for very narrow classes of motors significantly similar to those which were produced and measured before the new design. From the designers point of view the main advantage of this approach is its simplicity and ease of application.

This traditional approach to design of electric motors fails in new situations. Utilization of new magnetic materials enables developing of new designs. Precise prediction of motor characteristics before a motor is manufactured is one of the essential prerequisites for good, concurrent design and cost-effective production. Accordingly, more sophisticated methods of analysis based on electromagnetic field theory which enable more accurate modelling of electric motors are required to be implemented in the design procedures. Numerical field analysis is the only available tool capable of dealing with problems which arise in the design of the new generation of electric motors. The most widely spread numerical method for electromagnetic field analysis in electric motors is the finite element method (FEM). Its application to the calculation of two main integral characteristics of electric motors: torques and reactances is described here.

2. CALCULATION OF TORQUES

One of the most important characteristics of electric motors is torque as a function of rotor position. It can be derived from the FEM solution of the magnetic field in the electric motor. Two distinct approaches for directly calculating the torque from the FEM solution are Maxwell

stress tensor integration and the virtual work approach.

2.1 Maxwell Stresses

The torque on a rigid body enclosed by a surface S via Maxwell's magnetic stress tensor integration can be obtained by calculating the surface integral [1]:

$$\vec{T} = \oint_S (\vec{r} \times \bar{\bar{t}})\, d\vec{S} \tag{1}$$

where n is an unit vector normal to the integration surface S, r is a distance vector, and t is Maxwell stress tensor defined by:

$$\bar{\bar{t}} = \vec{H} \cdot (\vec{B} \cdot \vec{n}) - \frac{1}{2}(\vec{H} \cdot \vec{B}) \cdot \vec{n} \tag{2}$$

In the case of the exact solution the integral in (1) is independent of the chosen integration surface. Approximate and discrete nature of the FEM solution introduces dependency of the accuracy of torque calculation upon the accuracy of the calculation of the local flux densities and upon the choice of the integration surface (3D models) or integration contour (2D models). High accuracy of the calculation of the local flux densities, which are obtained from potential solutions (scalar or vector) by differentiation, can be assured by increasing the FEM mesh density. The most convenient choice for the integration surface (contour) in the FEM models of electrical motors is in the airgap between the stator and the rotor. In a practical applications of this approach it is advisable to evaluate the torque using several surfaces (contours) and to average the results, or to apply relatively complicated iterative methods for selection of the best surface (contour) [2].The application of this approach in normal design practice is very complicated.

The main advantage of the Maxwell stress tensor integration approach to torque calculations is that it requires only one field solution to obtain the torque for one position. If it is necessary to obtain a complete torque-angle characteristics this advantage becomes obsolete.

2.2 Virtual Work

Since the extremization solution procedure used in the finite element method optimizes the calculation of stored energy, the virtual work method seems to be more stable and accurate approach to torque calculation. The torque can be calculated from the coenergy of a system by [3,4]:

$$T = \frac{\partial W_c}{\partial \alpha} \tag{3}$$

where W_c is the total coenergy of a system and α is the angular displacement. Total coenergy of a system can be calculated from the FEM solution by:

$$W_c = \sum_e \left\{ \int_{V^e} H^e B^e dV^e - \int_{V^e} \left(\int_0^{B^e} H^e dB^e \right) dV^e \right\} \tag{4}$$

The main disadvantage of this approach is the calculation of the coenergy derivatives with respect to a small perturbation of the rotor position. The numerical realisation of this method can give rise to a significant round-off error in computing a finite difference approximation of the required derivative because of near identical coenergies for small displacements. On the other hand using increased displacements of the rotor in order to achieve greater differences in the system coenergy decreases the accuracy of the finite difference approximation.
In order to overcome those difficulties, a cubic spline interpolation of the coenergy function through points calculated in several rotor positions is introduced [5]. The interpolation of the coenergy on the i-th segment is defined by [6]:

$$\begin{aligned} W_c(\alpha) = {} & m_{i-1} \frac{(\alpha_i - \alpha)^2 (\alpha - \alpha_{i-1})}{h_{i-1}^2} - \\ & - m_i \frac{(\alpha - \alpha_{i-1})^2 (\alpha_i - \alpha)}{h_{i-1}^2} + \\ & + y_{i-1} \frac{(\alpha_i - \alpha)^2 [2(\alpha - \alpha_{i-1}) + h_{i-1}]}{h_{i-1}^3} + \\ & + y_i \frac{(\alpha - \alpha_{i-1})^2 [2(\alpha_i - \alpha) + h_{i-1}]}{h_{i-1}^3} \end{aligned} \tag{5}$$

where:

$$h_i = \alpha_{i+1} - \alpha_i \;\; ; \;\; m_i = \frac{\partial W_c(\alpha)}{\partial \alpha}\Big|_{\alpha = \alpha_i} \;\; ; \;\; i = 0,1...n$$

$$y_i = W_c(\alpha_i) \;\; ; \;\; \alpha \in [\alpha_{i-1}, \alpha_i] \;\; ; \;\; i = 1,...n$$

The unknown coefficients of the interpolation m_i are derived from the condition of smooth joints (equal first derivatives) at points α_i (i=1,..n-1). The first derivatives at the first point (i=0) and the last point (i=n) of interpolation are set to the zero, which is natural for this problem. The torque is calculated by derivation of the

cubic spline interpolation of the coenergy function with respect to displacement α.

2.3 Example: Torque in a Switched Reluctance Motor

The usage of switched reluctance motors (SRM) has increased in recent years due to their simplicity and controllability. As a variable speed driver they are much more efficient compared to variable speed induction motors. The motor has salient poles on both the stator and the rotor, the windings on the stator are of simple form and there are no windings on the rotor. This results in a relatively simple construction of such motors. The currents in the stator circuits are switched on and off in accordance with the rotor position and with simple control the motor develops the torque-speed characteristics typical for series-connected d.c. motors. The main characteristics of the magnetic field analysis in SRM are:

- complex geometry and very small airgap between stator and rotor,
- deep saturation of magnetic material in normal operation,
- eddy currents can be neglected.
- the influence of edge effects must be taken into account.

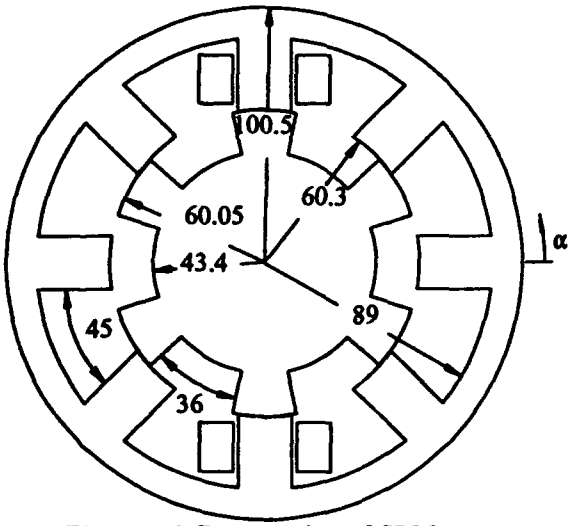

Figure 2.1 Cross-section of SRM motor

Taking into consideration the aforesaid one can conclude that a 3D nonlinear static model of SRM is sufficient for design analysis. The importance of 3D calculation is emphasized in the case of deep saturation of magnetic material and/or in the case of rotor-stator position with maximum reluctance. In those cases the magnetic field is leaked out of iron parts of the motor.

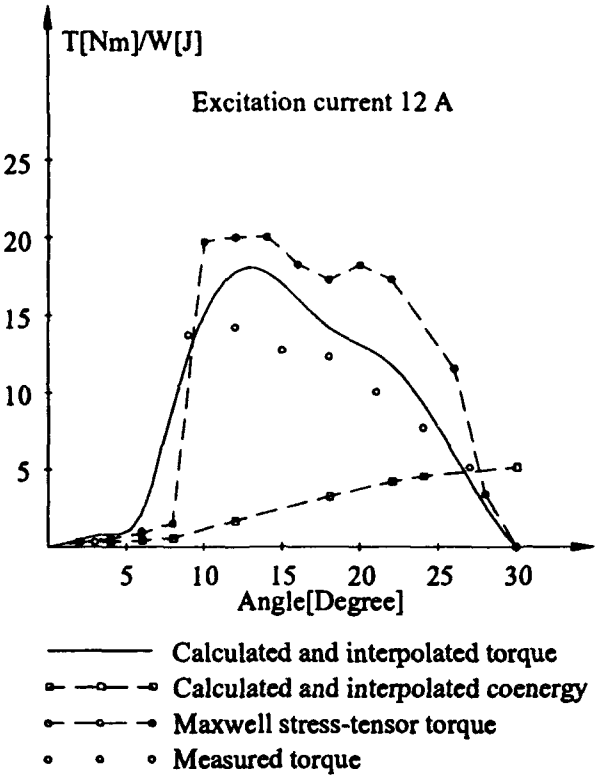

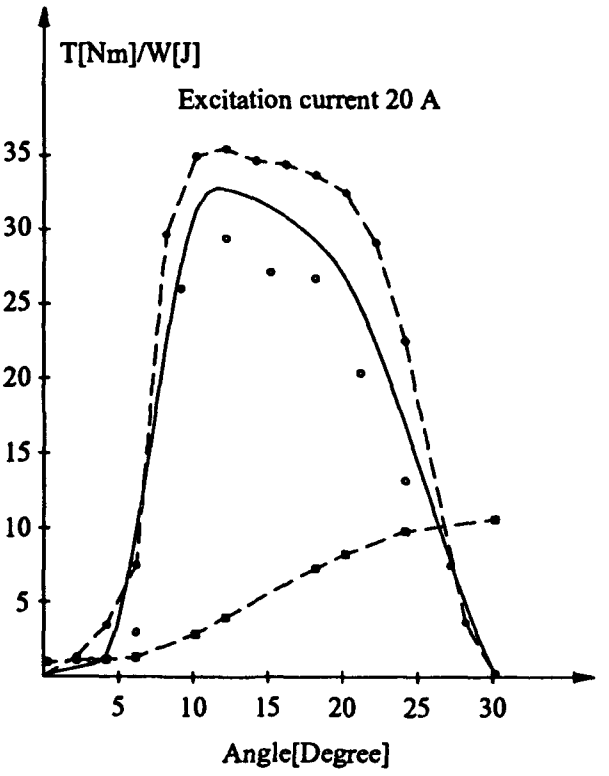

Figure 2.2 Calculated and measured torques and coenergies

Because of the static model, a total scalar potential approach to the numerical field calculation is chosen. The main advantages of this approach are [7]:

- one unknown per node,
- current regions are not included in the discretization,
- the influence of current sources is taken into account by applying the Biot-Savart law.

The finite element discretization of the SRM model is based on the application of twenty-node isoparametric brick elements. This ensures good approximation of the motor geometry as well as giving a good approximation to the field values (gradients of the potentials). The space around the active part of the SRM must be included in the finite element mesh.

The above mentioned approach was applied to the computation of the torque/angle characteristics of the SRM shown in Figure 2.1. The surface for Maxwell stress tensor integration was chosen to be a cylinder through the middle of the airgap. The airgap was discretized by three layers of finite elements. Total coenergy of the system was calculated from the same FEM solution. The resulting curves showing the comparison of the virtual work approach and the Maxwell stress tensor integration with the measurements are shown in Figure 2.2.

3. INDUCTANCE CALCULATIONS

The main objective of inductance calculations in electric motor design is the computation of the reactances in the direct and quadrature axis system (X_d and X_q). The two-axis system was introduced into classical theory of electric machines as a mean of facilitating analysis of salient pole machines [8]. Reactances X_d and X_q are the basis for further representation of the motor in system studies. Two fundamental approaches to inductance calculations are:

- calculation of inductance from flux linkage,
- calculation of inductance from stored magnetic energy.

Both approaches can be applied in the case of the FEM magnetic field solution.

3.1 FEM Modelling of Electric Motors

A specific problem in applying the FEM to the design of electric motors is that in most cases the source (currents in stator slots) and load angle (relative position rotor-stator) are not specified. Under normal operating conditions for electric motors the state of the system is defined by the external quantities (terminal voltage and mechanical load) while source currents and load angle which are necessary for the FEM problem formulation are unknown. Solving a problem under these new constraints requires an iterative application of the FEM solution. The iterative scheme starts with the initial estimate of the load angle and field source currents which can be obtained by the classical design approach. The FEM solution is then applied and a first estimate for problem external sources can be determined. The derived terminal voltage is then compared with the specified conditions and the inputs to the FEM solution are iterated until a solution which agrees with the load point specification is obtained.

One way of forming the FEM models of electric motors is to specify source currents densities in stator slots which correspond to phase currents determined from the three phase excitation current system. Utilization using that approach requires rotating the FEM mesh as load angle varies, which complicates the iterative scheme of the FEM application. In most electric motors the fundamental component of excitation is dominant, while higher harmonics can be neglected. It enables decomposition of the lumped stator winding distribution into Fourier components and only the fundamental component of the current sheet is retained [9]. Stator currents in the FEM model of the motor are then assigned to the stator slots proportional to the area under the current sheet density distribution associated with each slot. The three phase sum of the fundamental components rotates in synchronism with the rotor, which means that changing load angle can be simulated by changes in the fundamental current sheet distribution while the FEM mesh remains the same.

3.2 Definition of Reactances

The quantities obtainable from the FEM magnetic field solution are direct and quadrature axis flux linkages and energies. In order to find them, taking into account saturation of magnetic material, a three step procedure for FEM solution is given in [10]:

Step 1. Nonlinear solution of the FEM problem where the sources are excitation current together with total armature current (both d and q components)

Step 2. The permeability for each element achieved in nonlinear iteration procedure (step 1.) is fixed.

Step 3. Two linear solutions of the FEM problem with separately applied d and q components of armature current while excitation current is set to zero. Permeabilities in the FEM mesh for this step are the ones fixed in step 2.

Direct axis flux linkage ψ_d and stored magnetic energy W_d are calculated from the FEM solution in step 3 when the

direct axis component of armature current is applied, while quadrature axis flux linkage ψ_q and stored magnetic energy W_q are calculated from the FEM solution in step 3 when the quadrature axis component of armature current is applied. The reactances are then defined as:

$$X_d = \frac{\omega \Psi_d}{I_d} \quad ; \quad X_d = \frac{2\omega W_d}{3 I_d^2} \tag{7}$$

$$X_q = \frac{\omega \Psi_q}{I_q} \quad ; \quad X_q = \frac{2\omega W_q}{3 I_q^2} \tag{8}$$

where I_d and I_q are the direct and quadrature axis components of armature current respectively.

3.3 Example: Synchronous Permanent Magnet Motor (SPMM)

The high energy density of rare earth permanent magnets and relatively low costs of their utilization has permitted them to replace classical DC excitation systems of electric motors. The elimination of the excitation winding (copper losses, brushes...) results in more reliable and mechanically simpler motor. The rare earth permanent magnets have near linear characteristics over normal operating conditions. This fact greatly simplifies their modelling in the FEM. They can be replaced with simple current sheets surrounding a material having a permeability equal to the recoil permeability of the permanent magnet material which is, in the case of rare earth materials, slightly greater than the one of free space. The geometry of such motors enables utilization of a two-dimensional model. FEM approach based on magnetic vector potential is applied in the solution procedure. The cross-section of the analyzed motor can be seen in Figures 3.2 to 3.4. The fundamental component of decomposition of lumped stator winding into Fourier component is given as [9]:

$$ni(\xi) = \frac{9}{\pi^2} N_s \sqrt{2}\, I_a \sin(\xi - \alpha) \tag{9}$$

where:

- I_a is the root mean square value of the armature current,
- N_s is the number of turns in the stator winding per pole and per phase,
- ξ is the electrical angle with respect to the d axis,
- α is the electrical angle between the phasor of the armature current and the d axis.

Current I_i associated with i-th slot of the stator winding is:

$$I_i = \frac{9}{\pi^2} N_s \sqrt{2}\, I_a \sin(\xi - \alpha)\, \Delta\xi \tag{10}$$

A set of equations which define the external environment in steady state operation of a permanent magnet electric motors can be deduced from the d-q theory by adopting the Park transformation in rotor reference frame. The equations are [11]:

$$\begin{aligned} V_q &= R I_q + \omega \phi_d \\ V_d &= R I_d - \omega \phi_q \end{aligned} \tag{11}$$

V_q and V_d are q and d components of the terminal voltage, I_q and I_d are the corresponding current components, R is ohmic resistance of the winding, ω is steady state frequency and Φ_d and Φ_q are the corresponding flux linkages. These equations can be expressed in phasor form and combined to obtain the phase stator voltage V_a in phasor form:

$$\bar{V}_a = (R + jX_q)\bar{I}_a + j(X_d - X_q)\bar{I}_d + \bar{E}_0 \tag{12}$$

E_0 is the open circuit voltage (I_d=I_q=0) resulting only from permanent magnets (excitation) and can be considered as a constant. This voltage is computed from the FEM solution of the model excited only by permanent magnets. A phasor diagram derived from (12) is presented in Figure 3.1.

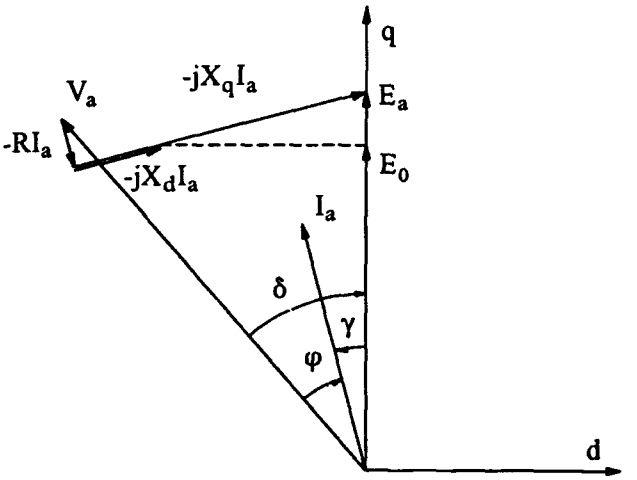

Figure 3.1 Phasor diagram of SPMM

Unknown reactances X_d and X_q are obtained from the FEM field solution using the idea of distributed turns in the flux linkage calculations as described in [10]:

$$\Psi_d = \int_0^{\pi} 2A(\xi) \frac{6N_s}{\pi^2} \sin\xi \, d\xi \qquad (13)$$

$$\Psi_q = \int_{-\frac{\pi}{2}}^{\frac{\pi}{2}} 2A(\xi) \frac{6N_s}{\pi^2} \cos\xi \, d\xi \qquad (14)$$

Stored magnetic energy is calculated from the FEM solution by:

$$W_m = \sum_e \int_{S^e} \left(\int_0^{B^e} H^e \, dB^e \right) dS^e \qquad (15)$$

The iterative procedure described in section 3.1 was performed and after three iterations an agreeable solution (successive solutions for X_d and X_q differed by less than 3.5%) was obtained. FEM field solutions for step 1 and step 3 in the third iteration are illustrated in Figures 3.2 to 3.4.

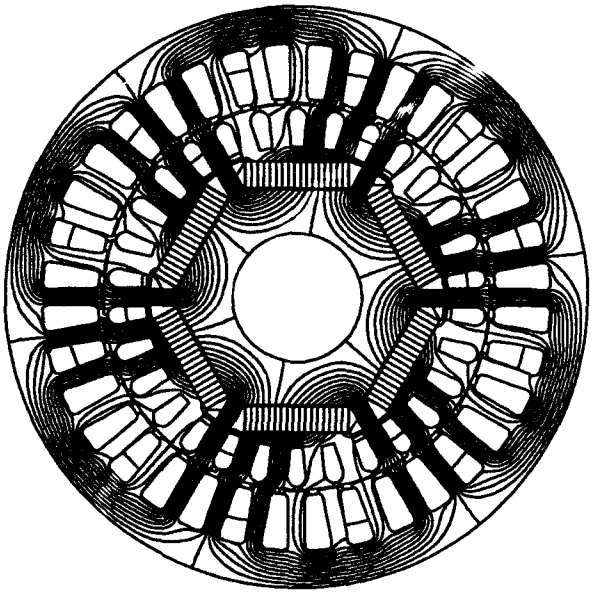

Figure 3.2 Nonlinear FEM magnetic field solution (third iteration, step 1)

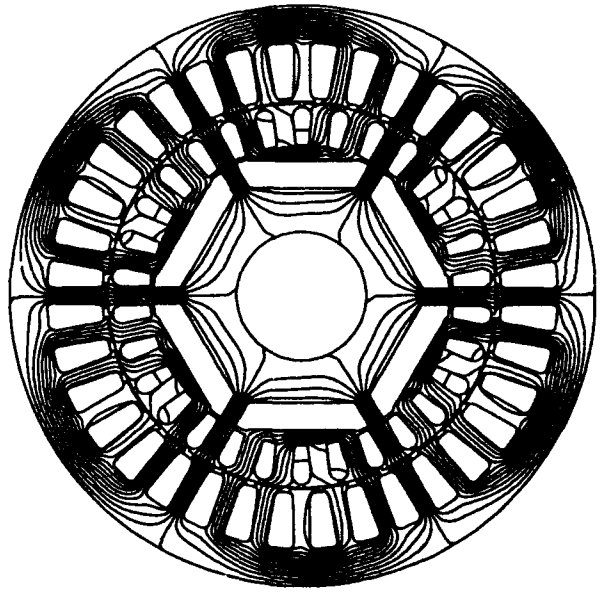

Figure 3.3 Linear FEM solution in q axis (third iteration, step 3)

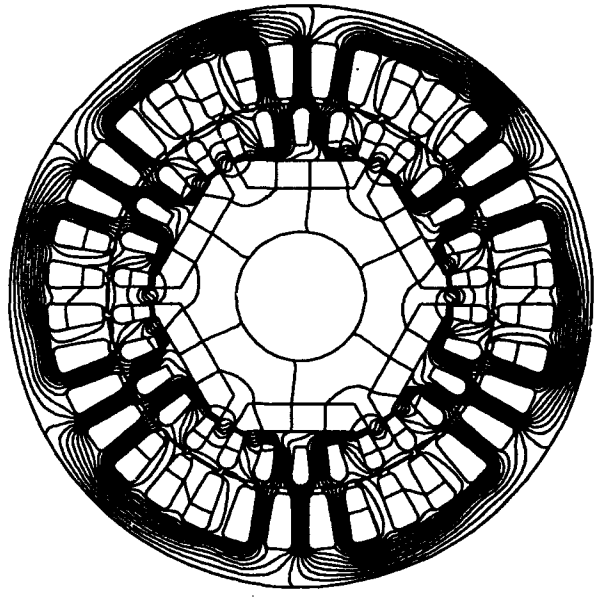

Figure 3.4 Linear FEM solution in d axis (third iteration, step 3)

The results of the computation of the reactances calculated from flux linkages as well as the reactances calculated from stored energy are given in Table 1.

	Energy		Flux Linkage	
	X_d	X_q	X_d	X_q
Iteration 1	55.44	87.83	53.42	78.88
Iteration 2	43.97	93.80	42.80	89.82
Iteration 3	42.76	96.50	41.60	92.15

Table 1. Reactances through iterations 1 to 3

4. CONCLUSIONS

The application of the finite element method in computation of integral parameters of electric motors cannot be avoided in today's design practice. The problem in applying of the method is that a certain level of specialist's knowledge is required from a designer. Some aspects of that knowledge are clarified in this paper. The most important parameters of electric motors are torques and reactances. In order to calculate them additional computations must be performed after the FEM solution.

The torques can be computed by the application of Maxwell stress tensor integration or by the virtual work approach. The virtual work approach is improved by the introduction of cubic spline interpolation of coenergy/angle dependence. This results in the smooth approximation of the coenergy/angle curve and well defined differentiation with respect to rotor/stator position. The method is based on computation of the total coenergy of a system and thus less sensitive to meshing of the model. The described approach was applied on a test example and compared with the Maxwell stress method and measurements.

Computation ot reactances of electric motors requires iterative application of FEM magnetic field solution because the field sources and load angle are unknown. The iterative procedure is simplified because only the fundamental component of the lumped stator winding distribution is taken into consideration instead of three-phase winding excitation. Three phase sum of the fundamental components rotates in synchronism with the rotor and rotating of rotor the FEM mesh is unnecessary. Direct and quadrature axis reactances are computed from the FEM solution by flux linkage and stored energy approaches. The method was tested on a synchronous permanent magnet motor.

The final conclusion is that the stored energy approach to torque and inductance calculations is better for use in traditional design procedures because of the nature the FEM (minimization of energy functional) and weak dependence on local errors due to bad meshing of the model.

5. REFERENCES

[1] D.A. Lowther, P.P. Silvester: ***Computer-Aided Design***, Springer-Verlag, New York, 1986.

[2] M. Moallem, C.M. Ong:"Predicting the Torque of a Switched Reluctance Machine from its Finite Element Field Solution," ***IEEE Trans. Energy on Conversion***, Vol.5, No. 4, 1990, pp. 733-739.

[3] J.L. Coulomb, G.Meunier:"Finite Element Implementation of Virtual Work Principle for Magnetic or Electric Force and Torque Computation," ***IEEE Trans. on Magnetics***, Vol. MAG-20, No.5, 1984, pp. 1894-1896.

[4] E.A. Aronson, J.R. Brauer:"Magnetic Torque or Force Calculation by Direct Differentiation of Finite Element Coenergy," ***IEEE Trans. on Magnetics***, Vol. MAG-25, No. 5, 1989, pp. 3587-3590.

[5] Z. Haznadar, Ž. Štih, S. Berberović, G. Manenica: "Torque Calculation in Switched Reluctance Motor Design," ***Proc. of The International Symposium on Nonlinear Phenomena in Electromagnetic Fields ISEM***, Nagoya, Japan 1992.

[6] J. Ahlberg, E. Nilson, J. Walsh: ***The Theory of Spline and Their Applications,*** Academic Press, New York, 1967.

[7] J. Simkin, C.W. Trowbridge: "Three-Dimensional Nonlinear Electromagnetic Field Computations Using Scalar Potentials," ***IEE Proc.***, Vol. 127, No. 6, 1980, pp. 368-374.

[8] A.E. Fitzgerald, C. Kingsley, S.D. Umans: **Electric Machinery**, McGraw-Hill, Tokio, 1983.

[9] M.V.K. Chari, Z.J. Csendes, S.H. Minnich, S.C. Tandon, J. Berkery: "Load Characteristics of Sinchronous Generators by the Finite-Element Method," ***IEEE Trans. on Power Apparatus and Systems***, Vol. PAS-100, 1981, pp. 1-13.

[10] J.W. Dougherty, S.H. Minnich: "Finite Element Modeling of Large Turbine Generators; Calculation Versus Load Test Data," ***IEEE Trans. on Power Apparatus and Systems***, Vol. PAS-100, 1981, pp. 3921-3929.

[11] A. Consoli, G. Renna: "Interior Type Permanent Magnet Synchronous Motor Analysis by Equivalent Circiuts," ***IEEE Trans. on Energy Conversion***, Vol. 4, 1989, pp. 681-689.

COMPUTATION OF STATIC AND QUASISTATIC ELECTROMAGNETIC FIELDS USING ASYMPTOTIC BOUNDARY CONDITIONS

Qiushi Chen, Adalbert Konrad and Paul P. Biringer

Department of Electrical and Computer Engineering, University of Toronto
Toronto, Ontario, CANADA M5S 1A4

Abstract **— This paper presents the computation of static and quasistatic electromagnetic fields using asymptotic boundary conditions (ABC). Asymptotic boundary conditions for eddy current problems due to external field excitations are derived. For electrostatic fields, ABC-s are used in conjunction with Laplace's equation while for quasistatic magnetic fields, ABC-s are employed in conjunction with the integrodifferential finite element method. The effect of outer boundary locations on the accuracy of the simulation results is examined. This study shows that in these cases, ABC-s can improve the computation accuracy compared to the usual truncation of outer boundaries.**

1. INTRODUCTION

The finite element method (FEM) is a powerful method for the computation of electromagnetic fields. However, special techniques must be used when the solution domain is infinite, since the exterior region must be properly represented. Researchers sometimes use a simple approach in which the outer boundary is truncated with a *Dirichlet* or *Neumann* boundary condition. In addition, there are a number of well-known techniques to modify the finite element method to accommodate the open regions [1]. Examples of such modifications are ballooning [2], infinitesimal scaling [3], spatial transformations [4], infinite elements [5] and others. Unfortunately, these modifications are limited by various shortcomings. An alternative approach is to combine the finite element method with the integral equation method or Green's function approach to account for the open region. Good examples of such combination are the hybrid finite element - boundary integral equation method [6] and the integrodifferential finite element - Green's function method [7]. Usually, hybrid approaches destroy the sparsity of the finite element matrices. The measured equation of invariance (MEI) method, which was presented in [8], uses the assumed charge distributions on the conductors to determine the relationships of the unknown potentials around outer boundaries. The relationships thus obtained are subsequently employed in the finite element or finite difference simulations. The MEI method can preserve the sparsity of the finite element or finite difference matrices. However, the proof of convergence for this method has yet to be found in the published papers.

Recently, absorbing and asymptotic boundary conditions have been used in conjunction with the finite element method [9]-[12]. The sudden popularity of the ABC is due to the fact that it is local as compared to hybrid approaches. This locality preserves the sparsity of finite element matrices. However, most of the studies are focussed on wave problems. This paper applies the asymptotic boundary conditions to the study of static and quasistatic problems. Although there are studies using the ABC for static or quasistatic problems [13]-[16], there are still unanswered questions such as the effects of outer boundary locations on the solution accuracy. In addition, the use of asymptotic boundary conditions for eddy current problems due to external field excitations has not been reported.

This paper investigates the employment of asymptotic boundary conditions in conjunction with finite elements for the computation of static electric and quasistatic magnetic field problems. For the electrostatic problem, the electric scalar potential and stored energy of two parallel infinitely long, circular cylindrical conductors are calculated. For the quasistatic magnetic field problem, the ABC-s due to external field excitations are derived and used for the calculation of the induced eddy current power losses of an infinitely long, circular cylindrical conductor, excited by a uniform transverse magnetic (TM) field.

The accuracy of ABC-s are compared with analytical and known numerical results, where applicable, as well as brute force truncations. The objective of this study is to evaluate the usefulness and limitations of asymptotic boundary conditions.

The subject matter of this paper under the same title was originally presented at the *Progress in Electromagnetics Research Symp.*, Jet Propulsion Laboratory, Pasadena, CA, U.S.A., July 12-16, 1993.

2. FORMULATION OF ASYMPTOTIC BOUNDARY CONDITIONS

The essence of using the finite element method for the solution of unbounded field problems is the proper representation of the exterior region. The spectrum of the various techniques for such solutions are not without shortcomings. The recent flurry of work on absorbing and asymptotic boundary conditions underscores the need for and importance of an efficient technique suitable for the finite element implementation. The ABC-s resolve the difficulties associated with an infinite boundary by emulating the field behaviour at infinity on the finite boundary. The absorbing boundary conditions are used for wave propagation and scattering. In this paper, we are only concerned with asymptotic boundary conditions which are derived for static or quasistatic fields.

The outer boundary used in the asymptotic boundary conditions serves as an impedance junction to connect the region internal to it with the region external to it. Such a connection is facilitated by the surface integrals of the normal derivatives of the unknowns which represent the flux continuity conditions. As a result, the derivation of asymptotic boundary conditions centres on the representation of the normal derivatives of the unknown scalar potentials.

For a source-free static field, the potential ϕ, subject to suitable boundary conditions, is governed by *Laplace*'s equation

$$\nabla^2\phi = 0 \tag{1}$$

For a two-dimensional problem, if the potential is zero at infinity, the solution in the infinite exterior region in the polar coordinates can be expressed as the following harmonic expansions:

$$\phi = \sum_{n=1}^{\infty} \frac{a_n}{r^n} \cos(n\theta+\alpha_n) \tag{2}$$

where a_n and α_n are the coefficient and phase angle of the nth harmonic, respectively.

Differentiation of (2) with respect to r leads to

$$\frac{\partial\phi}{\partial r} = -\sum_{n=1}^{\infty} n\frac{a_n}{r^{n+1}} \cos(n\theta+\alpha_n) \tag{3}$$

The division of (2) by r yields

$$\frac{\phi}{r} = \sum_{n=1}^{\infty} \frac{a_n}{r^{n+1}} \cos(n\theta+\alpha_n) \tag{4}$$

Summation of (3) and (4) produces

$$\frac{\partial\phi}{\partial r} + \frac{\phi}{r} = -\sum_{n=1}^{\infty} n\frac{a_n}{r^{n+1}} \cos(n\theta+\alpha_n) + \sum_{n=1}^{\infty} \frac{a_n}{r^{n+1}} \cos(n\theta+\alpha_n) \tag{5}$$

$$\frac{\partial\phi}{\partial r} + \frac{\phi}{r} = \sum_{n=2}^{\infty} (1-n)\frac{a_n}{r^{n+1}} \cos(n\theta+\alpha_n) \tag{6}$$

If we omit the third and higher harmonics, the dominant error will be determined by the second harmonic and we have

$$\frac{\partial\phi}{\partial r} + \frac{\phi}{r} = -\frac{a_2}{r^3}\cos(2\theta+\alpha_2) \tag{7}$$

Equation (7) can be subsequently rewritten as

$$\frac{\partial\phi}{\partial r} + \frac{\phi}{r} = O(r^{-3}) \tag{8}$$

The first order asymptotic boundary operator is therefore

$$B_1 = \frac{\partial}{\partial r} + \frac{1}{r} \tag{9}$$

Consequently, the first order asymptotic boundary condition is

$$B_1(\phi) = 0 \tag{10}$$

If we let $u=B_1\phi$, then

$$u = \sum_{n=2}^{\infty} (1-n)\frac{a_n}{r^{n+1}} \cos(n\theta+\alpha_n) \tag{11}$$

The derivative of u with respect to r is

$$\frac{\partial u}{\partial r} = -\sum_{n=2}^{\infty} (1-n)(1+n)\frac{a_n}{r^{n+2}} \cos(n\theta+\alpha_n) \tag{12}$$

The ratio of u to r is given by

$$\frac{u}{r} = \sum_{n=2}^{\infty} (1-n)\frac{a_n}{r^{n+2}} \cos(n\theta+\alpha_n) \tag{13}$$

Therefore,

$$\frac{\partial u}{\partial r} + \frac{3u}{r} = \sum_{n=3}^{\infty} (n-2)(n-1)\frac{a_n}{r^{n+2}} \cos(n\theta+\alpha_n) \tag{14}$$

It is obvious that the dominant error is due to the third harmonic. Thus,

$$\frac{\partial u}{\partial r} + \frac{3u}{r} = 2\frac{a_2}{r^5} \cos(5\theta+\alpha_5) \tag{15}$$

Equation (15) can be represented by

$$\frac{\partial u}{\partial r} + \frac{3u}{r} = O(r^{-5}) \tag{16}$$

The second order asymptotic boundary operator is therefore

$$B_2 = (\frac{\partial}{\partial r} + \frac{3}{r})(\frac{\partial}{\partial r} + \frac{1}{r}) = O(r^{-5}) \qquad (17)$$

Due to the presence of the second order radial derivative $\partial^2\phi/\partial r^2$ in (17), the second order asymptotic boundary operator cannot be used directly for the finite element implementation. To overcome this difficulty, we rewrite (17) as

$$\frac{\partial^2\phi}{\partial r^2} + \frac{4}{r}\frac{\partial\phi}{\partial r} + \frac{2\phi}{r^2} = 0 \qquad (18)$$

To eliminate the second order radial derivative, we substitute (18) back into the *Laplace*'s equation in the polar coordinates. The resultant second order asymptotic boundary expression is

$$\frac{\partial\phi}{\partial r} = -\frac{2}{3r}\phi + \frac{1}{3r}\frac{\partial^2\phi}{\partial\theta^2} \qquad (19)$$

As a result, the first and second order asymptotic boundary conditions can be subsequently expressed as

$$\frac{\partial\phi}{\partial r} = a(r)\phi + b(r)\frac{\partial^2\phi}{\partial\theta^2} \qquad (20)$$

where $a(r)$ and $b(r)$ are given as follows:

$a(r) = -\frac{1}{r}$; $b(r) = 0$ for *first order ABC*

$a(r) = -\frac{2}{3r}$; $b(r) = \frac{1}{3r}$ for *second order ABC*

3. FINITE ELEMENT IMPLEMENTATION

For a generalized *Helmholtz* equation of the form

$$\nabla\cdot(p\nabla\phi) + k^2 q\phi = 0 \qquad (21)$$

we can use *Galerkin*'s criterion to transform it into

$$\int_\Gamma [p\nabla W\cdot\nabla\phi - k^2 qW\phi]dv = \int_{\Gamma_i} pW\frac{\partial\phi}{\partial n}ds + \int_{\Gamma_o} pW\frac{\partial\phi}{\partial n}ds \qquad (22)$$

where p and q are related to material properties and angular frequencies, W is the weighting function which is the same as the interpolation function of the finite elements, Γ_i is the regular *Neumann* boundary and Γ_o is the asymptotic boundary.

In the case of static electric fields, (21) is reduced to *Laplace*'s equation.

In the case of time-harmonic quasistatic magnetic fields, (21) can be transformed into the integrodifferential equation in the conductors [17] and *Laplace*'s equation outside the conductors with p corresponding to the reluctivity of the medium and k^2 representing $j\sigma$. These transformed equations are amenable to the use of asymptotic boundary conditions by the substitution of the appropriate asymptotic boundary expressions into the surface integrals involving the asymptotic boundaries.

4. APPLICATIONS

To illustrate the application of ABC-s, we study an electrostatic potential problem and a quasistatic magnetic field problem.

4.1 Electrostatic Problem

The electrostatic problem consists of two parallel infinitely long circular cylindrical conductors as shown in Fig. 1. The two conductors are at potentials of 1 and -1 volt, respectively. The potential distribution and stored energy are calculated and compared with analytic and published results [13]. Due to symmetry, only the upper region (above the line *CB*) is discretized.

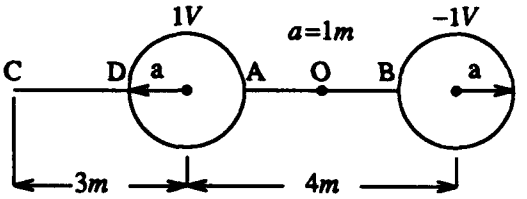

Fig. 1 Two circular cylindrical conductors with different potentials.

Figures 2 and 3 depict the potential distributions along the lines *AOB* and *CD*, respectively. Table 1 shows the stored electric energy. It is noted that the ABC improves the calculated results. While the homogeneous *Neumann* boundary condition (no-ABC FEM) can yield very accurate potentials along the line *AOB* (see Fig. 3), it produces much larger errors along the line *CD*. The asymptotic boundary condition, however, renders accurate solutions at both *AOB* and *CD*. The asymptotic boundary is at a radius of *6m* in Ref. [13]. In this paper, the asymptotic and the homogeneous *Neumann* boundaries are both half circles with a radius of *5m* and centred at *O*.

Table 1 Stored Electric Energy ($\times 10^{-10} J$)

ABC FEM	NO-ABC FEM	Ref. [12]
0.3855	0.3631	0.3946

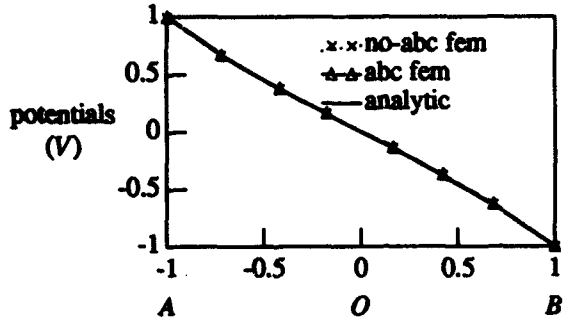

Fig. 2 Potential distribution along the line *AOB*.

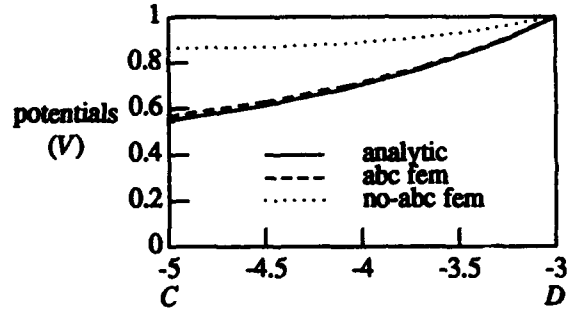

Fig. 3 Potential distribution along the line *CD*.

4.2 Quasistatic Magnetic Field Problem

The quasistatic magnetic field problem consists of an infinitely long circular cylindrical conductor excited by a uniform transverse magnetic field as shown in Fig. 4. The induced power loss in the conductor is calculated and compared with analytic results [17] and results obtained with the hybrid integrodifferential finite element - Green's function method [18].

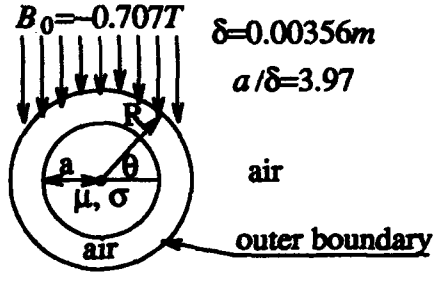

Fig. 4 A circular cylindrical conductor excited by a TM field.

It should be noted that in this eddy current problem, the *z*-component of the magnetic vector potential A is composed of two terms; one is the source term and the other is the reaction term. It is the reaction term, not the source term, that satisfies the ABC-s. Therefore, it is necessary to make appropriate transformations to accommodate this. In this 2D problem, the *z*-component of the magnetic vector potential A is denoted by *A* hereafter.

The integrodifferential equation governing eddy currents in the conductor is given in [7] as

$$\frac{1}{\mu}\nabla^2 A - j\omega\sigma A + j\omega\sigma \frac{\int \sigma A \, dS}{\int \sigma \, dS} = 0 \tag{23}$$

Let A be the total magnetic vector potential, it can be expressed as

$$A = A_e + A_s \tag{24}$$

where A_e is the reaction magnetic vector potential and A_s is the source magnetic vector potential. A_e satisfies the asymptotic boundary conditions. If the asymptotic boundary is circular, we have

$$\frac{\partial A}{\partial r} = \frac{\partial A_e}{\partial r} + \frac{\partial A_s}{\partial r} \tag{25}$$

From (20), we have

$$\frac{\partial A_e}{\partial r} = a(r)A_e + b(r)\frac{\partial^2 A_e}{\partial \theta^2} \tag{26}$$

Substituting for A_e and $\frac{\partial A_e}{\partial r}$ from (24) and (25) into (26) leads to

$$\frac{\partial A}{\partial r} = a(r)(A - A_s) + b(r)\left[\frac{\partial^2 A}{\partial \theta^2} - \frac{\partial^2 A_s}{\partial \theta^2}\right] + \frac{\partial A_s}{\partial r} \tag{27}$$

Rearranging of (27) produces the following expression

$$\frac{\partial A}{\partial r} = a(r) + b(r)\frac{\partial^2 A}{\partial \theta^2} + M_s \tag{28}$$

where M_s is given by

$$M_s = -a(r)A_s - b(r)\frac{\partial^2 A_s}{\partial \theta^2} + \frac{\partial A_s}{\partial r} \tag{29}$$

Substituting (28) and (29) into the integrodifferential finite element equation accomplishes the asymptotic boundary formulation for eddy current problems due to external field excitations.

If the outer boundary is at a sufficiently large distance from the eddy current conductor, the normal derivative of the reaction magnetic vector potential can be assumed to be zero.

Therefore, (25) can be rewritten as

$$\frac{\partial A}{\partial r} = \frac{\partial A_s}{\partial r} \tag{30}$$

Substitution of (30) into (22) leads to the inhomogeneous *Neumann* boundary condition integrodifferential finite elements.

In this eddy current problem, the uniform transverse magnetic field can be represented by the source magnetic vector potential as follows [19]:

$$A_s = -B_0 r \cos\theta \tag{31}$$

where B_0 is the source flux density and θ is as shown in Fig. 4.

Fig. 5 shows calculated power loss errors using first and second order ABC integrodifferential finite elements. Fig. 6 illustrates the loss errors employing the inhomogeneous *Neumann* boundary condition integrodifferential finite elements. The power loss error using the hybrid integrodifferential finite element - Green's function method is 0.12% [19]. In these plots, the abscissa is the ratio of the radius R of the outer boundary and the conductor skin depth δ.

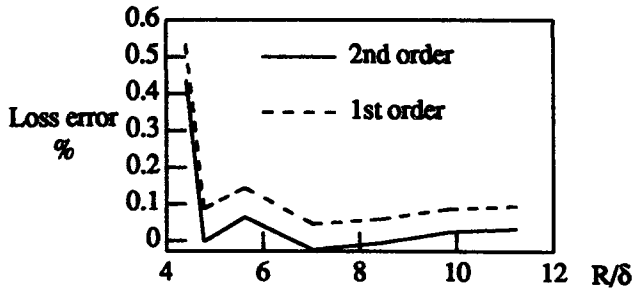

Fig. 5 Power loss errors using first and second order ABC integrodifferential finite elements as a function of the locations of the outer boundary.

It is noted that ABC-s using integrodifferential finite elements, like the hybrid integrodifferential finite element - Green's function method, can provide very accurate results. On the other hand, inhomogeneous *Neumann* boundary condition can only yield accurate solutions when the outer boundary is sufficiently far away from the conductors (R/δ is greater than 45). It is also observed that the second order ABC is generally better than the first order ABC and the ABC boundary need not be placed far from the conductor to obtain accurate results. It is sufficient to place the outer boundary half a skin depth away from the conductor surface. The mesh generation of the outer region also bears impact on the solution accuracy. The meshes should not be severely

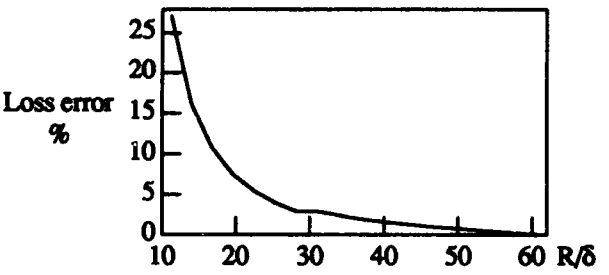

Fig. 6 Power loss errors with the inhomogeneous *Neumann* boundary condition as a function of the locations of the outer boundary.

unequilateral.

Since ABC with finite elements preserves the sparsity of the finite element matrices, it is a better choice compared to hybrid approaches in terms of computer memory and programming complexities.

5. CONCLUSIONS

This paper presents a study of the computation of static and quasistatic electromagnetic fields using finite elements with the asymptotic boundary conditions. Asymptotic boundary conditions for eddy current problems due to external field excitations are also derived. The effect of outer boundary locations on the solution accuracy is investigated. The study reveals that the employment of asymptotic boundary conditions improves the calculation results compared to the use of homogeneous and inhomogeneous *Neumann* boundary conditions. The accuracy of finite elements with ABC-s, like hybrid approaches, is very satisfactory. For eddy current problems, it is sufficient to place the outer boundary half a skin depth away from the conductor surface.

REFERENCES

[1] P. Bettess, "Finite element modelling of exterior electromagnetic problems," *IEEE Trans. Magn.*, Vol.24, No. 1, Jan. 1988, pp. 238-243.

[2] P. Silvester, D.A. Lowther, C.J. Carpenter and E.A. Wyatt, "Exterior finite elements for two-dimensional field problems with open boundaries," *Proc. IEE*, Vol. 124, Dec. 1977, pp. 1267-1270.

[3] H. Hurwitz, Jr., "Infinitesimal scaling - a new procedure for modeling exterior field problems," *IEEE Trans. Magn.*, Vol. 20, No.5, Sep. 1984, pp. 1918-1923.

[4] R.L. Ungless, *An Infinite Finite Element* , MSc Thesis, Univ. of British Columbia, 1973.

[5] I.R. Ciric and S.H. Wong, "Inversion transformation for the finite-element solution of three-dimensional exterior-field problems," *COMPEL*, Vol. 5, No. 2, 1986, pp. 53-64.

[6] B.H. McDonald and A. Wexler, "Finite element solution of unbounded field problems," *IEEE Trans. Microwave Theory Tech.*, Vol. 20, No. 12, Dec. 1972, pp. 841-847.

[7] Q. Chen, A. Konrad and P.P. Biringer, "An integrodifferential finite element - Green's function method for the solution of unbounded eddy current problems," *IEEE Trans. Magn.*, Vol.29, No. 2, Mar. 1993, pp. 1874-1877.

[8] K.K. Mei, R. Pous, Z. Chen, Y. Liu and M. Prouty, "Measured equation of invariance: a new concept in field computations," *IEEE Trans. Antennas Propagat.*, Vol. 42, No. 3, Mar. 1994, pp. 320-328.

[9] B. Engquist and A. Majda, "Radiation boundary conditions for the numerical simulation of waves," *Math. Comp.*, Vol. 31, No. 139, July 1977, pp. 629-651.

[10] A. Bayliss, M. Gunzburger and E. Turkel, "Boundary conditions for the numerical solution of elliptic equations in exterior regions," *SIAM J. Appl. Math.*, Vol. 42, No. 2, April 1982, pp. 430-451.

[11] T.G. Moore, J.G. Blaschak, A. Taflove and G.A. Kriegsmann, "Theory and application of radiation boundary operators," *IEEE Trans. Antennas Propagat.*, Vol. 36, No. 12, Dec. 1988, pp. 1797-1812.

[12] M. Feliziani, "Numerical solutions of low-frequency scattering problems," *IEEE Trans. Magn.*, Vol. 28, No. 2, Mar. 1992, pp. 1224-1227.

[13] J.R. Brauer, S.M. Schaefer and R. Mittra, "Simulation of static open boundary problems in MSC/EMAS," *The MSC 1991 World Users' Conf.*, Mar. 1991, E/EAD Paper# 69.

[14] J.R. Brauer, S.M. Schaefer, J.F. Lee and R. Mittra, "Asymptotic boundary condition for three dimensional magnetostatic finite elements," *IEEE Trans. Magn.*, Vol.27, No. 6, Nov. 1991, pp. 5013-5015.

[15] J.R. Brauer and F. Hirtenfelder, "Surface integrals on 3D and 2D finite element models for skin effect excitations and open boundaries," *IEEE Trans. Magn., Vol.28, No. 2, Mar. 1992, pp. 1659-1662.*

[16] A. Khebir, A.B. Kouki and R. Mittra, "Asymptotic boundary conditions for finite element analysis of three-dimensional transmission line discontinuities," *IEEE Trans. Microwave Theory Tech.*, Vol. 38, No. 10, Oct. 1990, pp. 1427-1432.

[17] A. Konrad, "The numerical solution of steady-state skin effect problems - an integrodifferential approach," *IEEE Trans. Magn.*, Vol. 17, No. 1, Jan. 1981, pp. 1148-1152.

[18] M.P. Perry, *Low Frequency Electromagnetic Design*, New York: Marcel Dekker, Inc., 1985, pp. 135-144.

[19] Q. Chen, A. Konrad and P.P. Biringer, " A hybrid approach to the solution of open boundary eddy current problems under TM field excitation," *IEEE Trans. Magn.*, Vol.29, No. 6, Nov. 1993, pp. 2485-2487.

THREE METHODS FOR EVALUATION OF FREQUENCY-DEPENDENT RESISTANCES AND INDUCTANCES OF MULTICONDUCTOR TRANSMISSION LINES

Antonije R. Djordjević
School of Electrical Engineering
University of Belgrade, Yugoslavia

Tapan K. Sarkar
Electrical and Computer Engineering Department
Syracuse University, Syracuse, N.Y. 13244-1240

Abstract. Three methods for the analysis of frequency-dependent resistances and inductances of multiconductor transmission lines are outlined and compared. The first method comes from power-engineering applications, and it is based on a numerical solution of an integral equation for the distribution of the conductor volume currents. The second method is based on the perturbation technique. The third method comes from high-frequency applications, and it is based on the principle of equivalent surface electric and magnetic currents.

1. INTRODUCTION

We consider a multiconductor transmission line, consisting of $(N+1)$ infinitely long cylindrical conductors of arbitrary cross sections (Figure 1). In the circuit-theory analysis of the response of such a line, usually the quasi-TEM approach is applied [Djordjević et al., 1987]. Thereby, one of the conductors is assumed to be the reference conductor ("ground"), for example conductor $\#(N+1)$, and the other N conductors are referred to as the signal conductors. In the circuit theory, the state of the line is represented in terms of currents of the signal conductors and voltages between the signal conductors and the reference conductor.

The circuit-theory analysis starts from the primary parameters of the line. For a multiconductor line, these parameters are the matrix $[B']$ of electrostatic-induction coefficients per unit length (often improperly referred to as the the capacitance matrix), the matrix $[G']$ of conductances per unit length, the matrix $[L']$ of inductances per unit length and the matrix $[R']$ of resistances per unit length. The dimensions of all these four matrices are N by N. Following the quasi-TEM approach, these matrices are evaluated from quasi-static analyses. More precisely, the matrices $[B']$ and $[G']$ are evaluated simultaneously from one electrostatic analysis of a two-dimensional system, in which the dielectric permittivity is taken to be complex [Djordjević et al., 1989]. The dielectric permittivities vary with frequency, and so do the matrices $[B']$ and $[G']$. In most practical cases, the relative variations of the matrix $[B']$ are very small, but they must be included in order to obtain a causal response in the time domain [Arabi et al., 1991].

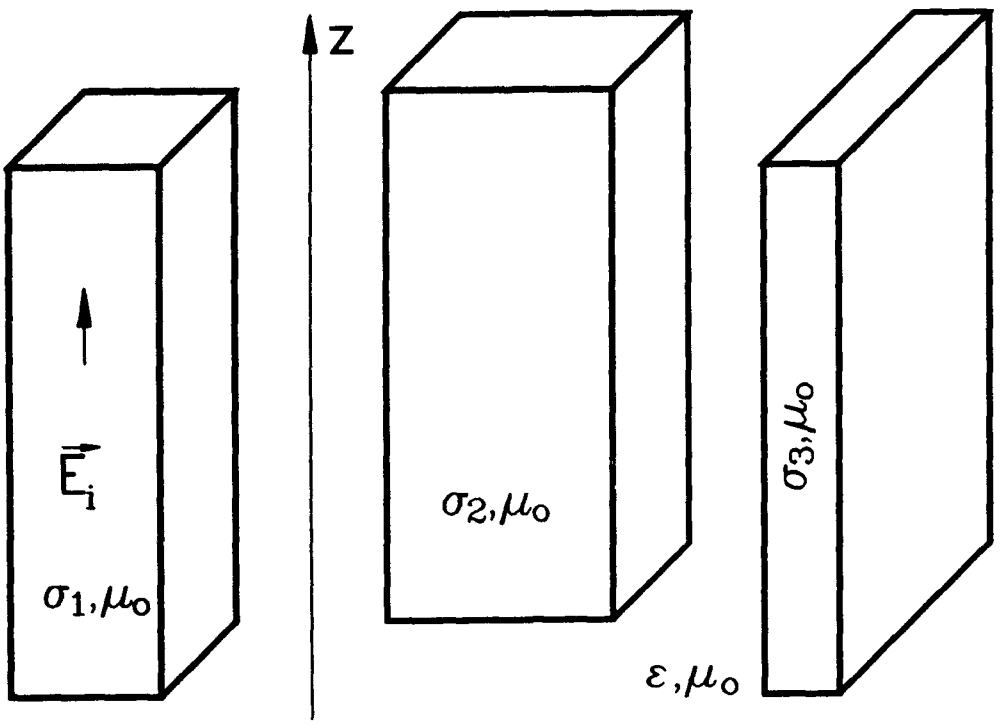

Figure 1. Sketch of a multiconductor transmission line (N=2).

The matrices $[L']$ and $[R']$ are evaluated from another analysis. In many cases, the results are required only for high frequencies, when the skin effect is fully developed. In those cases, the matrix $[L']$ is computed by inverting the matrix $[B'_o]$ which is evaluated when the transmission line dielectrics are replaced by vacuum, and the matrix $[R']$ is thereby evaluated by the perturbation method. The resulting matrix $[L']$ is frequency independent, while the matrix $[R']$ is proportional to $\sqrt{f}$, where f is the operating frequency. However, even in this case, a correction to the matrix $[L']$ is required in order to obtain a causal response, which consists in adding $[R']/\omega$ (where $\omega=2\pi f$ is the angular frequency) to the matrix $[L']$.

However, if a broader frequency range is of interest, the frequency variations of the matrices $[L']$ and $[R']$ are more complicated [Djordjević and Sarkar, 1994]. At the low-frequency end (towards the d.c. case), the current is practically uniformly distributed over a conductor cross section, there exist effects of the internal inductance, and the resistance tends to the d.c. value. In the intermediate region between the low and high frequencies, the edge and proximity effects take part in addition to the skin effect. These variations may be important not only for broadband signals in ordinary transmission lines, but also for integrated circuits, where the conductor thickness can be very small (e.g., thin-films), so that the skin effect need not be developed even in the gigahertz region.

The variations of the matrices $[L']$ and $[R']$ in a broad frequency range can be evaluated using several numerical techniques. We will concentrate our

attention to three of them. All of them treat the multiconductor transmission line of Figure 1 as a two-dimensional system, in which only axial currents are excited. For simplicity, we will assume the medium to be nonmagnetic everywhere.

The first technique is based on formulating an integral equation for the volume current distribution within the conductors, and it will be referred to as the volume-current method. This method has been successfully used for quite some time in solution of various power-engineering problems involving eddy currents [Popović and Popović, 1972]. The second method is a high-frequency approximation based on an electrostatic analysis with the perturbation technique [Djordjević et al., 1989], and it will be referred to as the perturbation method. The third method is a high-frequency technique, which is based on the equivalence theorems and the concept of equivalent surface currents, and it will be referred to as the surface-current method [Djordjević et al., 1985, Djordjević and Sarkar, 1986]. These three methods are briefly presented in Sections 2, 3 and 4, respectively, and in Section 5 a comparison between these techniques is given and illustrated by numerical examples. Thereby, the accuracy, ease of programming, cpu time and applicable frequency range of each method are evaluated. Of course, in addition to the three presented techniques there exist a variety of other methods for the analysis of multiconductor transmission lines which include the conductor losses [Faraji-Dana and Chow, 1990, Kiang, 1991]. The most sophisticated of these methods even take into account the dispersion effects of inhomogeneous dielectrics.

For all three techniques, each conductor of Figure 1 is assumed to be made of a linear homogeneous nonmagnetic material of a finite conductivity $(\sigma_1,\ldots,\sigma_{N+1})$. A time-harmonic regime is assumed, of an angular frequency ω. For each conductor the condition $\sigma \gg \omega\varepsilon_c$ is assumed to be fulfilled (where ε_c is the conductor permittivity), so that each conductor can be characterized by its complex permittivity $\varepsilon_e = -j\sigma/\omega$. The conductors are placed in a linear homogeneous dielectric, of parameters ε and μ_o. A Cartesian coordinate system is associated with the transmission line, where the z-axis is parallel to the conductor axis.

2. VOLUME-CURRENT METHOD

This technique has been applied in the solution of power-engineering problems of analyzing various buses [Popović and Popović, 1972]. It is based on formulating an integral equation for the distribution of the current within the conductor volume, and solving this equation using the method of moments [Harrington, 1993].

We assume that the excitation of the system of Figure 1 is modeled by an impressed (known) axial electric field ($\bar{E}_i = E_{iz}\hat{u}_z$, where $\hat{u}_z$ is the unit vector of the z-direction), which is uniform over the cross section of each conductor, as well as in the z-direction. This field actually replaces the axial component of the electric field produced by the transmission-line charges, as these charges are not included into the model [Djordjević et al.,

1985]. As a response to this field, axial volume currents are induced in the conductors. Their density ($\vec{J}=J_z\hat{u}_z$) depends only on the transverse coordinates, and not on z (two-dimensional case), and there are no charges associated with this current. At each point of a conductor, the current density is related to the electric field by

$$\vec{J} = \sigma(\vec{E} + \vec{E}_i) \ , \tag{1}$$

where $\vec{E}$ is the electric field produced by the conductor currents, and it can be expressed in terms of the magnetic vector-potential ($\vec{A}$) as

$$\vec{E} = -j\omega\vec{A} \ . \tag{2}$$

Assuming the medium to be nonmagnetic everywhere (i.e., $\mu=\mu_o$), and neglecting retardation in the dielectric in which the array of conductors is located (which is a valid assumption in power-engineering problems), the magnetic vector-potential is related to the currents, in the two-dimensional case, as

$$\vec{A} = - \int_S \vec{J} \log(r) \, dS \ , \tag{3}$$

where r is the distance between the source and the field points, and S denotes the cross section of all conductors, subject to the condition that the total current of the (N+1) conductors is zero,

$$\int_S \vec{J}\cdot d\vec{S} = 0 \ . \tag{4}$$

Equations (1-3) result in an integral equation for the z-component of the volume-current density vector (J_z),

$$-j\omega \frac{\mu_o}{2\pi} \int_S J_z(x',y') \log(r) \, dx'dy' + \frac{J_z(x,y)}{\sigma} = E_{iz}(x,y) \ , \tag{5}$$

which is valid for any point within any conductor of the line, where x and y are transverse coordinates. For convenience, the coordinates of the source point are denoted by primes, and

$$r = \sqrt{(x-x')^2+(y-y')^2} \ . \tag{6}$$

Equation (5) can be solved numerically, using the method of moments. The simplest choice is the pulse approximation for the current distribution. (More sophisticated approximations can involve entire-domain expansion functions, or even inclusion of skin-effect terms.) To that purpose, we divide the cross section of each conductor in a number of rectangular cells, and assume the current to be uniformly distributed over each cell. We utilize here equal-size cells, but a better policy would be to take cells to be progressively smaller going towards the conductor surfaces in order to obtain results valid in a broader frequency range [Dinh et al., 1990]. The simplest choice for testing is the point-matching method, with the matching points located at the cell centroids. The resulting integrals can be solved analytically. Having solved

for the current distribution, the total current of each conductor can be easily found.

The matrices $[R']$ and $[L']$ can be evaluated in the following way [Djordjević and Sarkar, 1986]. In order to properly model a TEM transmission line, the condition (4) must be fulfilled, which can be rewritten as

$$\sum_{m=1}^{N+1} I_m = 0 \ , \tag{7}$$

where the reference directions for conductor currents (I_m) coincide with the z-axis of Figure 1. The voltage drop per unit length between the signal conductor #m and the reference conductor is

$$\frac{dV_{m(N+1)}}{dz} = -(E_{imz} - E_{i(N+1)z}) \ . \tag{8}$$

From telegraphers' equations we have

$$\frac{d[V]}{dz} = -[Z'][I] = -([R']+j\omega[L'])\ [I] \ , \tag{9}$$

where $[V]$ is the vector of voltages between the signal conductors and the reference conductor, $[I]$ is the vector of signal conductor currents, and $[Z']$ is the matrix of line impedances per unit length. We introduce the augmented vector of currents of currents of all $(N+1)$ conductors, $[I^a]$, and the vector $[E_i]$ of impressed electric fields in the $(N+1)$ conductors. The system being linear, the following relation must be valid:

$$[I^a] = [T][E_i] \ , \tag{10}$$

where $[T]$ is a square matrix ($(N+1)$ by $(N+1)$). The matrix element T_{mn} numerically equals the current I_m when E_{inz}=1 V/m, and all the other impressed fields are zero. We now take $n=1,\ldots,(N+1)$, solve equation (5) and hence evaluate the elements of the matrix $[T]$. Note that this procedure has no physical interpretation if the volume-current method is used, because each time the currents are evaluated, equation (4) is violated. Nevertheless, this numerical procedure yields correct final results for the matrices $[R']$ and $[L']$. From (10) we have

$$[E_i] = [Z^{a\prime}][I^a] \ , \tag{11}$$

where $[Z^{a\prime}] = [T]^{-1}$ is the augmented matrix of impedances per unit length. From equations (7-9) and (11) we can express the elements of the matrix $[Z']$ in terms of the elements of the matrix $[Z^{a\prime}]$ as

$$Z'_{mn} = Z^{a\prime}_{mn} - Z^{a\prime}_{m(N+1)} - Z^{a\prime}_{(N+1)n} + Z^{a\prime}_{(N+1)(N+1)} \ , \quad m,n=1,\ldots,N \ . \tag{12}$$

3. PERTURBATION METHOD

This is a well-known high-frequency approximation [Harrington, 1961], valid when the skin-effect is fully pronounced. In the analysis, the conductors are first assumed to be perfect, and the tangential magnetic field at the conductor surface ($\vec{H}_{tan}$) is evaluated. Then the conductors are assumed to have small losses, so that the magnetic field at the surface is negligibly affected by the presence of losses. The surface density of the power loss in the conductors is evaluated as

$$\frac{dP_c}{dS} = R_s |\vec{H}_{tan}|^2 , \tag{13}$$

where

$$R_s = \sqrt{\pi \mu_o f / \sigma} \tag{14}$$

is the surface resistance of the conductor. In the quasi-static analysis of transmission lines, the presence of inhomogeneous (nonmagnetic) dielectrics is assumed to have no influence on the distribution of the currents and magnetic field. Hence, the magnetic field is evaluated for the case when the dielectric is taken to be vacuum everywhere [Djordjević et al., 1989], which is reduced to solving a two-dimensional electrostatic problem. This solution is based on substituting the conductors by their surface free charges (of density ρ_s), located in vacuum. The current density can be expressed in terms of the charge density as $J=c_o\rho_s$, where $c_o=1/\sqrt{\varepsilon_o\mu_o}$. Setting the electric scalar-potential V at a conductor surface equal to the corresponding conductor potential, the following integral equation is obtained for the charge density

$$-\frac{1}{2\pi\varepsilon_o}\int_s \rho_s \log(r)\, ds = V , \tag{15}$$

where s denotes the contours of all conductors. Similarly to equation (3), equation (15) is valid only if the total charge of the system is zero, i.e.,

$$\int_s \rho_s \, ds = 0 . \tag{16}$$

The integral equation (16) is solved numerically, using the method of moments. The simplest approximation for the charge distribution are pulses (i.e., a piecewise-constant approximation), with the point-matching technique. The condition (16) can be forced if the last point-matching equation is subtracted from all the previous equations, and substituted by (16). The numerical accuracy is improved if the pulses are of nonuniform widths, being smaller in the regions where the charge density varies rapidly (such as near edges or wedges). Another improvement can be achieved by using Galerkin's technique [Harrington, 1993] instead of the point-matching. In any case, the resulting integrals can be evaluated explicitly, resulting in a very efficient technique for the analysis of arbitrary structures [Djordjević et al., 1989].

Having evaluated the conductor charge densities for a set of independent driving conditions, the matrix of electrostatic induction coefficients $[B'_o]$

can be calculated, and the external inductance matrix of the multiconductor transmission line is related to this matrix by

$$[L'_e] = \frac{1}{c_o^2} [B'_o]^{-1} . \tag{17}$$

The matrix $[R']$ is calculated from the power loss per unit length of the line, evaluated for various driving conditions of the line. From the boundary conditions for a perfect conductor, the density of the surface currents ($\vec{J}_s$) has the same magnitude as the intensity of the tangential magnetic field, so that the loss power per unit length of the transmission line is

$$P'_c = \int_s R_s J_s^2 \, dl . \tag{18}$$

The elements of the matrix $[R']$ are evaluated from the power P'_c when one signal conductor carries a current at a time, and when two signal conductors carry currents at a time, while the currents of other conductors is zero. The matrix $[R']$ varies with frequency as $\sqrt{f}$ due to equation (14). (In many practical cases, due to the surface roughness of the conductors, the measured conductor losses can be substantially higher than theoretically predicted for a smooth surface.) A more careful insight into the perturbation approach results in a reactive power in the conductors, in addition to the loss power (these two powers are equal in magnitude). This amounts to the internal inductance of the conductors which can be evaluated as

$$[L'_i] = [R']/\omega , \tag{19}$$

and which should be added to $[L'_e]$ to obtain $[L']$.

3. SURFACE-CURRENT METHOD

The basic idea of this method is to use equivalence theorems [Harrington, 1961] to break the system under considerations into a number of subsystems, each of them being filled with a homogeneous medium. To achieve this, a layer of surface electric currents (of density $\vec{J}_s$, which are in our case axial), and a layer of surface magnetic currents (of density $\vec{M}_s$, which are in our case transverse) must be placed on the conductor surfaces, with the objective to produce a zero total field in a region. The first subsystem consists of the region external to the conductors, with zero fields in the regions occupied by the conductors (external subsystem). The medium in the latter regions can be substituted by that of the external region, thus homogenizing the medium. The second subsystem (the first internal subsystem) consist of the internal region of the conductor #1, with zero field in the remaining space, which can be filled by the same medium of which conductor #1 is made, etc. [Djordjević et al., 1985]. For a transmission line of $(N+1)$ conductors, the number of internal subsystems is $(N+1)$. The homogenization of the medium is required in order to use a simple form of Green's functions in the equations for the potentials. For this technique we use retarded potentials, where Green's function for the two-dimensional case for the external subsystem is

$$g(r) = -\frac{j}{4} H_o^{(2)}(kr) \ , \tag{20}$$

where $H_o^{(2)}$ is Hankel's function of the second kind and order zero, and $k=\omega\sqrt{\varepsilon\mu}$. In the limiting quasi-static case Green's function (20) tends to $-\frac{1}{2\pi}\log(kr)$, thus yielding the kernels of equations (5) and (15). For an internal subsystem Green's function is

$$g(r) = \frac{1}{2\pi}\left[ker(|\gamma|r) + j\, kei(|\gamma|r)\right] \ , \tag{21}$$

where *ker* and *kei* are Kelvin's functions, and $\gamma=\sqrt{j\omega\mu\sigma}$ is the propagation coefficient in the conductor.

The fields can be expressed in terms of the potentials as

$$\vec{E} = -j\omega\vec{A} - \frac{1}{\varepsilon}\,\mathrm{curl}\,\vec{F} + \vec{E}_i \ , \tag{22}$$

$$\vec{H} = -j\omega\vec{F} - \mathrm{grad}\,V_m + \frac{1}{\mu}\,\mathrm{curl}\,\vec{A} + \vec{H}_i \ , \tag{23}$$

where $\vec{F}$ is the electric vector-potential, V_m the magnetic scalar-potential, and $\vec{E}_i$ and $\vec{H}_i$ impressed fields. (The -grad V term is missing in (22) because we again assume the electric currents to be z-directed, with no z-variation.) The potentials are given by

$$\vec{A} = \mu \int_s \vec{J}_s\, g(r)\, ds \ , \tag{24}$$

$$\vec{F} = \varepsilon \int_s \vec{M}_s\, g(r)\, ds \ , \tag{25}$$

$$V_m = \frac{1}{\mu}\int_s \rho_{ms}\, g(r)\, ds \ , \tag{26}$$

where

$$\rho_{ms} = \frac{j}{\omega}\,\mathrm{div}_s\,\vec{M}_s \tag{27}$$

is the density of surface magnetic charges. In our case $\mu=\mu_o$ everywhere.

In order to have a zero field within a region, we impose the boundary conditions that the tangential component of the electric field for the external subsystem is zero, i.e.,

$$\vec{E}_{tan} = 0 \ , \tag{28}$$

which leads to an electric-field integral equation (EFIE) for the equivalent surface currents. We also impose the boundary condition that the tangential

component of the magnetic field for each internal subsystem is zero, i.e.,

$$\vec{H}_{tan} = 0 \ , \tag{29}$$

which leads to magnetic-field integral equations (MFIE). As in the volume-current method, the impressed electric field, $\vec{E}_i$, is taken to be uniform over the cross section of each conductor, and this field replaces the field actually produces by the electric charges. This field is present only in the external subsystem. When the fields are expressed in terms of the potentials, and the potentials in terms of the equivalent surface sources, using equations (20-27), a set of coupled integral equations is obtained for $\vec{J}_s$ and $\vec{H}_s$.

An approximate solution of these equations is obtained using the simplest combination of pulse expansion functions and point-matching. Line magnetic charges are associated with this approximation of the magnetic currents. The pulses are taken to have nonuniform widths (narrower near wedges), and the matching points are located at the pulse midpoints, at the appropriate faces of the boundary surfaces (within regions occupied by conductors for the external subsystem, and outside the conductors for the internal subsystems). Taking into account

$$\text{grad } g(r) = \frac{dg}{dr} \hat{u}_r \ , \tag{30}$$

where $\hat{u}_r$ is the unit vector in the radial direction, for the external subsystem we have for the field components produced by an expansion function (carrying uniform surface currents of densities $\vec{J}_s$ and $\vec{H}_s$),

$$-j\omega\vec{A} = -j\zeta \vec{J}_s \int_s (-\tfrac{j}{4}) H_o^{(2)}(kr) \, d(ks) \ , \tag{31}$$

$$-\frac{1}{\epsilon} \text{curl } \vec{F} = \vec{H}_s \times \int_s \frac{j}{4} H_o^{(2)}(kr) \hat{u}_r \, d(ks) \ , \tag{32}$$

where $\zeta=\sqrt{\mu/\epsilon}$ is the wave impedance of the dielectric. For an internal subsystem we have similarly

$$-j\omega\vec{F} = -\frac{\vec{H}_s}{|\hat{\zeta}|} \int_s \frac{1}{2\pi} [ker(|\gamma|r) + j \, kei(|\gamma|r)] \, d(|\gamma|s) \ , \tag{33}$$

$$-\frac{1}{\epsilon} \text{curl } \vec{A} = -\vec{J}_s \times \int_s \frac{1}{2\pi} [ker'(|\gamma|r) + j \, kei'(|\gamma|r)] \hat{u}_r \, d(|\gamma|s) \ , \tag{34}$$

$$-\text{grad } V_m = -|\vec{H}_s| \left[\frac{j}{2\pi|\hat{\zeta}|} [ker'(|\gamma|r) + j \, kei'(|\gamma|r) \hat{u}_r \right]_{r=r_1}^{r_2} \ , \tag{35}$$

where r_1 and r_2 are distances between the end points of a pulse and the field point, and $\hat{\zeta}=\sqrt{j\omega\mu/\sigma}$ is the wave conductor impedance.

The above system is solved for a set of independent driving conditions, following a similar procedure as for the volume-current method. Hereby, the current of a conductor is obtained by integrating the surface-current density $\vec{J}_s$ around the conductor circumference. The matrices $[R']$ and $[L']$ can now be evaluated from equations (9-12).

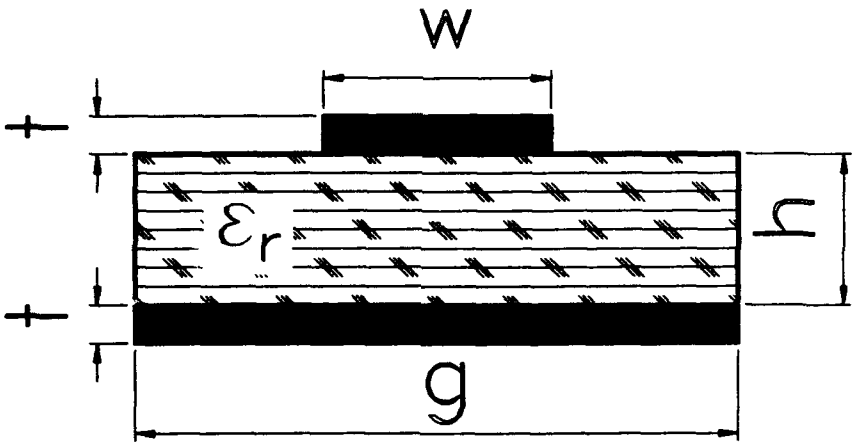

Figure 2. Sketch of a microstrip line.

5. EXAMPLES

The first example is the microstrip line, sketched in Figure 2, of dimensions w=0.2 mm, h=0.1 mm, g=2 mm, and t=0.01 mm. The conductors are made of copper, of conductivity σ=56 MS/m. Shown in Table 1 are the resistance per unit length and the inductance per unit length of this line, versus frequency, obtained by the three techniques presented in this paper. For the volume-current method, the conductors were uniformly divided into pulses (rectangles): n_w=10 along w, n_g=40 along g and n_t=3 along t, resulting in the total of 150 unknowns. For the perturbation technique, the numbers of nonuniformly distributed pulses were n_w=25, n_t=3 and n_g=85 along the corresponding lengths, resulting in a total of 141 unknowns (the thickness of the ground plane was taken to be zero). For the surface-current method, the number of nonuniformly distributed pulses were n_w=25, n_g=50 and n_t=3, respectively, resulting in a total of 324 unknowns (for electric and magnetic currents).

Table 1 illustrates some features of the three techniques. The volume-current method yields excellent results at low frequencies. For example, for f=10 kHz, the numerical results are L'=440.5 nH/m and R'=9.821 Ω/m, while the analytically calculated values [Djordjević and Sarkar, 1993] are L'=439.27 nH/m and R'=9.821 Ω/m. The surface-current method yields a smaller accuracy, especially as the frequency becomes very low. The accuracy can be improved at the expense of taking more pulses. The results of the perturbation method for low frequencies are a large underestimate of R' and an overestimate of L', and they are practically useless.

In the medium-frequency region (300 kHz-50 MHz) the agreement between the volume-current and surface-current methods is excellent, while the results of the perturbation method are still poor. Above about 100 MHz, in the high-frequency (skin-effect) region, the results for R' obtained by the volume-current method tend to saturate, instead of increasing as $\sqrt{f}$. This is due to the pulse approximation for the current distribution, as there must always be a current in the outermost layer of pulses. In the real system, however, the thickness of the current layer constantly decreases with increasing the frequency. The results for R' obtained by the surface-current method follow very well the $\sqrt{f}$ behavior and they are facein a good agreement with the perturbation method. However, at very high frequencies (above about 10 GHz) R' obtained by the surface-current method starts increasing much faster. This is a consequence of radiation. Namely, the structure behaves like a two-dimensional magnetic dipole, the radiation resistance of which is proportional to f^3 [Djordjević et al., 1985]. There would be no radiation effects in the numerical model if the quasi-static kernel of equation (5) were used instead of (20).

Table 1. Primary parameters of microstrip line sketched in Figure 2.

f [Hz]	Volume-current method		Perturbation method		Surface-current method	
	R' [Ω/m]	L' [nH/m]	R' [Ω/m]	L' [nH/m]	R' [Ω/m]	L' [nH/m]
10.00 k	9.821	440.5	0.131	2365.	9.630	431.9
17.78 k	9.822	440.5	0.174	1845.	9.630	433.1
31.62 k	9.822	440.5	0.232	1456.	9.630	434.2
56.23 k	9.823	440.4	0.310	1163.0	9.631	435.3
100.0 k	9.826	440.2	0.413	943.8	9.633	436.1
177.8 k	9.835	439.3	0.551	779.3	9.642	436.2
316.2 k	9.862	436.7	0.735	656.0	9.669	434.4
562.3 k	9.942	429.3	0.980	563.6	9.749	427.4
1.000 M	10.14	411.6	1.306	494.2	9.946	409.6
1.778 M	10.48	382.5	1.742	442.2	10.29	380.2
3.162 M	10.87	353.3	2.323	403.2	10.68	350.6
5.623 M	11.23	333.7	3.098	374.0	11.05	330.9
10.00 M	11.59	322.9	4.131	352.0	11.43	320.2
17.78 M	12.07	316.3	5.509	335.6	11.94	313.6
31.62 M	12.67	311.8	7.346	333.3	12.69	308.8
56.23 M	13.40	308.7	9.796	314.0	13.80	305.1
100.0 M	14.42	306.7	13.06	307.1	15.61	302.4
177.8 M	16.13	305.1	17.42	301.9	18.70	299.7
316.2 M	18.72	303.5	23.23	298.0	23.54	297.2
562.3 M	22.14	302.3	30.98	295.1	30.80	294.9
1.000 G	26.42	301.3	41.31	292.9	41.54	293.0
1.778 G	30.27	300.5	55.09	291.2	55.64	291.3
3.162 G	32.38	300.1	73.46	290.0	73.73	290.1
5.623 G	33.24	300.0	97.96	289.1	98.1	289.3
10.00 G	33.52	299.9	130.6	288.4	133.7	288.7
17.78 G	33.61	299.9	174.2	287.9	199.2	288.7
31.62 G	33.64	299.9	232.3	287.5	387.5	289.5

The second example are two coupled microstrip lines, sketched in Figure 3, of dimensions w=0.6 mm, s=0.02 mm, g=2 mm, h=0.1 mm, t=0.02 mm, and the

conductors are made of copper. Given in Table 2 are the elements of the matrices $[R']$ and $[L']$ for several frequencies, as computed by the three techniques. For comparison, the exact d.c. values for the elements of the matrix $[R']$ are $R'_{11}=R'_{22}=1.935\ \Omega/m$ and $R'_{12}=R'_{21}=0.446\ \Omega/m$. This example confirms the conclusions drawn from the previous example about the behavior of the results of the three methods.

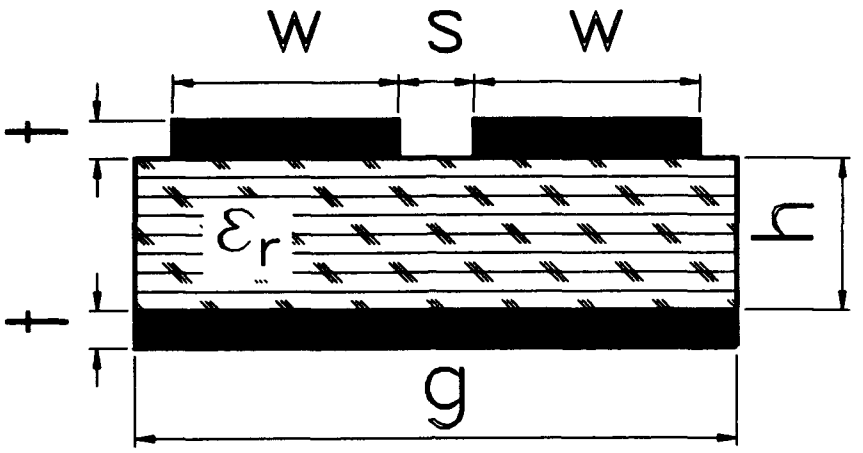

Figure 3. Sketch of two coupled microstrip lines.

Table 2. Primary parameters of coupled microstrip lines sketched in Figure 3.

f [Hz]	Volume-current mehod		Perturbation mehod		Surface-current mehod	
	$R'_{11}=R'_{22}$ $R'_{12}=R'_{21}$ [Ω/m]	$L'_{11}=L'_{22}$ $L'_{12}=L'_{21}$ [nH/m]	$R'_{11}=R'_{22}$ $R'_{12}=R'_{21}$ [Ω/m]	$L'_{11}=L'_{22}$ $L'_{12}=L'_{21}$ [nH/m]	$R'_{11}=R'_{22}$ $R'_{12}=R'_{21}$ [Ω/m]	$L'_{11}=L'_{22}$ $L'_{12}=L'_{21}$ [nH/m]
10.00 k	1.935 0.446	253.9 -26.4	0.074 -0.008	1309. -90.7	1.898 0.459	247.8 -24.3
100.0 k	1.945 0.440	250.7 -23.9	0.235 -0.025	501.7 -3.7	1.908 0.451	247.9 -23.1
1.000 M	2.183 0.316	187.1 15.6	0.742 -0.080	246.3 23.9	2.149 0.327	184.8 16.5
10.00 M	2.576 0.161	156.2 30.2	2.347 -0.253	165.6 32.6	2.694 0.075	152.8 11.9
100.0 M	4.653 0.912	149.1 29.9	7.422 -0.800	140.0 35.3	6.829 -0.263	139.7 35.4
1.000 G	7.576 1.437	146.0 29.0	23.47 -2.53	131.9 36.2	23.28 -2.25	131.9 36.1
10.00 G	7.748 1.457	145.9 29.0	74.22 -8.00	129.4 36.5	77.19 -1.80	122.9 36.4

Regarding the complexity of the programing, the volume-current method is simplest, the perturbation method is somewhat more complicated, and the surface-current method is much more complicated than the other two methods. Regarding the c.p.u. time, the perturbation technique is faster than the other

two methods even if only one frequency is considered, because for a given accuracy (in the high-frequency region, where this method is valid) it usually requires much less unknowns than the other two methods, and it involves only real arithmetics. In addition, results for various frequencies can thereafter be obtained even by hand calculations. The c.p.u. times of the volume-current and surface-current methods are comparable in most cases.

6. CONCLUSION

Three numerical methods for analysis the frequency-dependent matrices of resistances and inductances per unit length of multiconductor transmission lines are presented and compared. The overall performance of the volume-current method is best at low and medium frequencies (when the skin effect is not yet developed), but it can be extended into the skin effect region using nonuniform segmentation, adapted to the skin depth at the highest operating frequency. For the frequencies deep in the skin-effect region, the perturbation technique is superior. The surface-current method is the only one that covers the full frequency range, at the expense of a more complex programing than the other two techniques, and a somewhat reduced accuracy at very low frequencies. Therefore, a combination of the volume-current method and the perturbation method seems to be the best choice for most applications, with a particular caution taken to obtain a good overlap of results at the beginning of the high-frequency region (when the skin depth is of the order of the conductor thickness). However, the surface-current method is indispensable for an independent check of the results in this transition region.

REFERENCES

Arabi, T.R., Murphy, A.T., Sarkar, T.K., Harrington, R.F., Djordjević, A.R., "On the modeling of conductor and substrate losses in multiconductor, multidielectric transmission line systems", *IEEE Trans. on Microwave Theory and Techniques*, vol. MTT-39, no. 7, pp. 1090-1097, July 1981.

Dinh, T. Vu, Cabon, B., Chilo, J., "Time domain analysis of skin effect on lossy interconnections", *Electronics Letters*, vol. 26, no. 25., pp. 2057-2058, December 1990.

Djordjević, A.R., Sarkar, T.K., Rao, S.M., "Analysis of finite conductivity cylindrical conductors excited by axially-independent TM electromagnetic field", *IEEE Trans. on Microwave Theory and Techniques*, vol. MTT-33, no. 10, pp. 960-966, October 1985.

Djordjević, A.R., Sarkar, T.K., "Frequency behaviour of multiconductor transmission line inductances and resistances", *Archiv für Elektronik und Übertragungstechnik*, B. 40, H. 4, pp. 254-256, April 1986.

Djordjević, A.R., Sarkar, T.K., Harrington, R.F., "Time-domain response of multiconductor transmission lines", *Proc. IEEE*, vol. 75, no. 6, pp. 743-764, June 1987.

Djordjević, A.R., Harrington, R.F., Sarkar, T.K., Baždar, M.B., *Matrix Parameters for Multiconductor Transmission Lines (Software and User's Manual)*, Boston: Artech House, 1989.

Djordjević, A.R., Sarkar, T.K., "Closed-form formulas for frequency-dependent

resistance and inductance per unit length of microstrip and strip transmission lines", in print in *IEEE Trans. on Microwave Theory and Techniques*, 1994.

Faraji-Dana,R., Chow,Y. L., "The current distribution and AC resistance of a microstrip structure", *IEEE Trans. on Microwave Theory and Techniques*, vol. 38, no. 9, pp. 1268-1277, September 1990.

Harrington,R.F., *Time-Harmonic Electromagnetic Fields*, New York: McGraw-Hill, 1961.

Harrington,R.F., *Field Computation by Moment Methods*, New York: IEEE Press, 1993.

Kiang,J.F., "Integral equation solution to the skin effect problem on conductor strips of finite thickness", *IEEE Trans. on Microwave Theory and Techniques*, vol. 39, no. 3, pp. 452-460, March 1991.

Popović,B.D., Popović,Z.D., "Method for determining power-frequency current distribution in cylindrical conductors", *Proc. IEE*, vol. 119, no.5, pp. 569-574, May 1972.

NUMERICAL SOLUTIONS OF WAVE PROPAGATION IN DISPERSIVE AND LOSSY TRANSMISSION LINES

Junwei LU, Yukio KAGAWA*, and David V. THIEL

School of Microelectronic Engineering, Faculty of Science & Technology,
Griffith University, Nathan, Qld 4111, AUSTRALIA
* Department of Electrical and Electronic Engineering, Faculty of Engineering,
Okayama University, Okayama 700, JAPAN

ABSTRACT: *A numerical model is proposed for application to dispersive transmission lines. Numerical results are compared with the analytical solution of the dispersive wave equation based on the wave propagation solved by means of finite element method in one dimension case and Newmark-β method in the time domain. This comparison between numerical and analytical solutions validates this numerical method as a suitable method to study wave propagation in dispersive transmission lines. Several practical applications including electromagnetic propagation in a plasma and the transient response of a surge wave in high-voltage transformer windings are presented in this paper.*

1. INTRODUCTION

Transmission lines can be used to model a large variety of important applications in addition to the transmission of a signal from one point to another [1]. Physical phenomena such as the propagation of solitons [2]; breakdown process of an avalanche diode [3,4]; high-voltage resistance divider [5]; various plasma physics phenomena [6,7]; propagation in multi-layered earth media [8] have practical applications which have been modeled by transmission lines. While most of these problems can be solved analytically some of them are extremely difficult or impossible to solve by purely analytical methods.

Since the computational power of even quite small computers has rapidly developed, numerical methods are playing an increasingly important role in solving the mathematical equations[9,10]. Such numerical techniques have made wave propagation problems easy to solve using numerical models and results can be represented graphically for rapid understanding [11].

In this research, a one dimensional finite element model is employed for a variety of dispersive transmission lines with a variety of boundary conditions. The emphasis taken in this paper is that the calculation technique itself is very important if accurate and convergent solutions are to be obtained. Calibration factors such as the ratio of lumped capacitors (see fig. 1), velocity of traveling wave, the element size and time step have dependent relationships which can not be ignored. The numerical errors can be controlled by sufficiently fine discretization. Initially the method is validated by comparing numerical solutions with the analytical solutions for the case of the dispersive wave equation for a linear, homogeneous transmission line. In the case of inhomogeneous and nonlinear problems the most suitable method is often a numerical method. Appropriate models for nonlinear dispersive transmission lines are the subject of this paper.

2. A BASIC EQUATION FOR DISPERSIVE TRANSMISSION LINES

Typical transmission lines with dispersive properties can be categorized into linear and nonlinear transmission lines. Fig. 1. shows generalized dispersive transmission lines with both loss and nonlinear characteristics.

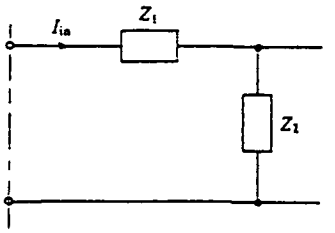

a. Linear parameter

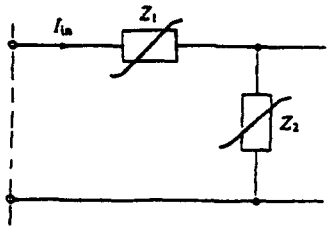

b. Nonlinear parameter

Fig. 1. Typical sections of transmission lines with linear and nonlinear parameters

As a start in the numerical formulation of a number of simple cases, the basic analytical solutions of dispersive wave equations for a linear transmission line must be obtained and compared with numerical solutions. In this section the basic solutions of dispersive wave equations are discussed:

2.1 Lossless dispersive transmission line

The lossless dispersive transmission line in Fig. 2 can be described by a set of partial differential equations in instantaneous voltage u and current i as follows [2]:

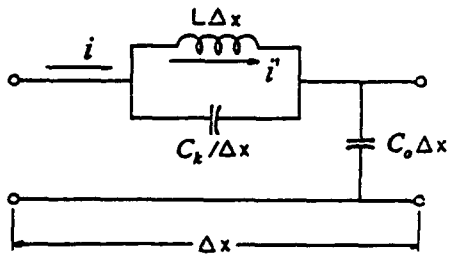

Fig.2. A section of lossless dispersive transmission line

$$-\frac{\partial i'}{\partial x} = C_0 \frac{\partial u}{\partial t} - C_k \frac{\partial^3 u}{\partial t \partial x^2} \qquad (1)$$

$$-\frac{\partial u}{\partial x} = L \frac{\partial i'}{\partial t} \qquad (2)$$

where C_k and C_0 are the series and parallel capacitances per unit length and L is the series inductance per unit length; i is the total instantaneous current, i' is the current in the inductive branch, u is the instantaneous voltage and x is the direction of the transmission line. From (1) and (2), we can derive a dispersive wave equation for the voltage u

$$\frac{\partial^2 u}{\partial t^2} - C_S^2 \frac{\partial^2 u}{\partial x^2} - \lambda_D^2 \frac{\partial^4 u}{\partial t^2 \partial x^2} = 0 \qquad (3)$$

where

$$C_S^2 = 1/LC_0 \qquad (4)$$

$$\lambda_D^2 = C_k / C_0 \qquad (5)$$

The dispersion relation is obtained by assuming a solution of the form $u \sim u_0 \exp(j\omega t \mp jkx)$.

$$\omega^2 = \frac{C_S^2 k^2}{1 + k^2 \lambda_D^2} \qquad (6)$$

where ω is the angular frequency and k is the wave number of propagation. The dispersion relation is shown schematically in Fig. 3 [13].

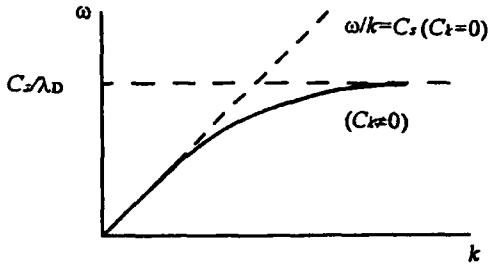

Fig. 3. Dispersion relation of wave equation, where C_S is the velocity of the wave.

In the case of $C_k \to 0$, λ_D in the third term of eq.(3) tends to zero. The lossless wave equation is retrieved, there is no dispersion, and the initial waveform does not change during propagation. It is the well known wave equation [12]. However, when λ_D (which is called Debye shielding length in plasma physics) is

larger than zero, the wave is significantly dispersive and the waveform changes as the wave progresses.

Since eq. (3) is a linear dispersive wave equation, the analytical solutions are obtained using the method of Laplace transformation. Consider the transient response for which the initial conditions of transmission line and its derivative are

$$u(x,0)=0,\ \left\{\frac{\partial u(x,t)}{\partial t}\right\}_{t=0}=0 \qquad (7)$$

and the boundary conditions for the open circuit at terminal N are

$$u(0,t)=1,\ \left\{\frac{\partial u(x,t)}{\partial x}\right\}_{x=\ell}=0 \qquad (8)$$

where l is the total length of transmission line.

With the inverse Laplace transformation of solution using Heaviside's expansion theorem, the exact solution of Eq.(3) for the open boundary condition is given by

$$u(x,t)=1-\sum_{m=1}^{\infty}\frac{16\ell^2\sin\{(2m-1)\pi x/2\ell\}}{\{4\ell^2+(2m-1)^2\lambda_D^2\pi^2\}(2m-1)\pi}\cdot\cos(\omega_{2m-1})t \qquad (9)$$

where

$$\omega_{2m-1}=\frac{(2m-1)\pi}{\{4\ell^2/C_s^2+(2m-1)^2\lambda_D^2\pi^2/C_s^2\}^{1/2}} \qquad (10)$$

In the case of the boundary conditions for the terminal short-circuited, the spatial initial conditions are the same and the boundary conditions are given by

$$u(0,t)=1,\ u(\ell,t)=0 \qquad (11)$$

The exact solution obtained using the same procedure as above, can be written

$$u(x,t)=(1-\frac{x}{\ell})-\sum_{m=1}^{\infty}\frac{2\ell^2\sin\{m\pi x/\ell\}}{\{\ell^2+m^2\lambda_S^2\pi^2\}m\pi}\cdot\cos(\omega_m)t \qquad (12)$$

where

$$\omega_m=\frac{m\pi C_s}{\left[\ell^2+\lambda_D^2 m^2\pi^2\right]^{1/2}} \qquad (13)$$

For both cases, as λ_D tends to zero, the solutions (9) and (12) reach the well-known solutions of the non dispersive wave equation [12]. The details of the procedure of solving eq. (3) by using the method of Laplace transformation can be found in [14].

2.2 Dispersive transmission line with loss

A natural extension of the dispersive transmission line approach is the inclusion of resistance. The transmission line with loss is shown in Fig. 4, in which linear and homogeneous parameters are assumed [15].

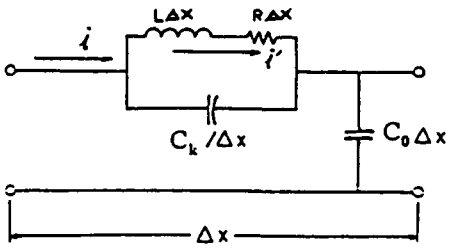

Fig. 4. A section of linear dispersive transmission line with loss

The equivalent circuit corresponding to the following partial differential equation for the voltage u is obtained as

$$\frac{\partial^2 u}{\partial t^2}-C_s^2\frac{\partial^2 u}{\partial x^2}-\lambda_D^2\frac{\partial^4 u}{\partial t^2\partial x^2}+\alpha^2\frac{\partial u}{\partial t}-\alpha^2\lambda_D^2\frac{\partial^3 u}{\partial x^2\partial t}=0 \qquad (14)$$

where $\alpha = (R/L)^{1/2}$. The dispersion relation for this equation is derived as follows:

$$\omega^2 = \frac{C_S^2 k^2}{1 + k^2 \lambda_D^2} \pm j\omega\alpha^2 \qquad (15)$$

We consider the transient response for which the initial conditions and the boundary conditions for the open circuited terminal are the same as (7) and (8) respectively. With the inverse Laplace transformation of solution using Heaviside's expansion theorem, we derive the exact solution of Eq.(14).

$$u(x,t) = 1 - \sum_{m=1}^{\infty} A_m e^{-\delta t} \sin\left(\frac{2m-1}{2\ell}\pi x\right) \cdot \cos(\omega_o)t \qquad (16)$$

where l is the total length of the transmission line, A_m is

$$A_m = \frac{2j}{-\delta \pm j\omega_o \ell \frac{1}{2}\left[\frac{1+\{R+(-\delta \pm j\omega_o)L\}(-\delta \pm j\omega_o)C_k}{\{R+(-\delta \pm j\omega_o)L\}(-\delta \pm j\omega_o)C_o}\right]^{1/2}} \cdot \frac{1}{\frac{C_o\{R+2L(-\delta \pm j\omega_o)\}}{\{1+C_k(-\delta \pm j\omega_o)(R+L)\}^2}} \qquad (17)$$

δ and ω_0 are expressed as follows:

$$\delta = R/2L \qquad (18)$$

$$\omega_o^2 = \frac{\{(2m-1)\pi\}^2}{4\ell^2 LC_o + (2m-1)^2\pi^2 LC_k} - \frac{R^2}{4L^2} \qquad (19)$$

The case of the boundary conditions for the short-circuited terminal must be considered here, when the initial conditions are the same as that of eq. (11). Using the same procedure as before, the exact solution is

$$u(x,t) = (1 - \frac{x}{\ell}) - \sum_{m=1}^{\infty} A_m e^{-\delta t} \sin\left(\frac{2m}{2\ell}\pi x\right) \cdot \cos(\omega,)t \qquad (20)$$

where

$$A_m = \frac{2j}{-\delta \pm j\omega,\ell \frac{1}{2}\left[\frac{1+\{R+(-\delta \pm j\omega,)L\}(-\delta \pm j\omega,)C_k}{\{R+(-\delta \pm j\omega,)L\}(-\delta \pm j\omega,)C_o}\right]^{1/2}} \cdot \frac{1}{\frac{C_o\{R+2L(-\delta \pm j\omega,)\}}{\{1+C_k(-\delta \pm j\omega,)(R+L)\}^2}} \qquad (21)$$

ω_S is expressed as

$$\omega_s^2 = \frac{(m\pi)^2}{\ell^2 LC_o + m^2\pi^2 LC_k} - \frac{R^2}{4L^2} \qquad (22)$$

For both cases, as R tends to zero, the solutions of (16) and (20) will be the same as that the solutions of (9) and (12) which are the dispersive transmission lines without loss.

3. NUMERICAL MODEL OF DISPERSIVE TRANSMISSION LINE

The wave propagation of an arbitrary waveform on a dispersive transmission line is a time-dependent problem. Such problems can usually be simplified and solved as a unidimensional problem in time and space. The finite element method requires that the spatial field can be divided into a number of elements and discretized by means of the Variational method or Galerkin approach [16]. The system matrix equations obtained can be then solved by Newmark-β method or the Runge-Kutta method. If the problems are related to nonlinear properties, then the Newton-Raphson or Relaxation methods can be used to solve the nonlinear system matrix equations.

3.1 Lossless dispersive transmission line

Using the Galerkin method, equation (3) for the one dimensional case can be written as

$$G_i = \int_0^{\ell}\left(\frac{\partial^2 u}{\partial t^2} - C_S^2\frac{\partial^2 u}{\partial x^2} - \lambda_D^2\frac{\partial^4 u}{\partial t^2 \partial x^2}\right)N_i dx = 0 \qquad (23)$$

where N_i is a shape function, the matrix equation for a single element is obtained as

$$[M]^e\{\ddot{u}\}^e + C_s^2[S]^e\{u\}^e + \lambda_D^2[S]^e\{\ddot{u}\}^e = \{0\} \quad (24)$$

where $(\cdot\cdot)$ indicates the derivative with respect to time. [M] and [S] are

$$[M]^e = \frac{\ell^e}{6}\begin{bmatrix} 2 & 1 \\ 1 & 2 \end{bmatrix} \quad (25)$$

$$[S]^e = \frac{1}{\ell^e}\begin{bmatrix} 1 & -1 \\ -1 & 1 \end{bmatrix} \quad (26)$$

where ℓ^e is the length of element. Then we use the Newmark-β method to solve for increasing time steps [17]. The system matrix equation will be written as for the Newmark-β method.

$$(\lambda_D^2[S]+[M])\{\ddot{u}\}+C_s^2[S]\{u\}=\{0\} \quad (27)$$

A comparison between numerical solutions and analytical solutions is given in Fig. 5 where the element number is 20 and the number of nodes is 21. The initial voltage at all *i* nodes $u(i)=0$ at t=0, and the boundary condition at terminal $u(21)=0$ for the short-circuited case and $\partial u/\partial x=0$ for the open circuit. To simplify the problem the mutual inductance is not considered. Clearly, the numerical solution is in good agreement with the analytical solution. In addition, it was found that λ_D, the time step Δt and the element length Δx must be related by the conditions to ensure a stable solution.

$$\Delta x / \Delta t \rangle C_s \quad (28a)$$

and

$$\lambda_D \langle \Delta x \langle 3\lambda_D \quad (28b)$$

where Δt is the time step size, Δx is the element length and C_s is wave propagation velocity. λ_D is the Debye shielding length [13] or ratio of lumped capacitors in the section of dispersive transmission line.

The error control of time-dependent problems has been discussed in many numerical method books and articles, but the numerical solution of a dispersive wave equation does not appear in those books and articles. To obtain a convergent solution with minimum error, we found that the normal wave equation only needs condition (28a). For the dispersive wave equation, the numerical solution must not only satisfy (28a), but (28b) as well. The physical meaning of Eq. (28a) is that the wave must not propagate more than one subdivision in space during one time step. Eq. (28b) means that the element length must be chosen between λ_D and $3\lambda_D$ [14]. Since this transmission line is a homogeneous problem, to gain minimum error from (28a) and (28b) the element number was found to be 20 elements.

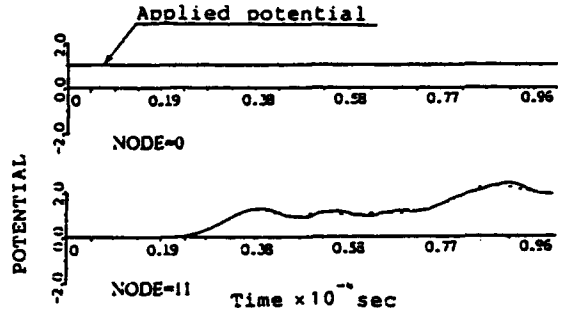

(a) Terminal is open

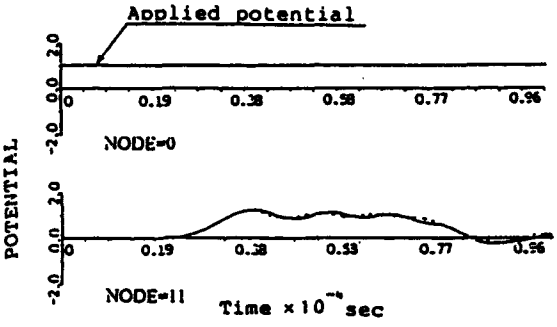

(b) Terminal is short circuited

Fig. 5. Comparison of numerical solutions with step wave excitation. The continuous line is the analytical results and the dashed line indicates the numerical results.

The parameters used in calculation are the element number = 20, C_S = 5.68 cm/sec, λ_D=3.29cm, and l=95.2cm.

3.2. Dispersive transmission line with loss

Using the same procedure, the single element matrix equation for a dispersive transmission line with loss is obtained as follows:

$$[M]^e\{\ddot{u}\}^e + C_s^2[S]^e\{u\}^e + \lambda_D^2[S]^e\{\ddot{u}\}^e + \alpha^2[M]^e\{\dot{u}\}^e + \alpha^2\lambda_D^2[S]^e\{\dot{u}\}^e = \{0\} \quad (29)$$

where [M] and [S] have the same details as (25) and (26). Thus, the system matrix equations can be written as eq. (30). The same numerical procedure as above is used to solve the system matrix equations.

$$([M] + \lambda_D^2[S])\{\ddot{u}\} + (\alpha^2[M] + \alpha^2\lambda_D^2[S])\{\dot{u}\} + C_s^2[S]\{u\} = \{0\} \quad (30)$$

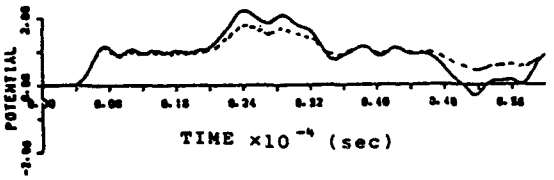

(a) Terminal is open, the continuous line is for no loss, the dashed line is the loss case.

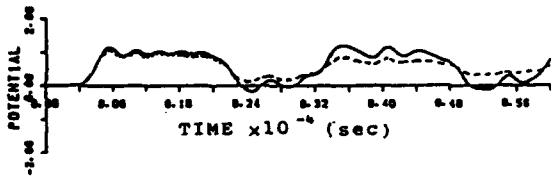

(b) Terminal is short circuited, the continuous line is for no loss, the dashed line is the loss case.

Fig. 6. Dispersive transmission line with loss. element number=20, Cs=5.68cm/sec, λ_D=52.91cm, α= 175.25sec, and l=95.2cm.

Fig. 6 shows the results of eq.(30) solved by Newmark-β method. The results indicate that the wave is not damped significantly during propagation, even at the present value of parameter (α= 175.25sec) used in the calculation.

3.3 Inhomogenous dispersive transmission line

Sometimes it is of interest to consider inhomogenous problems in a continuous transmission line with finite length. The distributed parameters of the transmission line for each section may be different, but this does not result in a significant difference in the solution. The matrix equation for inhomogenous problems can be written as

$$[M]^e\{\ddot{u}\}^e + \left(\frac{C_k(n)}{C_0(n)}[S]^e\right)\{u\}^e + \left(\frac{1}{L(n)C_0(n)}[S]^e\right)\{\ddot{u}\}^e = \{0\} \quad (31)$$

where the parameters of $C_0(n)\cdot\Delta l$, $L(n)/\Delta l$, and $C_k(n)/\Delta l$ are dependent on each section, and n is the section number of an inhomogenous transmission line.

4. NUMERICAL MODEL OF NONLINEAR DISPERSIVE TRANSMISSION LINE

Nonlinear dispersive transmission lines have been used for describing various physical phenomena. In particular, the soliton wave propagating in a plasma is governed by the well studied Kortewg-de Vries (KdV) equation has been investigated [18,19], and the numerical solution of the KdV equation has been proposed by Tadahiko Kawai etc. [20]. In other practical applications in which $L(i')$ and $C_0(u)$ have various characteristics, the KdV equation can no longer be used. One must then find a numerical model which can be used with various nonlinear parameters. The matrix equations of nonlinear dispersive transmission lines for each element are proposed as follows:

4.1 Dispersive transmission line with nonlinear inductance

For simplifying the problem, the lossless dispersive transmission line shown in fig. 7 is considered, where $L(i')$ is a nonlinear inductor dependent on the current

or the voltage difference between two points of each section.

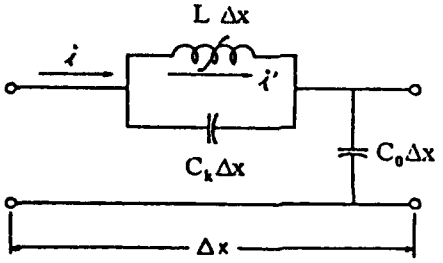

Fig. 7. A section of dispersive transmission line with nonlinear parameter L

The matrix equation for the dispersive transmission line with nonlinear inductance problem can be written as

$$[M]^e\{\ddot{u}\}^e + \left(\frac{C_k}{C_0}[S]^e\right)\{u\}^e + \left(\frac{1}{L(i')C_0}[S]^e\right)\{\ddot{u}\}^e = \{0\} \tag{32}$$

where L(*i'*) is a nonlinear inductance related to current *i'*.

4.2 Dispersive transmission line with nonlinear capacitance

In the same consideration, the lossless dispersive transmission line can be described as fig.8, where $C_0(u)$ is a nonlinear capacitor dependent on the voltage u. The matrix equation for the dispersive transmission line with nonlinear capacitance problem can be written as

$$[M]^e\{\ddot{u}\}^e + \left(\frac{C_k}{C_0(u)}[S]^e\right)\{u\}^e + \left(\frac{1}{LC_0(u)}[S]^e\right)\{\ddot{u}\}^e = \{0\} \tag{33}$$

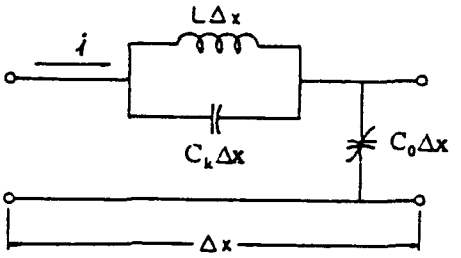

Fig. 8 A section of dispersive transmission line with nonlinear parameter $C_0(u)$

Equations (32) and (33) can be solved by using the Newton-Raphson method or the decelerating relaxation method which has been often used in the nonlinear electromagnetic fields analysis [21,22].

5. APPLICATIONS OF DISPERSIVE TRANSMISSION LINE

As we discussed in the introduction, the dispersive transmission line can be used for modeling various physical phenomena and practical application problems. In this section, dispersive transmission lines are used to investigate wave propagation in a plasma and the transient response of a surge in transformer windings.

5.1 Dispersive wave propagation in plasma

It is well known that the electron plasma waves and ion-acoustic waves are electromagnetic waves which propagate in nonmagnetized plasmas. Since the characteristic frequency of the ion-acoustic wave is lower than the ion-plasma frequency (Ω_{pi}), both electrons and ions participate in this wave motion. The ion-acoustic wave is not strongly damped only when the ion temperature T_i is much lower than the electron temperature T_e. The ion-acoustic wave equation for the perturbed ion density n is defined as follows [23]:

$$\frac{\partial^2 \tilde{n}_i}{\partial t^2} - C_S^2 \frac{\partial^2 \tilde{n}_i}{\partial x^2} - \lambda_D^2 \frac{\partial^4 \tilde{n}_i}{\partial t^2 \partial x^2} = 0 \tag{34}$$

where C_s and λ_D are the ion-acoustic wave velocity and Debye shielding length respectively.

$$C_s = (T_e / M)^{1/2} \tag{35}$$

$$\lambda_D = (T_e / 4\pi n_0 e^2)^{1/2} \qquad (36)$$

T_e, M and n_0 are the electron temperature, mass of ion and steady component of the ion density respectively.

Assuming $u = \tilde{n}_i$, the dispersive transmission line can be used to describe the ion-acoustic wave in the plasma. Hence, the C_s and λ_D can be replaced as

$$C_s = (T_e / M)^{1/2} = (1 / LC_0)^{1/2} \qquad (37)$$

$$\lambda_D = (T_e / 4\pi n_0 e^2)^{1/2} = (C_k / C_0)^{1/2} \qquad (38)$$

where $C_0 = 1/T_e$, $L = M$ and $C_k = 1/4\pi n_0 e^2$.

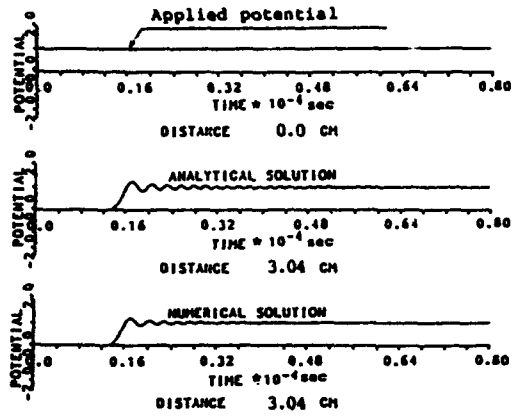

Fig. 9 Step wave response. $\lambda_D = 4\times10^{-2}$cm, Cs=$2\times10^{+5}$cm/sec, l=40cm, element number=500.

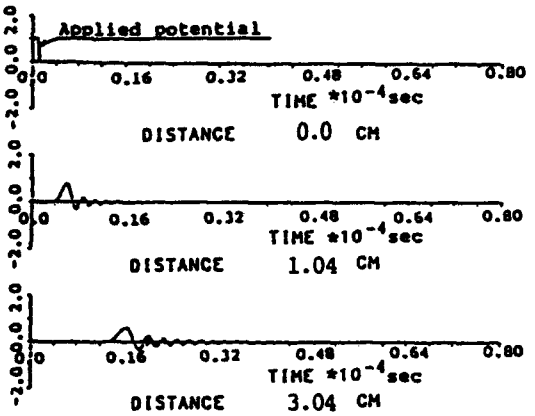

Fig. 10. Pulse response, $\lambda_D = 4\times10^{-2}$cm, Cs=$2\times10^{+5}$cm/sec, l=40cm, element number=500.

Using the same numerical approach of the previous section, the ion-acoustic wave of the plasma with different input pulses can be obtained [14]. These are illustrated in Fig. 9 and Fig. 10. From Fig.9, we found that the numerical solution has a good agreement with the analytical solution from (12). There are some phase shift between them after several oscillations, which can be considered as a computer processing error. Fig. 10 shows the pulse response in plasma. The comparison between numerical and experimental results has made for the pulse response in plasma [14].

5.2 Dispersive wave propagation in high-voltage (HV) transformer windings

In order to choose a proper winding arrangement and insulation structures in the design of HV transformer windings, the transient voltage stresses to all sub-components of the structure must be known. To investigate voltage oscillations and impulse-voltage stresses in HV transformer windings during impulse test and design reliable insulation structure for the HV transformer windings which can withstand various kinds of transient over voltage, the most convenient and lowest cost method of acquiring transient voltage response data is using a numerical model of the transformer windings and solving for the time function response to applied voltage pulses by means of a suitable numerical analysis. Normally, the impulse response and produced higher transient voltage in the transformer windings can be calculated by using the distributed equivalent circuit of transformer windings as a transmission line has been used as shown in Fig. 11 [24,25]. To simplify the problems the case of the mutual and nonlinear inductance is not considered in this calculation.

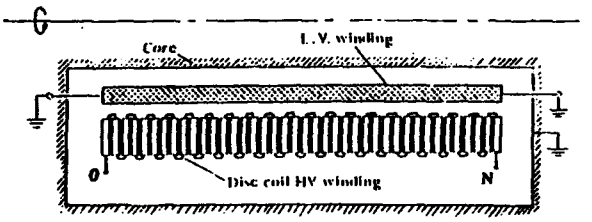

(a) Cross-section of a typical 2-winding H.V. transformer

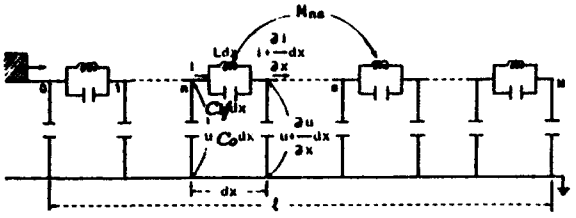

(b) Distributed equivalent circuit of transformer winding

Fig.11 Numerical model of H.V. transformer windings, Element number=20, L=4.5mH/Δl, C_o=67.5pF·Δl, C_k=383.5pF/Δl, and l=95.2cm.

The impulse voltage oscillations caused by resonant circuit which is excited by any impulse can be calculated by numerical or analytical method. The voltage oscillations in the transformer windings is a kind of dispersive wave propagation and the frequency of oscillations and amplitude of transient voltages can be calculated by eq. (9) and (12) where the applied impulse is a step wave.

For the other different shapes of impulse voltage (including the IEC standard lightning impulse voltage waveform [26]) and the inhomogenous distributed equivalent circuit of transformer winding, the calculation can be easily done by numerical methods. The numerical results for transient responses from various applied impulses are shown in Fig. 12 [15].

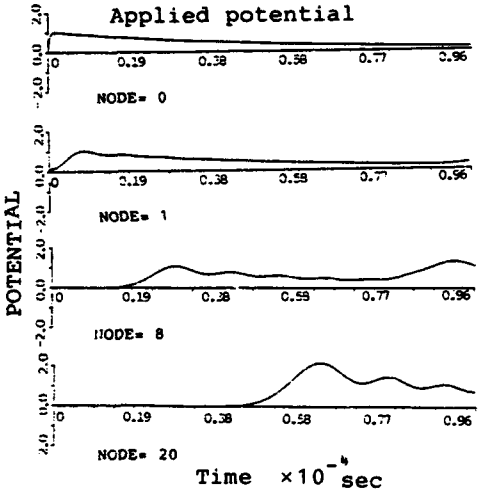

(a) Terminal is open

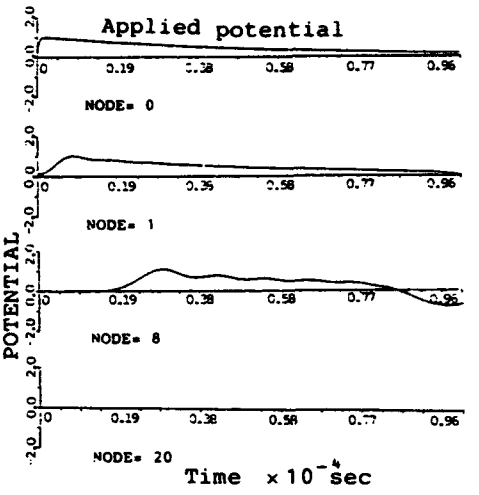

(b) Terminal is Short-circuited

Fig. 12. Standard lightning impulse voltage response, element number=20, L=4.5mH/Δl, C_0=67.5pF·Δl, C_k=383.5pF/Δl, and l=95.2cm.

The effect of dispersion is an oscillating voltage which is up to 1.5 times the input impulse voltage in the case of shorted-circuit and the oscillating voltage will be larger than 2.0 times the input impulse voltage at the opened terminal, if the initial voltage is not zero. Alternatively, for the chopped waveform, there is no significant transient overvoltage along the transformer windings [15].

6. CONCLUSIONS

In this paper, dispersive wave propagation in various transmission line configurations is discussed. Basic analytical solutions with step wave excitation were found and compared to finite element solutions. The results show good agreement. The error control of numerical solution can be worked out by using eq. (28a) and (28b). The numerical model has advantages in dealing with some practical systems excited by different excitation waveforms, especially for inhomogenous, lossy and nonlinear problems. Appropriate numerical models have been proposed. Although while only two applications were modelled by dispersive transmission lines, there are many more interesting phenomena which can be modeled using these techniques.

ACKNOWLEDGMENT

The authors are indebted to Professor T. Yamabuchi for his help during the calculation of this work. The authors express their gratitude to reviewers for their important comments. The authors also grateful to Professor J.D. Lavers and A. Konrad for their very useful suggestions.

REFERENCES

[1] Brian C. Wadell: *Transmission Line Design Handbook*, Artech House, Inc. 1991

[2] Karl E. Lonngren: *Observation of Solitons on Nonlinear Dispersive Transmission Lines, Solitons in Action*, Academic Press, London, 1978

[3] K. Daikoku and Y. Mizushima: *New Instability Concept in Avalanche Diode Oscillation*, Jap. J. App. Phys., 13 pp. 989-994, 1974

[4] M. Agu and T. Kinoshita: *Avalanche Breakdown as a Nonlinear Wave*, Jpa. J. App. Phys., 16, pp. 835-839, 1977

[5] S. Kato: *Application of Finite Element Method to the Analysis of Distributed Constant Circuit*. Jap. J. Denkigakkai Ronbunshi 61-A25, pp195-202, 1986

[6] S.V. Kiyashko, V.V. Papko and M. I. Rabinovich: *Model Experiments on the Interaction of Plasma and Ion-acoustic Waves*, Soviet J. Plasma Phys., pp. 553-554, 1976

[7] K. E. Lonngren, etc.,: *Properties of plasma waves defined by the dispersion relation* ϖ , IEEE Trans. Plasma Science, PS-2, pp. 93-108 1974.

[8] Wait, J.R., 1976. *Electromagnetic waves in stratified media*. Pergamon Press, N.Y.

[9] Eikichi Yamashita, editor: *Analysis Methods for Electromagnetic Wave Problems*, Artech House, Inc. 1990

[10] Matthew N. O. Sadiku: *Numerical Techniques in Electromagnetics*, CRC Press, 1992

[11] Rodney W. Cole and Edmund K. Miller: *Learning About Fields and Waves Using Visual Electromagnetics*, IEEE Trans. on Education, Vol. 33, No. 1, pp81-94; Feb. 1990

[12] D.K. Cheng: *Field and Wave Electromagnetics*, Addison-Wwsley, 1983

[13] F.F. Chen, *Introduction to Plasma Physics*, Plenum Press, New York, 1974

[14] J. Lu and Y. Kagawa: *Solution of Ion-Acoustic Wave Propagation in Plasma - in one dimensional case*, International Journal for Computation and Mathematics in Electrical and Electronic Engineering, Vol. 6-4. pp 227-236, 1987

[15] J. Lu, Y. Kagawa and K. Bessho: *A numerical Analysis of Transient Response in High- Voltage Transformer Winding by Using Finite Element Model*,Proceedings, Beijing International Symposium on Electromagnetic Field, 1988

[16] D. R. J. Owen and E. Hinton: *A Simple Guide to Finite Element*, Pineridge Press Ltd. 1980

[17] Y. Kagawa, *Finite Element Analysis in Acoustical Engineering-Fundamentals and Applications*, Baifukan, Tokyo, 1981

[18] F.F. Cap: *Handbook on Plasma Instabilities*, Vols 1-3, Academic Press, London, 1982

[19] D.G.Swanson: *Plasma Waves*, Academic Press, Inc. 1989

[20] T.Kawai and M.Watanabe: *Finite Element Analysis of the Nonlinear Dispersive Wave in Plasma*,Proceedings, 2nd int. Sympo. on FEM in Flow Problems, S.Margherita,Ligure ICCAD,1976

[21] T. Nakada, etc.: *Finite element method for electrical engineering*, 2nd edition, Morikida publisher Ltd. 1986

[22] P. P. Silvester and R. L Ferrari: *Finite element method for electrical engineers*, 2nd Edition, Cambridge university press. 1990

[23] H.Ikezi: *Experiments on Solitons in Plasmas*, Eds. K. Loongren and A. Scott, Solitons in Action, Academic Press, London, 1978

[24] W.J.Mcnut, T.J.Blaock and R.A.Hinton: *Response of Transformer Windings to System Transient Voltages*. IEEE PAS-93 No.2 March/April 1974, pp457-467

[25] P.I.Fergestad and T. Henriksen:*Transient Oscillations in Multiwinding Transformers*, IEEE PAS-93 No.2 March/April 1974, pp500-509

[26] E. Kuffel and M. Abdullah: *High-voltage Engineering*, Pergamon Press Ltd., 1970

Equivalent electric circuits approach for the modeling of non-linear electromagnetic fields

M. Gimignani, A. Musolino, M. Raugi, A. Tellini
Dip. di Sistemi Elettrici ed Automazione, Università di Pisa, Via Diotisalvi 2, 56100 Pisa.

***Abstract*- In this paper a method for the analysis of non-linear three dimensional electromagnetic field is presented.**

The conductive and magnetic regions of the examined system are subdivided in elementary volume elements in which a uniform current density J and magnetization M is assumed. By integrating Ohm's law inside the conductive regions, a set of equations representing the equilibrium equations of an equivalent electric network is obtained.

The knowledge of the currents in the conductive regions allows the evaluation of the electromagnetic fields and the determination of the forces among different bodies.

Applications of the method to the solution of benchmark problems of time varying linear systems, and non-linear static cases are presented.

I. INTRODUCTION

The historical concepts of the electromagnetic theory, characterized by the fields as the quantities that are physically significant, have been recently discussed by John Carpenter in a series of papers [1-3], where he investigated the consequences of a change of approach to electromagnetism. In his view the electric potential V and the magnetic vector potential A become the principal quantities respectively defining a measure of the potential and kinetic energy of a system of charges, while the field vectors E and B are no more than symbols denoting derivatives. Therefore, in this charge based approach, the energy density $w = (\rho V + J \cdot A)/2$ represents the kinetic energy and potential energy of the source charges, while in field theory it is considered as a mathematical equivalent. Even though the two approaches to electromagnetism lead to the same equations in terms of the potentials V and A, they differ substantially from the physical viewpoint. The essence of the V, A treatment is that there is no concern about how the actions are conveyed through space, since V and A quantify all possible interactions between any groups of charges. The potentials V and A at the considered frequencies, can be obtained from the source q's and J's :

$$V(r) = \frac{1}{4\pi\varepsilon}\int_{\Omega}\frac{\rho(r')}{|r-r'|}\,d\Omega(r');\quad A(r) = \frac{\mu}{4\pi}\int_{\Omega}\frac{J(r')}{|r-r'|}\,d\Omega(r') \quad (1)$$

where the charge density ρ and current density J in the integrals are due to the actual charge and current density distributions plus the a priori unknown distributions of the equivalent charges and currents due to the presence of dielectric and magnetic materials.

The approach makes no direct use of the concept of flux, although it provides convenient means of introducing it, therefore for several purposes the field-based and charge-based approaches are equivalent. Hence most of the numerical methods in terms of the potentials V and A can use the same basic equations. Nevertheless the integral formulation presented here can be considered as the logical outcome of the charge-based view of electromagnetism, and its inherent logic differs from other differential and integral methods relating to low frequency electromagnetic fields [4-7].

Since the sources are limited to the q's and J's, the proposed scheme makes no use of magnetic poles, thus the concept of magnetic circuit has no part in this model and the field equations are modelled by electric circuits only. Therefore the presented model has the advantage of a natural and easy linkage of circuit and field equations. Furthermore, it is not affected by numerical instabilities when it takes into account the relative motion among conducting bodies. As an integral formulation, it needs the modelling of conductive regions only, and do not require the specification of boundary conditions. Furthermore the proposed procedure has the characteristic of an easy data input for the definition of the arrangement of the ferromagnetic and non-ferromagnetic regions. By utilizing the symmetries of the examined system it is possible to reduce both the computational time and the required memory workspace.

II. MODEL

The whole volume Ω of conductive and magnetic regions is subdivided in N elementary volume elements, that can have several shapes (tetrahedrons, bricks, cylinder sectors), as shown in the 2-D decomposition of figure 1. Consequently, the vector potential A can be evaluated from the eq. (1), considering instantaneous propagation for the application of interest, adding the integrals relating to every elementary volume.

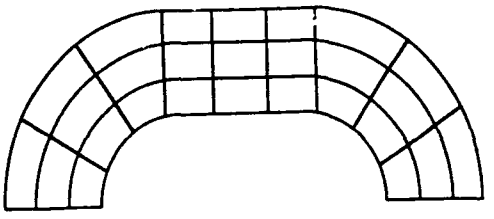

Fig. 1 First decomposition

Connecting the centres of nearby elements by means of segments parallel to the coordinate system unit vectors, we obtain a 3-D grid as shown in the figure 2.

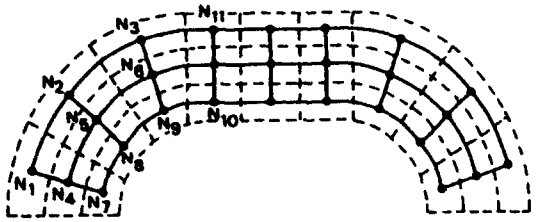

Fig. 2 Grid (solid lines)

Then we associate to every segment of the grid a new elementary volume element having four edges parallel to the segment, and the faces normal to the segment with their centres placed at nodes of the grid, see fig. 3. We assume that, inside every volume element, only the current density and magnetization component parallel to the segment associated to the volume element exists.

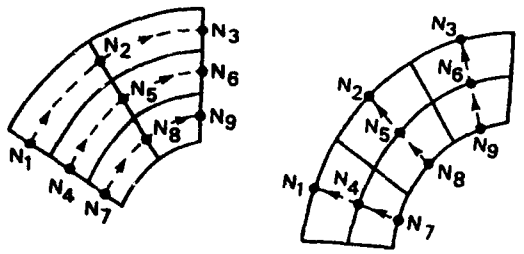

Fig. 3 Association between volume elements (solid lines) and segments (dashed lines)

The vector potential in the generic k-th element is:

$$A_k(t) = \frac{\mu_o}{4\pi}\left[\iiint_{V_s}\frac{J_s(t,x')}{|x_k - x|}dV_s + \sum_{j=1}^{3N}\iiint_{V_j}\frac{J_{ij}(t,x')}{|x_k - x'|}dV_j\right] + \frac{\mu_o}{4\pi}\left[\sum_{j=1}^{N}\iint_{S_j}\frac{n_j' \times M_j(t)}{|x_k - x'|}dS_j + \sum_{j=1}^{3N}\iiint_{V_j}\frac{J_{mj}(t,x')}{|x_k - x'|}dV_j\right] \quad (1a)$$

where V_j is the j-th elementary volume, J_S are the current sources, J_{ij} the induced currents, J_{mj} the volume magnetization currents, M_j the magnetization of the j-th volume element and n_j is the normal to the j-th element surface.

Assuming an uniform distribution of the magnetization M_j inside each volume, we have no volume current densities $J_{mj} = \mathrm{curl}(M_j) = 0$. Furthermore assuming an uniform distribution of the current density $J_{ij}(t,x) = J_{ij}(t)$ and $J_S(t,x) = J_S(t)$ we obtain that the magnetic vector potential A, and consequently the flux density B are proportional to the currents I_{ij} and I_S and to the magnetizations M_j. In this way, we can derive the coefficients α, β and λ of eq. (2a), (2b), (2c) by means of analytical expressions [8,9] developed in previous works, thus obtaining a quick and accurate evaluation of the electric parameters of the equivalent circuit. The flux density $B(P,t) = \nabla \times A(P,t)$ or $B_k = \nabla \times A_k$ is equal to:

$$B_k = B_{mk} + B_{sk} + B_{ik} \quad (2); \quad B_{mk} = \sum_{j=1}^{3N}\alpha_j \cdot M_j \quad (2a);$$

$$B_{sk} = \sum_{j=1}^{R}\beta_j \cdot I_{sj} \quad (2b); \quad B_{ik} = \sum_{j=1}^{3N}\lambda_j \cdot I_{ij} \quad (2c).$$

The B_{sk} field, due to the current sources, is obtained by subdividing the current sources in R elementary elements (slabs or rings). The B_{ik} field ,due to the induced currents, is obtained by adding the contributions of all volume elements, while the B_{mk} field, due to the magnetizing currents, is obtained by taking the curl of the surface integrals, shown in eq. (1a), on the boundaries among every volume element. Considering isotropic materials, we can write the relations between the magnetic field H, the magnetic flux B and the magnetization M inside the material as:

$$H_k = H_{mk} + H_{sk} + H_{ik} \quad (3); \quad H_{mk} = \frac{B_{mk}}{\mu_o} - M_k \quad (3a);$$

$$H_{sk} = \frac{B_{sk}}{\mu_o} \quad (3b); \quad H_{ik} = \frac{B_{ik}}{\mu_o} \quad (3c).$$

Then, substituting the equation groups (2) and (3) in the characteristic of the material $H_k = H(B_k)$ we obtain the equation:

$$M_k = F[B_k] = F[M_1,..,M_{3N},I_{i1},..,I_{i3N},I_{s1},..,I_{sR}] \quad (4)$$

Then we write Ohm's law inside every volume element:

$$\rho_k J_k(t) = -\nabla V_k(t) - \frac{\partial A_k(t)}{\partial t} \quad (5)$$

where A_k is the magnetic vector potential in the k-th elementary parallelepiped, ∇V_k is the irrotational component of the electric field E_k and J_k is the current density in the k-th volume.

We combine equations (1a) and (4) in order to express the derivative of the vector potential with respect to time as a function of the currents inside volume elements.

$$\frac{\partial A_k(t)}{\partial t} = \frac{\mu_o}{4\pi}\left[\frac{\partial J_s(t)}{\partial t}\iiint_{V_s}\frac{1}{|x_k - x'|}dV_s + \sum_{j=1}^{3N}\frac{\partial J_{ij}(t)}{\partial t}\iiint_{V_j}\frac{1}{|x_k - x'|}dV_j + \sum_{j=1}^{3N}\frac{\partial M_j(t)}{\partial t}\iint_{S_j}\frac{1}{|x_k - x'|}dS_j\right] \quad (6)$$

dM/dt can be expressed as a function of dI_{ij}/dt and dI_S/dt in the volume elements by differentiating the constitutive eq. (4) inside every volume element:

$$M_k - F[M_1,..,M_{3N},I_{i1},..,I_{i3N},I_{s1},..,I_{sR}] = 0\ ,$$

$$\frac{\partial}{\partial t}\left[M_k - F[M_1,..,M_{3N},I_{i1},..,I_{i3N},I_{s1},..,I_{sR}]\right] = 0\ ,$$

$$\frac{\partial F}{\partial M1}\frac{\partial M1}{\partial t} + \ ... \ + \frac{\partial F}{\partial M3N}\frac{\partial M3N}{\partial t} + \frac{\partial F}{\partial Ii1}\frac{\partial Ii1}{\partial t} + \ ...$$

$$+\frac{\partial F}{\partial I3N1}\frac{\partial I3N1}{\partial t} + \frac{\partial F}{\partial Is1}\frac{\partial Is1}{\partial t} + \ ... \ + \frac{\partial F}{\partial IsR}\frac{\partial IsR}{\partial t} - \frac{\partial Mk}{\partial t} = 0$$

or:

$$\left[\frac{\partial M}{\partial t}\right] = [D_M]\left[\frac{\partial I}{\partial t}\right] \qquad (7)$$

dF/dI and dF/dM constitute the elements of the matrix D_M that gives the relation between dM/dt and dI/dt. These terms are functions of the currents I_{ij} and I_S and of the magnetizations M, that are known at every time instant. Integrating eq. (5) in each volume element Γ_k and meaning the result on the surface S_k we obtain:

$$R_k I_k + \sum_{j=1}^{3N} L_{kj}\frac{\partial I_j}{\partial t} + \sum_{j=1}^{3N}\frac{\partial M_j}{\partial t} + \sum_{j=1}^{R}\bar{L}_{ksj}\frac{\partial I_{sj}}{\partial t} = U_k \qquad (8)$$

where U_k is the electric potential difference between the centres of two nearby parallelepipeds, R_k is the electric resistance of the volume Γ_k, I_k is the current in Γ_k , the L_{kj} are the mutual inductances between Γ_k and Γ_j and L_{ksj} are the mutual inductances between the volume Γ_k and the current sources volumes Γ_{sj}. Substituting (7) in (8) we obtain the equation :

$$R_k I_k + \sum_{j=1}^{3N}(L_{kj} + D_{M_{kj}})\frac{\partial I_j}{\partial t} + \sum_{j=1}^{R}\bar{L}_{ksj}\frac{\partial I_{sj}}{\partial t} = U_k \qquad (9)$$

where D_{Mkj} is the element of position k j in the matrix D_M. This equation represents the electric equilibrium equation of a branch of a network where resistive and inductive elements, corresponding to the physical resistances, self and mutual inductances of the elementary volume elements are present.

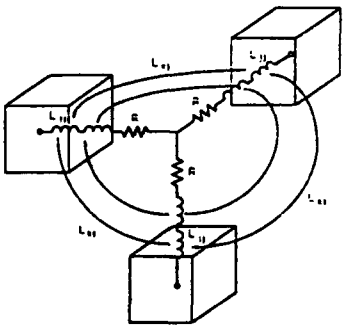

Fig. 4 Branches of the equivalent network

Each of the NO nodes of the network is the center of a star of six branches. Every branch is inductively coupled with all the other branches of the network. Therefore we can consider the segments composing the grid obtained in fig. 1 as branches of an equivalent electric network, and we can write the mesh equations for the loop currents in the network, then obtaining a system of 3N-NO+1 equations. Minimum path meshes are selected in order to have a diagonally dominant matrix. If external voltage generators, capacitor banks, inductances or resistances are electrically connected to the conductive regions, their circuital branches are connected to nodes of the grid. These nodes correspond to the volume elements that are physically in contact with the electrical cables that connect the external elements to the conductive regions. Then their electrical branches are added to the equivalent network of the conductive regions, and the equilibrium of the network is examined.

The solution of the equilibrium equations of the equivalent network, by means of a single-step time-marching method [10], allows the evaluation of the currents in the elementary volumes, and therefore the evaluation of the eddy current distribution in the conductive regions. In order to reduce the computational times the matrix D_M and the magnetizations M are considered constant during every step, being updated only at the beginning of each time interval integration. The complete procedure is constituted by the following steps:

Initialise the currents in the branches of the network;
t:=0
for i := 1 to n (last instant) repeat
1• Find the $M(t_i)$ by solving (4)
2• Update the matrix D_M (that express dM/dt as a function of dI/dt at the instant t_i) by means of (7)
3• Make the time marching step by solving (9)
4• t := t + Δt
end for

The computational cost of the method, due to the presence of dense matrixes, is similar to other integral formulations [11]. Nevertheless, the presence of a diagonally dominant matrix and the analytical evaluation of its elements, can significantly reduce the computational times. Furthermore, the impact of parallel processing and the use of iterative algorithms [12] should significantly enhance the numerically efficiency of the method.

III. MOVING ELEMENTS.

We consider a system with a fixed body and a moving one having a velocity v(t). In order to take into account the presence of a moving element, we have to modify eq. (6), that becomes:

$$\frac{\partial A_k(t)}{\partial t} = \frac{\mu_o}{4\pi}\left[\frac{\partial J_s(t)}{\partial t}\iiint_{V_s}\frac{1}{|x_k - x'|}dV_s + \right.$$

$$+J_s(t)\iiint_{V_s}\frac{\partial}{\partial t}\frac{1}{|x_k - x'|}dV_s + \sum_{j=1}^{3N}\frac{\partial J_{ij}(t)}{\partial t}\iiint_{Vj}\frac{1}{|x_k - x'|}dV_j$$

$$+J_{ij}(t)\iiint_{Vj}\frac{\partial}{\partial t}\frac{1}{|x_k - x'|}dV_j + \sum_{j=1}^{3N}\frac{\partial M_j(t)}{\partial t}\iiint_{Sj}\frac{1}{|x_k - x'|}dS_j$$

$$\left.+M_j(t)\iiint_{Sj}\frac{\partial}{\partial t}\frac{1}{|x_k - x'|}dS_j\right] \qquad (10)$$

When the point x_k belongs to the fixed body eq. (10) is equal to eq. (6), when the point x_k belongs to the moving body, we have that

$$\frac{\partial}{\partial t}\left[\frac{1}{|x_k - x'|}\right] = \frac{1}{|x_k - x'|^3}\frac{\partial x_k}{\partial t} = \frac{v(t)}{|x_k - x'|^3} \tag{11}$$

and

$$J_{ij}(t)\iiint_{V_j}\frac{\partial}{\partial t}\left[\frac{1}{|x_k - x'|}\right]dV_j = J_{ij}(t)v(t)\iiint_{V_j}\frac{1}{|x_k - x'|^3}dV_j$$

$$M_j(t)\iiint_{S_j}\frac{\partial}{\partial t}\left[\frac{1}{|x_k - x'|}\right]dS_j = M_j(t)v(t)\iiint_{S_j}\frac{1}{|x_k - x'|^3}dS_j$$

then we can obtain analytical expressions for the volume and surface integrals. These terms modify eq. (9) which becomes:

$$R_k I_k + \sum_{j=1}^{3N}(L_{kj} + D_{M_{kj}})\frac{\partial I_j}{\partial t} + vK_1 I_j + vK_2 M_j + \sum_{j=1}^{R}\bar{L}_{ksj}\frac{\partial I_{sj}}{\partial t} = U_k \tag{12}$$

Therefore we can repeat the procedure described in the previous paragraph, substituting eq. (9) with eq. (12) in the step 4.

IV. Linear Systems

When we deal with linear characteristics, eq. (4) becomes:

$$Mk = \frac{1}{\mu_o}\left(1 - \frac{1}{\mu_r}\right)\left[\sum_{j=1}^{R}\beta j \cdot Isj + \sum_{j=1}^{3N}\lambda j \cdot Iij + \sum_{j=1}^{3N}\alpha j \cdot Mj\right] \tag{13}$$

therefore we obtain a linear relation between the magnetizations inside the elementary volumes, and the source and induced currents I_s and I_i.

Consequently dF/dI and dF/dM in the eq.(7) are no more functions of the currents I_i, I_s and of the magnetization M, but are constant values. Therefore the relation between dM/dt and dI/dt is constant in time and the matrix D_M does not have to be updated during the time stepping. Then we can substitute these expressions in the eq. (9) and eliminate the step 3.

The energy of a conductor can be obtained from the equation:

$$W = \frac{1}{2}\iiint_{\Omega} A \cdot J \, d\Omega \tag{14}$$

then the force on the conductor can be obtained by:

$$F = \frac{\partial W}{\partial x} = \frac{\partial}{\partial x}\frac{1}{2}\iiint_{\Omega} A \cdot J \, d\Omega \tag{15}$$

Substituting eq. (2) for A in eq. (15) we have:

$$F = \frac{\partial}{\partial x}\iiint_{\Omega}\frac{\mu_o}{8\pi}\left[\iiint_{V_s}\frac{J_s(t)}{|x_k - x'|}dV_s + \sum_{j=1}^{3N}\iiint_{V_j}\frac{J_{ij}(t)}{|x_k - x'|}dV_j + \sum_{j=1}^{N}\iint_{S_j}\frac{n_j \times M_j(t)}{|x_k - x'|}dS_j\right]\cdot J_{ik}\, d\Omega$$

then carrying out the integral with respect to the volume Ω, summing the contribution of every volume element V_i and taking the derivative with respect to x similarly as in the eq. (10) we have:

$$F = \frac{\mu_o}{8\pi}\sum_{j=1}^{3N}J_{ij}(t)\left[\iiint_{V_s}\frac{J_s(t)}{|x_k - x'|}dV_s + \iiint_{V_j}\frac{J_{ij}(t)}{|x_k - x'|^3}dV_j + \sum_{j=1}^{N}\iint_{S_j}\frac{n_j \times M_j(t)}{|x_k - x'|^3}dS_j\right] \tag{16}$$

that can be evaluated by means of analytical expressions [13]. The evaluation of the electromagnetic force on the moving body allows the determination of its law of motion by means of the mechanical equilibrium equation:

$$\frac{\partial^2 x}{\partial t^2} = \frac{F}{m}$$

V. Results

The method has been tested against benchmarks for *linear and non-linear ferromagnetic systems.*

The first one is a magnetostatic problem proposed by the Institute of Electrical Engineers of Japan [14,15]. The geometry is shown in fig. 5, where the permeability of the iron core is 1000 and the coil was energised with 3000 AT.

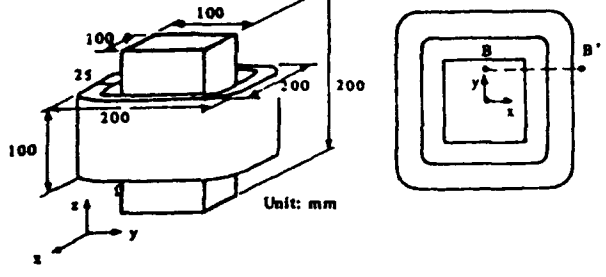

Fig.5. Geometry of the standard IEEJ problem

Fig. 6 displays the z component of the magnetic induction along the x direction at a distance of 10mm from the top of the iron element with y = 45mm.

One eighth of the system was discretized in 250 elementary cubes with good agreement between calculated and experimental results.

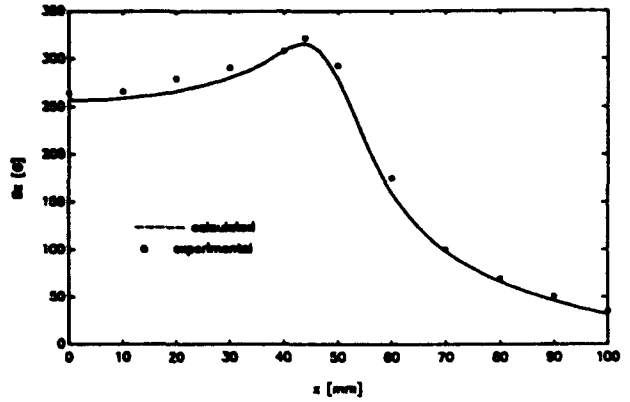

Fig.6. Magnetic induction on the line B-B'

The second problem also proposed by the Institute of Electrical Engineers of Japan [16], featured a time-varying sinusoidal excitation relating to linear ferromagnetic characteristic. The experimental arrangement shown in fig. 7, is composed by a coil energised with 1000 AT, two aluminium plates and a ferrite block, the relative permeability of the ferrite is assumed to be 3000 and the frequency is 50 Hz.

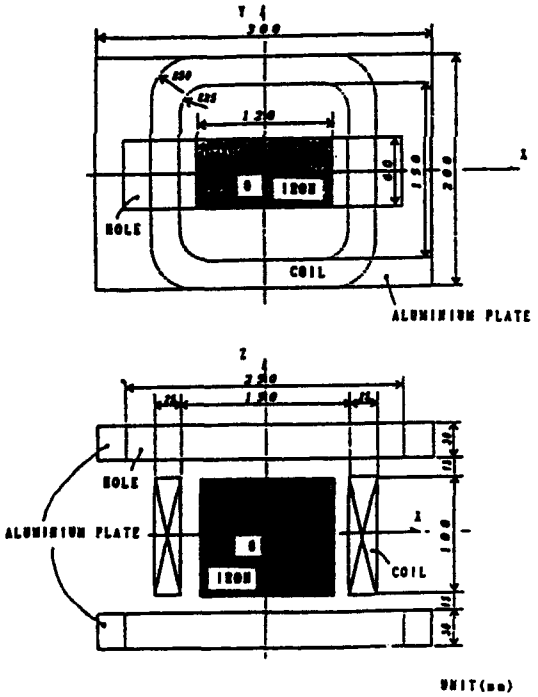

Fig.7. Geometry of the standard IEEJ problem

Figures 8 and 9 show that a good agreement between calculated and experimental results was obtained with 370 elements.

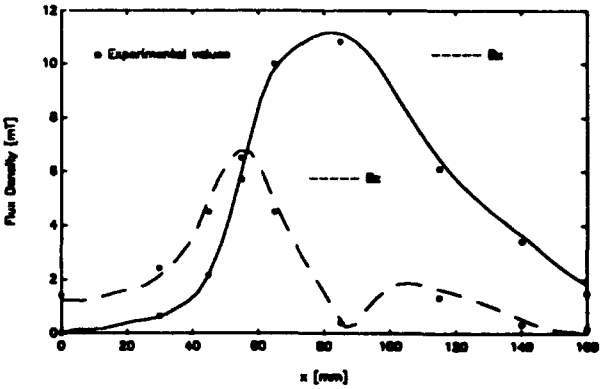

Fig.8. Magnetic flux density at z=57.5mm, y=0.0

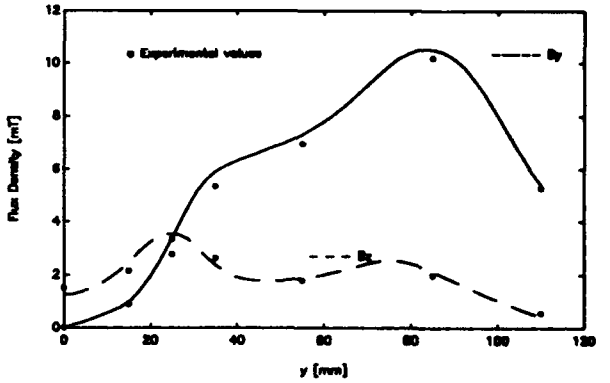

Fig. 9. Magnetic flux density at z=57.5mm, x=0.0

Experimental measurements are given also when a hole in the aluminium block is present. Figures 10 and 11 show a good agreement between calculated and experimental results with the same discretization.

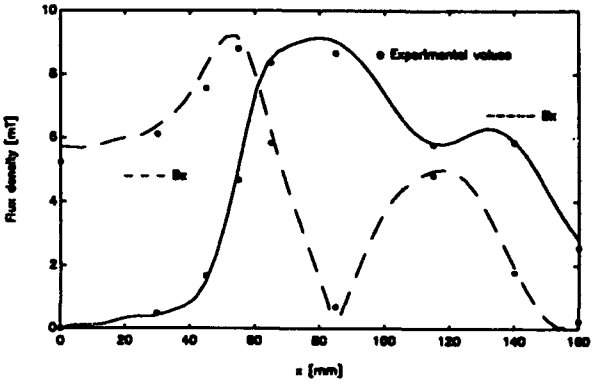

Fig. 10. Magnetic flux density at z=57.5mm, y=0.0

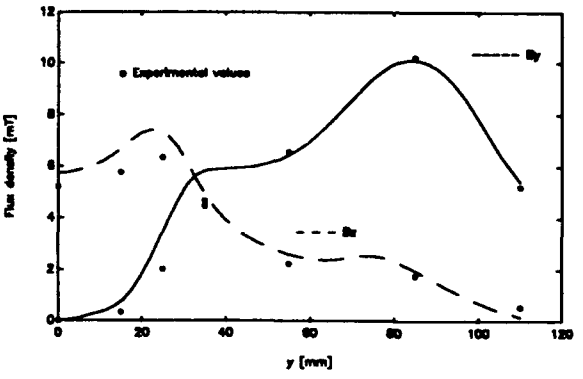

Fig. 11. Magnetic flux density at z=57.5mm, x=0.0

Furthermore, the method was tested by comparing calculated and experimental results relating to the TEAM problem 13 [17] as shown in fig. 12.

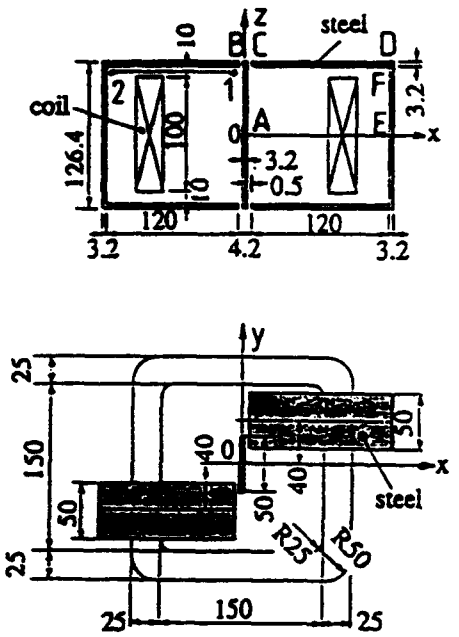

Fig.12. TEAM Problem 13 geometry.

The calculated results shown in the figures 13 and 14 agree with the experimental results and with results obtained with other models.

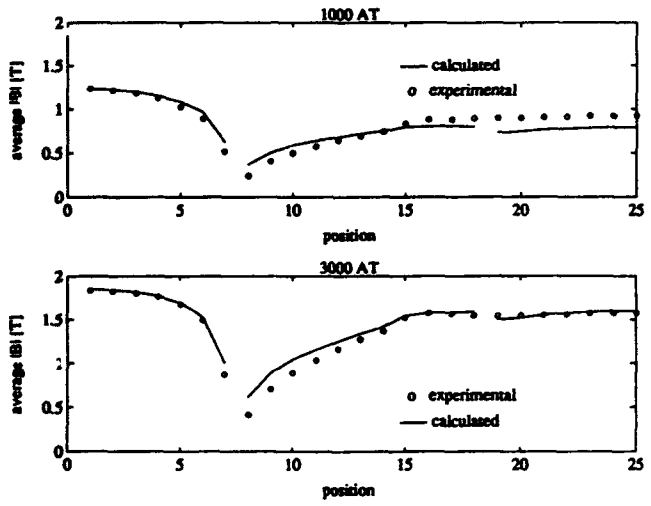

Fig.13. Comparison of average flux densities in iron

Only one fourth of the system was discretized, by using 430 elements. A modified Newton-Raphson algorithm [17] with a relaxation factor r = 0.5 was used for the solution of the non-linear system, the linear solution was taken as starting value for the calculation, and convergence was reached in 10 steps .

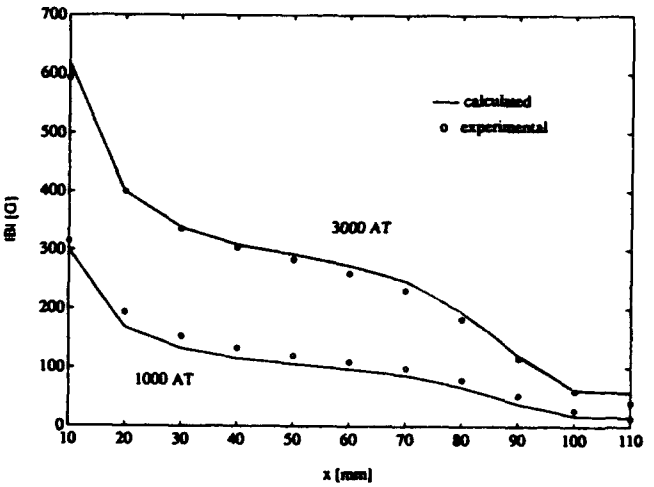

Fig.14. Comparison of flux densities in air

VI. Conclusions

An integral formulation for 3-D non-linear electromagnetic fields analysis has been presented. The method was formulated for the analysis of non-linear systems including the presence of moving bodies.

The method allows an easy modeling of homogenous and inhomogenous materials, can simply take into account the relative motion and the electromagnetic forces among conducting bodies, and allows an easy linkage between circuit and field equations.

The method has been tested on standard problems both for linear time varying systems and non-linear static systems and has given a good agreement with experimental results. Work is in progress for the implementation and validation of the non-linear time-varying case, and for the inclusion of the motion of bodies.

References

[1] C.J. Carpenter: "Digital-pulse approach to electromagnetism", IEE Proceedings Pt. A, n. 7, Sept 1988,pp 477-486

[2] C.J. Carpenter:"Comparison of the practical advantages of alternative descriptions of electromagnetic momentum"IEE Proceedings Pt. A, n. 3, May 1989,pp 101-114

[3] C.J. Carpenter: "Electromagnetic theory without flux", IEE Proceedings Pt. A, n. 4, July 1992,pp 188-209

[4] D. Rodger, C. Eastham:"A formulation for low-frequency eddy current solutions" IEEE Trans. on Mag. Vol 19 Nov. 1983.

[5] D. Briant, C. Emson, W. Trowbridge: " A general purpose 3-D formulation for eddy currents using the Lorentz gauge", Intermag Conference 1990.

[6] W.M.Rucker, K.R.Richter:" A BEM code for 3D eddy current calculation " IEEE Trans. on Mag. Vol 26 pp 462-465

[7] L. Turner, L. Kettunen: " A volume integral formulation for non linear magnetostatic and eddy currents using edge elements" IEEE Trans on MAG, Vol 28, n.2 March 1992

[8] B. Azzerboni,E. Cardelli,M. Raugi,A. Tellini,G. Tina:"Analytic expression for magnetic fields from finite curved conductors" IEEE Trans. n Mag. Vol 27 Mar. 1991.

[9] B. Azzerboni, E. Cardelli, M. Raugi, A. Tellini, G. Tina: "Magnetic fields evaluation for thick annular conductors". IEEE Trans. on Mag, Vol. 29, n. 3 May 1993.

[10] P.J.Leonard, D.Rodger, "Some Aspects of Two- and three-Dimensional Transient-Eddy-Current Modelling Using Finite Elements and Single-Step Time-Marching [illegible]ithms", *IEE. Proc.*, Vol. 135, Pt. A, No. 3, Mar. 1988.

[11] C.W. Trowbridge: " Electromagnetic computing: the way ahead?" IEEE Trans on MAG, Vol 24, n.1 Jan. 1988
[12] L.P.Barra, G.A. Coutinho, W.J. Mansur J.C. Telles: " Iterative solution of BEM equations by GMRES algorithm" Computers and Structures Vol 44 no 6 pp1249-1253
[13] B. Azzerboni, E. Cardelli, G. Tina: "Three dimensional forces and energy computation software package FEMAN and its application" IEEE Trans. on Mag. Vol 29, n.1 Jan. 1993
[14] M. Koizumi, M. Onisawa, M. Utamara:"Three dimensional magnetic field analysis method using scalar potential formulated by Boundrary Element Method". IEEE Trans. on Mag. Vol 26, n. 2, Mar. 1990, pp 360-363.
[15] K. Sawa, T. Hirano:"An evaluation of the computational error near the boundary with Magnetostatic field calculation by B.E.M.". IEEE Trans. on Mag. Vol 26, n. 2, Mar. 1990, pp 403-406.
[16] Y. Tanaka:"Three-dimensional eddy current analysis by the finite element method with integral equations using T-Ω" IEEE Trans. on Mag. Vol 28, n. 2, Mar. 1992, pp 1150-1153.
[17] T. Nakata, K. Fujiwara:"Summary of results for benchmark problem 13 (3-D non linear magnetostatic model" Proceedings of the European TEAM workshop and International Seminar on Electromagnetic field analysis, Oxford, England, 22-25 April 1990.

AN IMPROVED NETWORK MODEL FOR EDDY CURRENT PROBLEMS

Chi-Chung WONG

Department of Communication and Electronic Engineering
Royal Melbourne Institute of Technology
GPO Box 2476V, Melbourne
Vic., 3001
Australia

ABSTRACT. *This paper describes improvements in modelling Maxwell's equations in two dimensions using the electrical network analogue. Two network models are described with major emphasis placed on diffusion dominated problems. The first one is the combined fine-coarse mesh approach which was initially developed for the method of transmission-line modelling (TLM). The combined fine-coarse mesh technique is then modified by introducing controlled sources at the interfacing between the fine and the coarse mesh. Several numerical experiments, including one with both a conducting region and free space, are used to study the two models. They are also compared with the standard network analogue using a regular meshing. Numerical results are compared with analytical or published data. In all cases, SPICE (or PSPICE) has been used to solve the resulting network analogues.*

1. INTRODUCTION

In 1944 Kron [1] derived an electrical circuit equivalent of Maxwell's equations and subsequently many researchers had used electrical analogues to simulate Maxwell's equations [2-4]. In general, the electrical analogue is built around R, L and C components and the appropriate electrical quantities measured experimentally. With the advent of digital computers, numerical methods such as the finite-difference and finite-element [5] became popular and the use of experimental methods became unattractive. However, it is sometimes desirable to have a physical electrical network analogue for the field region to be modelled and in addition, standard network solver can be used to solve the resultant network analogue without the need of a special finite-element program, for example. Solutions can be sought without the prior knowledge of numerical analysis/methods. In this paper, SPICE[1] (or PSPICE[2]) which is now a *de facto* standard circuit simulator in electronic engineering, is used to solve the resulting network analogue. Another advantage of the network analogue is that it can be used to develop another class of numerical routine, namely the method of transmission-line modelling (TLM) [6]. In principle, SPICE can also be used to implement the transmission-line equivalent of Maxwell's equations, however, this will not be discussed here, because the routine used in SPICE is relatively inefficient for solving transmission-line problems.

The electrical analogue with lumped passive elements is in fact a variant of the finite-difference scheme (in particular with the method of lines) where the space is discretized with a mesh of finite mesh size and the time is left continuous. One major problem associated with this method (and the finite-difference) is that a large number of cells are needed if a regular meshing is used to cover the entire field region. To reduce the number of cells, an irregular meshing can be used [7] as shown in Fig. 1. This approach cannot drastically reduce the total number of cells since some regions outside the area of interest (or where the field gradient is not very steep) still need fine spacings. Another disadvantage of using an irregular meshing is that it is less straightforward to implement and is inherently less accurate [8]. To overcome these problems, the multigrid algorithm has been introduced. This method has been used in finite-difference [9,10] and been successfully applied to the method of TLM for transient diffusion problems [11]. This technique solves two (or more) networks; one with a coarse-mesh grid and the other with a fine-mesh grid. The coarse

[1]SPICE stands for *Simulation Program with Integrated Circuit Emphasis.*
[2]A registered trademark of MicroSim Corporation.

grid overlaps the fine grid (Fig. 2). The coarse grid network is first solved and the appropriate information transferred to the fine grid network and vice versa. Regular cells are commonly used although irregular cells can also be used. In order to reduce the memory requirement, computing time and the interpolation process needed in the multigrid technique, a combined fine-coarse mesh method has been proposed [12]. This arrangement is shown in Fig. 3, where it can be seen that the field region is covered with a combination of fine and coarse but regular cells. The interface between the fine and coarse cell is connected by a "busbar" (Fig. 3a). Therefore, it is only necessary to solve one network and the need to store (and transfer) different sets of information is eliminated. The major drawback of this approach is that accuracy is sacrificed because positions "a", "b" and "c" of Fig. 3a are forced to have the same potential. In this paper a new network model is proposed. The new model is based on the combined fine-coarse mesh technique but the disadvantage associated with this method is eliminated. This is achieved by breaking the "busbar" and use controlled sources at the interface (Fig. 3b). The performance of the original fine-coarse mesh approach and the proposed topology is studied in detail and compared with the standard technique which utilises cells of equal mesh size.

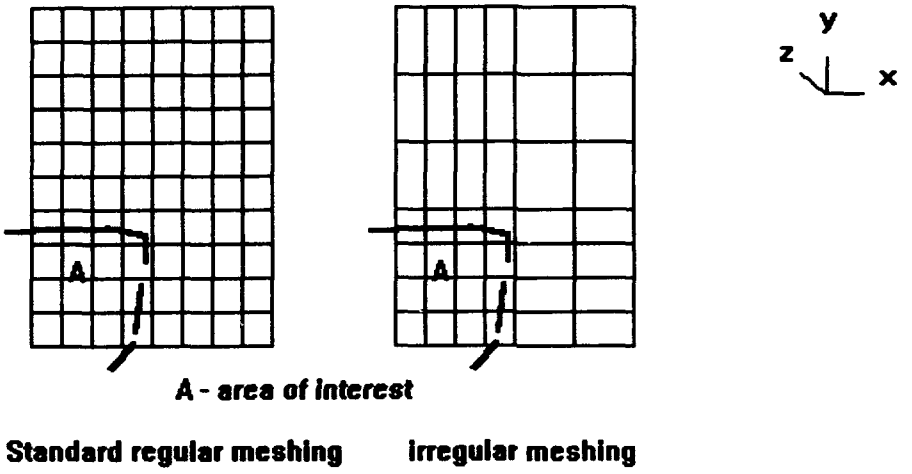

Fig. 1 Typical mesh arrangements.

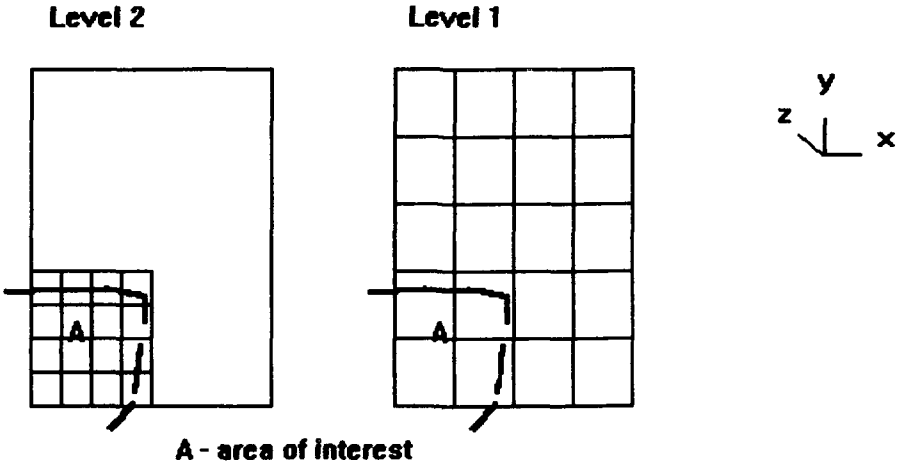

Fig. 2 A multigrid arrangement with two levels shown.

2. THE IMPROVED NETWORK MODEL FOR MAXWELL'S EQUATIONS

2.1 Equivalence between field and network quantities

Consider a typical regular network cell shown in Fig. 4a, the describing equations are

$$\begin{aligned} \frac{\partial iy}{\partial y}+\frac{\partial ix}{\partial x} &= -c\frac{\partial vz}{\partial t}-gvz \\ \frac{\partial vz}{\partial x} &= -rix-l\frac{\partial ix}{\partial t} \\ \frac{\partial vz}{\partial y} &= -riy-l\frac{\partial iy}{\partial t} \end{aligned} \qquad (1)$$

where l, r, g and c are the inductance, resistance, conductance and capacitance in per unit length respectively.

Maxwell's equations in two dimensions are (assuming that there is only one component of the H-field)

$$\begin{aligned} -\frac{\partial Ex}{\partial y}+\frac{\partial Ey}{\partial x} &= -\frac{\partial B}{\partial H}\frac{\partial Hz}{\partial t} \\ \frac{\partial Hz}{\partial x} &= -\sigma Ey-\varepsilon\frac{\partial Ey}{\partial t} \\ \frac{\partial Hz}{\partial y} &= +\sigma Ex+\varepsilon\frac{\partial Ex}{\partial t} \end{aligned} \qquad (2)$$

where σ, ε and $\partial B/\partial H$ are the conductivity, permittivity and differential permeability of the medium respectively; all units are in per unit length. Comparing eqs. (1) and (2), the following equivalence can be drawn

$$\begin{aligned} &Hz = vz \;\;;\;\; Ex = -iy \;\;;\;\; Ey = ix \;\; and \\ &\sigma = r \;\;;\;\; \varepsilon = l \;\;;\;\; \frac{\partial B}{\partial H} = c \;\;;\;\; g = 0 \end{aligned} \qquad (3)$$

Therefore, an interconnected network of Fig. 4a forms a space discrete model of Maxwell's equations. The resulting network may be solved by various methods. For example, SOR (successive overrelaxation) can be used for steady-state problems. For transient problems, a set of first order ordinary differential equations can be derived and the solution obtained by integration using schemes such as the Runge-Kutta. Alternatively, the time can be further discretized using finite-difference; this is similar to the finite-difference time-domain method. More conveniently, the network may be solved by standard circuit simulators, such as PSPICE which is used in the paper. In this case, it is a simple matter to generate an input file describing the interconnections of the cells shown in Fig. 4a.

2.2 The improved network topology

One major drawback of the network equivalent (and the finite-difference method) is that a large number of cells are needed for typical problems if regular fine cells are used to cover the entire field region. In many cases, fine cells are used in regions where the field variation is less steep. A number of modifications have been proposed as reviewed in the *Introduction*. Among the various methods, the fine-coarse mesh approach, which has been proven to be a viable alternative to the multigrid technique, is the most straightforward to implement. It is only necessary to provide a number of subcircuits (each representing a regular network cell of a given mesh size) for PSPICE. However, this method assumes that the potentials (=H-field) at "a", "b" and "c" are identical (see Fig. 3a). This assumption may be unacceptable at high frequencies, during the initial transient phase or for some special cases. This problem is eliminated by breaking the busbar and replace it by three controlled sources as shown in Fig. 3b. Parameters associated with each of these sources may be determined as shown below.

Using Taylor series expansion and with reference to Fig. 3b, v(z) can be determined in terms of v(z-1) and v(z+1):

$$v(z) = \frac{p(v(z+1))+q(v(z-1))}{p+q} - \frac{1}{2}K\left(\frac{\partial^2 vz}{\partial^2 y}\right)+O(h^3) \qquad (4)$$

where

$$K = pqh^2 \; and \; \frac{\partial^2 vz}{\partial^2 y} = \frac{\partial B}{\partial H}\left(\sigma\frac{\partial vz}{\partial t}+\varepsilon\frac{\partial^2 vz}{\partial^2 t}\right) \qquad (5)$$

If $p = q = 0.5$ and the region is diffusion dominated, eq. (4) becomes

$$\begin{aligned} v(z) &= 0.5(v(z-1)+v(z+1)) \\ &\quad -0.125h^2\left(\frac{\partial B}{\partial H}\sigma\frac{\partial vz}{\partial t}\right)+O(h^4) \end{aligned} \qquad (6)$$

Eq. (6) has a better error term. Therefore, it is recommended that the coarser mesh size should double the preceding one. Likewise, equations (similar to eq. (4)) can be derived for v(z-1) and v(z+1).

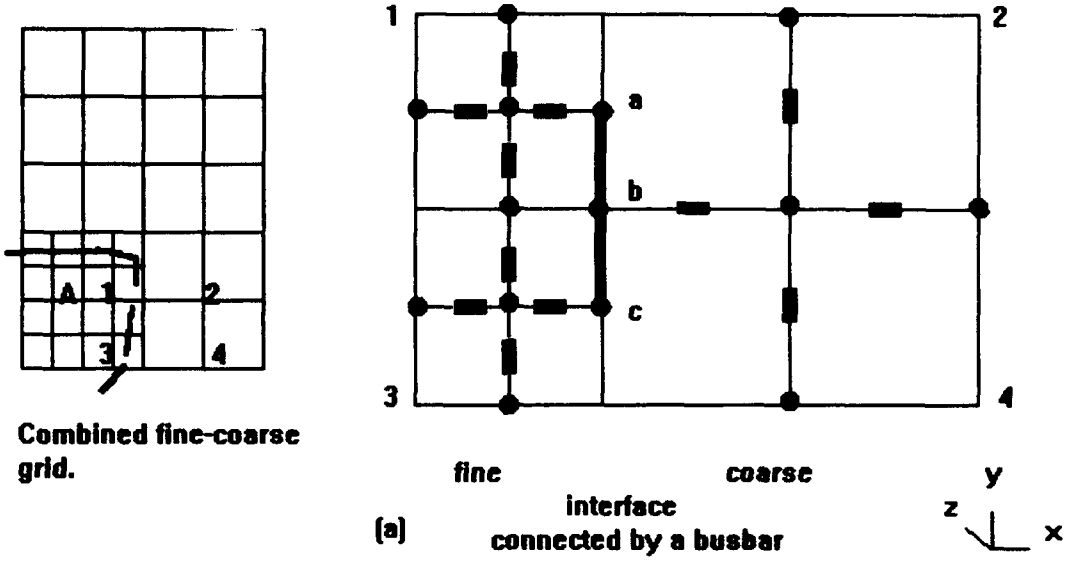

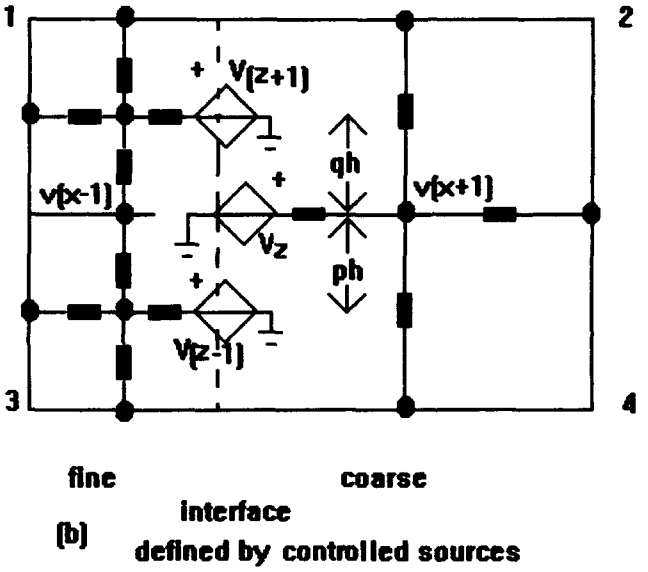

Fig. 3 The combined fine-coarse mesh model and the improved model.

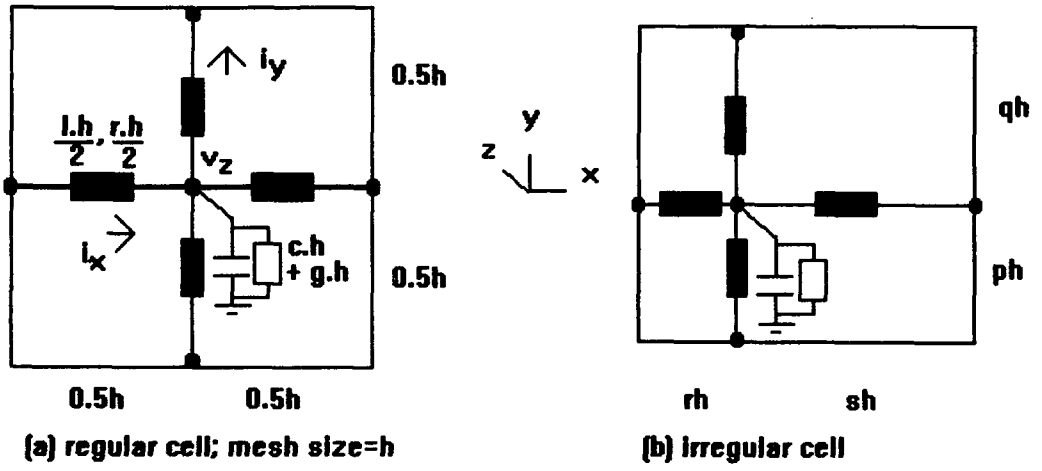

Fig. 4 Typical irregular and regular cells.

The first term of eq. (6) can be easily implemented in PSPICE with controlled sources, however, an additional subcircuit built from a pure inductor (or capacitor) circuit is required to model the second term. This is illustrated in Fig. 5 where the inductor value (L) equals $0.125h^2\sigma(\partial B/\partial H)$.

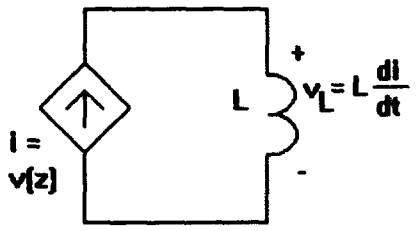

Fig. 5 A subcircuit model for the second term of eq. (6).

The accuracy of eq. (6) may be improved if v(x-1) and v(x+1) are included in the interpolation. Eq. (6) becomes:

$$v(z) = 0.333(v(z-1)+v(z+1)) + 0.222v(x-1)$$
$$+0.111v(x+1) - 0.0833h^2\left(\frac{\partial B}{\partial H}\sigma\frac{\partial v_z}{\partial t}\right) \qquad (6a)$$

However, initial results show that the improvement gained in using eq. (6a) is marginal for the examples discussed in the following section and therefore only eq. (6) is used for the improved model.

3. RESULTS

3.1 Flux penetration into a long bar due to an axial H-field

Figure 6 shows the cross-section of a long square bar subjected to the excitation of an axial H-field (H_z). The rise of the magnetic field is determined at two representative positions ("a" and "b_1") when H_z is an impact excitation. Due to symmetry, only one-eighth of the region (for example, OAB) is solved. In the fine mesh region, the mesh size, h, is set to W/8, whereas h = W/4 for the coarse mesh region. For convenience, normalised units and all default settings of PSPICE have been used.

Figure 7 shows the results from the different network models, and they are compared with the exact solution. Both fine-coarse mesh models provide results which are very close to the regular fine mesh model (within 1% for the period shown) but the computing time is cut by at least 50%. The improvement in efficiency is dependent on the "size" of the problem and a better gain can be achieved for larger problems.

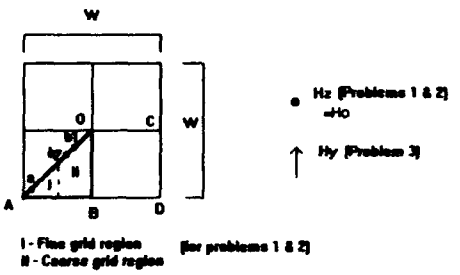

Fig. 6 A long square bar subjected to external H-field excitation.

Accuracy of the network models is best assessed by their corresponding frequency responses. PSPICE provides an efficient way to generate the frequency response curves of the various models. The results are shown in Figures 8a and 8b. The problem is similar to the first case, except that the excitation is sinusoidal and that only steady-state solutions are sought.

It can be seen that the response curves of the new model and the regular fine mesh model are all very close for position "a". The original combined fine-coarse mesh result trails slightly behind. At position "b_1", all three frequency response curves are similar with the original combined fine-coarse model stands out marginally. It should be noted that for the latter case, h = 1/4. A further error analysis is shown in Table 1 where the rms error for the different models are calculated. (Note that the default tolerance of PSPICE is 0.1% and therefore, the errors calculated below are mainly due to the modelling process.)

Table 1 shows that the new model improves the accuracy by approximately 50% (or better) when compared with the original fine-coarse mesh arrangement at position "a". No advantage is observed at the other position, however, both show an improvement over the regular mesh model since fine-mesh information are available to the coarse mesh. The relatively poor accuracy at position "b_1" is not reflected in the transient curves (Fig. 7) because the high frequency components are highly attenuated at this position. This shows that fine cells are not essential at this region for transient studies.

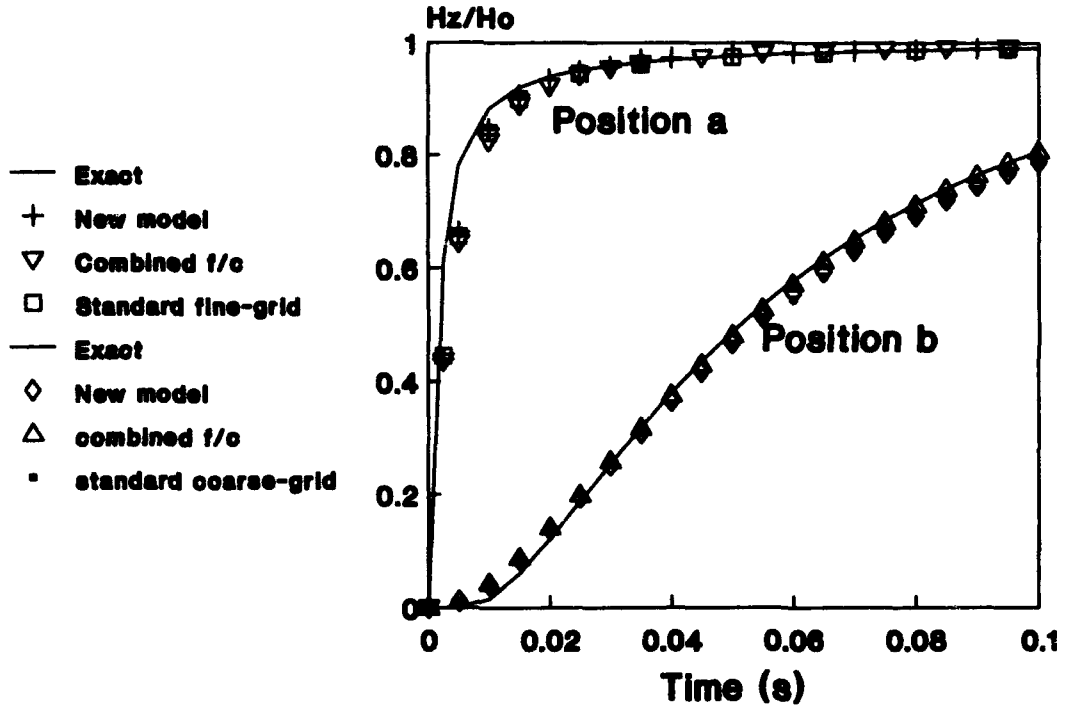

Figure 7 Flux penetration into a long square bar under an impact excitation (position "b" = "b_1").

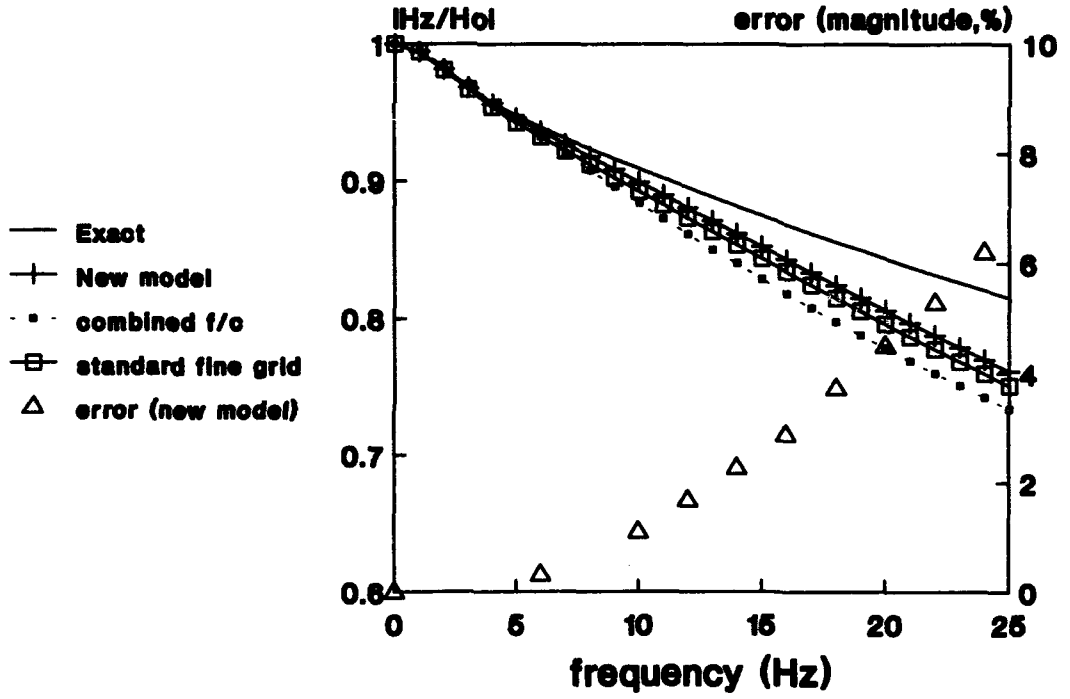

(a) Position "a" (h = W/8 and W = 1).

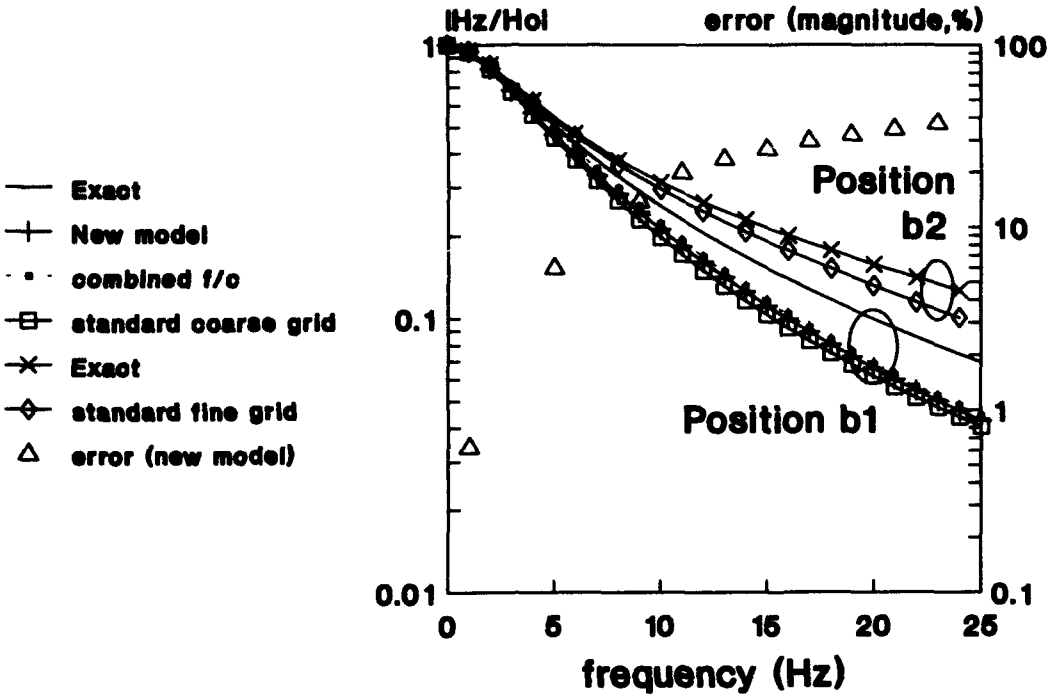

(b) Position "b_1" (h = W/4 and W = 1) and position "b_2" (h = W/8).

Figure 8 Frequency responses for the different network models at two representative positions. The horizontal axis can be converted to the dimensionless parameter $(h/\delta)^2$ by multiplying the factor πh^2, where δ is the skin depth.

	rms error,	(Position a)	
Freq. range (h/δ)	new model	combined fine-coarse	standard, with fine mesh
1 Hz to 20 Hz (0.222-0.992)	1.88%	3.96%	2.30%
1 Hz to 10 Hz (0.222-0.702)	0.29%	1.13%	0.84%

	rms error,	(Position b_1)	
Freq. range (h/δ)	new model	combined fine-coarse	standard, with coarse mesh
1 Hz to 20 Hz (0.443-1.984)	19.47%	17.78%	24.44%
1 Hz to 10 Hz (0.443-1.403)	9.12%	6.45%	12.88%

Table 1 Accuracy of various network models

3.2 Eddy current loss in a long square bar subjected to a transverse field

The third problem determines the eddy current loss in a long square bar excited by a transverse magnetic field. In this case, the electric field has one component (E_z) whereas the magnetic field has two (H_x and H_y). Maxwell's equations are:

$$-\frac{\partial Hx}{\partial y}+\frac{\partial Hy}{\partial x}=\varepsilon\frac{\partial Ez}{\partial t}+\sigma Ez$$
$$\frac{\partial Ez}{\partial y}=-\frac{\partial B}{\partial H}\frac{\partial Hx}{\partial t} \qquad (7)$$
$$\frac{\partial Ez}{\partial x}=\frac{\partial B}{\partial H}\frac{\partial Hy}{\partial t}$$

The equivalence between network and field quantities is:

$$vz=Ez \;;\; ix=-Hy \;;\; iy=Hx \;;$$
$$l=\frac{\partial B}{\partial H} \;;\; c=\varepsilon \;\; and \;\; g=\sigma \qquad (8)$$

The field in the vicinity of the bar is unknown and consequently the air region has to be solved. It is assumed that the field is unaffected by the presence of the bar in regions 2W from it. Other parameters used are:

$$\frac{\partial B}{\partial H}=\mu 0 \;;\; \varepsilon=\varepsilon 0 \;;\; W=1\,cm$$
$$and \;\; \sigma=10^7\,S/m\,(in\ conductor)$$
$$=0\,(in\ free\ space) \qquad (9)$$

For the frequency range used, the reactance of the shunt capacitor (C = εh) is at least 10 orders of magnitude larger than 1/(gh) or the reactance of lh. Therefore, the capacitors are assumed to be open-circuited. Due to symmetry, only one-quarter of the region is solved. In this case, the bar is covered with fine cells with h = 1/6 cm and the outer part of free space is covered with coarse cells. The power losses in per unit volume are determined in terms of P_o (power loss when δ = W/2 = 0.5 cm). The results are plotted in Figure 9. This problem involves two domains and is relatively large when compared with the previous two. The memory requirement recorded was approximately 130 k and the computing time was about 7.3 seconds on a standard 486 machine for 8 frequencies. As a comparison, results using a larger air region (4Wx4W) and results from reference 13 are included in Figure 9. SPICE3 running on a SUN workstation has been used for the former case. The interfacing busbar of the original combined fine-coarse mesh topology will force local potentials (= E_z) to be identical. In regions close to the boundary, where H_y is assumed constant, this assumption ($\partial E_z/\partial x$ = 0), along the x-direction, is unacceptable (see eq. (7)) and may produce erroneous results.

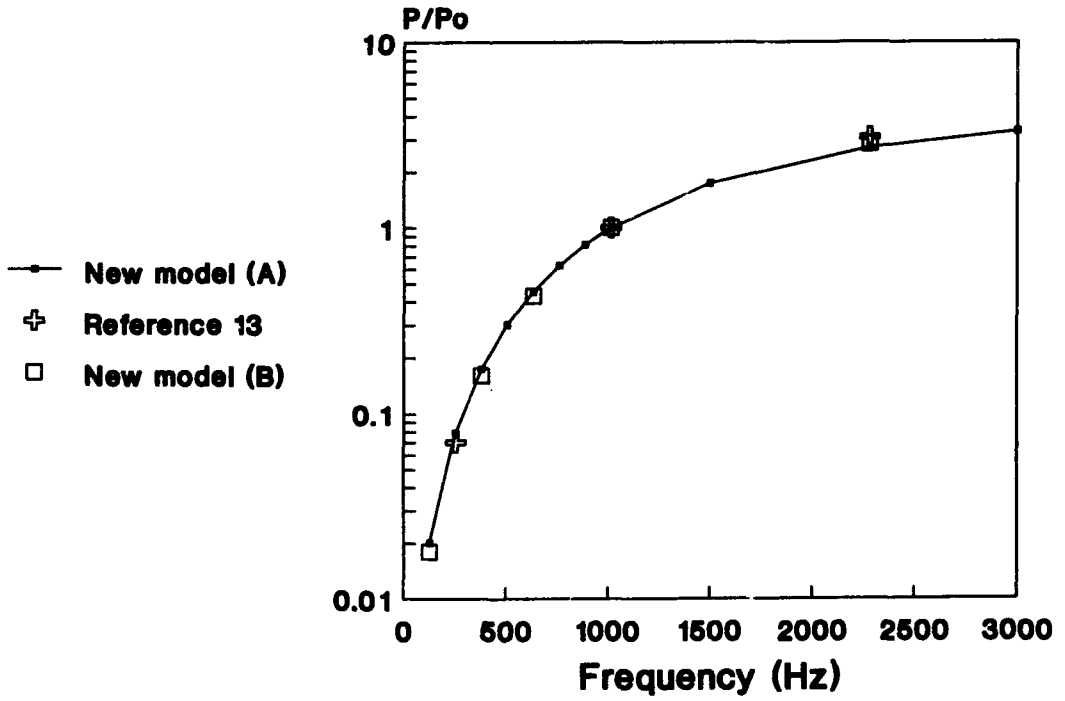

Fig. 9 Eddy current loss in a square bar due to a transverse magnetic field.
(A) - air region = 2Wx2W; (B) - air region = 4Wx4W.

The validity of this approach may be assessed by comparing adjacent node potentials around the interface between the fine- and coarse-cell. Consequently, the use of the original model must be exercised with care. On the other hand, the new model does not have this limitation.

4. CONCLUSIONS

This paper describes two network models for Maxwell's equations in two dimensions. The first model, which is based on the original combined fine-coarse mesh technique, is very straightforward to implement. However, it uses "busbars" at the fine- and coarse-cell interface and the resulting error may be unacceptable in some cases. In the new model the "busbars" are replaced by controlled sources and this problem is eliminated. Both models allow a reduction in the total number of cells within a field region to be modelled without compromising accuracy (this may be problem dependent for the original combined fine-coarse mesh technique) and can be easily solved by PSPICE, SPICE or other circuit simulators. Based on the new network analogues, field modellers can solve most two-dimensional field problems without the prior knowledge of numerical methods or the need of a dedicated software package.

5. REFERENCES

1. G. Kron, "Equivalent circuit of the field equations of Maxwell-I", *Proc. Inst. Radio Engr.*, **32**, 289-299 (1944).

2. J. Roberts, "Analogue treatment of eddy-current problems involving two-dimensional fields", *Proc. IEEE*, **107C**, 11-18 (1960).

3. P. Silvester, "Network Analog solution of skin and proximity effect problems", *IEEE Trans. Power Appar. Syst.*, **PAS-86**, 241-247 (1977).

4. J. Vine, "Impedance network", in *Field Analysis*, Vitkovitch (Ed.), Van Nostrand, London, 1966.

5. R. J. Lari and R. Turner, "Survey of eddy current programs", *IEEE Trans. Magnet.*, **MAG-19**, 2474-2477 (1983).

6. P. B. Johns, "A simple explicit and unconditionally stable numerical routine for the solution of the diffusion equation", *Int. j. numer. methods eng.*, **11**, 1307-1328 (1977).

7. S. Pulko, A. Mallik and P. B. Johns, "Application of transmission-line modelling (TLM) to the thermal diffusion in bodies of complex geometry", *Int. j. numer. methods eng.*, **23**, 2303-2312 (1986).

8. K. J. Binns and P. J. Lawrenson, *Analysis and computation of electric and magnetic field problems*, Part IV, Pergamon Press, Oxford, 1973.

9. W. Hackbusch and U. Trottenbery (Eds.), *Lecture Notes in Mathematics: Multigrid Methods II*, Springer-Verlag, New York, 1986.

10. R. E. Phillips and F. W. Schmidt, "Multigrid techniques for the numerical solution of the diffusion equation", *Num. Heat Transfer*, **7**, 251-268 (1984).

11. C. C. Wong, "Multigrid TLM for diffusion problems", *Int. j. numer. modelling*, **2**, 103-111 (1989).

12. R. Ait-Sadi, A. J. Lowery and B. Tuck, "Combined fine-coarse mesh transmission-line modelling method for diffusion problems", *Int. j. numer. modelling*, **3**, 111-126 (1990).

13. R. L. Stoll, *The analysis of eddy currents*, chapter 8, Clarendon Press, London, 1974.

ON THE USE OF PLANAR SCATTERING PROBLEM TECHNIQUES TO ANALYZE THIN PLANAR QUASI-MAGNETO-STATIC SHIELDING

by

Charles D. Hechtman,† Erik H. Lenzing,‡ and Barry S. Perlman ‡

ABSTRACT

A metallic screen scattering technique developed for microwave and millimeter wave applications is adapted, using the principle of duality to a quasi-magnetostatic shielding problem. In the limiting case of low frequency (0.01 Hz) the results compare favorably with the static solution. Moreover, this adaptation is expanded to treat finite permeability shields.

1. INTRODUCTION

In the past there has been numerous examples of borrowing and adapting methods and techniques across disciplines, for example Harrington's adaptation of the method of moments[1] for electromagnetics or the use of electrostatics for specialized wire-routing problems.[2] In this work a scattering technique, usually applied to conductive screens at high frequency and the principle of duality, is applied to quasi-static and static magnetic field shielding problems.

Magnetic fields emanating from static and quasi-static sources such as power lines or permanent magnets are often considered undesirable and require mitigation. Attenuation may be provided locally by shields designed for quasi-static and static fields. These shield designs rely upon material properties, e.g., high permeability, and geometric configuration, e.g., thin inhomogeneous sheeting, to satisfy engineering and economic requirements. The large number of possible shield designs warrants simulation and modeling to optimize shield efficacy and provide manufacturing cost control.

Traditionally, shield geometries are analyzed at zero frequency with an assortment of techniques that solve Laplace's equation. Analytic solutions, which provide the most insight, are most tractable in 2 dimensions, where conformal mapping is available. Moreover, geometries found in most magnetostatic problems do not have analytic solutions. Therefore, most static field solutions are found numerically in terms of a scalar potential using techniques such as a finite difference[3] or finite element method[3] or in terms of a boundary charge distribution using techniques such as a static moment method[3] or a static spectral domain method.[3]

For the limiting case of thin shields with finite permeability in free space, the methods identified above are problematic. Using the finite difference or finite element techniques would require an enormous numbers of grids or elements in and around the regions of the shield. Such conditions spawn an inefficient, huge set of equations and other problems are associated with their solutions. In addition, the static moment method or the static spectral domain method are only effective for infinite permeability. In contrast, the quasi-magneto-static problem could be posed as a scattering problem for both infinite and finite permeability where the resulting magnetic field integral equation (MFIE) is solved with a moment method[4] in the spatial domain (most effective for non-periodic structures) or in the spectral domain[5] (effective for periodic and non-periodic structures). Both of these methods would be useful for planar shields and could be modified for truncated cylindrical shields.

In the next sections the shielding problem is recast into a quasi-static scattering problem with infinite permeability. The results are compared with the static solution and the result is generalized to finite permeability.

† Stevens Institute of Technology, Castle Point on the Hudson, Hoboken, New Jersey 07030

‡ U.S. Army Research Lab, EPSD, Microwave and Photonics Division, Ft. Monmouth, New Jersey

2. *A scattering problem with infinite permeability*

Scattering problems commonly have feature sizes on the order of a wavelength. In this example we consider feature sizes (several meters) that are a small fraction of the wavelength (λ approximately 3,000 miles). This is still a scattering problem, given the proviso of non-zero frequency, where phase retardation exists between the shield and source. An illustrative example appears in figure 1 for the 2 dimensional version. The left hand side consists of a typical scattering problem, where an electric field is incident on a perfectly conducting strip. An electric surface current is induced on the strip with a resulting scattered electric field that nulls the incident electric field on the surface.

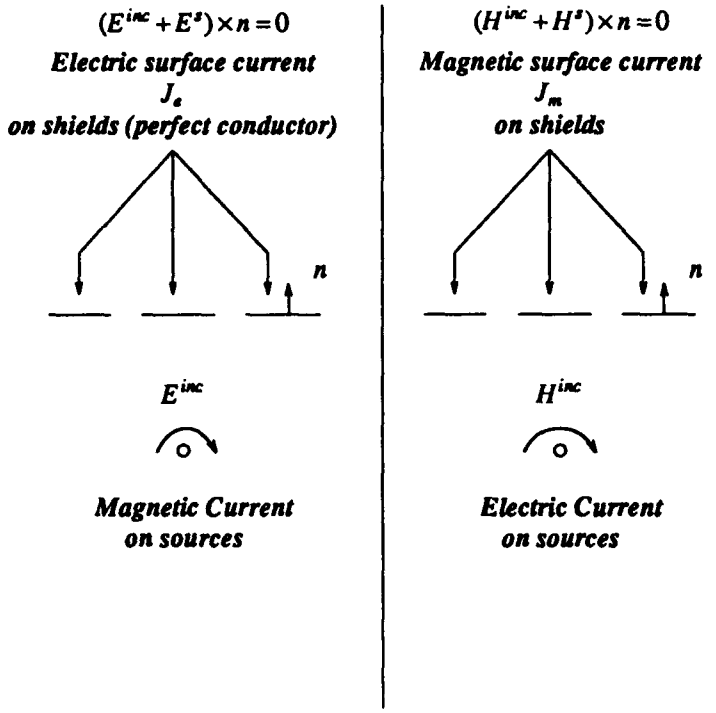

Figure 1. Two dimensional scattering, Electric and Magnetic Duality

On the right hand side similar field behavior exists for the magnetic field. The electric and magnetic field scattering problems are equivalent and are related by the principle of duality.[6] In what follows the formulation is developed in terms of the electric field.

Initially, for the case of infinite conductivity (infinite permeability) the sum of the tangential incident electric field, E^{inc}, and the scattered electric field, E^{scat}, must be zero.

$$(E^{inc}+E^{scat})\times n=0\,. \tag{1}$$

The electric field integral equation (EFIE) corresponding to the special case of two dimension strips on the $y = 0$ plane (geometry and coordinates shown in Figure 2) and an incident electric field that contains only an x component is given by

$$E_x^{inc}+\int_{strip} J_{ex}(x')g(x,x')dx'=0\,, \tag{2}$$

where x is a coordinate on the shields,

$$g(x)=-\frac{\beta\eta}{8}[H_0^{(2)}(|\beta x|)+H_2^{(2)}(|\beta x|)]\,, \tag{3}$$

is a 2-D modified Green's function that describes the scattered electric field on the strip, $H_i^{(2)}$ is a Hankel function of second kind, and β is the wave number. This EFIE may be found in Balanis[7] with a detailed dervation presented in the Appendix of this paper. Determining the correct current density on the strips, $J_e(x)$, for the integral equation (2) is the key task in this problem. This may be accomplished in a number

of ways with various levels of approximation. The scattered electric field may then be determined for all space by,

$$E^{scat}(r) = \int_{strip} J_{ex}(r')g(r,r')dr' , \tag{4}$$

where r is a position vector and $E^{inc}(r)$ is the incident electric field.

2.1 Point Collocation Method[8]

The point collocation method is a familiar technique[8] that satisfies the boundary condition (1) at discrete points only. Boundary segments off these points may not be satisfied. Hence, the resulting current density distribution and the scattered field are only an approximation. The current expansion is in terms of pulse functions.

The following test case will demonstrate the efficacy of this technique. While applying the point collocation method, the Green's function was approximated as follows:

$$g(x) = -\frac{\beta\eta}{8}[H_0^{(2)}(|\beta x|) + H_2^{(2)}(|\beta x|)] \approx -\frac{\beta\eta}{8}[1 + \frac{(\beta x)^2}{8} - j(\frac{2}{\pi}\ln(\frac{\gamma|\beta x|}{2}) - \frac{4}{\pi x^2})] , \tag{5}$$

where η is the free space impedance and $\ln(\gamma = 1.781)$ is Euler's constant. Referring to figure 2, two infinitesimally thin shields lie on the abscissa, each of length $L=1$ separated by a distance $W=0$ (i.e., a single shield of length 2 centered about the origin).

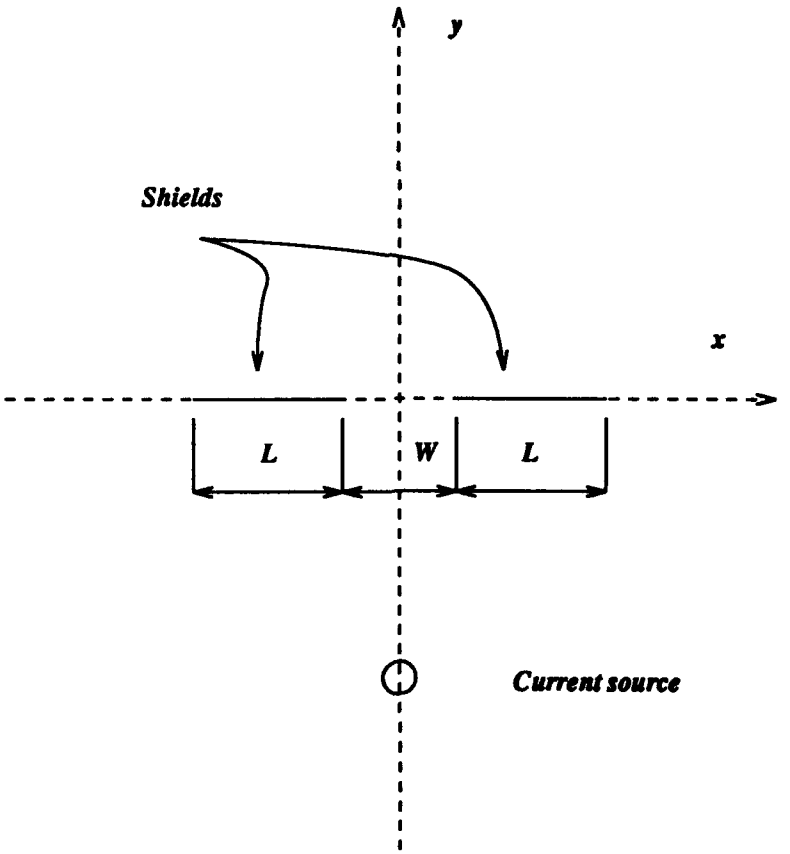

Figure 2. Test case shield geometry

The shields are of infinite permeability and an electric current source is located -5 meters beneath the origin. An analytic solution found by conformal mapping exists for this geometry and is compared with the collocation point matching solution, in figure 3.

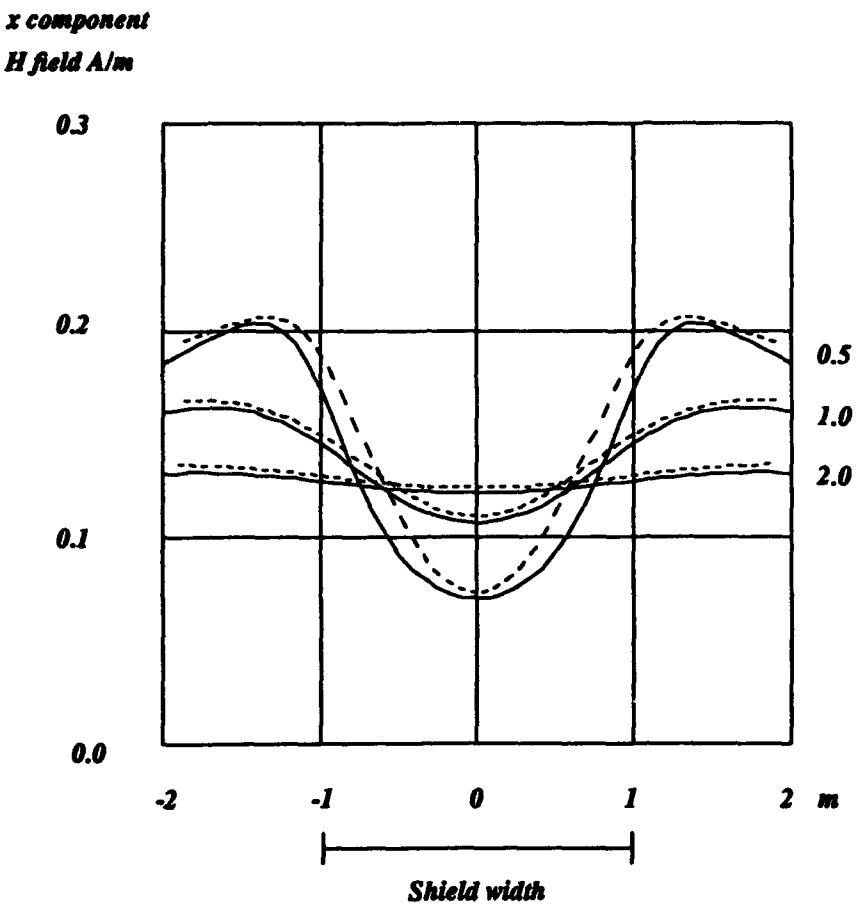

Figure 3. Comparison of H_x variation with x when $y=0.5, 1.0, 2.0$, where dashed lines represent conformal mapping solution and the solid lines represent the point collocation method

The x component of the magnetic field for the analytic solution (dashed lines) and the point matching solution (solid lines) using 20 points are plotted as a function of x for $y=0.5, 1.0, 2.0$. The case where $y=0.5$ shows the largest error, $\leq 15\%$, and as y increases the deviation decreases. This is expected since the 20 discrete boundary points appear to smear with larger distance. Increasing the number of points improves the result marginally but the spectral domain method outlined in the next section is a better choice. Figures 4,5, and 6 are three dimensional plots of the variation of the x component of the electric field for shields separated by $W=0.5, 0.1, 0.0$ meters and length, $L=1$ meters, centered at the origin. Figures 4 and 5 show the magnetic field leaking through the shield gap. These pictures clearly illustrate the shielding futility in using long strips perpendicular to the magnetic field lines.

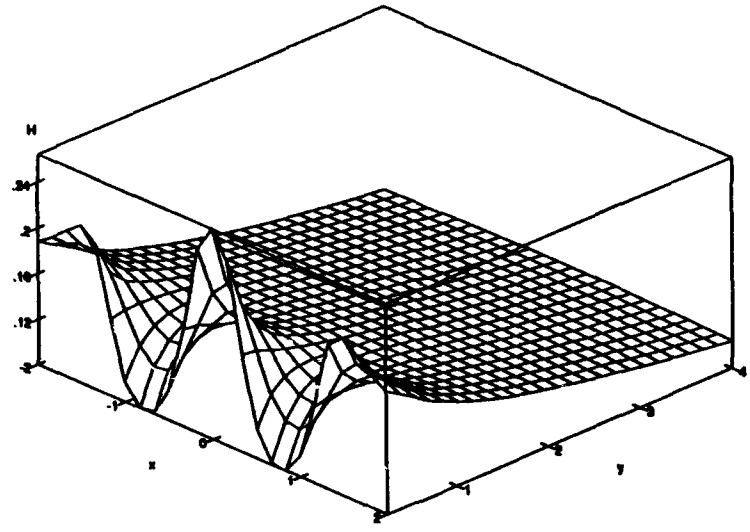

FIGURE 4. MAGNETIC FIELD VARIATION WITH POSITION FOR THE CASE OF TWO SHIELDS 1 METER WIDE SEPARATED BY 0.5 METERS WITH A SOURCE AT -5 METERS

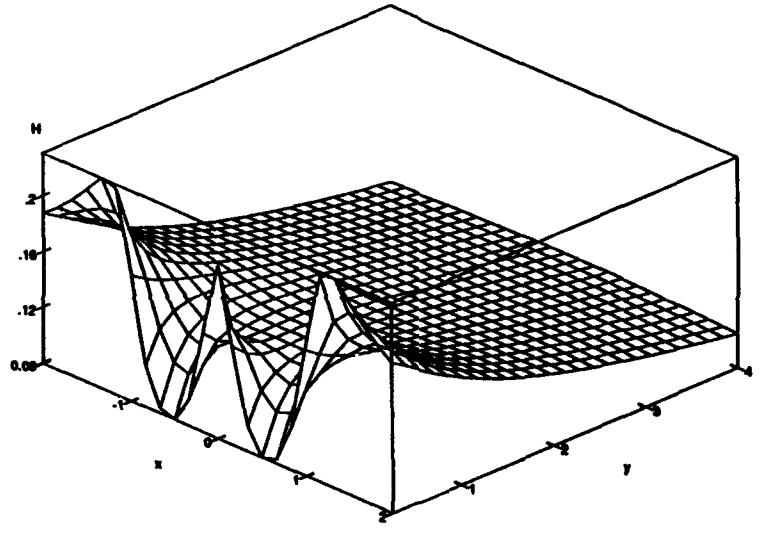

FIGURE 5. MAGNETIC FIELD VARIATION WITH POSITION FOR THE CASE OF TWO SHIELDS 1 METER WIDE SEPARATED BY 0.1 METERS WITH A SOURCE AT -5 METERS

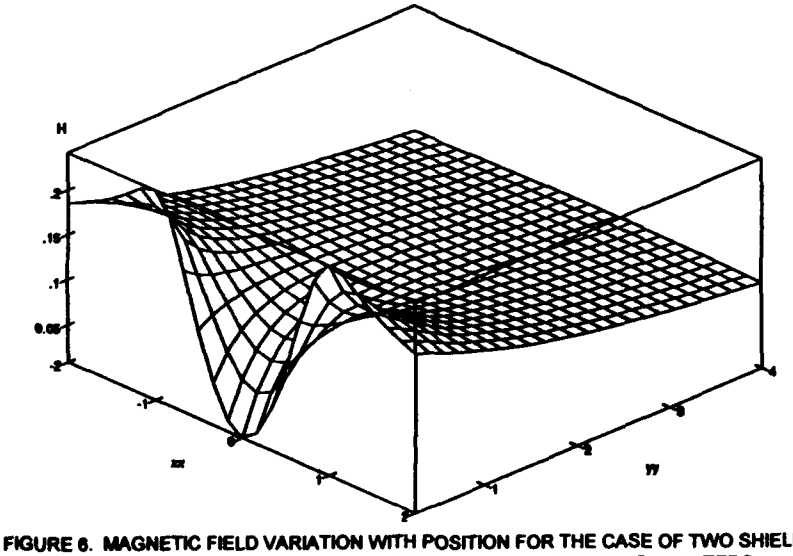

FIGURE 6. MAGNETIC FIELD VARIATION WITH POSITION FOR THE CASE OF TWO SHIELDS 1 METER WIDE SEPARATED BY 0.0 METERS WITH A SOURCE AT -5 METERS

2.2 Spectral Domain Method[5] and finite permeability

Whereas the point collocation method seeks to satisfy the boundary condition at discrete points on the boundary, the Spectral Domain Method seeks to force uniform convergence of the boundary condition in the fourier transform domain. The Fourier transform of the EFIE yields

$$\tilde{E}^{inc}(\alpha)+\tilde{J}_s(\alpha)\tilde{g}(\alpha)=\tilde{E}^{total}(\alpha) \tag{6}$$

where the tilde represents the fourier transform of the function and the Fourier transform pair is defined as

$$\tilde{E}(\alpha)=\int_{-\infty}^{\infty}E(x)e^{-j\alpha x}dx \tag{7}$$

and

$$E(x)=\frac{1}{2\pi}\int_{-\infty}^{\infty}\tilde{E}(\alpha)e^{j\alpha x}d\alpha \ . \tag{8}$$

The Fourier transform of the Green's function (equation (3)) is given by

$$\tilde{g}(\alpha)=-\int_{-\infty}^{\infty}\frac{\beta\eta}{8}[H_0^{(2)}(|\beta x|)+H_2^{(2)}(|\beta x|)]\ e^{-j\alpha x}dx=-\frac{\eta}{\beta}\sqrt{\beta^2-\alpha^2} \ . \tag{9}$$

See Appendix A of C. Scott[5] for derivation. The current may be represented as a sum of aperture-limited basis functions with unknown coefficients and appropriate edge condition,[1] where for the strip above

$$\tilde{J}_s(\alpha)=\sum_{n=1}^{N}a_n\tilde{\psi}_n(\alpha) \tag{10}$$

and

$$\psi_n(x)=a_n\frac{\cos(nx\pi/2)}{\sqrt{x^2-1}} \ . \tag{11}$$

Multiplication and integration of equation (6) with $\tilde{\psi}_n(\alpha)$ yields the following:

$$\int_{-\infty}^{\infty}\tilde{\psi}_n(\alpha)\tilde{E}^{inc}(\alpha)d\alpha+\int_{-\infty}^{\infty}\tilde{\psi}_n(\alpha)\sum_{m=1}^{N}a_m\tilde{\psi}_M(\alpha)(-\frac{\eta}{\beta}\sqrt{\beta^2-\alpha^2})d\alpha= \tag{12}$$

$$\int_{-\infty}^{\infty}\tilde{\psi}_n(\alpha)\tilde{E}^{total}(\alpha)d\alpha \quad n=1,2,...,N \ ,$$

where for the case of infinite conductivity (or infinite permeability) $\tilde{E}^{total}(\alpha)=0$. Therefore there are N equations in N unknowns where the values of a_m are the constants to be determined. This determines the current on the shield where N is chosen for the desired degree of accuracy. Of course, the choice of basis functions is critical for rapid convergence.

The following plot (figure 7) revisits the two dimensional example of the last section where the magnetic field is computed above a shield 2 meters wide with a line source -5 meters beneath the thin high permeability shield. This plot illustrates the use of one well chosen basis function, namely N=1, from equation (12) for the determination of the field 0.5 meters above the shield and is compared with the corresponding conformal mapping solution.

1. Aperture with infinitely sharp edges require that the current density vector follow specific behavior near the edge. This is known as the edge condition.

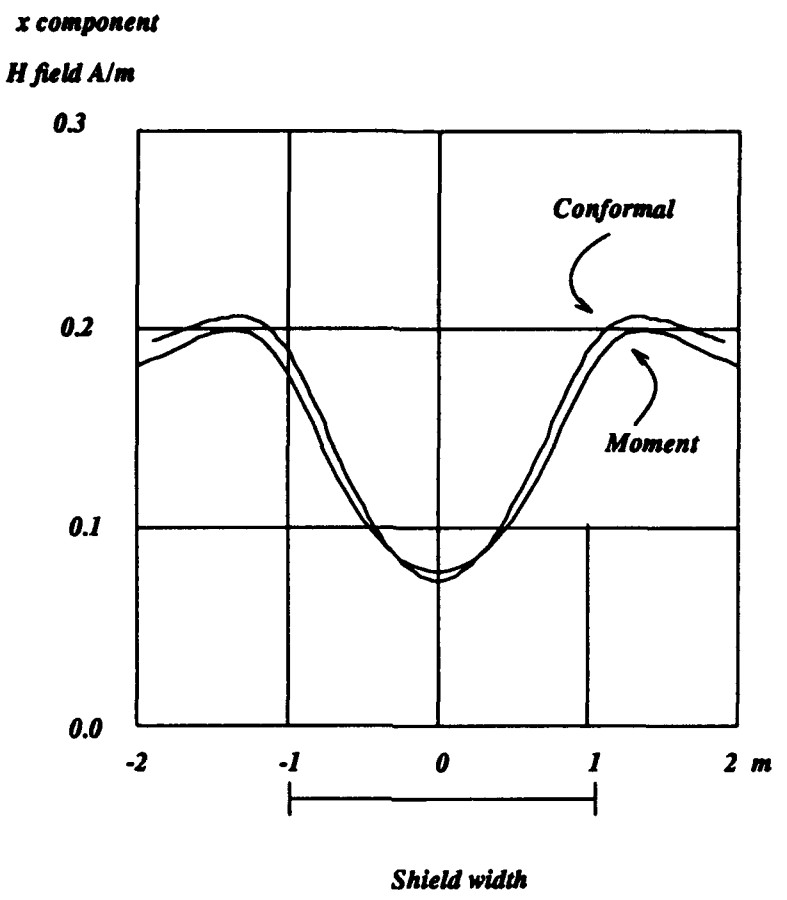

Figure 7. Comparison of single term moment method with conformal mapping solution.

Even with only a single term the approximation is quite good. Figure 8 is a three dimensional plot of the variation of the x component of the magnetic field for a distance 0.5 to 2 meters above the shield. In this example we consider a single basis function, $N=1$, to illustrate the effectiveness of a well chosen function. Moreover, it most be pointed out that using more terms of the basis functions (Equation 11), e.g., $N=2$ and $N=3$, improves the accuracy of the solution much like it does in the high frequency analog.

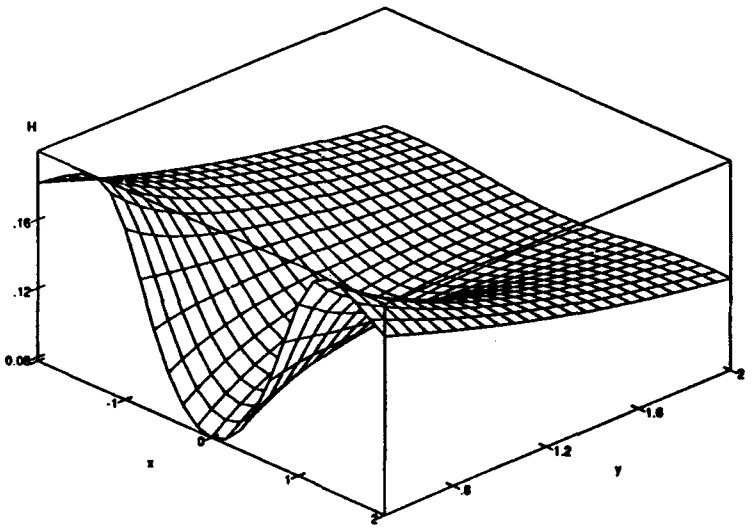

Figure 8. Magnetic field variation with position for a shield 2 meters wide with a source at -5 meters

Finally, consider the case of a thin strip of finite conductivity (or permeability). Using Parseval's theorem on the last term in equation (12),

$$\int_{-\infty}^{\infty} \tilde{\psi}_n(\alpha)\tilde{E}^{total}(\alpha)d\alpha = \int_{-1}^{1} \psi_n(-x)E^{total}(x)dx \ , \tag{13}$$

allows the replacement of the total electric field in the space domain by

$$\frac{\sum_{m=1}^{N} a_m J_m(x)}{\sigma + j\omega\varepsilon t} \tag{14}$$

for metal surfaces or

$$\frac{\sum_{m=1}^{N} a_m J_m(x)}{j\omega\mu t} \tag{15}$$

for high permeability surfaces, where σ, ε, μ, and t are the surface conductivity, the permittivity, the permeability, and the sheet thickness. In the next figure the strip example is again considered with finite permeability. The graphs show that as the permeability thickness product decreases the degree of shielding decreases.

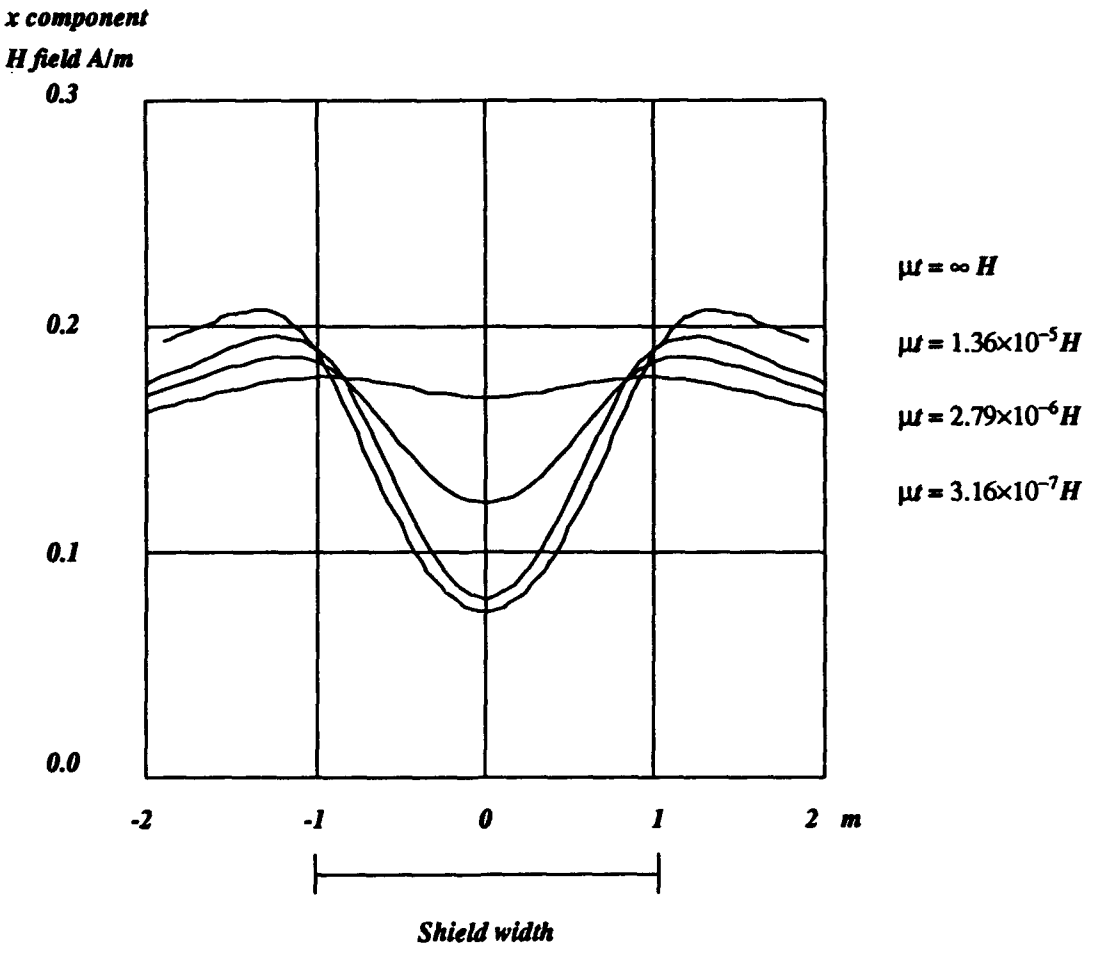

Figure 9. Field lines for source at -5 m. and shield 2 m. wide centered at the origin with $\mu t = \infty$, 1.36×10^{-5}, 2.79×10^{-6}, 3.16×10^{-7} H

3. Conclusions

It is shown that the moment method and the spectral domain techniques developed for high frequency applications may be successfully adapted for low frequency applications. The low frequency solutions found with the point collocation method and the spectral domain technique agree very well with the conformal mapping analytic solution and that unlike the static case, the finite permeability may be accounted for with relative ease. These are viable techniques for exploring cost effective high permeability inhomogeneous thin shields. The techniques may easily be extended to 3 dimensions for the analysis and design of thin inhomogeneous high permeability shields.

4. Appendix

Given the definition of the magnetic vector potential

$$\mathbf{A}=\frac{\mu}{4\pi}\int_{-\infty}^{\infty}\int\int\mathbf{J}(x',y',z')\frac{e^{\left[-j\beta\sqrt{\rho^2+(z-z')^2}\right]}}{\sqrt{\rho^2+(z-z')^2}}dx'dy'dz' \tag{A1}$$

and the current density

$$\mathbf{J}(x,y,z)=J_{ex}(x)\delta(y) \tag{A2}$$

where $\rho=\sqrt{(x-x')^2+(y-y')^2}$ and $\delta()$ is the Dirac delta function, the vector potential becomes

$$A_x=\frac{\mu}{4\pi}\int_{-\infty}^{\infty}\int_{-\infty}^{\infty}J_{ex}(x')\frac{e^{\left[-j\beta\sqrt{\rho^2+z'^2}\right]}}{\sqrt{\rho^2+z'^2}}dx'dz' \ , \tag{A3}$$

where $\rho=\sqrt{(x-x')^2+y^2}$ has been re-defined and z is assumed to be finite. Equation A3 may be recast as follows

$$A_x=\frac{j\mu}{4}\int_{-\infty}^{\infty}\frac{-j}{\pi}\int_{-\infty}^{\infty}J_{ex}(x')\frac{e^{\left[-j\beta\sqrt{\rho^2+z'^2}\right]}}{\sqrt{\rho^2+z'^2}}dx'dz' \ . \tag{A4}$$

The following substitutions

$$\beta\sqrt{\rho^2+z'^2}=\beta\rho\cosh t \tag{A5}$$

$$\frac{-jdz'}{\sqrt{\rho^2+z'^2}}=dt \tag{A6}$$

transforms Equation A4 into

$$A_x=\frac{j\mu}{4}\int_{-\infty}^{\infty}\frac{-j}{\pi}\int_{-\infty}^{\infty}J_{ex}(x')e^{\left[-j\beta\rho\cosh t\right]}dx'dt \tag{A7}$$

Equation A7 in conjunction with the integral definitions of the Bessel functions of the first and second kind, yields the desired vector potential.

$$A_x=\frac{j\mu}{4}\int_{-\infty}^{\infty}J_{ex}(x')H_0^{(2)}(\beta\rho)dx' \ . \tag{A8}$$

The x component of the electric field may be found from the vector potential as follows:

$$E_x^{scat}=\frac{-j}{\omega\mu\varepsilon}\left[\frac{\partial^2}{\partial x^2}+\beta^2\right]A_x \tag{A9}$$

$$=\frac{-\eta}{4\beta}\int_{-\infty}^{\infty}J_{ex}(x')\left[\frac{\partial^2}{\partial x^2}+\beta^2\right]H_0^{(2)}(\beta\rho)dx' \ ,$$

where ω is temperal angular frequency. Evaluation of A9 and Bessel function identities yields

$$E_x^{scat} = \frac{-\eta}{8\beta} \int_{-\infty}^{\infty} J_{ax}(x')[H_0^{(2)}(\beta\rho)+H_2^{(2)}(\beta\rho)]dx' \qquad (10)$$

where η is the free space impedance.

5. Acknowledgments

The authors wish to thank Harrison Rowe, Tim Hart, and Frank Boesch for their stimulating conversations.

REFERENCES

1. Harrington, R., *Field Computation by Moment Methods* (Reprint Edition), R.E. Krieger, Malabar, Fla., 1987; Original Edition, 1968.

2. Hechtman, C. and Levine, Z., *An Electrostatic Solution to a Specialized Routing Problem,* J. Appl. Phys., 62(5), pp. 2116-2122, 1 Sept. 1987.

3. Booton, R.C., *Computational Methods for Electromagnetics and Microwaves,* Wiley, 1992.

4. C. Balanis, *Advanced Engineering Electromagnetics*, pp. 707-717, J. Wiley, New York, 1989.

5. C. Scott, *The spectral domain method in electromagnetics*, Artech House, Norwood, Ma, 1989.

6. C. Balanis, *Advanced Engineering Electromagnetics*, pp. 310-312.

7. C. Balanis, *Advanced Engineering Electromagnetics*, pp. 702-705.

8. C. Balanis, *Advanced Engineering Electromagnetics*, pp. 681-683.

THE FINITE DIFFERENCE METHOD IN MAGNETIC FIELD PROBLEMS

by
Kent R. Davey
School of Electrical Engineering
Georgia Institute of Technology
Atlanta, GA 30332-0250

ABSTRACT

Finite difference techniques are widely used in the solution of electromagnetic boundary value problems, but seldom employed with static or quasi-static field problems. Historically this departure was warranted by (1) the relative ease by which problem geometries can be modeled using the finite element counterpart, and (2) the lack of symmetrical properties and large banding in the governing matrices. Presented here are some methods for generalizing the finite difference approach so that problem definition is easily modeled and Hermitian matrices result. The technique uses a conventional finite difference grid placed in the work area irrespective of the problem geometry. Finite difference equations are written in their simplest form across the problem work space. Boundary conditions are then introduced after the bulk equations are in place. The problem is solved using a non square governing matrix in a least square sense. This is accomplished most easily by pre-multiplying the matrix equation by its transpose. An alternative to the preconditioned conjugate gradient technique for solving the resultant matrix equation is to seek the eigenvalues for the system and express the answer as a sum of the eigenvectors. Results are shown for a salient pole motor. The technique is very useful in handling rotating or translating problems where considerable attention must be given to the proper connection and re-connection of the grid points.

BACKGROUND

Finite difference methods are often used to solve complex electromagnetic interaction problems. Because of the way in which the defining equations are represented, the banding of the resulting matrix equations can be quite large. It is also difficult to maintain symmetry in the matrix in order to speed up the solution. Many techniques have been proposed using equivalent circuit models and successive over relaxation techniques to address some of these problems[1], but odd geometries continue to present difficulties in representation of the constitutive equations. On the positive side, finite difference methods are intuitively appealing; governing equations are easily expanded and represented on a point by point basis in space. With homogeneous grids containing equally spaced points, the problem setup is quite straightforward [2].

At issue in this paper is how to apply the attractive features of the finite difference technique in problems with generalized geometries. The following two additional problems are invoked with the generalized geometry :
a. Representing the first and second-order derivatives in a nonuniform grid, one which 'fits' the problem boundaries.
b. Addressing the issue of iteratively refining the grid to enhance solution accuracy without reformulating the problem.

The technique offered in this paper has the flexibility of addressing the above problems, and springboards from the excellent work of Girdinio et al[3],[4]. Among other things, they point out the benefits of using not 4 but 5 points to represent the two-dimensional Laplacian operator as far as the freedom it affords in placement of points. The present work begins at that point and applies the idea not only to the internal volume to be modeled, but also to the enforcement of boundary conditions. The emphasis in this paper is on an easy implementation of the finite difference equations and iterative grid refinement to enhance solution accuracy.

THEORY

Consider a problem where the H field is represented as either a total or reduced scalar potential For the latter, we use

$$\vec{H}=\vec{T}-\nabla\Phi \tag{1}$$

where T is the magnetic intensity source term and is found in the current carrying region using the Biot-Savart law. The problem reduces to solving Laplace's equation for the unknown Φ,

$$\nabla\cdot(\mu\nabla\Phi)=\nabla\mu\cdot\nabla\Phi+\mu\nabla^2\Phi=0. \tag{2}$$

The simplest discretization for a multi-region problem is to continue a homogeneous grid through the problem space as indicated in Figure 1. The Laplacian operator is easily represented in either 2 or 3 dimensions for such a grid.

Referring to Figure 2, the 2-D expansion about point 0 is

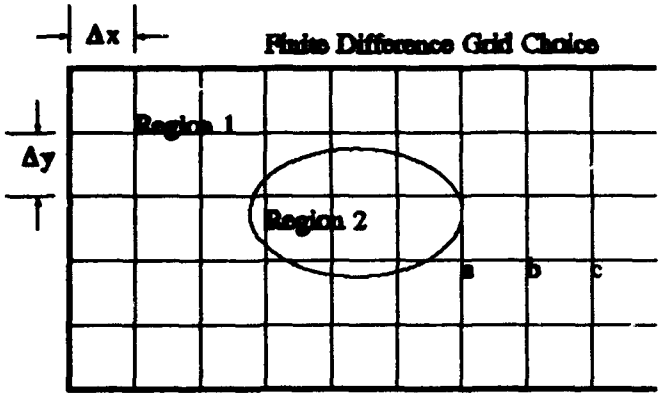

Figure 1. Grid continuation through the boundary of a dissimilar medium.

$$\frac{\Phi_4+\Phi_3-2\Phi_0}{\Delta x^2}+\frac{\Phi_1+\Phi_2-2\Phi_0}{\Delta y^2}=0, \qquad (3)$$

where Δx, Δy refer to the grid distance between points in the x and y directions. The problem setup proceeds by writing the Laplacian operator for Φ in all regions. It is assumed the material inhomogeneities are at least piecewise homogeneous, i.e., that the $\nabla\mu$ terms are negligible within any such piecewise homogeneous region. The only precaution to be taken is to use points from a common region when using a finite difference representation of the problem operator such as (3). In close proximity to the boundary interface, the one-sided second-order derivative should be used to represent the Laplacian. The second-order horizontal derivative represented in terms of the potential at adjacent horizontal positions b and c in Figure 1 is

$$\frac{\partial^2\Phi}{\partial x^2}=\frac{\Phi_c-2\Phi_b+\Phi_c}{\Delta x^2}+\mathcal{O}(\Delta x^3) \qquad (4)$$

The final term in (4) indicates the error terms are correct to order Δx^3.

The one sided expansion is the same regardless of which side of the boundary the derivative is taken. After writing (2) for all the grid points in the problem, the result is a N by N matrix for N unknowns. Over the bulk region of the problem, the standard finite difference representation of the Laplacian is employed because of its ease of implementation. This is, in fact, the motivation for using the finite difference method as opposed to the finite element method. The contribution of this paper is to show that it is possible to set up an evenly spaced finite difference grid irrespective of boundaries, and match boundary conditions after the bulk system equations are modeled. Furthermore, in a standard grid, 4 surrounding points (or 6 in 3D) are used to represent the Laplacian. Here it is shown that using five neighboring points (or 9 points in 3D) provides flexibility in modeling a variety of shapes while preserving the numerical accuracy to order Δ^3 where Δ represents the largest distance to any one of the neighboring points. Indeed, the technique allows one to place points on the interface randomly. The only penalty is the requirement of solving a 6 by 6 matrix for each interfacial point. The technique is also useful for increasing accuracy where the field has a high gradient, i.e., adding points randomly within a certain region of the problem.

This is made clear by the alternative representation of the second derivatives on x and y at point 0 in Figure 2, obtained by the set of equations

$$\Phi_j=\Phi_0+\frac{\partial\Phi_0}{\partial x}\Delta x_j+\frac{\partial\Phi_0}{\partial y}\Delta y_j+$$
$$\frac{1}{2}\frac{\partial^2\Phi_0}{\partial x^2}(\Delta x_j)^2+\frac{1}{2}\frac{\partial^2\Phi_0}{\partial y^2}(\Delta y_j)^2+\frac{1}{2}\frac{\partial^2\Phi_0}{\partial x\partial y}\Delta x_j\Delta y_j+\mathcal{O}(\Delta^3) \qquad (5)$$

where the index j refers to one of the nearest neighbors, and Δx_j, Δy_j refer respectively to the x and y differences from the point j to the field point at Φ_0. When (5) is repeated for each of the 5 nearest neighbors, there results a matrix equation for the unknown partial derivatives of Φ at point 0 in terms of the potential values at the nearest neighboring points and the self point Φ_0.

$$\begin{bmatrix} \Delta x_1 & \Delta y_1 & \frac{\Delta x_1^2}{2} & \frac{\Delta y_1^2}{2} & \frac{\Delta x_1\Delta y_1}{2} \\ \Delta x_2 & \Delta y_2 & \frac{\Delta x_2^2}{2} & \frac{\Delta y_2^2}{2} & \frac{\Delta x_2\Delta y_2}{2} \\ \Delta x_3 & \Delta y_3 & \frac{\Delta x_3^2}{2} & \frac{\Delta y_3^2}{2} & \frac{\Delta x_3\Delta y_3}{2} \\ \Delta x_4 & \Delta y_4 & \frac{\Delta x_4^2}{2} & \frac{\Delta y_4^2}{2} & \frac{\Delta x_4\Delta y_4}{2} \\ \Delta x_5 & \Delta y_5 & \frac{\Delta x_5^2}{2} & \frac{\Delta y_5^2}{2} & \frac{\Delta x_5\Delta y_5}{2} \end{bmatrix} \begin{bmatrix} \frac{\partial\Phi_0}{\partial x} \\ \frac{\partial\Phi_0}{\partial y} \\ \frac{\partial^2\Phi_0}{\partial x^2} \\ \frac{\partial^2\Phi_0}{\partial y^2} \\ \frac{\partial^2\Phi_0}{\partial x\partial y} \end{bmatrix} = \begin{bmatrix} \Phi_1-\Phi_0 \\ \Phi_2-\Phi_0 \\ \Phi_3-\Phi_0 \\ \Phi_4-\Phi_0 \\ \Phi_5-\Phi_0 \end{bmatrix} \qquad (6)$$

It is straightforward to invert this 5 by 5 matrix to arrive at the result

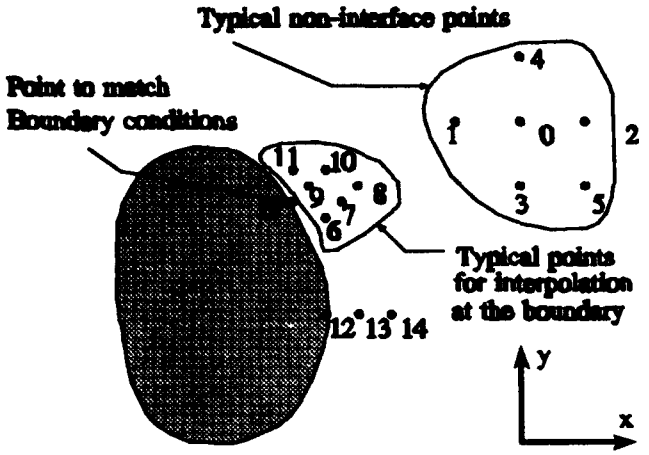

Figure 2. Typical points used for evaluating the Laplacian operator in the bulk and for interpolation near interfaces.

$$\begin{bmatrix} \frac{\partial \Phi_0}{\partial x} \\ \frac{\partial \Phi_0}{\partial y} \\ \frac{\partial^2 \Phi_0}{\partial x^2} \\ \frac{\partial^2 \Phi_0}{\partial y^2} \\ \frac{\partial^2 \Phi_0}{\partial x \partial y} \end{bmatrix} = C \begin{bmatrix} \Phi_1 - \Phi_0 \\ \Phi_2 - \Phi_0 \\ \Phi_3 - \Phi_0 \\ \Phi_4 - \Phi_0 \\ \Phi_5 - \Phi_0 \end{bmatrix} \tag{7}$$

C is the 5 by 5 inverse of the left hand side of (6). Thus, the Laplacian equation could be written at the point Φ_0 as

$$\sum_{j=1}^{5} C_{3j}\Phi_j + \sum_{j=1}^{5} C_{4j}\Phi_j - \sum_{j=1}^{5} (C_{3j}+C_{4j})\Phi_0 = 0. \tag{8}$$

The entire matrix is then built up from this principle, implementing (2) for every point in a piecewise homogeneous region. Because the $\nabla\mu$ term of (2) is zero in such regions, the permeability of the material will not appear in any of these equations.

The remaining step necessary to properly model the problem is to impose the boundary conditions. Referring back to Figure 2, it is necessary to interpolate Φ at the boundary points B in terms of the potential values on one side of the boundary only. As the boundary is approached from a given region, this interpolation must be realized using potentials located in the same region. If the points lie on a line in 2-D this interpolation requires 6 points, 10 in 3-D. The 6 conditions come from the Taylor expansion of the sought after boundary potential in terms of 6 nearest neighbors (points 6-11).

$$\Phi_j = \Phi_B + \frac{\partial \Phi_0}{\partial x}\Delta x_j + \frac{\partial \Phi_B}{\partial y}\Delta y_j + \frac{1}{2}\frac{\partial^2 \Phi_B}{\partial x^2}(\Delta x_j)^2 + \frac{1}{2}\frac{\partial^2 \Phi_B}{\partial y^2}(\Delta y_j)^2 + \frac{1}{2}\frac{\partial^2 \Phi_B}{\partial x \partial y}\Delta x_j \Delta y_j + \mathcal{O}(\Delta^3) \tag{9}$$

Equation (5) is repeated for all 6 nearest neighbors; it is understood that all the derivatives are evaluated at the boundary point B, and that Δx_j, Δy_j refer, respectively, to the x and y differences from the point j to the boundary point B. The solution of this 6 by 5 matrix equation is very fast, and yields not only the desired Φ, $\partial\Phi/\partial x$, and $\partial\Phi/\partial y$, but the higher-order derivatives as well. Any Dirichlet or Neuman condition can be matched with these derivative values.

It should be mentioned in passing that when the points lie on a line collinear with the local normal as the points 12-14 do in Figure 2, the first-order derivative at location 12 with respect to the local normal (x direction) is computed from 2 Taylor expansions about the point 12; since

$$\Phi_{13} = \Phi_{12} + \frac{\partial \Phi_{12}}{\partial x}\Delta x + \frac{\partial^2 \Phi_{12}}{\partial x^2}\frac{\Delta x^2}{2!} + \ldots \tag{10}$$

and

$$\Phi_{14} = \Phi_{12} + \frac{\partial \Phi_{12}}{\partial x}2\Delta x + \frac{\partial^2 \Phi_{12}}{\partial x^2}\frac{4\Delta x^2}{2!} + \ldots \tag{11}$$

it follows that

$$\frac{\partial \Phi_{12}}{\partial x} = \frac{4\Phi_{13} - \Phi_{14} - 3\Phi_{12}}{2\Delta x}. \tag{12}$$

This conventional alternative for enforcing the boundary conditions will be employed by way of making a comparison in the results section.

MATRIX SOLUTION

Suppose there are a total of N unknown potential points Φ. Also consider that (2) is implemented at every one of these N points yielding N equations. Suppose that the boundary conditions, that tangential H and normal B be continuous, are imposed at P boundary points yielding an additional 2P constraints. The total number of equations is now 2P+N with only N unknowns. It is best to solve this non-square matrix in a least square sense using eigenvalues.

The resulting matrix for the N unknowns could be written as

$$A\vec{\Phi}=\vec{b} \tag{13}$$

where $\vec{\Phi}$ is the vector of unknown potentials, A contains all the geometry, and the right hand side b contains the source terms. Pre-multiplying by the transpose of A yields the positive definite matrix H in the equation

$$H\vec{\Phi} = A^t\vec{b} = \vec{z} \tag{14}$$

Although this new matrix H is more ill conditioned than the original matrix A, it is positive definite and can be treated by some valuable techniques [5]. In particular, one can use the eigenvalues λ and eigenvectors $\vec{q}$ directly to get an accurate solution. Because the eigenvectors of H are orthogonal, both sides of (14) can be multiplied by each of the eigenvectors to obtain the solution vector $\vec{\Phi}$ as a weighted sum of the eigenvectors. That is, assuming

$$\vec{\Phi}=\sum_{i=1}^{N}\alpha_i\vec{q}_i \tag{15}$$

where we express $\vec{\Phi}$ as a weighted sum of all eigenvectors $\vec{q}_i$, it then follows that

$$\alpha_i=\frac{\vec{q}_i\vec{z}}{\lambda_i}. \tag{16}$$

GRID REFINEMENT

Adding points to refine the grid is usually quite desirable when solution accuracy is suspect in a given region or where the field is varying considerably. Adding extra points would normally mean preprocessing from scratch to set all the bulk constitutive equations since the counting sequence on unknowns would be all wrong. Using the Taylor's expansion in (5) obviates the need to redo the preprocessing of the problem; one simply adds a number of additional equations for each of the additional points added to the grid. With this approach the designer has the liberty of literally placing the grid points anywhere. It is necessary to keep a table of each point's coordinates and material region. The program must in turn identify the 5 (9 for 3D) nearest neighbors still within its own region. Points could be placed on the boundary itself if desired to increase accuracy in these regions.

RESULTS

The motor of Figure 3 was analyzed in attempting to assess the accuracy of this method. The stator is doubled sided. Sandwiched in between is a permanent magnet rotor comprising the bulk of the air gap.

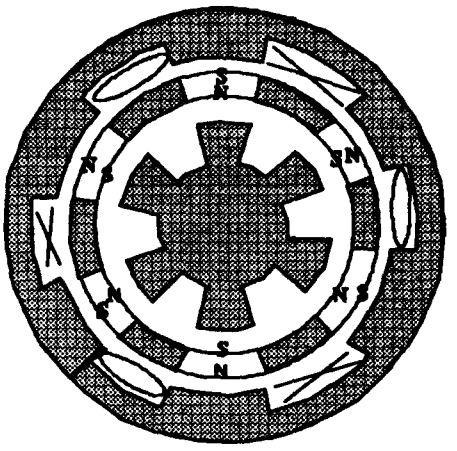

Figure 3. Double sided motor with permanent magnet shell rotor.

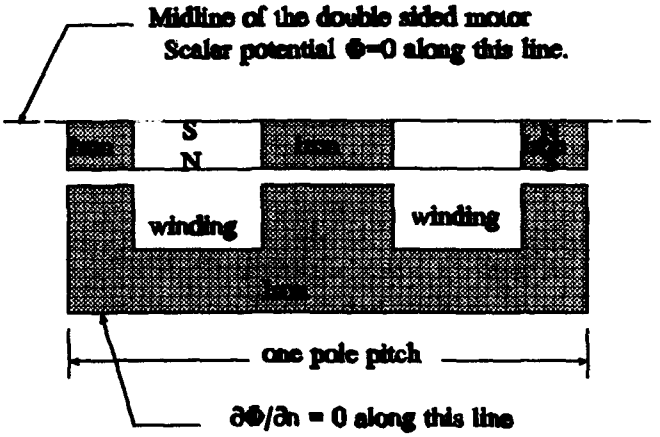

Figure 4. Section of the motor to be analyzed in a linear geometry.

Due to symmetry, only one pole pitch of the motor has been analyzed. The problem is divided down the center of a stator tooth and spans a complete pole pitch. Since no flux exits the lower portion of the stator, a Neuman condition $\frac{\partial\Phi}{\partial n}=0$ exists there. Also at the midline inside the shell rotor of this double sided motor, no tangential B field exists. Thus the potential Φ can be set to zero along this line as shown in Figure 4. A polar grid would necessarily be used for this inherently cylindrical problem if the radius is small. In practice, very little error was found in examining

one pole pitch in this quasi-linear grid and then multiplying by the number of such poles to get the total torque.

The problem is analyzed by two methods, first using a conventional reluctance grid as suggested in [6]; this approach is delineated "normal" in the figures. Here an equal grid distribution is employed and the spacing chosen to force the unknown potentials to have a spacing wherein some of the potentials naturally fell on the interfaces. Second, the boundary constituted by the iron - air interface is modeled using the method detailed above (except at corners where for convenience the reluctances were kept). The bulk equations were altered to be one sided as in (4) in close proximity to the teeth. Furthermore, the potential derivatives needed to insure continuity of field density B across the interface were modeled using the one sided derivative expressed in (12).

The x directed field was predicted in both cases along the air gap, midway between the stator teeth and rotor

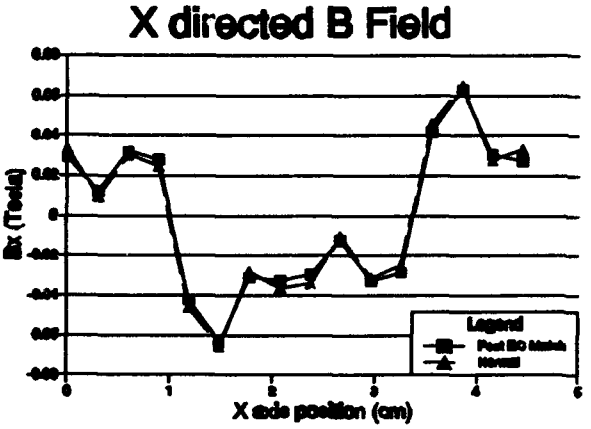

Figure 5 X directed B along the air gap.

magnets. The results are shown in Figure 5. The number of unknowns was 128. With the post boundary condition technique, an additional 20 equations were added to insure continuity of the normal component of the magnetic field density. The post boundary condition match has good agreement with the normal field approach.

The additional prediction of the y directed B fields is shown in Figure 6.

CONCLUSIONS

A method is presented for predicting magnetic fields using a uniform grid placed incognizant of the interfacial inhomogeneities. Boundary conditions are imposed after the bulk equations are in place and the non-square system is solved for the least square solution. The

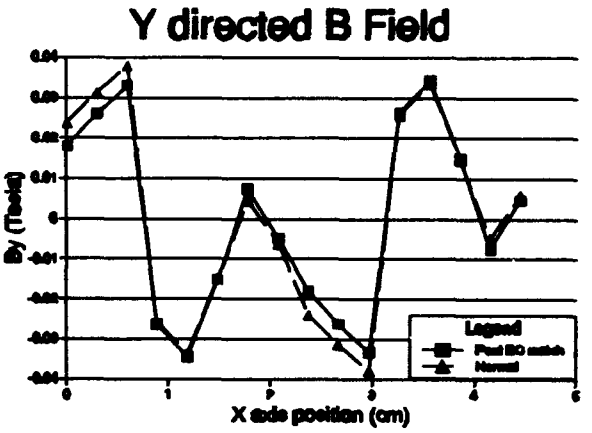

Figure 6 Y directed B field along the air gap.

primary advantage of the method is the flexibility afforded in the arbitrary placement of modeling points and in the improvement of accuracy by the ease of adding additional points. The fact that the resulting matrices are always non-square having more rows than columns does not appear to incur numerical inaccuracies for the problems studied. The author has found in parallel that the non-square matrix solution presents no problem for matrices sized at 3000 by 1000, indicating the method would be feasible for large problems.

ACKNOWLEDGMENT

The support of the Veterans Administration in this research is gratefully acknowledged.

REFERENCES

[1] S.R.H. Hoole, Computer-Aided Analysis and Design of Electromagnetic Devices, New York, Elsevier, 1989, pp. 73-82.

[2] R. W. Hornbeck, Numerical Methods, Prentice Hall, New Jersey, 1975, pp 269-289.

[3] P. Girdinio, P. Molfino, G. Molinari, L. Puglisi, and A. Viviani, "Finite difference discretization procedures with improved continuity of interpolation functions," IEEE Trans. Magn., Vol. Mag-19, No. 6, 1983, pp. 2558-2561.

[4] P. Girdinio, P. Molfino, G. Molinari, L. Puglisi, and A. Viviani, "Finite Difference and Infinite Element Grid Optimization by the Grid Iteration Method," IEEE Trans. Magn., Vol. Mag-19, No. 6, 1983, pp. 2543-2546.

[5] J.M. Varah, "On the numerical solution of ill conditioned linear systems with applications to ill posed problems," SIAM J. Numer. Analysis, Vol. 10, No. 2, pp. 257-267.

[6] R. Varga, Matrix Iterative Analysis, Prentice Hall, New Jersey, 1962, pp. 173-191.

A Case Study Comparing the Lossy Wave Equation to the Continuity Equation in Modeling Late-Time Fields Associated with Lightning*

Michael E. Baginski A. Scottedward Hodel

Abstract

An investigation is presented into lightning-related transient electric fields and conduction current densities due to the redistribution of charge by the return stroke (late-time effects). A qualitative comparison is made between the late-time vertical electrical field magnitudes predicted by two solutions via the continuity equation/Poisson's equation and the continuity equation in conjunction with the lossy wave equation. The differences between these results indicate that the magnetic energy density created by a lightning discharge generally provides relevant changes in the resulting electrical field waveforms as radial and vertical distances increase from the lightning discharge. That is, the accuracy of the conservative field assumption $\nabla \times E = 0$ decreases with the distance from the point of excitation to the point of observation of the electric field for the study conducted. This observation suggests the use of the lossy full wave equation, when computationally feasible, for the prediction of late-time electric field behavior. This study addresses trends in the general behavior of the two solutions over region $0 \leq r \leq 30$ km and $30 \leq z \leq 50$ km.

1 Introduction

The purpose of this research is to examine the necessity of using both Ampere's current law and Faraday's law on induction as opposed to using the quasi-static solution to describe the late-time field recovery of electromagnetic transients associated with lightning. This has been a major area of controversy for several decades [1], [2], [3] due to the fact that solutions based on quasi-static analysis are far simpler to solve numerically and to formulate than solutions based on the lossy wave equation. In the following, a brief overview of some of the previous research and the true nature of the problem to be discussed is presented.

Late-time electromagnetic fields stem from the non-propagating portion of the electromagnetic transient from lighting and are therefore associated with the electrostatic and magnetostatic energy created when lightning occurs. Since a multitude of approximations are required in the modeling of the late-time effects of the lightning event, the digital simulations presented in the following sections employed commonly accepted charge distributions conductivity profiles, and general atmospheric parameters [4], [5]. It is hoped that this research will be of value not only to atmospheric scientists but also those studying EMP, HEMP, corona discharges, etc.

In this work, a finite element code was used to compute the vertical electric fields in the middle atmosphere via (1) the continuity equation

$$\nabla \cdot J + \frac{\partial \rho}{\partial t} = 0$$

and Poisson's equation

$$\nabla^2 \phi = -\frac{\rho}{\epsilon_0},$$

and (2) the complete set of Maxwell's equations

$$\begin{aligned} \nabla \times E &= -\mu_0 \frac{\partial H}{\partial t} \\ \nabla \times H &= \sigma E + \epsilon_0 \frac{\partial E}{\partial t} + \text{additional sources of charge movement.} \end{aligned}$$

Both sets of equations used identical atmospheric parameters. The respective vertical electric field waveforms were then compared with waveforms over a wide range of values of radial distance r and altitude z. A detailed analysis of the waveforms generated by the two different numerical solutions was performed

*The authors are with the Auburn University Department of Electrical Engineering, 200 Broun Hall, Auburn AL 36849

by comparing the mean squared error difference between the solutions. The results showed that there is a radial and vertical position where the electric field signatures begin to deviate significantly from one another. It is the view of the authors that this would be the logical region that would mandate the use of the complete set of the Maxwell equations. It should be emphasised that the results presented herein are only for a specific set of atmospheric conditions and, thus, may show sensitivity to several atmospheric parameters.

2 Historical Perspective

Since the 1950's several electrical models describing the interaction of thunderstorms with the atmosphere have been published. Holser and Saxon [6] have assumed concentrated charges in a dipole configuration with spatially varying conductivities to obtain temporally invariant field patterns in the lower atmosphere and ionosphere. The lightning return stroke, however, generates transients in the electric field pattern known as "field changes" [7]. Early workers attributed this temporal recovery to recharging within the thundercloud. Tamura [8] is credited as the first to note that the surrounding atmosphere is also involved. He defined solutions based on the conservative field assumption (i.e., $\nabla \times E = 0$) that depend on the conductivity at the point of observation. Kasmir [9] constructed the first dynamic model of the thundercloud system using resistors, a capacitor, and a spark gap. His model connected a current generator, a capacitor, and a resistor in parallel to model the cloud ionospheric connections with the path to earth replaced by a resistor. More dynamic models began to follow. Anderson and Freier [10] incorporated dynamic changes in the dipole structure with spatially varying conductivities. However, they only include the quasi-static relaxation in their model instead of solving the total set of Maxwell's equations. Additional solutions were developed based on the "monopole" model of Wilson [11], Illingworth [12], Park and Dejnakarintra [13], Greifinger and Greifinger [14], Holsworth and Chiu [5], Baginski *et al* [15], and Driscoll *et al* [16]. The transient lightning event was investigated recently by Hoole and Hoole [17] using a finite element code. Discussion on guided waves in lightning plasma channels is presented in [18].

3 Thunderstorm Modeling

3.1 Charging Mechanisms

The most difficult phenomenon to explain in thunderstorm research has been the process involved in cloud electrification. The difficulty is twofold: Firstly, there exist a large number of possible mechanisms responsible for charge separation and current generation; further, it is usually impossible to isolate such mechanisms and test each for its relative effect. Regardless of the mechanisms, what is known is that a thunderstorm is sustained by a charge separation which can be approximated by net positive and negative charge centers. The height of the charge centers is somewhat affected by seasonal changes and the geographic location. Typical heights of 10 km for the upper charge center and 6 km for the lower charge center are widely found in the literature and have been selected for this research [19]

The magnitudes and profiles of the charge centers and currents vary significantly from storm to storm. Kasmir [9], for instance, has measured values ranging from 20 C up to 1000 C for thundercloud charges and cloud electrification currents from less than 0.1 A to 10 A. Lightning return stroke currents are reported to have an even larger range of values [7]. The existence of such large variations complicates selection of the currents and the charge deposition profile. After a review of the relevant literature [20], [14], a choice of the forcing current and profile of charge deposition was made. The selection was based upon widely used current and charge profiles. The charge perturbation used was developed based on Sunde's [4], [20] lightning return stroke current model.

Sunde's [20] lightning return stroke model is selected for this research primarily because of its extensive commercial and military use in work requiring an analytic formulation of the lightning return stroke current. This model was developed based on the statistics of a very large number of measurements during lightning events. Sunde's model is relatively simple compared to some [7], but includes the fundamental attributes necessary to predict "average" electromagnetic field behavior [20]. The charge generation (in units of A or C/s) may be expressed in terms of this lightning return stroke current temporally as follows:

$$G_s = \frac{dQ(t)}{dt} = i(t) = I_0 \left(e^{-at} - e^{-bt}\right) \qquad (3.1)$$

where $i(t)$ = the lightning return stroke current from

Sunde's modified model, $a = 10^4\ s^{-1}$, $b = 0.1 \times 10^3\ s^{-1}$, and I_0 is proportional to the amount of charge displaced during the return stroke.

It is well known that the deposition of charge from the return stroke current is primarily responsible for the charge perturbation [21]. The deposition rate of charge due to the the lightning return stroke current is proportional to the time derivative of the charge perturbation [19]. Therefore, the total charge deposited at time t may be expressed as the integral of the lightning return stroke current in time, given by

$$Q(t) = \int i(t)dt \tag{3.2}$$

where $i(t)$ is the lightning return stroke current and $Q(t)$ is the total displaced charge of the return stroke.

Consider equation (3.1). The term e^{-bt} describes the rise time of the charge generation inducing the perturbation, i.e., how rapidly the maximum return stroke current, but not charged deposited, is attained. Since the amount of charge exchanged during a return stroke is related to its time integration, omission of the term e^{-bt} causes no appreciable change (for time greater than 5×10^{-6} s) in the amount of charge displaced, and therefore, no appreciable change in the simulated electrodynamic response. The spatial and temporal structure of the deposited charge G_s is given by a modified spherical Gaussian profile:

$$G_s = (2\pi\lambda)^{-1.5}\exp\left(-\frac{r^2 + (z-z')^2}{2\lambda}\right) \times \left(\frac{e^{-t/\tau_1}}{\tau_1}\right) \tag{3.3}$$

where

τ_1 = 10^{-3} s is the decay time of the force charge event

λ = $4 \times 10^6\ m^2$ is the effective variance

z' = the altitude of the charge perturbation.

The spatial distribution of the charge perturbation does not noticeably affect electric field signatures far from its interior [4]. This condition exists for our model (electrical fields of interest in the present study are at least 20 km from the charge perturbation) which allows a certain degree of freedom in the specification of the distribution. Also, since virtually no published data is available describing the spatial structure of the deposition of the charge from the lightning return stroke current [22], the selection is even more arbitrary. Further, the modified Gaussian distribution is used in the modeling of many man-made and naturally occurring forced charge events [4] which justifies our choice for this model.

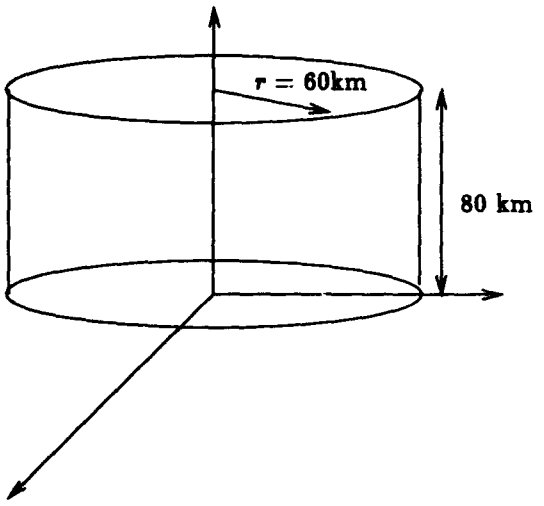

Figure 1: Region of simulation

Geometry of the Region: Before describing the geometry, consider again the phenomenon of interest: charge perturbations, located at altitudes no greater than approximately 10 km, induce electric fields throughout the atmosphere, but only those fields induced within the middle atmosphere are to be simulated. Thus,

1. If not obviously constrained, the geometrical limits of the model will approximate the entire atmosphere's electrical effect on the regions where the simulations take place.

2. The boundary conditions of the region will be electrically equivalent to those of the atmosphere.

The region selected (Figure 1) is contained within a perfectly conducting right circular cylinder with a radius of 60 km and height of 80 km. A discussion of how each of the boundaries was arrived at follows:

Lower Plate: The earth's surface is electrically modeled as a perfect conductor. This assumption is based on the very large difference that exists between the

earth's conductivity and adjacent atmosphere's conductivity. Typical values of .001 to 0.01 mhos/m [23] are given for the earth's conductivity, while 10^{-13} to 10^{-14} mhos/m is the usual range of the adjacent atmosphere's conductivity. This difference of more than 11 orders of magnitude makes the earth appear (electrically) as a perfect conductor.

Upper Plate: The selection of 80 km for the height of the upper boundary was a necessary consequence since the atmospheric conductivity structure is complicated by the Hall and Pederson components above an altitude of approximately 70 km [24]. The tensor conductivity components result when the mean free path and velocities of the charge carriers are sufficient to allow their trajectories to be altered by the effect of the earth's magnetic field [25]. In the present model tensor quantities have been excluded to keep the algorithm simple without adversely affecting numerical accuracy. Further, in past studies [3], [2] an altitude limit is set in the vicinity of 70 km. Dejnakarintra and Park [2] note that this level is an appropriate choice since the conductivity becomes anisotropic at this altitude.

For this study, the 80 km altitude was selected based on the following considerations:

1. The relative magnitude of the Hall and Pederson tensor conductivity components is approximately proportional to the additional distance in altitude (beyond 70 km) considered, i.e., the difference in components is proportional to $(z-70)$. The maximum value of either of these components with respect to the parallel σ conductivity's magnitude (for the range of altitudes considered) is less than 10 percent [24].

2. The middle and upper atmospheric electric fields resulting from lightning (with the exception of the propagating component) are approximately vertically oriented [24], i.e., the horizontal component is negligible.

3. The off-diagonal tensor components of the high-altitude conductivity only interact with electric fields that are not aligned with the earth's magnetic field [24]. Since the earth's magnetic field, with the exception of the equatorial regions, is primarily vertically aligned [21], the influence of both the Pederson and Hall components on the lightning-induced vertical electric fields will be, to first order, negligible. The inclusion of these components would tend to prolong the simulated atmospheric transient response at altitudes of 70 km and above. Since this investigation focuses on altitudes less 50 km the impact of these terms on our results would be insignificant.

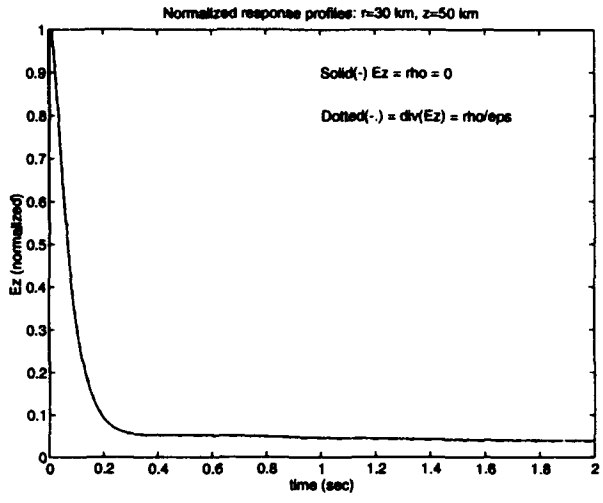

Figure 2: Effect of 80 km upper plate in vertical E-field computation

An obvious concern is the influence this 80 km altitude limit may have on the simulations. A previous study [3] used simulations based on the full wave equation to determine the maximum error in the vertical electric field in the region of interest in the present study. The results showed that the maximum electric field error induced by the 80 km ceiling occurs at $z = 50$ km and produced a relative error of less than 1%. To investigate the maximum possible error in the electric field due to this assumption (assuming an electrically passive atmosphere), two further sets of simulations were conducted with the 80 km upper plate electrically described by: 1) The vertical electric field and charge density are set to zero ($E_z = \rho = 0$). 2) The divergence of the electric field is set to the value of the charge density divided by the permittivity of free space ($\nabla \cdot E = \rho/\epsilon$). These simulations indicate a maximum error at radial distance $r = 30$ km and altitude $z = 50$ km. A representative plot of respective vertical waveforms is shown in Figure 2. Use of the conservative field assumption reduces the associated error even further. The change in the two boundary conditions provided above pro-

vides a worst-case error analysis. In all simulations, comparison of results showed little if any difference for the time frames of interest (0-2 s).

The probable reason for this behavior is that in general, for lightning-induced transients, the electric properties of the atmosphere below the point of observation of the field rather than above it, govern the transient's response [26]. This may be explained by simply considering the fact that, in general, the conductivity rapidly increases with altitude (i.e. resistivity decreasing), and therefore its influence (restrictive effect) on the total global charge movement decreases. Hence, it seems reasonable to assume the middle atmosphere's simulated response to low-altitude charge perturbations is governed by the adjacent and lower altitude conductivity values.

Outer Cylindrical Surface: The lateral boundary had no distance constraint and could have been extended indefinitely. However, there exists a tradeoff between resolution (both temporal and spatial), and computational resources: reduction in the model dimensions yields improved accuracy in numerical solution of the differential equations. Therefore, the errors resulting from the adoption of finite boundaries for the model must be weighed against those resulting from degrading the numerical resolution of the code by involving too large a volume.

The simulations were found to be insensitive to increases in the radial limit beyond 50 km. No visible difference could be detected in the response using either the 50 km or 60 km radial boundaries when plotted together; see Figure 3. Therefore, selecting the 60 km radial limit is a measure to provide additional confidence in the simulations.

Axis of Symmetry: Since $r = 0$ defines an axis of symmetry and since there are no discontinuities in the charge distribution, the derivatives of the vertical electric field ($\partial E_z/\partial r$) with respect to radial distance reduces to zero on this axis.

The differential forms of the four boundary conditions are summarised as follows:

1. At the z-axis, $\partial E_z/\partial r = 0$
2. at the upper and lower boundaries $E_r = 0$
3. at the outer radial boundary $E_z = 0$

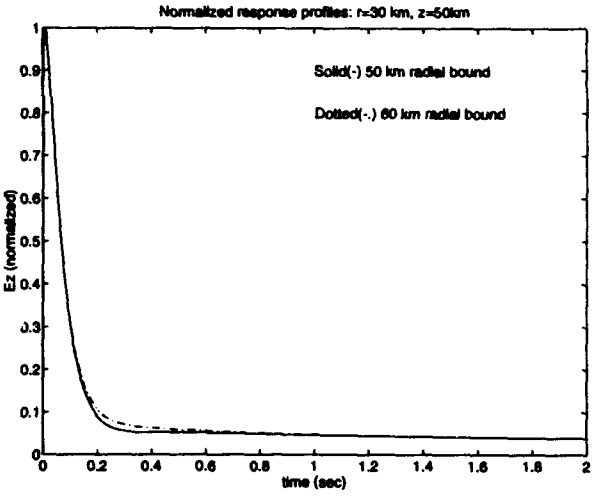

Figure 3: Effects of changes in radial limits on E-field computations.

Maxwell's Equations: To those familiar with classical electromagnetism, the analysis of the post-stroke atmospheric response may seem rather simple at first. A charge imbalance induced in a conducting region would be expected to decay exponentially with time at a rate determined by the local relaxation time of the region [25]. The corresponding electric fields, being proportional to the overall charge distribution, should decay in a like manner. When electric field measurements obtained from parachute-borne payloads [27] are considered, however, a significant deviation from the exponential decay is at times observed. In some cases a gradual peaking is observed hundreds of ms after the return stroke has ceased. This behavior suggests, at least for some circumstances, that a more complicated description is required and that a careful analysis of the governing equations should be undertaken.

Beginning with Maxwell's equations, a single equation is derived where the electric field is dependent on the charge density only as follows:

$$\nabla \times E = -\mu \frac{\partial H}{\partial t} \tag{3.4}$$

$$\nabla \times H = J + \frac{\partial D}{\partial t} + \text{additional sources of charge movement} \tag{3.5}$$

$$\nabla \cdot D = \rho \tag{3.6}$$

$$\nabla \cdot H = 0 \tag{3.7}$$

$$J = \sigma E \quad (3.8)$$

$$D = \epsilon E \quad (3.9)$$

By taking the divergence of the $\nabla \times H$ we derive the continuity equation that will be used in the analysis of both systems of simulations:

$$0 = \sigma\rho/\epsilon + \nabla\sigma \cdot E + \frac{\partial \rho}{\partial t} + G_s \quad (3.10)$$

where $G_s = \nabla \cdot J_f$ and J_f is the source charge generator causing the perturbation.

The lossy wave equation is developed using the above equations:

$$\nabla \times \nabla \times E = -\mu\sigma\frac{\partial}{\partial t} - \mu\epsilon\frac{\partial^2 E}{\partial t^2} \quad (3.11)$$

$$\nabla\rho/\epsilon = \nabla^2 E - \mu\left(\sigma\frac{\partial E}{\partial t} + \frac{\partial J_f}{\partial t}\right) - \mu\epsilon\frac{\partial^2 E}{\partial t^2} \quad (3.12)$$

The resulting second order partial differential equation is analytically solvable for only the simplest cases. The types of solutions required for altitude-dependent conductivities are not obvious. If one wishes to pursue this problem further, assumptions must be made or numerical methods must be applied. The most common assumption used in the past (e.g., [12], [1]) is to define the electric field as the gradient of the electric potential ($E = -\nabla\phi$), the conservative field equation. The mathematical consequence of this, if strictly enforced, is to constrain the electric field to decay exponentially in time. This can be shown as follows: $E = -\nabla\phi$ yields the vector identity

$$\nabla \times E = \nabla \times (-\nabla\phi) = 0. \quad (3.13)$$

Equation (3.4) and equation (3.13) imply that

$$-\mu\frac{\partial H}{\partial t} = \nabla \times (-\nabla\phi) = 0$$

i.e., H is time invariant. Since the H field in this case is time invariant, the E field is necessarily time-invariant as well for the study conducted. The general solution for the electric field is given by

$$E(r,z,t) = E_0(r,z)\exp(-t/\tau(r,z)) + E_1(r,z) \quad (3.14)$$

where $\tau(r,z) = \epsilon/\sigma(r,z)$.

This type of solution has a definite range of validity. However, for the general case, a computer solution of the above equation, not limited by the conservative field assumption, would provide more information about the true time dependent shape of the electric field. The final equation required for both simulations is the continuity equation. This is derived by taking the divergence of equation (3.14).

Critical comments on the Full Wave Equation

There are several questions that need to be addressed prior to continuing this discussion in regard to the use of the lossy full wave equation. The first is the usual spatial/temporal requirement that generally must not be violated and depends on the number of dimensions. (That is,

$$c\Delta t \leq h/\sqrt{n},$$

where h is the spatial step and n is the number of dimensions). However one can use the theory put forth by Courant and Hilbert [28] that shows that the above inequality can be modified for certain circumstances, especially when the region analysed is lossy (i.e., σ is non-zero). (Kunz and Luebers [29] have presented a similar theory for the time-domain finite difference method.) In the lossy full wave equation used in the research, the grid size and time step were reduced until no appreciable difference was observed in the results and thereby confirm their assertions.

A second point to be made is that because of the extremely high amount of loss (very low Q) of the region, the propagation delay caused by the $\mu\epsilon\partial^2 E/\partial t^2$ term is of negligible significance compared with the loss associated with either $\mu\sigma\partial E/\partial t$ (lossy full wave equation) or the continuity equation. When several preliminary computer simulations were conducted, the actual number of triangles required to achieve accurate results was found to be 520 with a final triangulation being proportional to $r^{-1/2}$ where r is the distance from the charge center. A simulation was also performed with 1000 triangles; no significant deviation was observed from results with 520 triangles. (Quadratic elements were used in all simulations in this study; the final triangulation is shown in Figure 4.) The time step was also made proportional to $t^{-0.55}$. These two deviations from the traditional stability criteria were a cause of concern in earlier related research [15]. For comparison, simulations were also performed using a uniform mesh with uniform grid spacing in space and a constant time step; no appreciable difference was observed between the

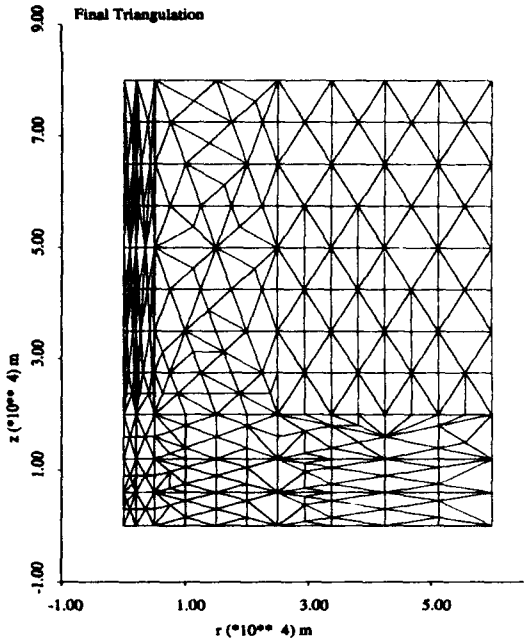

Figure 4: Triangulation used in simulations

computed solutions. The obvious benefit of the use of non-uniform mesh and varoab;e time steps is that there are enormous savings in CPU time and in-core memory. In our experiments, a single simulation involved 12-15 hours of computation on a SPARC 10 computer with the method used and probably would have required at least an order of magnitude more time if the time step and grid spacing were based on the stability criteria stated above for the time step derived from the rise time of the charge perturbation waveform.

3.2 Summary of the two equations used

The two sets of equations that are used in the comparative simulations are the following:

SET 1

$$0 = \sigma\rho/\epsilon + \nabla\sigma \cdot E + \frac{\partial \rho}{\partial t} + G_s \quad (3.15)$$

$$0 = \nabla^2\phi + \rho/\epsilon \quad (3.16)$$

SET 2

$$\nabla\rho/\epsilon = \nabla^2 E - \mu\left(\epsilon\frac{\partial E}{\partial t} + \frac{\partial J_f}{\partial t}\right) - \mu\epsilon\frac{\partial^2 E}{\partial t^2} \quad (3.17)$$

$$0 = \sigma\rho/\epsilon + \nabla\sigma \cdot E + \frac{\partial \rho}{\partial t} + G_s \quad (3.18)$$

where $G_s = \nabla \cdot J_f$.

4 Numerical Results

As stated earlier, the intent of this research was to investigate, via a finite element code based on a solution of the differential equations [30], [31] the necessity of solving the lossy full wave equation (3 equations) versus the much less computer intensive conservative field equations for charge perturbations in the middle atmosphere. The method used will now be presented. The comparison was based on the use of the mean squared error difference between the two simulations to identify the difference versus position and time. The grid used was spaced radially at points of $r = 0, 5, 10, 15, 20, 25$, and 30 km and at altitudes of $z = 30, 35, 40, 45$,and 50 km.

Let $e_\infty(r, z, t)$ denote the magnitude of the electric field at radial distance r, altitude z, and time t, under the assumption that Faraday's law of induction is omitted; i.e., when using only the continuity equation (3.15) and Poisson's equation (3.16). Similarly, let $e_c(r, z, t)$ denote the electric field when using the full wave equation (3.17) in tandem with the continuity equation (3.18). The PROTRAN program [30] was used to compute e_∞ and e_c over a range of radial distances r and altitudes z for several seconds. A sample plot comparing the computed electric fields at radial distance 20 km are shown in Figures 5–9. (In Figures 5–9 the solid line denotes the quasi-static simulation (e_∞) and the broken line denotes the solution to the lossy full wave equation (e_c).)

In order to determine quantitatively the effects of the magnetic energy density on late-time electric-field magnitude, an error signal

$$\gamma(r, z, t) = e_\infty(r, z, t) - e_c(r, z, t)$$

was computed and an RMS error was normalized against the energy in $e_\infty(r, z, t)$ by computing

$$w(r, z, t) = \left(\frac{|\gamma(r, z, t)|^2\, dt}{|e_\infty(r, z, t)|^2\, dt}\right)^{1/2}. \quad (4.1)$$

Time-varying plots of $w(r, z, t)$ vs altitude and time are shown for varying radial distances r in figures Figure 10–Figure 16.

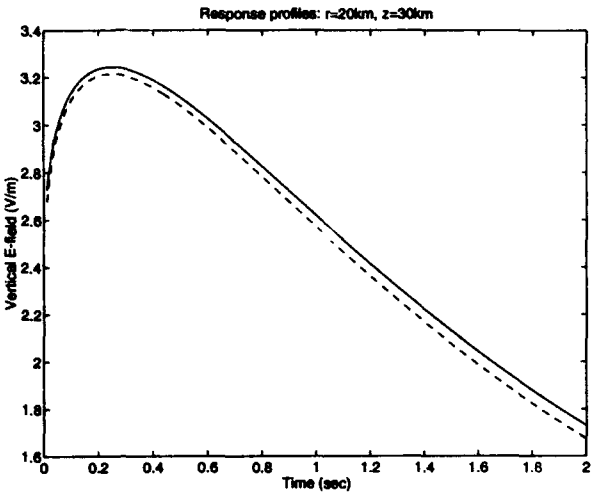

Figure 5: Electric field transient (altitude 30km)

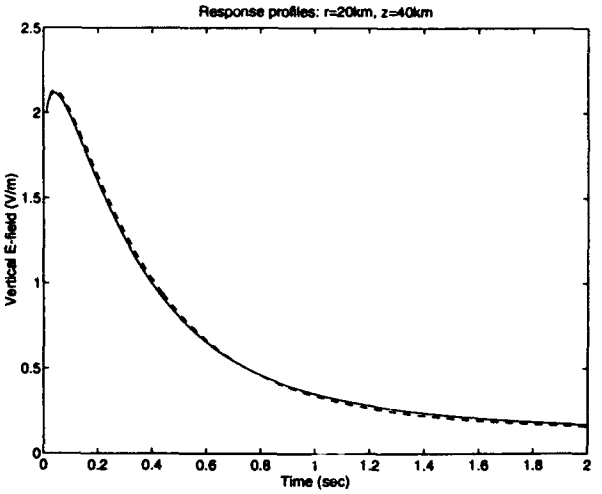

Figure 7: Electric field transient (altitude 40km)

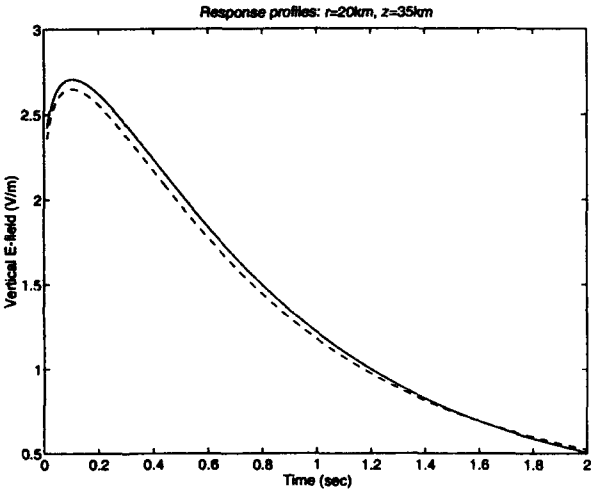

Figure 6: Electric field transient (altitude 35km)

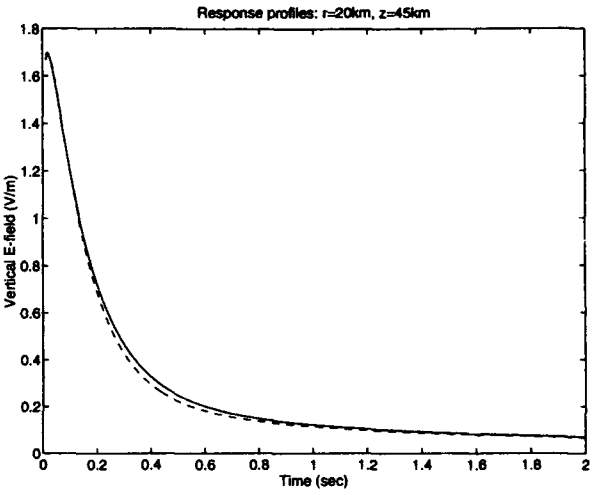

Figure 8: Electric field transient (altitude 45km)

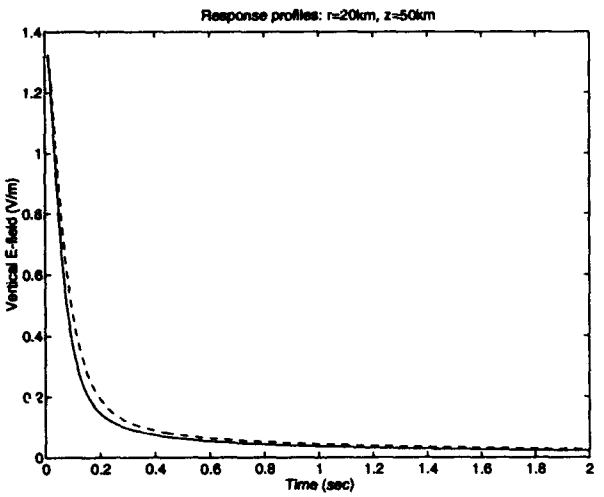

Figure 9: Electric field transient (altitude 50km)

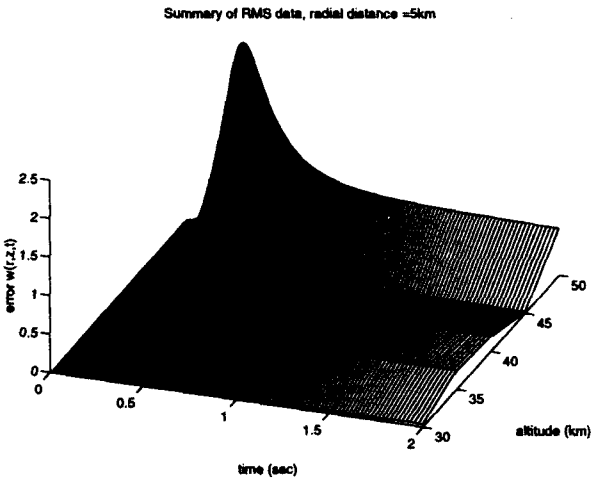

Figure 11: Error at radial distance 5km

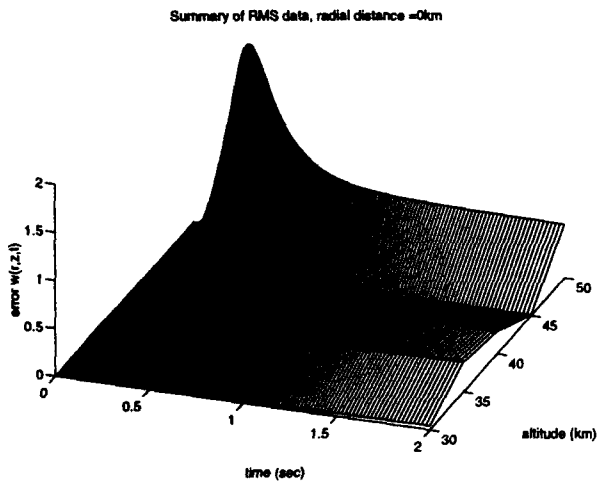

Figure 10: Error at radial distance 0km

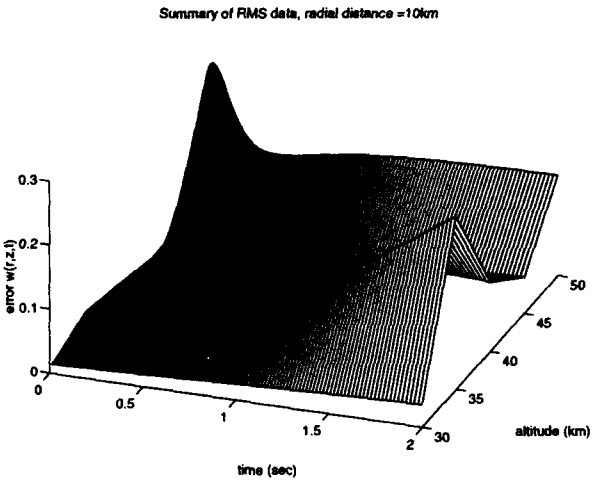

Figure 12: Error at radial distance 10km

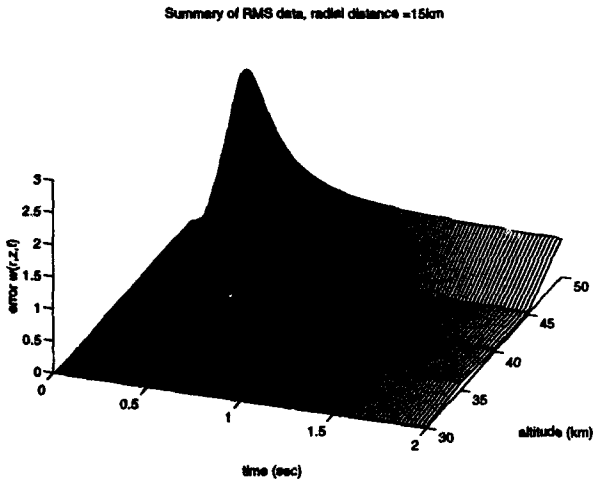

Figure 13: Error at radial distance 15km

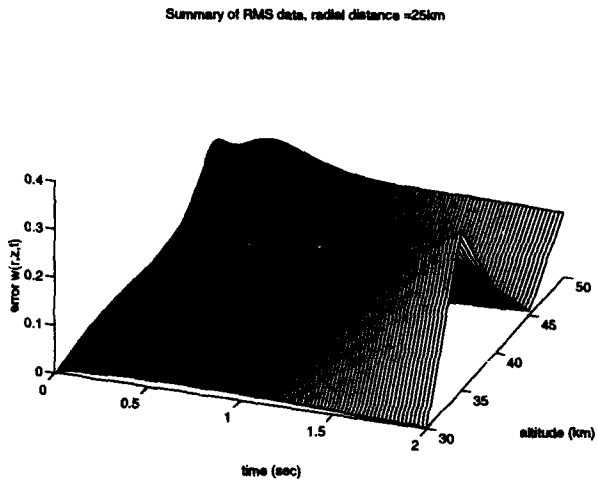

Figure 15: Error at radial distance 25km

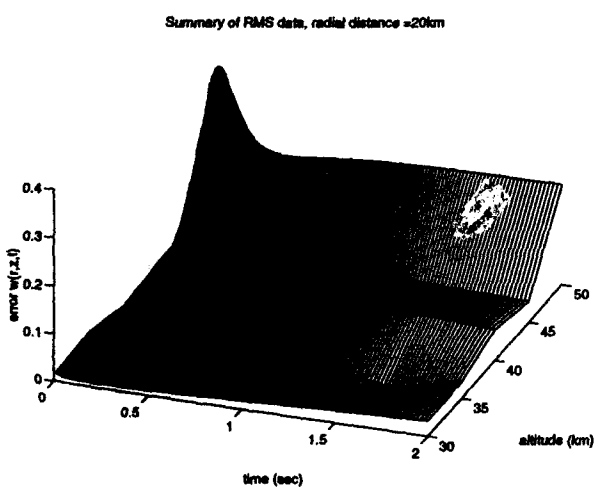

Figure 14: Error at radial distance 20km

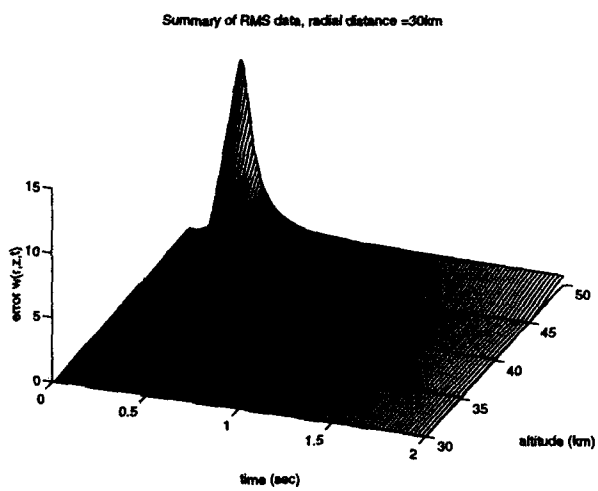

Figure 16: Error at radial distance 30km

Error comparisons were also made using de_∞/dt and de_c/dt; results were consistent with those of the electric field waveforms themselves. In each of these cases, a clear distinction can be seen between predicted electric field values at altitude 35 km and at altitudes in excess of 40km. These results indicate that the magnetic energy density plays an increasingly important role in defining late-time electric field behavior as distance is increased from the source to the point of observation.

5 Conclusions

Before examining the results in detail, it is important to keep in mind that the focus of this study is to characterise two standardly used sets of equations that describe the late-time lightning induced electric fields. Because the number of atmospheric parameters that effect the electrical phenomenology is large (e.g., ϵ, σ, scale height, cloud conductivity), this study serves as a precursor for future endeavors that can investigate the electric fields' sensitivity to all constitutive parameters as well as the effects that variable boundary conditions will have.

A comparison was made between the values of late-time the vertical electrical field magnitude predicted by (1) the continuity equation and Poisson's equation and by (2) the continuity equation in conjunction with the lossy wave equation, respectively. The comparison clearly identifies trends that suggest that as distance (either radial or horizontal) from the source of the charge perturbation is increased, the magnetic energy density significantly influences the vertical electric field signatures. The data also indicates that, under the conditions of this case study, at an altitude of approximately $z = 35$ km the effects of the magnetic energy density upon the vertical electric field are more apparent than at surrounding altitudes. However, further intensive studies are required to assert that these qualitative schema will be observed in the general case over arbitrary values of conductivity and charge perturbation altitudes.

Past studies have used various criteria to select either the conservative field assumption or the full wave equation for solving the problem of interest. For example, Dejnakarintra and Park [2] compare the conductivity σ to the susceptivity $j\omega\epsilon_0$ in order to decide which assumptions to use. Nisbet [1] implicitly advocates the use of a conservative field assumption since his model uses resistive and capacitive elements but not inductive elements. At present, the applicability of the conservative field assumption for late-time electric field recoveries resulting from lightning remains somewhat controversial.

The specific region ($0 < r < 30$ km, $30 < z < 50$ km) used in the investigation was selected somewhat arbitrarily based on two major factors. It was found that simulations below this altitude and within the same approximate radius have been investigated using several previous models (Nisbet [1], Dejnakarintra and Park [2], Greifinger and Greifinger [14] among others) and found to be consistent with the results of the current study, hence, of little interest. The transient fields associated with the charge deposited from lightning above 50 km have been investigated previously as well by Baginski *et al* [15] and Dejnakarintra and Park [2], and require a solution to the lossy full wave equation due to speed of light effects as well as the dielectric relaxation at the point of observation.

The investigation demonstrated that: 1) If the widely used conservative field assumption ($\nabla \times E = 0$) is rigorously enforced (both of Maxwell's curl equations solved simultaneously) then the electric field may only exhibit exponential decay that is generally in error. 2) When the two solutions of the late-time transient event (one using the conservative field assumption and omitting Faraday's Law of induction, the other solving the complete lossy wave equation) are compared, there is a measurable error in the behavior of the field waveforms between the altitudes of 30-50 km and radial distances of 0 - 30 km (equation (4.1)).

Cursory examination of the error diagrams (Figures 10–16) reveals that a large error occurs at approximately 0.2 s and at 50 km altitude. The error appears to decrease somewhat at altitudes $z = 20$ km and $z = 25$ km from the source, but increases significantly at $z = 30$ km. This error is most likely due to an "inductive surge" caused by the effects of the magnetic field being taken into account in the lossy full wave equation. At radial distance $r = 10$ km (see Figure 12), the error between the two models is especially pronounced and growing. The most likely cause of this effect is the error due to the interaction between the "inductive behavior" and the atmospheric time constant at the point of observation.

Acknowledgement The authors wish to thank Marcus Lankford for his assistance in preparation of the simulations in this study. The authors also wish to express their thanks to the reviewers for their many

helpful suggestions and improvements to the paper.

References

[1] John S. Nisbet. A dynamic model of thundercloud electric fields. *J. Atmos. Sciences*, 40:2855–2873, 1983.

[2] M. Dejnakarintra and C. G. Park. Lightning-induced electric fields in the ionosphere. *Journal of Geophysical Research*, 79(13):1903–1909, 1974.

[3] Michael E. Baginski. *Finite Element Simulation of the Atmosphere's Electromagnetic Response to Charge Perturbations Associated with Lightning.* PhD thesis, The Pennsylvania State University, 1987.

[4] C. E. Baum. Simulation of electromagnetic aspects of lightning. In *Proceedings of Lightning Technology, NASA Conference*, April 1980.

[5] R. H. Holsworth and Chiu Y. T. Chui. Spherics in the stratosphere. In *CRC Handbook of Atmospherics*, volume 1. CRC Press, Boca Raton, Florida, 1982.

[6] R E. Holzer and D. S. Saxon. Distribution of electrical conducting currents in the vicinity of thunderstorms. *Journal of Geophysical Research*, 57(207), 1952.

[7] M. A. Uman. *Lightning.* McGraw-Hill, New York, 1969.

[8] Y. A. Tamura. An analysis of the electric field after lightning discharges. *Geophys. Res. Paper*, 42:190–200, 1955.

[9] H. Kasmir. The thunderstorm as a generator in the global electric circuit. *Z. Geophys.*, 25:33, 1959.

[10] F. J. Anderson and G. D. Freier. Interaction of a thunderstorm with a conducting atmosphere. *J. Geophys. Res.,*, 74:5390, 1969.

[11] C. T. R. Wilson. Some thundercloud problems. *J. Franklin Inst.,*, 208, 1916.

[12] A. J. Illingworth. Electric field recovery after lightning as a response of a conducting atmosphere to a field change. *Quart. J. Roy. Meterorol. Soc.*, 98:604, 1972.

[13] C. G. Park and M. Dejnakarintra. Penetration of thundercloud electric fields into the ionosphere and magnetosphere 1. middle and subauroral latitudes. *Journal of Geophysical Research*, 78:6623–6633, 1973.

[14] C. Greifinger and P. J. Greifinger. Electric fields in the atmosphere. *Journal of Geophysical Research*, 81:2237–2247, 1976.

[15] M. E. Baginski, L. C. Hale, and J. J. Olivero. Lightning related fields in the ionosphere. *Geophysical Research Letters*, 15(8):764–767, August 1988.

[16] Keven T. Driscoll, Richard J. Blakeslee, and Michael E. Baginski. A modeling study of the time-averaged electric currents in the vicinity of isolated thunderstorms. *Journal of Geophysical Research*, 97(D11):11,535–11,551, July 20 1992.

[17] P. Ratnamahilan P. Hoole and S. Ratnajeevan H. Hoole. Finite element computation of magnetic fields from lightning return strokes. In Z. J. Cendes, editor, *Computational Electromagnetics*, pages 229–237. North Holland, July 1986.

[18] P. Ratnamahilan P. Hoole and S. Ratnajeevan H. Hoole. Guided waves along an unmagnetised lightning plasma channel. *IEEE Trans. Magn.*, MAG-24(8):3165–3167, November 1988.

[19] H. Israel. *Atmospheric Electricity*, volume two. Israel Program for Scientific Translations, Jerusalem, 1973.

[20] E. D. Sunde. *Earth Conduction Effects in Transmission Systems.* Dover, New York, 1968.

[21] J. A. Chalmers. *Atmospheric Electricity 2nd edition.,*. Pergamon New York, 1967.

[22] A. J. Illingworth. Charge separation in thunderstorms: small scale processes. *Journal of Geophysical Research*, 90:6026, 1985.

[23] H. Volland. *Quasi-Electrostatic Fields within the Atmosphere.* CRC Press, Boca Raton, Florida, 65, 1982.

[24] H. Volland. *Atmospheric Electrodynamics,Chemistry in Space.* Springer-Verlag, Berlin, Germany, 1984.

[25] J. A. Stratton. *Electromagnetic Theory.* McGraw Hill, New York, 1941.

[26] R. H. Golde. *Lightning, Volume I.* Academic Press, 1977.

[27] L. C. Hale. Middle atmosphere electrical structure, dynamics, and coupling,. *Adv. Space Res.*,, 4:175–186, 1984.

[28] R. Courant and D. Hilbert. *Methods of Mathematical Physics.* Interscience, New York, 1962.

[29] Karl S. Kuns and Raymond J. Luebbers. *The Finite Difference Time Domain Method for Electromagnetics.* CRC, 1993.

[30] Granville Sewell. *Analysis of a Finite Element Method: PDE/PROTRAN.* Springer-Verlag, 1985.

[31] Granville Sewell. *The Numerical Solution of Ordinary and Partial Differential Equations.* Academic Press, New York, 1988.

APPLICATION OF BEM FOR CALCULATING THE PARAMETERS OF CABLES AND TRANSMISSION LINES

Zhou Pei-bai Zhong Hon-yu

Dept.of Electrical Engineering
Xi'an Jiaotong University
Xi'an, Shaanxi, 710048
China

ABSTRACT. The capacitances of three phases cable and the characteristic impedance of coaxal transmission line with complicated shape of the cross sections are evaluated by using boundary element method. The calculated results obtained by the proposed method are coincident well with the results given by the literatures [2-9].

1 INTRODUCTION

In engineering practice, the capacitances of multiphases cable are calculated approximately by using curves and tables such as given in reference [3]. The numerical methods are rarely used to calculate the characteristic impedance of the coaxal transmission lines due to the accurate result of the flux density is not easy to obtain and the corner effect can not be dealt with well. Hence many authors intended to find a simple and accurate method to obtain the approximate analytical formulae for calculating characteristic impedance of coaxal transmission lines with complicated cross section.

By comparison with finite difference and finite element methods, the boundary element method is easy to obtain the distribution of the normal derivatives of potential along the boundary of the field region directly. It is profitable to calculate the total flux along the conductor surface. Hence, the parameters of the capacitance of multi conductors with any shape of the cross section can be obtained in a easy way with sufficient accuracy. The capacitances of multiphases cable and the characteristic impedence of transmission lines with complicated shape of the cross section for TEM mode wave are calculated by the boundary element method in following sections.

2 BRIEF INTRODUCTION OF BOUNDARY ELEMENT METHOD

Based on the weighted residual principle, the boundary integral equation of Laplace's equation is:

$$C_i u_i=\int_\Gamma (F\frac{\partial u}{\partial n} - u\frac{\partial F}{\partial n})d\Gamma \tag{1}$$

where u is the function of Laplace's operator, F is the fundamental solution of Laplace's equation, u_i is the function value at any point i of the boundary of the field region, Γ is the boundary of problem region, n represents the normal direction of the boundary. For smooth boundary, $C_i=1/2$ [1].

After using the discretization technique, Eq.(1) is approximated by

$$\frac{1}{2}u_i+\sum_{j=1}^{N}\int_{\Gamma_j} u\frac{\partial F}{\partial n}d\Gamma=\sum_{j=1}^{N}\int_{\Gamma_j} F\frac{\partial u}{\partial n}d\Gamma \tag{2}$$

where N is the total number of elements along the boundary which is discretized, Γ_j is the boundary of each element.

Suppose the unknown function u is approximated by

$$u=\sum_{i=1}^{n} N_i u_i \tag{3}$$

where N_i is the shape function. Let

$$\begin{cases} \hat{H}_{ij}=\int_{\Gamma_j}\frac{\partial F}{\partial n}[N]d\Gamma \\ G_{ij}=\int_{\Gamma_j} F[N]d\Gamma \end{cases} \tag{4}$$

and

$$H_{ij}=\begin{cases} \hat{H}_{ij} & i\neq j \\ \hat{H}_{ij}+\frac{1}{2} & i=j \end{cases} \tag{5}$$

then Eq.(2) is expressed by a matrix form

$$HU=GQ \tag{6}$$

Where H,G are coefficient matrices of order N×N, U,Q are column matrices of order N of potentials and its normal derivatives along the boundary. Solve Eq.(5), the normal derivatives of the potential are obtained with the same degree of accuracy as the potential itself.

In Eq.(3) the shape function [N] is depending on the type of discretization element. The fundamental solu- tion of Laplacian is

$$F=\frac{1}{2\pi}\ln\frac{1}{|r_i-r_j|} \tag{7}$$

where r_i, r_j are positions of field point and source point, respectively.

3 CAPACITANCES OF CABLES WITH ANY SHAPE OF CROSS-SECTION

3.1 Validation of the Method

Two examples are used to examine the accuracy of the method.

Example 1: A coaxial cable with radius of R_1=1cm, R_2=2cm is shown in Fig.1(a).

The inner and outer circles are subdivided into 16 and 24 linear elements. Suppose the imposed voltage is 1V. By using the boundary element method, the field strength at the inner and the outer conductors are 0.144535×10^4(V/m) and 0.72298×10^4 (V/m), and the relative are +0.18% and 0.29%,

respectively. The capacitance per unit length of the coaxal is 80.37065pf and the relative error of the capacitance is:

$$e_c=\frac{80.37065-80.2607}{80.2607}=0.1\%$$

The accuracy is quite good.

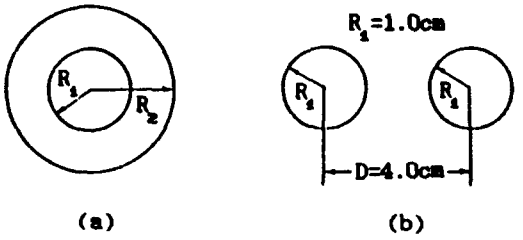

(a) (b)

Fig.1(a) Coaxal cylinder
(b) A pair of parallel cylinder

Example 2: Each contour of the cross section of a pair of parallel line as shown in Fig.1(b) is divided by 12 linear elements. By using the boundary element method, the capacitance per unit length of this system is 20.85378pf. The relative error is 1.2%.

3.2 Application:

The partial capacitances of multi-phases cables with different shape of the cross sections are usually calculated by means of figures and tables as introduced in reference[3]. The cross section of a symmetric three-phase cable is shown in Fig.2.

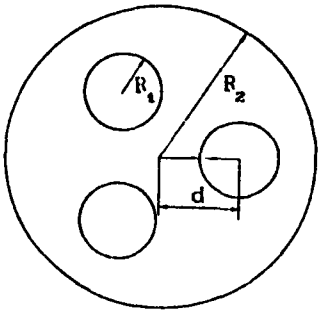

Fig.2 The cross section of a three phases cable ($R=1_1.0cm$ $R_2=4.0cm$ $d=2.0cm$)

Based on the definition of the inductive coefficients between multi conductors and the partial capacitance defined as Eq.(8), the parameters of C_{io}, C_{ik} can be calculated by the above method directly.

$$\begin{cases} Q_i=C_{io}U_{io}+C_{i2}U_{i2}+\ldots+C_{ik}U_{ik}+\ldots+C_{in}U_{in} \\ \cdots \\ Q_k=C_{k1}U_{k1}+C_{k2}U_{k2}+\ldots+C_{ko}U_{ko}+\ldots+C_{kn}U_{kn} \\ \cdots \\ Q_n=C_{n1}U_{n1}+C_{n2}U_{n2}+\ldots+C_{nk}U_{nk}+\ldots+C_{no}U_{no} \end{cases} \quad (8)$$

In Eq.(8), $U_{k2}=U_{ko}-U_{2o}$.

By using the above method, the partial capacitances of the three phase cable shown in Fig.2 are $C_{io}=C_{2o}=C_{3o}=13.3007pf$ and $C_{i2}=C_{23}=C_{3i}=9.977897pf$.

Compare the approximate solution obtained from reference [3], the error of C_{io} is:

$$E_{c_{io}}=\frac{13.3007-13.528}{13.528}=1.68\%$$

If the shape of the inner conductor is irregular, for example the sector approximte to elliptic, the partial capacitance can be calculate by the same way.

4 CHARACTERISTIC IMPEDANCE OF TRANSMISSION LINES

The characteristic impedance of coaxal transmission lines with different shape of cross sections both of the inner and the outer conductors are dealt with by many authors by means of analytical and semi-analytical formulations such as those given in references[2,4-9]. In this paper, the boundary element method is successfully used to calculate the characteristic impedance of the coaxal transmission lines constructed by an inner conductor with circular cross section surrounded by an outer conductor with a polygonal cross section and vice versa. For TEM mode transmission lines, the field distribution between conductors satisfies the Laplacian equation. The method introduced in former section is used. The characteristic impedances of the transmission lines with polygonal and circular conductors as shown in Fig.3(a),(b) and Fig.4 are calculated. The comparison of the numerical results calculated by BEM with those obtained from different literatures of these configuration is listed in Table 1 and 2. For Fig.3(a) and (b), the outer and the inner conductors are divided by 36 and 20 linear elements, respectively. For Fig.4, the circle is divided into 20 linear elements and the square is divided into 36 linear elements.

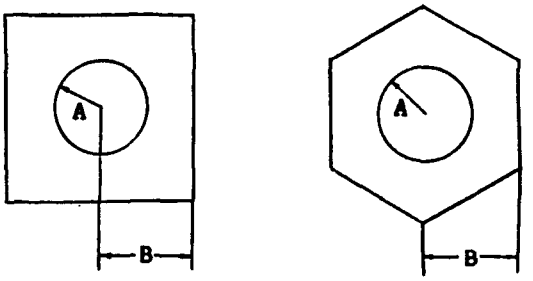

(a) N=4 (b) N=6

Fig.3 Polygonal transmission line with circular inner conductor

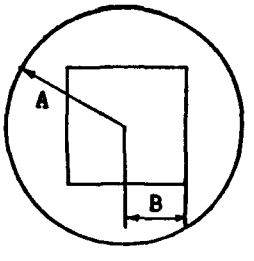

Fig.4 Circular transmission line with square inner conductor

Table 1 Characteristic impedance $Z_o(\Omega)$ of the polygonal transmission line with Circular inner conductor

	(a) N=4					(b) N=6				
A/B	present work	Estevez[2]	Lin[3]	Pan[4]	Riblet[9]	present work	Estevez[2]	Lin[4]	Ma[6]	Pan[8]
.05	183.72	185.21	183.77	184.14		181.44	182.10	182.36	182.79	181.62
.10	142.32	143.16	142.21	142.59		140.04	140.36	140.62	141.20	140.28
.20	100.92	101.02	100.66	101.02		98.64	98.60	99.27	99.61	98.71
.30	76.70	76.41	76.35	76.69		74.43	74.19	74.96	75.26	74.39
.40	59.52	59.02	59.10	59.42		57.24	56.90	57.71	58.02	57.14
.50	46.19	45.61	45.73	46.00	46.09	43.92	43.53	44.34	44.63	43.75
.60	35.29	34.71	34.80	35.00	35.15	32.03	32.64	33.41	33.69	32.80
.70	26.03	25.49	25.55	25.66	25.85	23.81	23.44	24.16	24.44	23.53
.80	17.90	17.44	17.55	17.46	17.68	15.80	15.46	16.16	16.43	15.47
.90	10.37	10.01	10.49	9.97	10.13	8.65	8.31	9.10	9.36	8.27
.94	7.28	6.99				5.93	5.55	6.49	6.75	5.53
.95	6.42	6.19	7.25	6.20	6.25	5.25	4.84		6.12	
.99	2.17	2.36				2.41	1.69	3.39	3.65	1.76
.996	2.49	0.99	4.29	1.07	1.00	1.54	0.66		3.16	

Table 2 Characteristic impedence $Z_o(\Omega)$ of the circular line with square inner conductor

B/A	present work	Lin[5]	Ma[6]	Pan[8]
.05	168.44	169.67	169.72	169.66
.10	127.05	128.11	128.13	128.12
.20	85.68	86.55	86.54	86.56
.30	61.45	62.24	62.21	62.23
.40	44.26	44.97	44.95	44.92
.50	30.67	31.51	31.56	31.36
.60	19.66	20.20	20.62	19.95
.70	9.25	8.85	11.37	7.32

Table 2 shows that if the inner conductor is square, the difference of the impedence between the numerical results and the analytical results looks obvious. However, for B/A=0.05—0.6, the differences are 0.73% — 2.6%. This influence is due to the corner effect of the inner conductor. If the inner conductor is larger then the influence is bigger. But for large ratio of B/A, the coincidence of the result looks well than the result obtained by different analytical methods.

Table 3 The convergence of the method

A/B	0.05	0.10	0.20	0.30	0.40	0.50	0.60	0.70	0.80	0.90	0.94	0.95	0.99	0.996
Element No.(36+20)	181.44	140.04	98.64	74.43	57.24	43.92	33.03	23.81	15.81	8.65	5.93	5.25	2.41	1.54
Element No.(30+32)	181.73	140.23	98.73	74.45	57.22	43.86	32.94	23.71	15.68	8.49	5.73	5.03	2.01	1.57

The convergence of the method is proved by using the construction of the transmission line shown in Fig.3(b). The outer and the inner conductors are subdivided by (36+20) and (30+32) linear elements, respectively, the characteristic impedances(Ω) are listed in Table 3. The results show that the value of the calculated characteristic impedance is different if the number of the discretization elements are different but the difference is very small. It shows that the numerical results are reliable.

5 CONCLUSIONS

1. The BEM can obtain more accurate results for the potential derivative along the conductor surface than the finite difference and finite element methods. Hence it can be used to calculate the capacitance and characteristic impedance of transmission lines with different shape of cross sections.
2. For the polygonal transmission line with circular inner conductor, the numerical results are coincident very well with the analytical results given by different approximate methods of different authors. In this case, the effect of the inner corner of the outer polygonal has no siginificant influence the field distribution. Hence, the corner effect in the numerical method has not present as a problem.
3. Table 2 shows that the accuracy of the characteristic impedance for the circular transmission line with square inner conductor is a little bit lower only if the inner conductor is larger.
4. Table 3 shows that the stablity of the numerical results are good.

5 REFERENCES:

[1] C.A.Brebbia, 'Boundary Element Method', Pentech Press, 1978

[2] H.Estevez, etal, 'A Method for Approximating The Characteristic Impedence of Coaxal Lines in Which The Inner Conductor Is Circular and The Outer Polygonal', IEEE Trans., Vol. MTT-37, pp.634-637, 1989

[3] Liu Ziyu, 'Design Principle of Electrical Isolation Construction', Power Cable Machnical Press, 1981

[4] W.G.Lin, 'Polygonal Coaxal Line With Round Center Conductor', IEEE Trans. Vol.MTT-33, pp, 545-550,1985

[5] W.G.Lin, 'A Critical Study of The Coaxal Transmission Line Utilizing Conductors of Both Circular And Square Cross Section', IEEE Trans. Vol. MTT-30, pp.1981-1988, 1982

[6] X.K.Ma, 'Characteristic Impedence of Coaxal Cylinder and Polygonal Transmission Lines Calculated by Elementary Function' (in Chinese), Optical Fibre and Cable, Vol.3, pp.5-7, 1981

[7] S.G.Pan, 'A New Method for Calculating The Characteristic Impedence With Complex Cross Sections of The Transmission Lines', Science in China(Serie A) ,Vol.9, pp.999-1006, 1986

[8] S.G.Pan, 'Approximate Determination of The Characteristic Impedence of The Coaxal System Consisting of An Irregular Outer Conductor And A Circular Inner Conductor', IEEE Trans., Vol.MTT-35, pp 61-63, 1987

[9] H.J.Riblet,'An Accurate Approximation of The Impedence of A Circular Cylinder Concentric with An External square Tube', IEEE Trans., Vol. MTT-31, pp.841-844, 1983

REGULAR PAPERS

HIGH FREQUENCY FFT ANALYSIS OF AN ELECTRICALLY LONG MONOPOLE ANTENNA

Saad N. Tabet

Department of Electrical and Computer Engineering
Mississippi State University
Mississippi State, MS 39762

ABSTRACT

In previous work the currents along a monopole, 20 meters long and operating at 299.8 MHz, placed over a perfectly conducting ground plane were analyzed using several modeling techniques and the Numerical Electromagnetics Code version two (NEC-2). An interesting topic to investigate is the presence of spurious modes of propagation along the monopole. Such modes of propagation are studied for each modeling technique, and conclusions are drawn accordingly. When the data are transformed into the k-space domain, using Fast Fourier Transforms (FFT), the spurious mode behavior along the monopole becomes clearly visible. This technique provides valuable information not yet documented.

INTRODUCTION

This work is a follow-on to previously published work, Reference [1]. In [1] three different modeling techniques, with NEC-2 [2, 3], were used to model a long monopole antenna placed over a perfectly conducting ground plane. The monopole antenna is 20 meters long, and has a radius of 1.5875 millimeters. Also, the monopole is operated at a frequency of 299.8 MHz, thus making the wavelength equal to one meter. The "EK" NEC command is used with the extended thin-wire kernel option, which guarantees accurate results for segment/radius ratio as low as 2. Since the shortest segment used in all the cases run is 0.01 meters (0.01λ), the smallest segment/radius ratio available exceeds 6, thus satisfying the extended thin-wire kernel condition for accurate results.

The three monopole antenna analysis techniques used are: Equal segmentation, entire grading, and partial grading. The purpose behind studying these techniques is to develop a new feasibility range for NEC to model extremely long (electrically) wire antennas as accurately as possible. Such long antennas are impossible to model with NEC by using the traditional techniques, and thus require special modeling techniques as the ones discussed here. These techniques take into consideration the memory limitation (16 MByte RAM for in-core solutions) of the DEC VAX 11/785 minicomputer used in the computational analysis of this effort.

In the equal segmentation technique the monopole, from source to end, was divided into 2000 equal segments of 0.01λ length each. In the entire grading technique, three cases were considered where the monopole segments were gradually increased from 0.01λ, at the source, to last segment lengths of approximately 0.25λ, 0.5λ, and 0.75λ, at the end, respectively. Finally, in the partial grading technique, and for every case studied, part of the monopole (starting with 0.01λ at the source) was segmented using the entire grading technique with a constant ratio RDEL = 1.1 (see Reference [1]), then equal segments of approximately the size of the last segment, from the entirely graded portion, were used to model the rest of the length of the monopole. For the cases studied, the equal segments had lengths of 0.25λ, 0.35λ, 0.45λ, 0.5λ, 0.55λ, 0.65λ, 0.75λ, 0.85λ, and 0.95λ.

As mentioned in [1], the use of very long segments (greater than 0.1λ) was not recommended by NEC-2. Also, segments very close to the source must be chosen to be even shorter (about 0.01λ). However, when electrically long antennas (20λ long in this case) are being analyzed, the use of short segments becomes almost impossible, due to the size of the interaction matrix in NEC-2 and computer memory limitations. Thus, the entire grading and partial grading techniques were implemented to study electrically long antennas. These techniques were compared with the equal segmentation technique to determine a new range of feasibility for NEC-2.

The conclusions presented in [1] were very informative. The "eye balling" technique (used to compare current versus distance data), the input impedance comparison, and the rms deviation analyses contributed to the resulting conclusions. Nonetheless, none of these analysis techniques gave any information about the presence and significance of spurious modes along the monopole antenna.

Spurious modes are defined as the appearance of eigenvalues of the static problem somewhere along the

wavenumber axis of the resonance problem. In other words, additional peaks occurring in the approximation to a system behavior that do not exist in the actual behavior of the system itself. To observe such spurious modes, the k-space domain data for the monopole antenna are needed. Such data are the result of the Fast Fourier Transform (FFT) of the current versus distance data. The resulting transformed data have the units of "Ampere-meters" and "radians/meters" for the vertical and horizontal axes, respectively. The following section describes the approach used to fulfill this technique.

GENERAL FFT APPROACH

As mentioned earlier, the FFT technique determines the k-space domain data from the current along the monopole versus distance data. To apply the FFT technique, the current data must be re-evaluated at equally spaced distances. This is a restriction imposed on any data that needs to be Fourier transformed. Moreover, the number of data points (N_{dp}) to be transformed must be an integer power of 2. This is another basic restriction for finding the FFT of any available data set.

The number of current samples chosen in this effort, for all the cases studied, is

$$N_{dp} = 2^{11} = 2048 \text{ samples.}$$

This choice is made to guarantee that the undulations in the current distribution will be well described. Also, after a few tests were undertaken, this number of samples proved to be high enough to avoid aliasing. To check for over-sampling or under-sampling, the reference data set was re-sampled at 8192 and 512 points, respectively, yet the FFT data plots maintained the same shape as seen in the 2048 points case used in this paper. Hence, 2048 points were found to be adequate to represent the waveforms at hand.

Since the monopole antenna under study is 20 meters long, then the distance between samples (Δx) will be,

$$\Delta x = 20/N_{dp} = 9.76563\text{E-}3 \text{ meters.}$$

This factor is needed due to its analogy to the sampling rate of discrete time domain data. Hence, the wavenumber sampling rate (Δk_x), in rad/meter, is given by,

$$\Delta k_x = 2\pi/(N_{dp} \cdot \Delta x) = 0.31416 \text{ radians/meter.}$$

Δk_x is analogous to the sampling rate of discrete frequency domain data, and is known as the wavenumber sampling rate. With all the necessary information available, the FFT routine can be applied to transform the current versus distance data, in [1], into the k-space domain.

The maximum wavenumber value ($k_{x,\ max}$) is given by,

$$k_{x,\ max} = 2\pi/\Delta x = 643.3982 \text{ radians/meter.}$$

Note that the k-space domain data will be plotted up to $k_{x,\ max}$ rather than to $k_{x,\ max}/2$, since the distance domain data are complex in nature, which means that the k_x-domain data will not necessarily be symmetric in nature (about the midpoint).

FFT OF MONOPOLE CURRENTS

A quick check on some of the cases reveals some valuable information. First, a Log-Log scale is necessary to clearly show the minima and maxima of each plot. Consequently, the point corresponding to $k_x = 0$ must be removed from the data before plotting the data, since $\text{Log}(0) \rightarrow -\infty$, which is impossible to show on a Log-scale. Hence, each plot will only show 2047 points instead of 2048 points. Even though both the magnitude and phase responses of the transformed data contain spurious mode information, only the magnitude of the FFT data will be considered in this analysis. The phase analysis is outside the intention of this effort.

The FFT of the reference case is shown in Fig. 1. Fig. 1 is the most accurate of all the results, and is assumed to be spurious mode free. Thus, any existing minimum and/or maximum in Fig. 1 is considered to correspond to the natural behavior of the current along the monopole. Hence, when Fig. 1 is observed carefully, it is obvious that the reference case has four visible extreme points, two minima and two maxima.

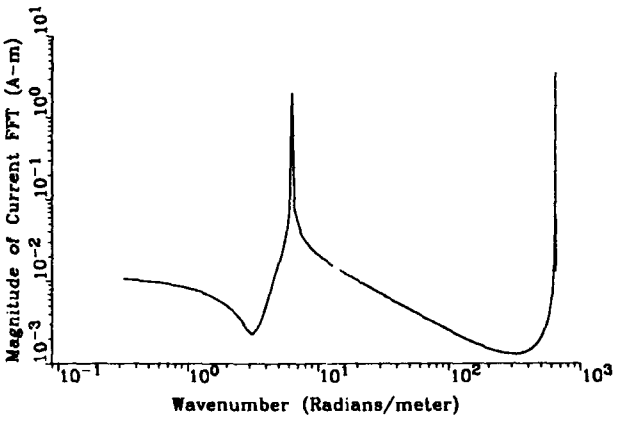

Fig. 1. Magnitude of Current FFT Versus Wavenumber Along a Monopole of Length 20λ Using 2000 Equal Segments of Length 0.01λ.

The minima and maxima in Fig. 1, and the sample number position where they exist, are shown in Table 1. The data in Table 1 will serve as a supplementary method used to compare results from other cases to those of the reference case. This is accomplished by comparing the sample value (SV) and the location of the corresponding sample number (SN) of the minima and maxima of the entire and partial grading techniques' cases to those of the reference case. The relative error method is used to compare the minima and maxima sample values (SV_{min1}, SV_{min2}, SV_{max1}, and SV_{max2}). The equation for relative error (RE) as determined in k-space is,

$$RE = \frac{(SV_{ref} - SV_{other})}{SV_{ref}} \cdot 100\%$$

For the entire grading technique, the FFT magnitude plots of the three cases studied (S_{NS} = Length of the last segment $\approx 0.25\lambda$, 0.5λ, and 0.75λ) are shown in Figs. 2, 3, and 4, respectively. The minima and maxima information for these cases can be found in Table 1.

Comparing Fig. 2 to Fig. 1 it is seen that spurious modes are virtually nonexistent. Yet, there exists a minor oscillatory behavior close to the point where the second minimum in Fig. 2 takes place. The relative error analysis for the $S_{NS} \approx 0.25\lambda$ case shows that the only error of concern is that of the first minimum (RE_{min1} = 17.33%). Now, keeping in mind that NEC-2 documentation, [2, 3], states that an error of at least 5% is to be expected, the remaining portion of the relative error values for the $S_{NS} \approx 0.25\lambda$ case are well within the acceptable range.

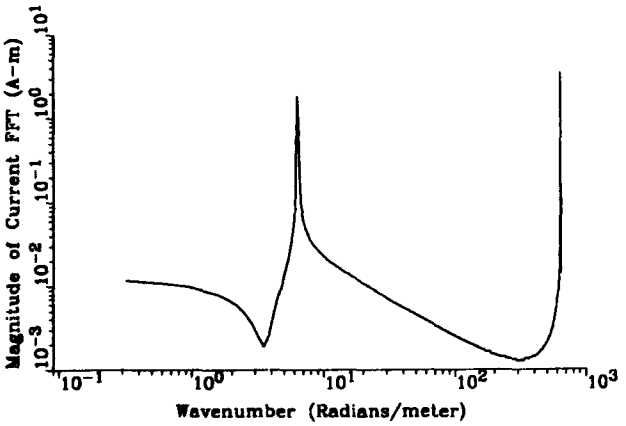

Fig. 2. Magnitude of Current FFT Versus Wavenumber Along a Monopole of Length 20λ Using Entire Grading with $S_{NS} \approx 0.25\lambda$.

Comparing Fig. 3 to Fig. 1 shows an oscillatory behavior just after the first maximum is observed. This behavior is more visible than that in Fig. 2, but is not significant enough to be considered as a spurious mode behavior. Yet, it is an indication that some form of instability in the solution does exist, mainly due to the use of some segments close to 0.5λ in length, which has been proven to violate the boundary conditions in NEC-2 [1]. Moreover, the first minimum dips far below that of Fig. 1. This can be clearly seen in the very large relative error value (RE_{min1} = 51.11%) corresponding to it in Table 1. Another value of some concern in Table 1 is that of RE_{max1} = 12%, since it represents a difference of 0.23 A-m, which is somewhat significant. Also, the negative sign in the value of RE_{max2} means that the SV_{max2} value for the $S_{NS} \approx 0.5\lambda$ case is larger than that of the reference case.

Fig. 4 shows many interesting results when compared to Fig. 1. First, it is noticed that the first minimum has almost totally disappeared. Second, the spurious mode behavior is clearly visible in the area preceding the first maximum. This behavior shows huge instability in the solution, and is definitely attributed to the extremely long segments $\approx 0.75\lambda$ used at the end of the antenna. The error analysis in Table 1 shows that RE_{min1} = -141.51% is tremendously large, and again amplifies the instability in that region. Nevertheless, when the rest of the error values are checked, it is noticed that the error values are extremely low and consequently might lead to very deceiving conclusions.

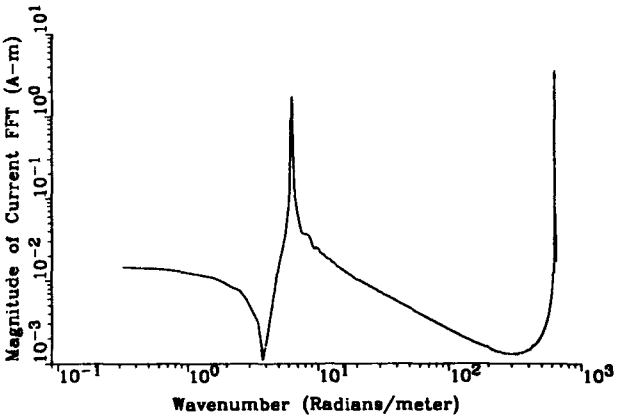

Fig. 3. Magnitude of Current FFT Versus Wavenumber Along a Monopole of Length 20λ Using Entire Grading with $S_{NS} \approx 0.5\lambda$.

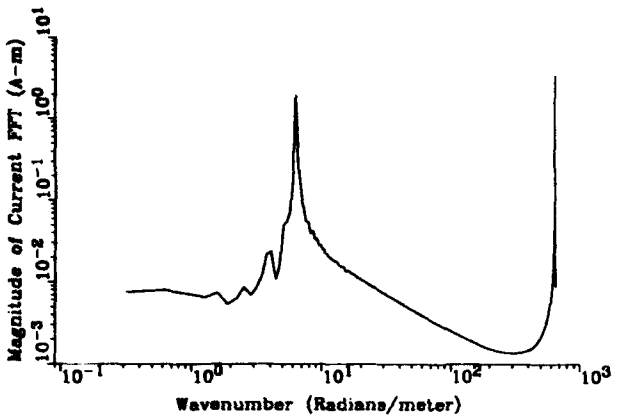

Fig. 4. Magnitude of Current FFT Versus Wavenumber Along a Monopole of Length 20λ Using Entire Grading with $S_{NS} \approx 0.75\lambda$.

For the partial grading technique, the FFT magnitude plots of the nine cases studied ($S_{NS} \approx 0.25\lambda$, 0.35λ, 0.45λ, 0.5λ, 0.55λ, 0.65λ, 0.75λ, 0.85λ, and 0.95λ) are shown in Figs. 5, 6, 7, 8, 9, 10, 11, 12, and 13, respectively. The minima and maxima information for these cases can be found in Table 1.

Comparing Figs. 5 and 6 to Fig. 1 it is noted that insignificant spurious modes exist. The error analysis in Table 1 shows that the largest error for the $S_{NS} \approx 0.25\lambda$ and 0.35λ cases at the first minimum (RE_{min1} = -8.89% and 13.33%, respectively), which are still very acceptable values considering the size of the problem at hand.

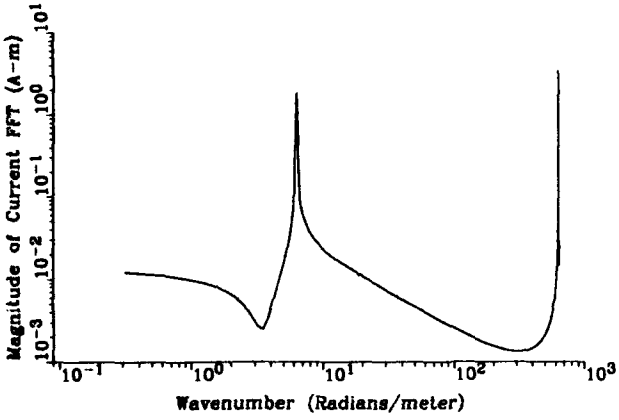

Fig. 5. Magnitude of Current FFT Versus Wavenumber Along a Monopole of Length 20λ Using Partial Grading with RDEL ≈ 1.1 and $S_{NS} \approx 0.25\lambda$.

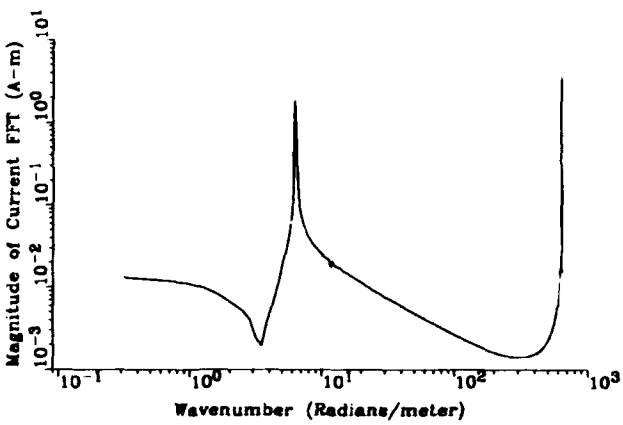

Fig. 6. Magnitude of Current FFT Versus Wavenumber Along a Monopole of Length 20λ Using Partial Grading with RDEL ≈ 1.1 and $S_{NS} \approx 0.35\lambda$.

In Fig. 7 a minor spurious mode behavior is registered in the region directly following the first maximum. Moreover, from Table 1, the error analysis shows that larger errors are registered, especially at the second minimum and first maximum (RE_{min2} = -13.24% and RE_{max1} = 21.75%, respectively). These larger errors reflect the use of extremely long segments, and the use of the segment lengths that are close to the undesired 0.5λ value.

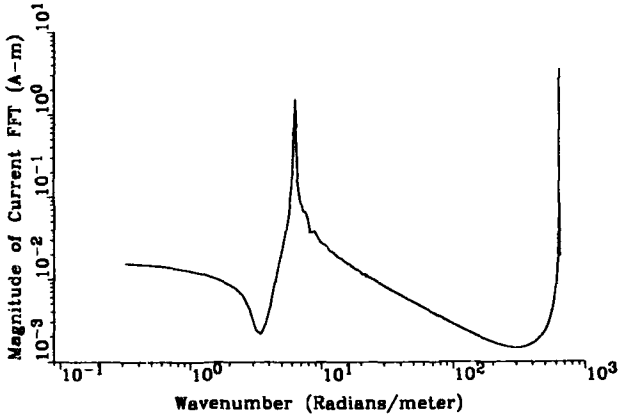

Fig. 7. Magnitude of Current FFT Versus Wavenumber Along a Monopole of Length 20λ Using Partial Grading with RDEL ≈ 1.1 and $S_{NS} \approx 0.45\lambda$.

Comparing Fig. 8 to Fig. 1 it is noticed that very strongly visible spurious modes exist, and the first minimum value is almost nonexistent. Moreover, the results of Fig. 8 are approximately an order of magnitude higher than those of Fig. 1. This observation is seconded by the data in Table 1. The error analysis for this case shows that the smallest error occurs at the second

maximum (RE_{max2} = -296.42%). This is a tremendously large value that clearly shows the violation of the boundary conditions in NEC-2.

Figs. 9, 10, 11, 12, and 13 all show strong spurious mode behavior, mainly in the region preceding the occurrence of the first maximum. Also, the spurious modes in Figs. 11, 12, and 13 are stronger than those of Figs. 9 and 10. Again, the error analysis in Table 1 shows that all the cases exhibit relatively high percentage errors, with the exception of the $S_{NS} \approx 0.65\lambda$ case where the errors remain moderately low. The $S_{NS} \approx 0.65\lambda$ is an exception without a clear reason to why are the errors so low. Nonetheless, the high errors in the other cases are a reflection of the very large segment sizes used in the equal segment portion of modeling the monopole antenna.

Finally, when the positions of the minima and maxima in Table 1 are compared, several observations are made. First, the positions of both maxima (SN_{max1} and SN_{max2}), in each entire and partial grading case, coincide with those of the reference case, respectively. Next, the positions of the first minimum (SN_{min1}), in each entire and partial grading case, varied slightly from that of the reference case, with the $S_{NS} \approx 0.5\lambda$ partial grading case being the furthest away. Last, the positions of the second minimum (SN_{min2}), in each entire and partial grading case, varies more significantly than the variation in the position of the first minimum. Again, the $S_{NS} \approx 0.5\lambda$ partial grading case possesses the largest shift.

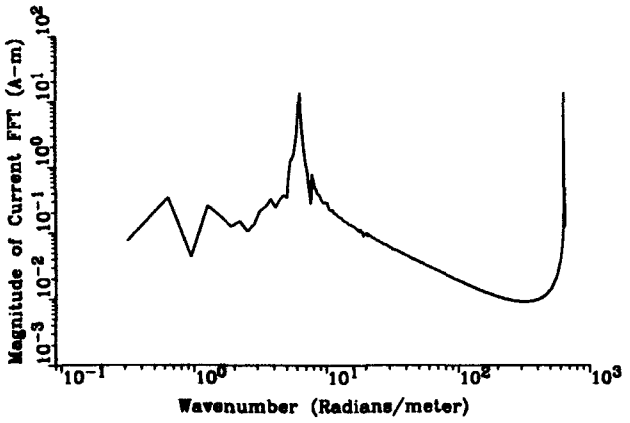

Fig. 8. Magnitude of Current FFT Versus Wavenumber Along a Monopole of Length 20λ Using Partial Grading with RDEL ≈ 1.1 and $S_{NS} \approx 0.5\lambda$.

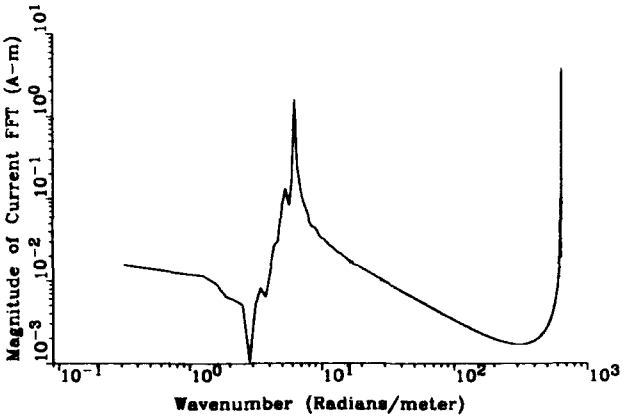

Fig. 9. Magnitude of Current FFT Versus Wavenumber Along a Monopole of Length 20λ Using Partial Grading with RDEL ≈ 1.1 and $S_{NS} \approx 0.55\lambda$.

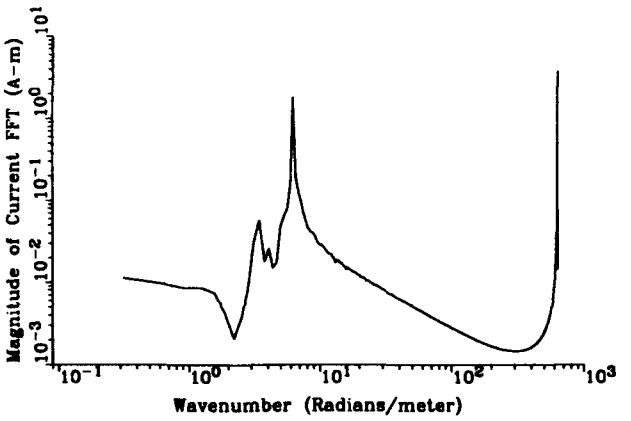

Fig. 10. Magnitude of Current FFT Versus Wavenumber Along a Monopole of Length 20λ Using Partial Grading with RDEL ≈ 1.1 and $S_{NS} \approx 0.65\lambda$.

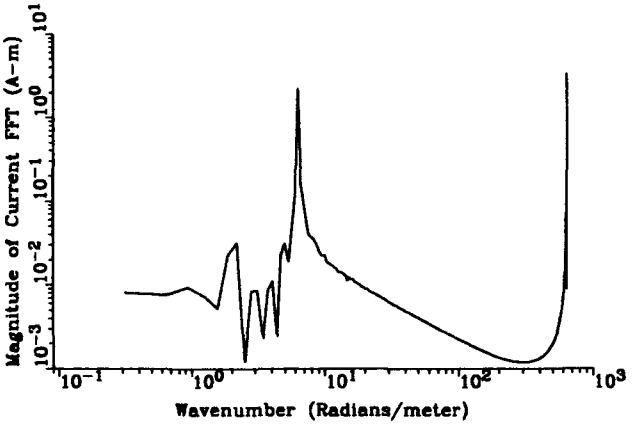

Fig. 11. Magnitude of Current FFT Versus Wavenumber Along a Monopole of Length 20λ Using Partial Grading with RDEL ≈ 1.1 and $S_{NS} \approx 0.75\lambda$.

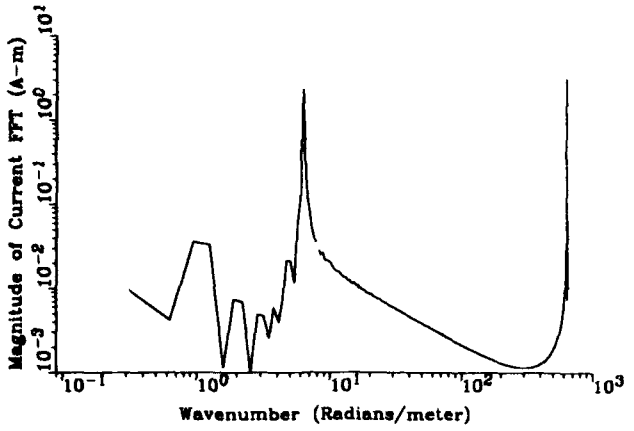

Fig. 12. Magnitude of Current FFT Versus Wavenumber Along a Monopole of Length 20λ Using Partial Grading with RDEL ≈ 1.1 and $S_{NS} \approx 0.85\lambda$.

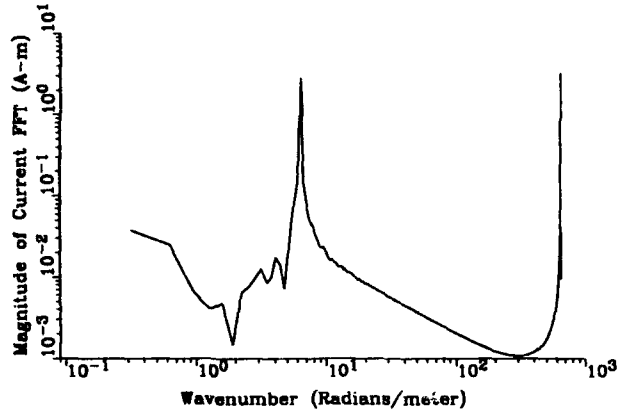

Fig. 13. Magnitude of Current FFT Versus Wavenumber Along a Monopole of Length 20λ Using Partial Grading with RDEL ≈ 1.1 and $S_{NS} \approx 0.95\lambda$.

CONCLUSIONS

The FFT k-space analysis technique was used to further investigate the use of the entire and partial grading techniques as alternative methods of modeling the monopole antenna over a perfectly conducting ground plane studied in [1]. Again, the comparisons were made to the data from the equal segmentation technique, of 2000 equal segments of length 0.01λ each, serving as a reference. This form of analysis was mainly concerned with locating spurious modes, if any existed, and determining the main reason of their existence. When Figures 2 through 13 were compared to Fig. 1, it was noted that the use of extremely long segments (greater than 0.45λ) was the major reason for existence of spurious modes. Moreover, the conclusion arrived at in [1] stating that segments equal to 0.5λ, or even close to that value, should never be used was strongly backed in this analysis. This can be seen in Fig. 8 and the data in Table 1 corresponding to that figure, where even the monopole characteristic peaks were alarmingly larger than those evaluated using the equal segmentation technique (Fig. 1). The behavior in Fig. 8 was an ideal example of the presence of spurious modes, and the consequences suffered due to such presence. Hence, for the entire and partial grading techniques, it is recommended that longer segments (not exceeding 0.4λ) can be used to model extremely long (electrically) wire antennas while maintaining acceptable results.

Moreover, the data in Table 1 showed that the values and locations of the minima were, in most cases, far more affected than their maxima counterparts. This can be attributed to the fact that numerical solutions to problems of this magnitude cannot guarantee 100% accuracy. Hence, the addition (or subtraction) of a small error value to (from) an already small number changes its value tremendously. On the other hand, the addition (or subtraction) of a similar small error value to (from) a large number changes its value only slightly.

Finally, the conclusions presented in [1] were re-established using a different technique. More importantly, the presence of spurious modes resulting from the use of large segments, as well as ill chosen segment lengths (0.5λ, for example), was shown. This technique reflected a far more visible way to show discrepancies in data when different methods of solution are used. Also, the spurious modes show that when a system is poorly modeled, false system characteristics (such as additional peaks) show up, and consequently, lead to erroneous results.

ACKNOWLEDGMENTS

Special thanks go to Dr. Clayborne D. Taylor for reviewing this manuscript, and Dr. Nicolas H. Younan for his valuable input toward this effort.

REFERENCES

[1] S.N. Tabet, J.P. Donohoe, and C.D. Taylor, "Using Nonuniform Segment Lengths with NEC to Analyze Electrically Long Wire Antennas," *Applied Computational Electromagnetics Society Journal*, Vol. 5, No. 2, Winter 1990.

[2] G.J. Burke and A.J. Poggio, "Numerical Electromagnetics Code (NEC) - Method of Moments," Vol. 2, *Naval Ocean Systems Center*, Technical Report NOSC TD 116, January 1981.

Response of externally excited coaxial cables with wire braided shields

Dr S Sali , Bsc , PhD
Department of Electrical and Electronic Engineering
Merz Court, The University of Newcastle, Newcastle upon Tyne NE1 7RU, United Kingdom

ABSTRACT

The frequency responses of coaxial cables employing wire braided shields, excited by external fields is studied using an algorithm based on distributed circuit model, which uses both electric and magnetic field parameters to model the external field coupling. Simplicity and fast speed of the model enable computer aided analysis of externally induced noise in cable interconnects to be carried out in a computationally efficient manner. A general CAD algorithm is developed based on this model and it is applied to study the response of cables over a lossless ground plane. The algorithm is then used to study the effects of different braid constructions on the responses of cables excited by external fields. Responses of cables with optimum braid designs in their shields are studied in detail. The model uses the experimental values of the leakage parameters which are measured separately using a standard triaxial text fixture.

INTRODUCTION

With the advent of smaller and denser integrated circuits very large electronic systems have resulted and these require very complex networks of interconnections within a limited space [Bayindir and Sali, 1990][Sali 1993]. Coaxial cables are used as signal carriers in such interconnection networks between the equipments when extra shielding against the external interfering fields is required. Since the interconnect cables have to be mechanically flexible usually braided coaxial cables are used as signal carriers. Price paid for the flexibility is a conducting shield with a large number of small diamond shaped holes [Sali 1993][Vance 1973] caused by the braiding of the shield wires. Such shields therefore do not provide complete immunity against external interfering fields, which may penetrate inside the cable. The mechanisms of wave penetration are directly related to the geometry of the braid and the frequency of the incident field [Sali, 1990]. At radio frequencies the coupling of the external magnetic field is governed by the Transfer Impedance (Z_T) per-unit-length and the coupling of the external Electric field is governed by Transfer Admittance (Y_T) per-unit-length . A detailed experimental and theoretical study on both parameters are given in [Fowler 1979]. These studies have already demonstrated that Z_T is purely inductive and Y_T is purely capacitive at frequencies above 2 MHz.

Inductive rise of Z_T at high frequencies is caused by two magnetic coupling process : the coupling by direct penetration of external fields to the interior through the holes in the shield which gives rise to hole inductance, and the magnetic flux coupling in the circuits between the inner and outer braid layers of the braid which results in braid inductance. It is known that [Tyni 1976] for braid angles less than 45° hole and braid inductances oppose each other and greatly reduced transfer impedance values may be obtained for certain braid constructions where the difference between the two is minimum and such braid designs are called optimum.

The objective of the work reported here is to develop a general algorithm for the computation of transmission line currents and voltages induced by the external field of arbitrary incidence at any point along the interior of the coaxial cable, placed over a finite-loss conducting plane. The model uses both Y_T and Z_T in contrast to earlier studies which ignores Y_T and hence do not applicable to optimised cables.

A large number of simulations have been carried out to illustrate the capability of the new algorithm. The effects of the high and low value passive load impedances on the amount of coupling are investigated in detail. The effect of polarisation of the incident wave on the coupling of the external field is studied against the angular orientation of the cable with respect to the direction of incidence.

BASIC MODEL FOR INTERFERENCE AND THE LINE RESPONSE

The basic interference model studied is shown in Fig.1, which shows a braided coaxial cable of length **L** ,placed over a finite-loss conducting plane at a height of **h**. The line is illuminated by an external electromagnetic plane wave at an elevation angle of θ and azimuth angle ϕ. Cross dimensions of the coaxial cable and its separation from the conducting plane is much smaller than the wavelength of the illuminating wave and hence the principal mode of propagation in the coax is **TEM.** The electric and magnetic field components of the incident wave couples to the exterior circuit between the shield and the metallic ground plane, inducing electric and magnetic flux there, as shown in Fig.2. This flux coupling is represented in terms of impressed sources $e(\upsilon)$ and $i(\upsilon)$ and per-unit-length equivalent circuit shown in Fig.3 is

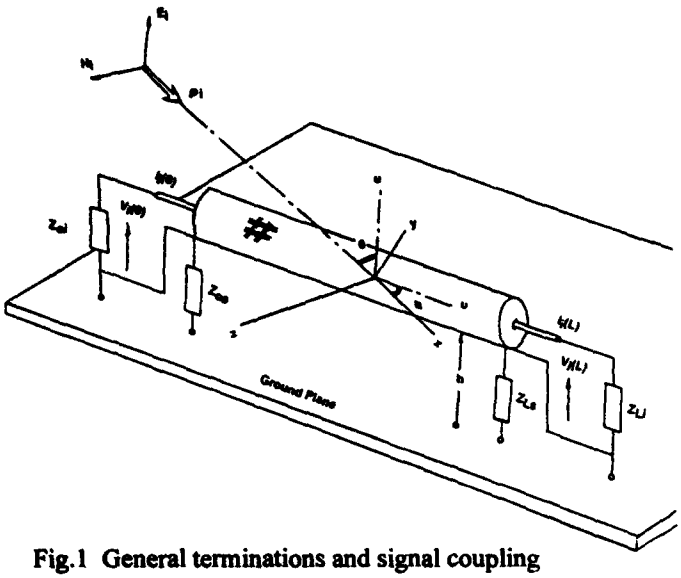

Fig.1 General terminations and signal coupling for a braided coaxial cable over a finite loss conducting plane excited by a plane wave.

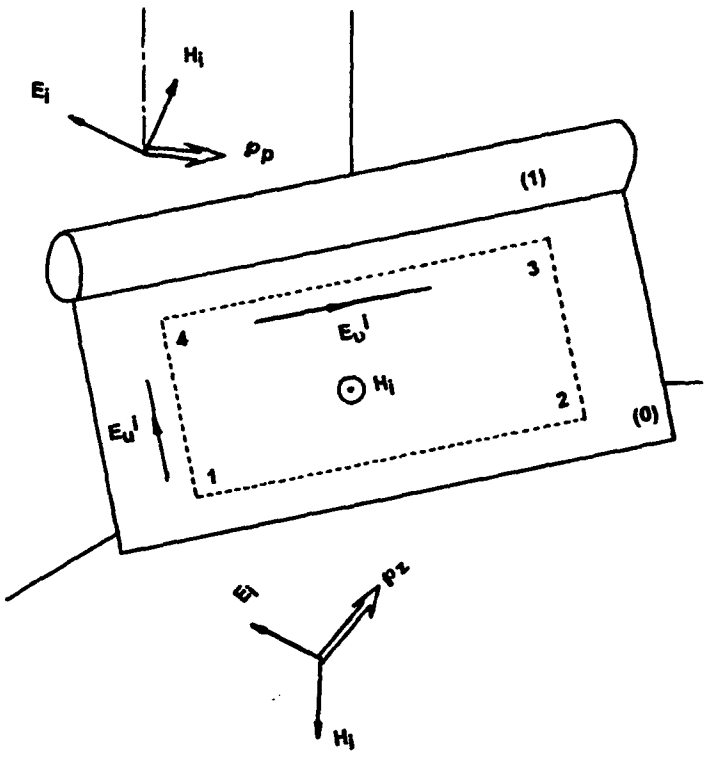

Fig.2 Geometry and contour integration for the calculation of the coupled sources induced by the plane wave.

employed for the interference problem shown in Fig.1. It is assumed that the tertiary circuit is terminated in passive impedances Z_{0s} at the near end and Z_{Ls} at the far end respectively.

The propagation of the coupled wave in the tertiary circuit is characterised by the propagation constant $\gamma_s = \sqrt{Y_s Z_s}$, and the characteristic impedance $Z_{cs} = \sqrt{Z_s/Y_s}$. Using the method developed in [Sali, 1993] the coupled voltage and current in the teriary are given by

$$V_s(\upsilon) = \cosh \gamma_s \upsilon V_s + Z_{cs} \sinh \gamma_s \upsilon \, I_s(0) + \vartheta_{ss}(\upsilon)$$

$$I_s(\upsilon) = \frac{1}{Z_{cs}} \sinh \gamma_s \upsilon \, V_s(0) + \cosh \gamma_s \upsilon \, I_s(0) + \delta_{ss}(\upsilon) \qquad (1)$$

$$\vartheta_{ss}(\upsilon) = \int_0^{\upsilon} \cosh \gamma_s(\upsilon-\zeta) e_s(\upsilon) d\zeta$$

$$- Z_{cs} \int_0^{\upsilon} \sinh \gamma_s(\upsilon-\zeta) i_s(\zeta) d\zeta \qquad (2)$$

$$\delta_{ss}(\upsilon) = - \frac{1}{Z_{cs}} \int_0^{\upsilon} \sinh \gamma_s(\upsilon-\zeta) e(\zeta) d\zeta$$

$$+ \int_0^{\upsilon} \cosh \gamma_s(\upsilon-\zeta) i_s(\zeta) d\zeta \qquad (3)$$

$$e_s(\upsilon) = [E_\upsilon^i(h,\upsilon) - E_\upsilon^i(0,\upsilon)] - \int_0^h \frac{\partial E_u^i(u,\upsilon)}{\partial \upsilon} du$$

$$i_s(\upsilon) = Y_s \int_0^h E_u^i(u,\upsilon) \, du \qquad (4)$$

The current and voltage in (1) now couple to the interior of the coaxial line giving rise to a TEM wave propagating inside. This wave coupling process is governed by the per-unit-length sources which are described as

$$e_{Ti}(\upsilon) = Z_T I_S(\upsilon) \qquad (5)$$

$$i_{Ti}(\upsilon) = Y_T V_S(\upsilon) \qquad (6)$$

Using the similar process as above the coupled current and voltage inside the coaxial cable are given by

$$V_i(\upsilon)=\cosh\gamma_i\upsilon V_i(0)$$

$$- Z_{ci}\sinh\gamma_i\upsilon I_i(\upsilon) + \vartheta_{si}(\upsilon)$$

$$I_i(\upsilon) = -\frac{1}{Z_{ci}}\sinh\gamma_i\upsilon V_i(0) + \cosh\gamma_i\upsilon I_i(0) + \delta_{si}(\upsilon) \qquad (7)$$

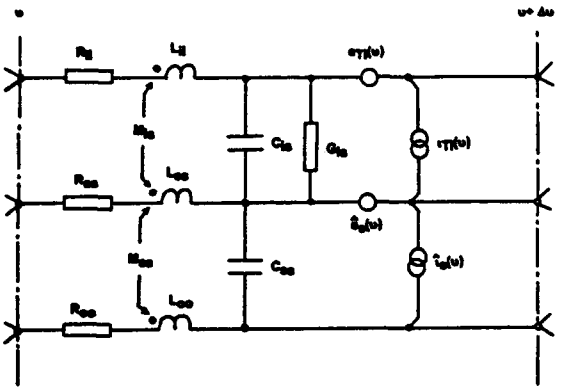

Fig.3 The per-unit-length equivalent circuit for the coaxial cable in *Fig. 1*

Since defining the field coupling in terms circuit parameters Y_T and Z_T isolates the two TEM waves inside and outside the coaxial cable the transmission line equations in (1) and (7) are independent. This allows the boundary conditions to be considered separately in terms of the passive terminations at both ends of each circuit. These are given by the Thevenin equations as $V_{s,i}(0) = - Z_{Os,i}\, I_{s,i}(0)$ $V_{s,i} = Z_{Ls,i} I_{s,i}(L)$ Inserting these boundary conditions in (1) and (7) the equivalent distributed sources inside the coaxial cable becomes

$$\vartheta_{si}(\upsilon)=\frac{Z_T}{Z_{cs}}\frac{\kappa_{ss}}{\Delta_{ss}}\int_0^{\upsilon}\cosh\gamma_i(\upsilon-\varsigma)\,X$$

$$\{Z_{Os}\sinh\gamma_s\varsigma+\cosh\gamma_s\varsigma\}d\varsigma$$

$$-\int_0^{\upsilon}\cosh\gamma i(\upsilon-\upsilon)\{\eta(0)\sinh\gamma_s\upsilon$$

$$+\int_0^{\upsilon}\sinh\gamma_s(\upsilon-\varsigma)\tau(\varsigma)d\varsigma\}d\upsilon$$

$$+ Z_{ci}Y_T\int_0^{\upsilon}\sinh\gamma_i(\upsilon-\varsigma)\,X$$

$$\{Z_{Os}\cosh\gamma_s\varsigma+Z_{cs}\sinh\gamma_s\varsigma\}d\varsigma$$

$$-\int_0^{\upsilon}\sinh\gamma i\,(\upsilon-\varsigma)\cosh\gamma_s(\upsilon-\zeta)\tau(\zeta)d\zeta$$

$$-\eta(\upsilon)+\eta(0)\cosh\gamma_s\upsilon\}d\upsilon \qquad (8)$$

$$\delta si(\upsilon)=-\frac{Z_T}{Z_{ci}Z_{cs}}\frac{\kappa_{ss}}{\Delta_{ss}}\int_0^{\upsilon}\sinh\gamma_i(\upsilon-\zeta)\,X$$

$$[Z_{Os}\sinh\gamma_s\zeta+Z_{cs}\cosh\gamma_s\zeta]d\zeta$$

$$+\int_0^{\upsilon}\sinh\gamma_i(\upsilon-\upsilon)\,X$$

$$\{\eta(0)\sinh\gamma_s\upsilon+\sinh\gamma_s(\upsilon-\zeta)\tau(\zeta)d\zeta\}d\upsilon$$

$$-Y_T\frac{\kappa_{ss}}{\Delta_{ss}}\int_0^{\upsilon}\cosh\gamma_i(\upsilon-\zeta)\,X$$

$$\{Z_{Os}\cosh\gamma_s\zeta+Z_{cs}\sinh\gamma_s\zeta\}d\zeta$$

$$+\int_0^{\upsilon}\cosh\gamma_i(\upsilon-\upsilon)\{\int_0^{\upsilon}\cosh\gamma_s(\upsilon-\zeta)\tau(\zeta)d\zeta$$

$$-\eta(\upsilon)+\eta(0)\cosh\gamma_s\upsilon\}d\upsilon \qquad (9)$$

With the Thevenin equations for the terminal conditions current and voltages inside the coaxial cable are obtained from above equations as

$$I_i(0) = \frac{\kappa_{ii}}{\Delta_{ii}}$$

$$V_i(0)=- Z_{Oi} I_i(0)$$

$$I_i(L)=\left(\frac{Z_{os}}{Z_{cs}}\sinh\gamma_i L+\cosh\gamma_i L\right)\frac{\kappa_{ii}}{\Delta_{ii}}+\delta_{si}(L)$$

$$V_i(L)=-(Z_{oi}\cosh\gamma_i L+Z_{ci}\sinh\gamma_i L)\frac{\kappa_{ii}}{\Delta_{ii}}+\vartheta_{si}(L) \qquad (10)$$

where

$$\kappa_{ii}=Z_{ci}[\vartheta_{si}(L)-Z_{Li}\delta_{si}(L)]$$

$$\kappa_{ss}=Z_{cs}[\vartheta_{ss}(L)-Z_{Ls}\delta_{ss}(L)]$$

$$\Delta_{ss}=(Z_{cs}Z_{os}+Z_{cs}^2)\sinh\gamma_s L+Z_{cs}(Z_{os}+Z_{Ls})\cosh\gamma_s L$$

$$\Delta_{ii}=(Z_{ci}Z_{oi}+Z_{ci}^2)\sinh\gamma_i L+Z_{ci}(Z_{oi}+Z_{Li})\cosh\gamma_i L \qquad (11)$$

Near end (υ=0) and far end (υ=L) responses of the line are obtained from the coupled voltages $V_i(0)$ and $V_i(L)$ as given above and the coupling factor is computed from the normalised values of this vectors to the maximum value of the incident field.

The incident plane waves are considered for parallel (E-field parallel to xz-plane, as shown in Fig.2) polarisation, for which E-field may be obtained as

$$E_x^i=E_0\cos\theta\cos\phi\{e^{jk_u u}-\rho e^{-jk_u u}\}e^{-jk_\upsilon \upsilon}$$

$$E_y^i=E_0\sin\{e^{jk_u u}+\rho e^{-jk_u u}\}e^{-jk_\upsilon \upsilon} \qquad (12)$$

where E_0 is the maximum field intensity, From Fig.1 the scalar wave numbers can be obtained as $k_\upsilon=(2\pi/\lambda)\sin\theta\sin\phi$, and $k_u=(2\pi/\lambda)\sin\theta\cos\phi$, ρ is the reflection coefficient for the oblique incidence on to ground plane of the incident wave and it is calculated using the expressions in [Frankel 1979].

RESULTS

In this section simulations have been carried out to investigate the response of a coaxial cable excited by an external plane wave with arbitrary polarisation and orientation with respect to cable axis. Several braid

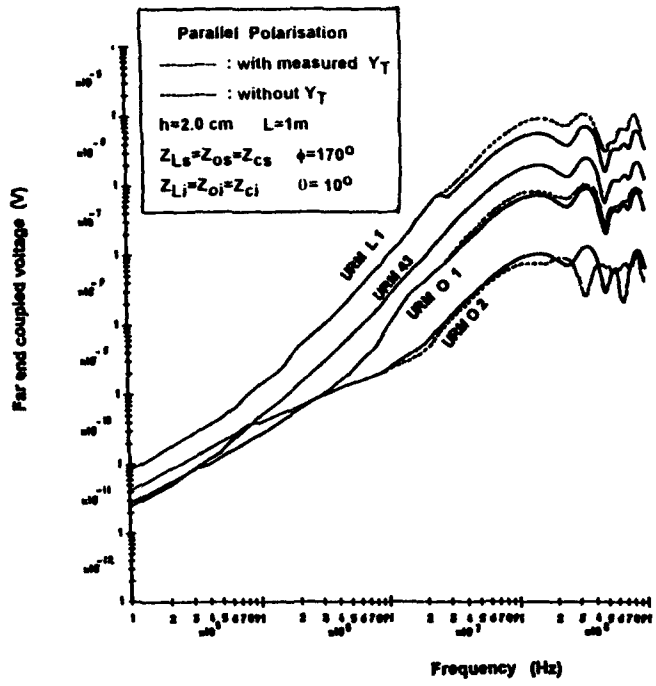

Fig.4 Frequency response of the cable samples examined. The sheath and cable matched at both ends. Results are computed by using measured values of Y_T.

designs under different load conditions in the tertiary circuit were investigated, using the standard (high optical coverage), optimised and leaky (low optical coverage) of URM43 size (2.95 mm over inner dielectric) cables. The results of these measurements are given in [Sali 1993] and [Sali 1990] and they are used in these studies also. The electrical and geometrical parameters of the cable samples used in the studies are given in Table I of the Appendix.

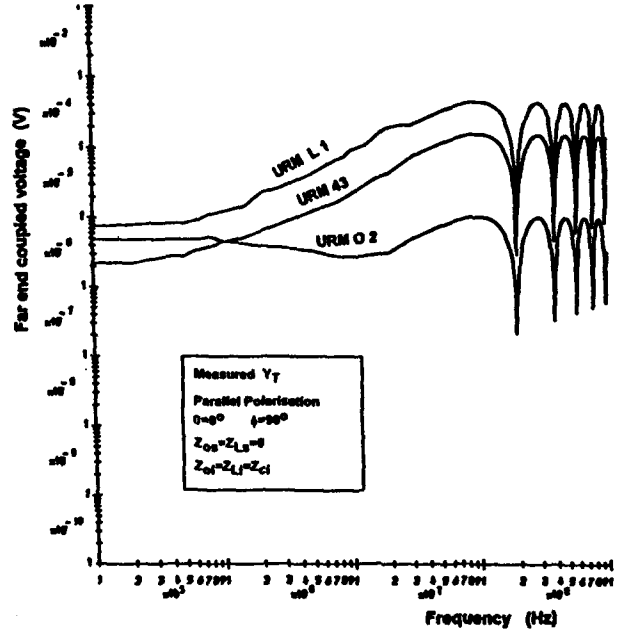

Fig.5 Frequency response for a 1m sample of URM L 1. The sheath is shorted to a conducting plane at both ends. The cable is matched. Results are computed using measured values of Y_T in the general method.

A general computer program was developed using the theoretical field coupling model in Section II. The frequency range was between 100 KHz and 1 GHz. In each case the incident field was a uniform plane wave with a maximum E-field intensity of 1V/m, and the conducting plane was assumed to be made of Aluminium. Since all the existing EMI studies on braid wire shielded cables ignore Electric field coupling no comparable study exists in the literature. However the accuracy of our EMI model is checked against the technique suggested in [Smith 1977]. Since Smith's model, is originally suggested for lossless shield above lossless conducting plane and ignores Y_T coupling our model had to be simplified to this simple case before the comparison. Results of these studies showed that both approaches produce identical results.

Fig.4 shows the results for the far end induced voltage for URM43 (standard), URM L 1 (leaky) , URM O 1 ,and URM O 2 (both optimised) cables respectively, when the tertiary circuit and the interior of the cables are matched. Graphs with solid lines show the responses of the cables when Y_T is returned zero in the interference model and those with broken lines show the results for the same cables when the measured values of Y_T are included in the calculations . The results for URM 43 (which has a high optical coverage and Z_T values) show that coupling curves with and without Y_T are almost identical. However curves for URM O 2 and L 1 give 20 dB difference in the standing wave region with and without Y_T included in the model. Fig.5 shows the results when external circuit is shorted to the conducting plane. The short circuits enhance the series magnetic currents in the tertiary at the expense of shunt voltages between the shield and the conducting plane. In this case the magnetic field coupling dominates. Further simulations have already confirmed that coupling curves with and without Y_T are almost identical for all cable samples with shorted external circuit and the electric field coupling may be ignored .

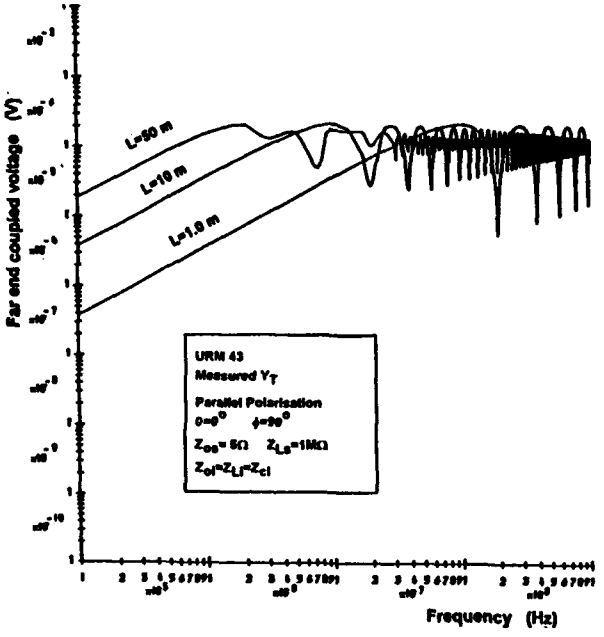

Fig.6 Frequency response of URM 43 versus coupling length.

The amount of energy coupled to the cable depends on the amount of flux induced by the dipole (or scattered) mode fields in the area between the braided shield and the ground plane, as illustrated in Fig.3. Simulations have been carried out to investigate the effect of increased surface area on the amount of the field coupling to inside of the cable, by simply varying either the length or the height of the shield from the ground plane.Fig.6 shows the results for the far -end coupled voltage against frequency when the length of the cable is varied between 1.0 m and 50.0 m. It is seen that increased length results in much higher coupling levels at low frequencies but no noticeable difference between the amplitude values is observed at high frequencies because of the increased attenuation which cancels the increased coupling levels at such frequencies. However the standing wave pattern is brought down to much lower frequencies when the length is increased, as expected. Further simulations have been carried out to investigate the variation of the coupled voltage when the height of the cable is varied from 0.5 mm to 5.0 cm and the results are shown in Fig.7 in the frequency domain. Increase in the coupled voltage is quite rapid at the initial stages but slows down gradually, and little increase is observed for heights greater than 7.0 cm.

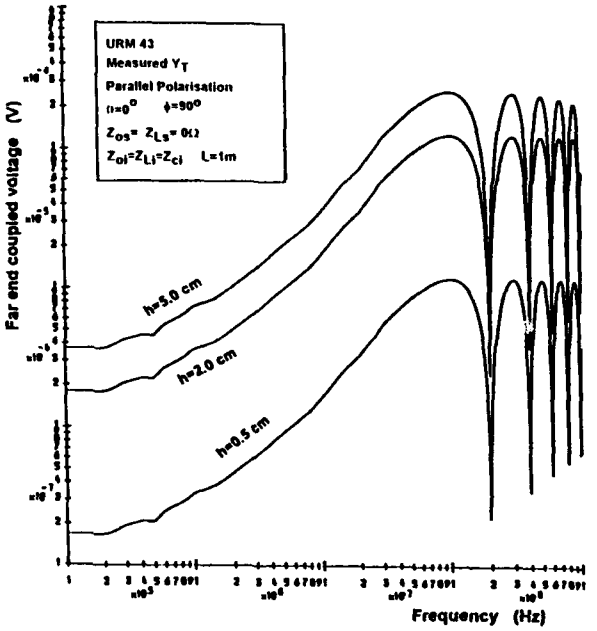

Fig.7 Frequency response for 1m sample of URM 43 cable versus height from the ground plane.

The effect of the cable height on the coupling power is further studied in Fig.8, which shows the coupled voltage induced from a 300 MHz plane wave along the cable length. Note that a coupling minima is expected to occur at 0.5m along the cable (the position here is slightly less as the velocity is taken as $c=3x10^8$). This translates to a position at around 150MHz in frequency domain which is exactly the same frequency position given by the coupling

curves in Fig.5. Results in Fig.6 to 8 clearly illustrate the spatial and frequency dependence of field coupling. Theoretically the positions of minimas are given by $L_n=n\pi/k_0$, as confirmed by these results.

Finally the angular dependence of the field coupling is studied in Figs. 9 and 10 where results for the far end coupled voltage are shown when elevation angle is fixed and azimuth angle is varied as in Fig. 9. and azimuth angle is fixed and elevation angle is varied , as in Fig. 10 Bear in mind that when the fixed angles were changed in both cases, different coupling results would be obtained. This clearly illustrates that there is a strong dependence between the angular orientation of the cable with respect to the direction of Poynting vector of the incident field.

CONCLUSIONS

A general algorithm is presented for the study for the response of coaxial cables with wire braided shields excited by external electromagnetic fields. The model includes both electric and magnetic coupling parameters in contrast to the existing studies on similar problem which only include magnetic field coupling. Numerical studies using this algorithm is concentrated on coupling of the external fields to the cable with various braid designs in their shields and different load conditions in the tertiary circuits between the shield and the ground plane. The studies have covered in detail the role of field orientation and geometry of the external tertiary circuit on the amount of energy coupled to the interior of the coax. The results show that at low frequencies the electric field coupling can be ignored but this is not so at high frequencies and accurate computation of the external field coupling requires that both coupling parameters must be included in the model for optimised cables. Even with short circuited tertiaries, the electric field coupling may contribute significantly to the overall response of the cable when optimised cables are used.

REFERENCES

[Bayindir and Sali, 1990] S.A. Bayindir and S Sali, " Radiation losses in microwave integrated circuits at micro and mm-wave frequencies", Proc. of 16'th QMC Ant. Symp., University of London, 1990.

[Sali, 1993] S. Sali, " Coupling of electromagnetic fields to coplanar striplines with discontinuities", IEE Proc. Pt.H, pp.481-487, Dec.1993.

[Sali, 1993] S. Sali, " A circuit based approach for crosstalk between coaxial cables with optimum braided shields", IEE Trans. EMC-35, No.2, May 1993 pp.300-311.

[Vance, 1973] E.F. Vance, "Comparison of electric and magnetic coupling through braided wire shields", Techn. Rep. No. AFWL-TR-73, 71 Stanford Research Inst., May 1973.

[Sali , 1992] S. Sali, "Screening efficiency of triaxial cables with optimum braided shields," IEEE Trans. EMC-32, May 1992, No.4, pp.123-134.

[Fowler, 1979] E.P. Fowler, "Super screened cables," The radio and Electronic Engineer, Vol.49, No.1, April 1979, pp.38-44.

[Tyni, 1976] M. Tyni, "Transfer impedance of coaxial cables with braided outer conductors", Pr. Nauk. Inst. Telekamun. X, Aukust, Politech Wrocklow, 27, Ser, Korf 1976, pp. 410-419.

[Frankel 1977] S. Frankel," Multiconductor transmission line analysis, Artech House Inc., 1977.

[Smith 1977] A.A Smith, Jr., "Coupling of electromagnetic fields to transmission lines", J. Willey & Sons Inc., NY 1977.

[Taylor and Younan, 1992] C.D. Taylor, and N.H. Younan," Effects of high power microwave illumination", Microwave Journal, June 1992, pp.80-96.

[Harrison ,1972] C.W. Harrison, Jr., "Generalised theory of impedance loaded multiconductor transmission lines in an incident field", IEEE Trans. Vol. EMC-14, No.2, May 1972, pp.56-63.

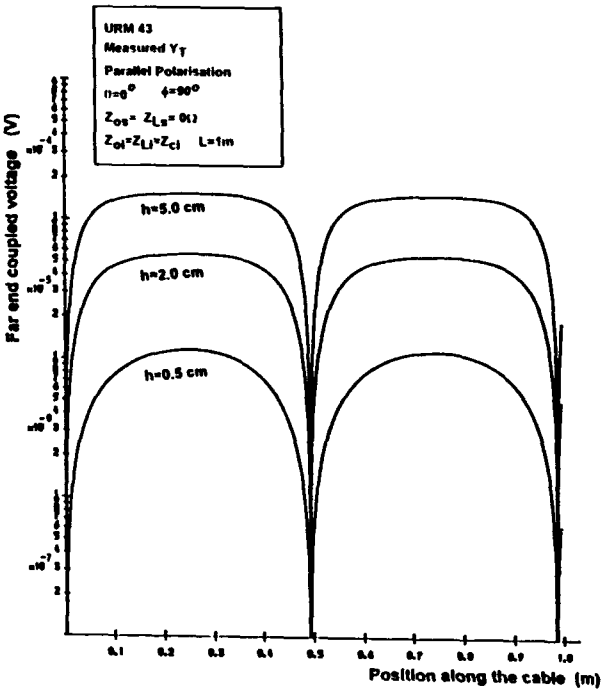

Fig.8 Response for a 1m sample of URM 43 cable versus height from the ground plane. The incident field is a 300 MHz plane wave with parallel polarization.

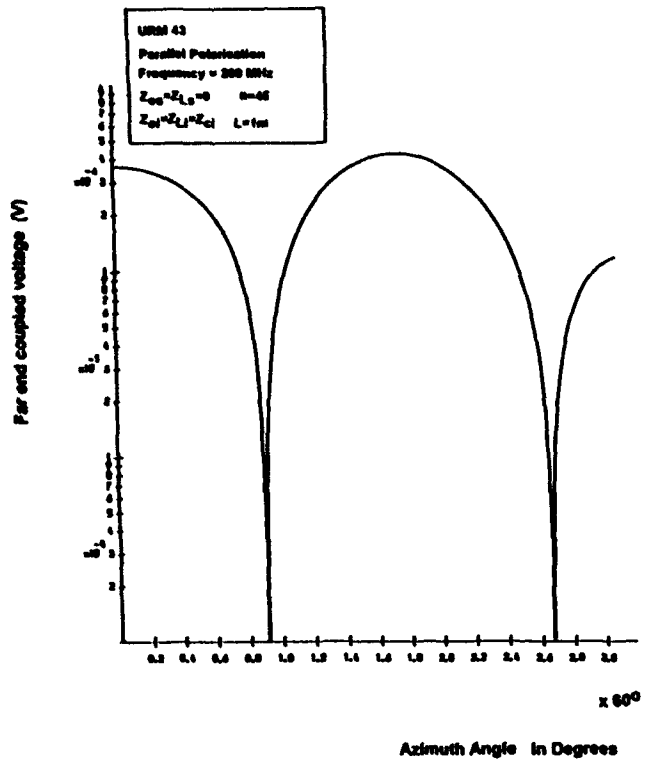

Fig.9 Response of the cable versus incident angle at elevation. Azimuth angle is fixed at ϕ=45°. Frequency of the incident wave is 200 MHz.

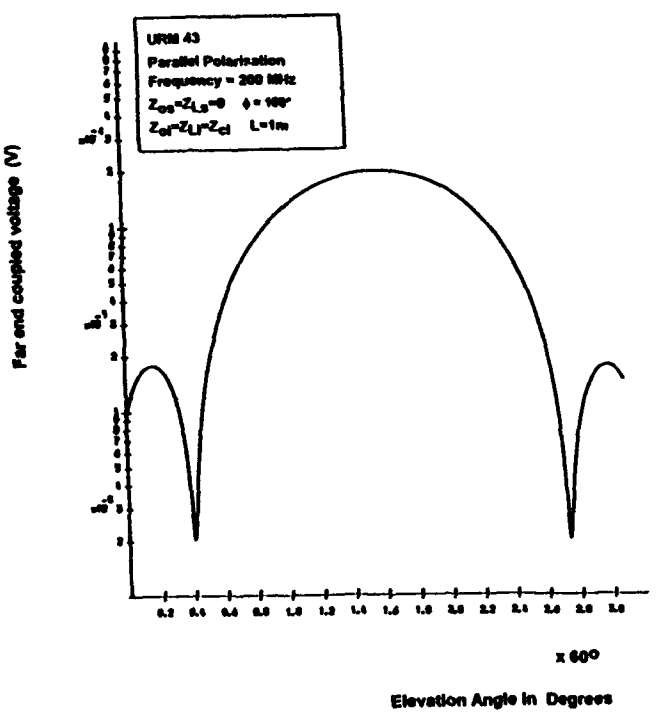

Fig.10 Response of the cable versus incidence angle at elevation. Azimuth angle is fixed at ϕ=100°. Frequency of the incident wave is 200 MHz.

APPENDIX

CABLE	M	n	DOD (mm)	BWD (mm)	LL (mm)	K_f	θ (Deg)	POL
URM 43	16	6	2.95	0.150	22.0	0.77	24.9	-
URM O 1	16	6	2.95	0.100	23.0	0.520	23.28	+
URM O 2	16	7	2.95	0.096	23.2	0.584	23.26	-
URM L 1	16	3	2.95	0.15	16.0	0.40	23.1	-

Table 1 - Geometrical parameters of the cable samples

DOD : Diameter over inner dielectric (do)

BWD : Braid wire diameter (dw)

LL : Lay Length (l)

θ : Braid angle (θ) = $\tan^{-1}(\pi (do + 2.25dw)/l)$

N : Number of spindles

n : Number of braid wires per spindle

K_f : Filling factor $K_f = Nndw/2\,l \sin\theta$

POL : Polarity of the transfer impedance (positive polarity indicates the dominance of the hole inductance and negative polarity that of braid inductance)

CABLE SAMPLES

High Spatial Resolution Analysis of Electric Currents Induced in Man by ELF Magnetic Fields

Weiguo Xi and Maria A. Stuchly
Department of Electrical and Computer Engineering
University of Victoria, Victoria, BC, Canada
V8W 3P6

Abstract This paper presents the formulation of the impedance network method that allows computation of the arbitrary injection currents on the boundary of a selected sub-region for an analysis of induced electric current distributions inside the human body exposed to extremely low frequency magnetic fields. The obtained formulation provides a high resolution modeling of a local region of interest without using an excessively large number of computational cells. The iterative equations for outer and inner nodes are derived in detail. Solutions for a double-layered sphere are then calculated to verify the derived equations. The errors involved in the calculation are also examined. To illustrate the method, its application to computations of the induced currents in the human head is described.

Introduction

Knowledge of the spatial distribution of the electric currents and fields induced in the human body by extremely low frequency (ELF) magnetic fields is important in the assessment of potential health hazards to people [1,2]. A high spatial resolution of these fields is also very useful in some medical applications, e.g., neural stimulation [3]. Although this problem for homogeneous biological bodies is well understood, considerable work remains to be done in the development of numerical methods and algorithms for heterogeneous systems. Among the methods developed for electromagnetic (EM) problems, two differential equation-based methods: the time-domain finite difference method (FDTD) and the impedance or admittance network method, have been found effective for modeling of heterogeneous and complicated 3D bodies representing biological subjects [4]. At ELF, the problem is a quasi-static one as the displacement current is negligible compared to the conduction current. This, together with the fact that a biological system does not perturb an exposing magnetic field, makes the impedance network method especially attractive for the ELF calculation.

As in any other numerical method for EM problems, the impedance method starts with discretizing the space analyzed into computational cells. With large memories (16-64 Mbytes) increasingly available on computers today up to 1 million cells can be routinely handled. A reasonable representation of the human anatomy and its surroundings can therefore be obtained. However, the computing time increases almost exponentially with the number of unknowns. As a result, an increase in the number of the computational cells leads to demands of a computing speed not available in most computers. To illustrate the problem, we evaluated the calculation of a double-layered sphere on an HP 9000/700 workstation. The computation using about 70,000 cubical cells takes about 5 minutes of CPU time and 800 iterations before it reaches convergence. When, to model the curved interfaces more accurately, the cell size is reduced by half in each dimension, resulting in 8 times more of computational cells, i.e., 560,000 cells, convergence is obtained after about 3,600 iterations and 160 minutes of CPU time. Moreover, to model the detailed anatomy and morphology of a whole human body, one needs much more than 1 million computational cells. This is a formidable task in terms of both the memory and the computing speed requirements.

There are many practical situations where high resolution modeling is of interest for only a certain part of the body. For example, such situations arise in case of the exposure evaluation of the head to the magnetic field produced by a hair-drier, or the arm from a hand-held drill. In these situations and others, a finer mesh can be chosen without leading to an excessively large number of cells in any single computation. In previous work, the sub-region was detached from the whole body and analyzed alone [5,6]. Dependent on the exposure situation, the results from such an analysis may be questionable due to the neglect of the injection currents on the boundary where the sub-region is detached.

In this paper, a new approach for the sub-region analysis with a high spatial resolution is presented. In this approach, the injection currents on the sub-region boundary are taken into account by using the previously

computed results for the whole-body as the sub-region boundary values. The formulation involved in the boundary condition is described and verified by modeling a double-layered sphere. Finally, this approach is applied to the calculation of the induced currents in the human head in uniform 60 Hz magnetic fields.

Formulation of Sub-Region Analysis

In the impedance method, at ELF a biological body is represented by a 3D resistance network in which each parallelepiped volume shown in Fig.1(a) is equivalent to three resistances $R_x^{i,j,k}$, $R_y^{i,j,k}$ and $R_z^{i,j,k}$ associated with the network node (i,j,k) as shown in Fig.1(b). The resistances are calculated as [7]:

$$R_m^{i,j,k} = \Delta_m/(S_m \sigma_m^{i,j,k}) \quad (m=x,y,z) \qquad (1)$$

where Δ_m is the cell length in the m-th direction, S_m is the area of the cell surface perpendicular to the m-th axis, and $\sigma_m^{i,j,k}$ is the cell electrical conductivity in the m-th direction. For each node, three line currents: $\hat{I}_x$, $\hat{I}_y$ and $\hat{I}_z$, and three loop currents: I_x, I_y and I_z are defined in Fig.1(c). Once the loop currents are known, the line current through each resistance element can be obtained by summing up the four loop currents which are common to that resistance element. As illustrated in Fig.1(d),

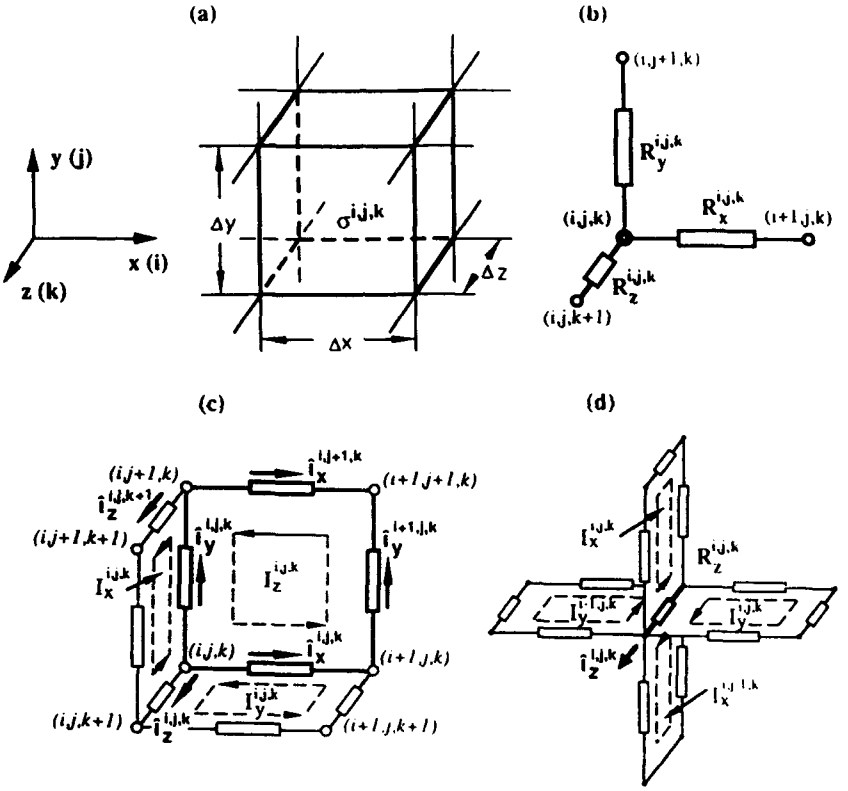

Figure 1. Cell impedance and current definition for the impedance network method.
(a) a parallelepiped tissue volume of the body forming a computation cell (i,j,k);
(b) the three directional impedances associated with node (i,j,k);
(c) the three line currents and loop currents, $\hat{I}_m$ and I_m (m=x,y,z), defined for node (i,j,k);
(d) the line current $\hat{I}_z^{i,j,k}$ composed of the superposition of four loop currents flowing through the resistance $R_z^{i,j,k}$.

the line current through $R_z^{i,j,k}$ can be expressed by the loop currents as

$$\hat{I}_z^{i,j,k} = -I_x^{i,j,k} + I_x^{i,j-1,k} + I_y^{i,j,k} - I_y^{i-1,j,k} \qquad (2)$$

Similarly, $\hat{I}_x^{i,j,k}$ and $\hat{I}_y^{i,j,k}$ can be found to be

$$\hat{I}_x^{i,j,k} = -I_y^{i,j,k} + I_y^{i,j,k-1} + I_z^{i,j,k} - I_z^{i,j-1,k} \qquad (3)$$

and

$$\hat{I}_y^{i,j,k} = -I_z^{i,j,k} + I_z^{i-1,j,k} + I_x^{i,j,k} - I_x^{i,j,k-1} \qquad (4)$$

respectively. Applying Kirchhoff's voltage equation to each loop associated with node (i,j,k), say the z-loop in Fig.1(c), the following relationship is obtained

$$R_x^{i,j,k}I_x^{i,j,k}+R_y^{i+1,j,k}I_y^{i+1,j,k}-R_x^{i,j+1,k}I_x^{i,j+1,k}-R_y^{i,j,k}I_y^{i,j,k}=emf_z^{i,j,k} \quad (5)$$

where $emf_z^{i,j,k}$ is the electromotive force generated by a magnetic field perpendicular to the loop

$$emf_z^{i,j,k}=\omega B_z^{i,j,k}S_z \quad (6)$$

and $\omega = 2\pi f$, where f is the frequency and B is the magnetic flux density.
Substituting Eqs.(3) and (4) into Eq.(5), $I_z^{i,j,k}$ can be solved as

$$\begin{aligned}I_z^{i,j,k}=&[emf_z^{i,j,k}-R_x^{i,j,k}(I_y^{i,j,k-1}-I_y^{i,j,k}-I_z^{i,j-1,k})\\&-R_x^{i,j+1,k}(I_y^{i,j+1,k}-I_y^{i,j+1,k-1}-I_z^{i,j+1,k})\\&-R_y^{i,j,k}(I_x^{i,j,k-1}-I_x^{i,j,k}-I_z^{i-1,j,k})-\\&-R_y^{i+1,j,k}(I_x^{i+1,j,k}-I_x^{i+1,j,k-1}-I_z^{i+1,j,k})]\\&/[R_x^{i,j,k}+R_x^{i,j+1,k}+R_y^{i,j,k}+R_y^{i+1,j,k}]\end{aligned} \quad (7)$$

Similar equations can be derived for $I_x^{i,j,k}$ and $I_y^{i,j,k}$. More details can be found elsewhere [7]. It should be pointed out that the (i,j,k) referred to so far is an inner node, that is, a node surrounded by non-boundary nodes. For outer nodes, some of the line currents in Eq.(5) are the boundary values and should not be converted into the loop currents. Eq.(5) is still valid for outer nodes, however, their final loop current equations differ from those for inner nodes.

Let's consider the generic parallelepiped region shown in Fig.2a. This region can representi either a biological body and its surrounding space or a sub-region identified from the whole body for the purpose of a high spatial resolution analysis. On its six surfaces: left (i=1), right (i=n_x), bottom (j=1), top (j=n_y), rear (k=1) and front (k=n_z), line currents are assumed to be known. In the sub-region analysis, the line current density on the boundary can be obtained by interpolating the results from the whole region analysis. The line currents on the boundary are sometimes called injection currents, however, they may also flow outward or parallel to the boundary as shown in Fig.2(a).

All the outer nodes at which the loop equations are formulated differently from those for inner nodes are classified in Table 1. They do not cover all the outer nodes because the loop currents at some outer nodes are not needed for inner node calculations, such as those loop currents parallel to the boundary surface. According to the number of the boundary line currents employed, the outer nodes in Table 1 fall into three categories: those on the upper surfaces, those along the edges and those on the lower surfaces. The corner node (n_x-1,n_y-1,n_z-1) is included in the case of the edge nodes.

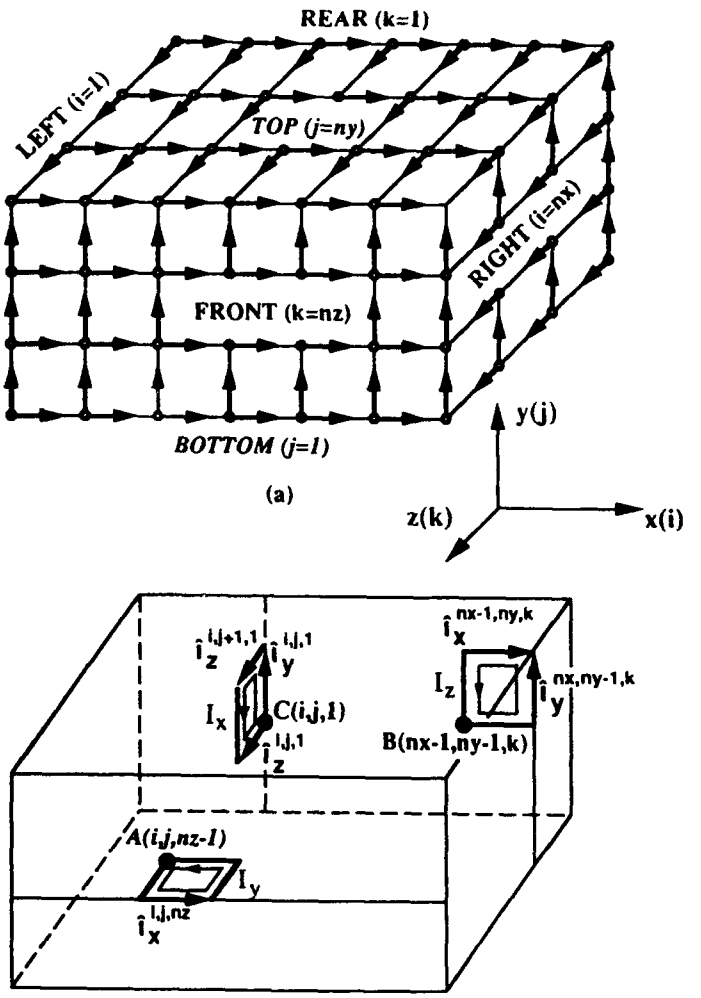

Figure 2 Model for the derivation of iterative loop current equations for the outer nodes of a parallelepiped sub-region.
(a) Line currents on the sub-region boundaries, i.e., left, right, bottom, top, rear and front surfaces;
(b) Three outer nodes: A(i,j,n_z-1), B(n_x-1,n_y-1,k) and C(i,j,1) and the boundary line currents involved in their loop current equations.

In Fig.2(b), the y-loop at A(i,j,nz-1), the z-loop at B(nx-1,ny-1,k) and the x-loop at C(i,j,1) are shown as representative of each category. The boundary line

currents involved around the loop are indicated by arrows; the unmarked line currents need to be decomposed into the loop currents. To illustrate the formulation of the method, the z-loop current equation at node B is derived in detail.

From Eq.(5), the z-loop equation at B(nx-1,ny-1,k) can be written as

$$R_x^{nx-1,ny-1,k} \hat{I}_x^{nx-1,ny-1,k} + R_y^{nx,ny-1,k} \hat{I}_y^{nx,ny-1,k} - R_x^{nx-1,ny,k} \hat{I}_x^{nx-1,ny,k} - R_y^{nx-1,ny-1,k} \hat{I}_y^{nx-1,ny-1,k} = emf_z^{nx-1,ny-1,k} \quad (8)$$

where line currents $\hat{I}_x^{nx-1,ny,k}$ and $\hat{I}_y^{nx,ny-1,k}$ have known values, and $\hat{I}_x^{nx-1,ny-1,k}$ and $\hat{I}_y^{nx-1,ny-1,k}$ are unknown. Using Eqs.(3) and (4), the unknown currents $\hat{I}_x^{nx-1,ny-1,k}$ and $\hat{I}_y^{nx-1,ny-1,k}$ can be expressed as

$$\hat{I}_x^{nx-1,ny-1,k} = -I_y^{nx-1,ny-1,k} + I_y^{nx-1,ny-1,k-1} + I_z^{nx-1,ny-1,k} - I_z^{nx-1,ny-2,k} \quad (9)$$

and

$$\hat{I}_y^{nx-1,ny-1,k} = -I_z^{nx-1,ny-1,k} + I_z^{nx-2,ny-1,k} + I_x^{nx-1,ny-1,k} - I_x^{nx-1,ny-1,k-1} \quad (10)$$

respectively. After substituting Eqs.(9) and (10) into Eq.(8) and rearranging it, $I_z^{nx-1,ny-1,k}$ can be readily found as

$$I_z^{nx-1,ny-1,k} = [emf_z^{nx-1,ny-1,k} + R_x^{nx-1,ny,k} \hat{I}_x^{nx-1,ny,k} - R_y^{nx,ny-1,k} \hat{I}_y^{nx,ny-1,k} + R_x^{nx-1,ny-1,k}(I_z^{nx-1,ny-2,k} + I_y^{nx-1,ny-1,k} - I_y^{nx-1,ny-1,k-1}) + R_y^{nx-1,ny-1,k}(I_z^{nx-2,ny-1,k} + I_x^{nx-1,ny-1,k} - I_x^{nx-1,ny-1,k-1})] / (R_x^{nx-1,ny-1,k} + R_y^{nx-1,ny-1,k}) \quad (11)$$

Using a similar procedure, other loop current equations at the outer nodes listed in Table 1 can be derived.

What complicates the loop current derivation at the outer nodes is the fact that loop currents are the iterative variables in the impedance network method whereas line currents are used as the boundary values. The reason for this is that a loop current is not a physical but an imaginary parameter which only facilitates the iterative calculation. Consequently, the loop currents obtained from the whole region analysis are not directly usable for the boundary formulation of the sub-region analysis.

Outer Node Location	Loop Current	Index Range	Boundary Line Currents Used
Right Surface (i=nx-1)	I_y	$2 \le j \le ny-1,\ 2 \le k \le nz-2$	$\hat{I}_z^{nx,j,k}$
	I_z	$2 \le j \le ny-2,\ 2 \le k \le nz-1$	$\hat{I}_y^{nx,j,k}$
Top Surface (j=ny-1)	I_x	$2 \le i \le nx-1,\ 2 \le k \le nz-2$	$\hat{I}_z^{i,ny,k}$
	I_z	$2 \le i \le nx-2,\ 2 \le k \le nz-1$	$\hat{I}_x^{i,ny,k}$
Front Surface (k=nz-1)	I_x	$2 \le i \le nx-1,\ 2 \le j \le ny-2$	$\hat{I}_y^{i,j,nz}$
	I_y	$2 \le i \le nx-2,\ 2 \le j \le ny-1$	$\hat{I}_x^{i,j,nz}$
Left Surface (i=1)	I_y	$2 \le j \le ny-1,\ 2 \le k \le nz-1$	$\hat{I}_x^{1,j,k}, \hat{I}_x^{1,j,k+1}, \hat{I}_z^{1,j,k}$
	I_z	$2 \le j \le ny-1,\ 2 \le k \le nz-1$	$\hat{I}_x^{1,j,k}, \hat{I}_x^{1,j,k+1}, \hat{I}_y^{1,j,k}$
Bottom Surface (j=1)	I_x	$2 \le i \le nx-1,\ 2 \le k \le nz-1$	$\hat{I}_y^{i,1,k}, \hat{I}_y^{i,1,k+1}, \hat{I}_z^{i,1,k}$
	I_z	$2 \le i \le nx-1,\ 2 \le k \le nz-1$	$\hat{I}_x^{i,1,k}, \hat{I}_y^{i,1,k}, \hat{I}_y^{i+1,1,k}$
Rear Surface (k=1)	I_x	$2 \le i \le nx-1,\ 2 \le j \le ny-1$	$\hat{I}_y^{i,j,1}, \hat{I}_z^{i,j,1}, \hat{I}_z^{i,j+1,1}$
	I_y	$2 \le i \le nx-1,\ 2 \le j \le ny-1$	$\hat{I}_x^{i,j,1}, \hat{I}_z^{i,j,1}, \hat{I}_z^{i+1,j,1}$
X-Edge (j=ny-1,k=nz-1)	I_x	$2 \le i \le nx-1$	$\hat{I}_y^{i,ny-1,nz}, \hat{I}_z^{i,ny,nz-1}$
Y-Edge (i=nx-1,k=nz-1)	I_y	$2 \le j \le ny-1$	$\hat{I}_x^{nx-1,j,nz}, \hat{I}_z^{nx,j,nz-1}$
Z-Edge (i=nx-1,j=ny-1)	I_z	$2 \le k \le nz-1$	$\hat{I}_x^{nx-1,ny,k}, \hat{I}_y^{nx,ny-1,k}$

Table 1 Summary of outer nodes and the boundary line currents involved in the loop current equations.

Verification

A solution for a double-layered sphere is used to verify the formulation and accuracy of the sub-region analysis. The sphere has radii of 0.15 m and 0.25 m, and electric conductivities of 1 S/m and 0.5 S/m for its inner and outer layers, respectively, and is placed in a uniform 60 Hz magnetic field in free space. An analytical solution is elementary for this problem and hence can be used to check the numerical results. The computation accuracy is evaluated by an average relative error defined as [8]:

$$\delta = \frac{\overline{\Delta J_\phi}}{\bar{J}_\phi} = \frac{\sum_{i,j,k} \left| J_\phi^*(i,j,k) - J_\phi(i,j,k) \right|}{N \bar{J}_\phi} \quad (12)$$

in which the summation is performed over all the non-air cells and N is the number of cells. J_ϕ^* and J_ϕ are the numerical and analytical magnitudes of the current density (the only component is in the ϕ direction), and a bar denotes the average value.

The verification is conducted in three steps. In the first step, computations are performed for the whole sphere. In the second step, one eighth of the sphere is considered for a sub-region analysis where the boundary values in the planes of x=0, y=0 and z=0 as shown in Fig.3 need to be assigned. The computational cell size is halved in each dimension, resulting in roughly the same number of cells as for the whole sphere. To examine the effect due to the error in boundary values, the computation of this eighth sphere is performed for two cases. For the first case, the numerical results from the whole sphere, and for the

second case the analytical results, are used as the boundary values. In the final step, a cubical region partially embeded in one eighth of the sphere (see Fig.4) is chosen for another stage of sub-region analysis and the cell size is again halved. The boundary values on the six surfaces of this cube are taken from the numerical results from case one and two, and from the analytical solution.

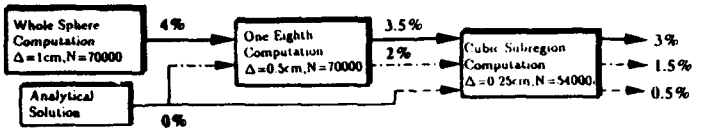

Figure 3 Eighth of a double-layered sphere with a partially embeded cubical sub-region (the mid-horizontal cross-section of the cube shaded.

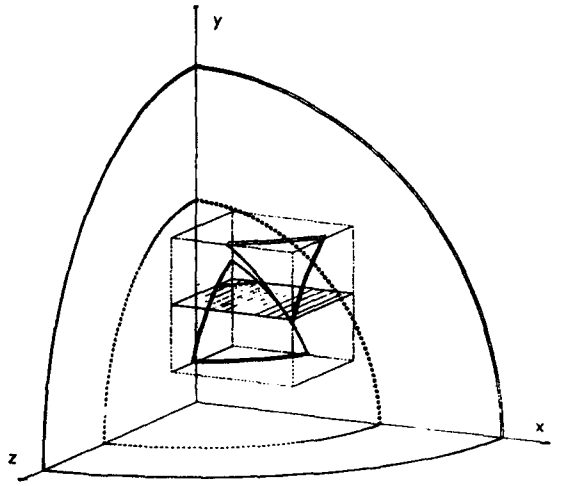

Figure 4 The relative errors in the computations of a double-layered sphere.

The error for each case is illustrated in Fig.4. The average error in the numerical results after each stage of sub-region cell size halving is reduced to at least half of the larger cell value, provided the boundary values used are accurate. This is, understandably, due to the use of finer meshes which model the interface better. The distributions of the induced current densities computed with cells of 1 cm, 0.5 cm and 0.25 cm on the mid-cross section of the cubical sub-region are shown in Fig.5, illustrating a higher spatial resolution with a finer cell modeling. On the other hand, the computational error is much larger when the numerical results are used as the boundary than when the analytical values are used. For instance, the error in the computation for one eighth of the sphere is 3.5% in the case of using the numerical boundary values as compared to 2% when using analytical boundary values. This indicates that the improvement in computation accuracy obtained from one or multi-stage sub-region analysis will be limited unless the whole region analysis is reasonably accurate.

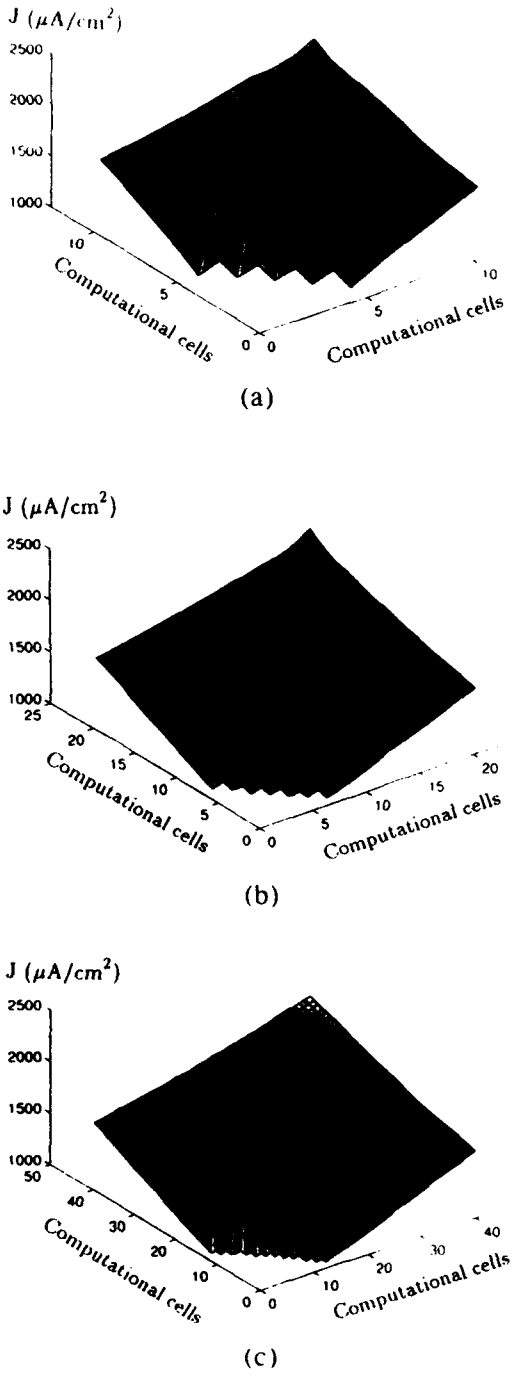

Figure 5 Distribution of the induced electric current density on the surface corresponding to the shaded cross-section in Fig.4, from the computations of
(a) whole sphere using 1 cm cell size;
(b) one eighth of the sphere using 0.5 cm cell size;
(c) cubical sub-region one eighth of the sphere using 0.25 cm cell size.

Sub-Region Analysis of Human Head

To illustrate the application of the above-described approach to sub-region analysis, electric currents and fields induced in the human head by a uniform 60 Hz magnetic field of 1 T directed from the back to the front are computed. The anatomically based man models developed at the University of Utah [4] are used in this computation. The data base of the man models was constructed from a cross-section anatomy book [9]. In creating this data base, a roughly quarter-inch grid (0.665cm) was first divided on each of the transverse body cross-sections which are equally spaced by the grid size. An electric conductivity was assigned to each of such cubical cells, according to the tissue type. Isotropic properties of muscle were used. The conductivity matrix for the body volume and its surrounding space has 90X48X268, i.e., about 1.16 million elements. Since this requires a memory too large for most readily accessible computers, the data for 2X2X2 = 8 cells are combined to form a smaller matrix of 45X24X134 with 144 720 elements. This half-inch model is used in the whole body computation, while the quarter-inch model is used in the computation of the head-region starting from the neck. The boundary values on the neck cross-section are obtained by interpolating (proportionally to the grid surface) the line current densities from the whole body computation.

The average and maximum values of the calculated electric currents and fields induced in the head are listed in Table 2 for three computation cases. The electric field strength is calculated by multiplying the current density by the corresponding conductivity for each cell. First, as case 1 the whole body response of the man model is used with the coarse grid (1/2-inch cell size). A head region is then separated from the neck up and calculations using the finer model (1/4-inch cell size) are performed for two cases which differ by the boundary values assumed on the neck cross-section, The results obtained from case 1 are used in case 2 and null values are used in case 3. Therefore, case 2 takes into account the effects of the whole body, whereas case 3 neglects current flowing between the head and the rest and thus only models an isolated detached head.

From Table 2, it can be seen that the maximum current density and field intensity for smaller computational cells are 2-3 times higher than those of case 1, though the average values are very close to those obtained with the coarser grid. It is expected that the ratio of the maximum to the average for both the current and field in the head would be even larger if the head were modeled with finer computational cells. Secondly, the differences in the average and the maximum values between case 2 and 3 are significant, indicating that the current flow between the head and the rest of the body should not be neglected. It is found that the densities of the current flow through the neck are of the order of 1,000 $\mu A/cm^2$, that is, about half of the maximum or 5 times the average value in the head region. Understandably, for an exposure to a field directed from the back to the front, much smaller electric currents and fields are induced in a detached head than in the head attached to the body because of the smaller coronal cross-sections. If the magnetic field is applied along the body vertical axis (head to toe), the difference between these two cases would be smaller.

The spatial distribution of induced current density on two cross-sections are presented in Fig.6 and Fig.7 for case 2 and 1, respectively. The cross-sections chosen are the frontal passing through the ears and the transverse through the nose. The distribution obtained with the smaller computational cells reflects more anatomical details than with the coarse grid. For instance, a realistic shape of the nose and a distinctive air cavity of the pharynx can be seen in Fig.6a. The difference between the current density in the facial bones (low conductivity) and the facial muscles (high conductivity) is also exhibited in Fig.6. Within the cranial cavity (brain), a relatively uniform current density is shown in both Fig.6 and Fig.7.

Computations Cases	Current Density ($\mu A/cm^2$)		E-Field (V/M)	
	Aver-age	Maxi-mum	Aver-age	Maxi-mum
Case 1: Whole Body Analysis (Δ = 1/2-inch, N = 144,700)	191	1440	14.0	105
Case 2: Head Sub-Region Analysis (Δ = 1/4-inch, N = 35,900)	206	2000	13.7	296
Case 3: Detached Head Analysis (Δ = 1/4-inch, N = 35,900)	161	1050	11.3	65.2

Table 2 Comparison of various computation cases of modeling the electric current and field induced in the human head by a 60 Hz uniform magnetic field of 1 T directed from the back to the front.

Conclusions

It is demonstrated that in calculations of the induced electric current distribution in a 3D - model of the heterogeneous human body, the impedance network method coupled with the sub-region analysis approach is a practicle way of dealing with theconflicting requirements of modeling resolution and computation manageability. Using one or multiple stages of sub-region analysis, a body region of interest can be dealt with in a "zoom" manner without resulting in an excessively large number of computation cells. Of course, a correspondingly fine model of man is required for this purpose. Our example

of the head analysis shows that the 1/4-inch man model results in spatial current distribution with a much higher resolution than those with the 1/2-inch model. However, to properly model some organs, such as eyes, an even finer anatomical model is needed. Computational accuracy can be significantly improved if accurate values of curents at boundaries of the sub-region are known and used in the analysis.

Figure 6 Spatial distribution of the current density induced in the human head on
(a) the frontal cross-section passing the ears and
(b) the transverse cross-section passing through the nose, obtained from the whole body analysis using 1/2-inch man model.

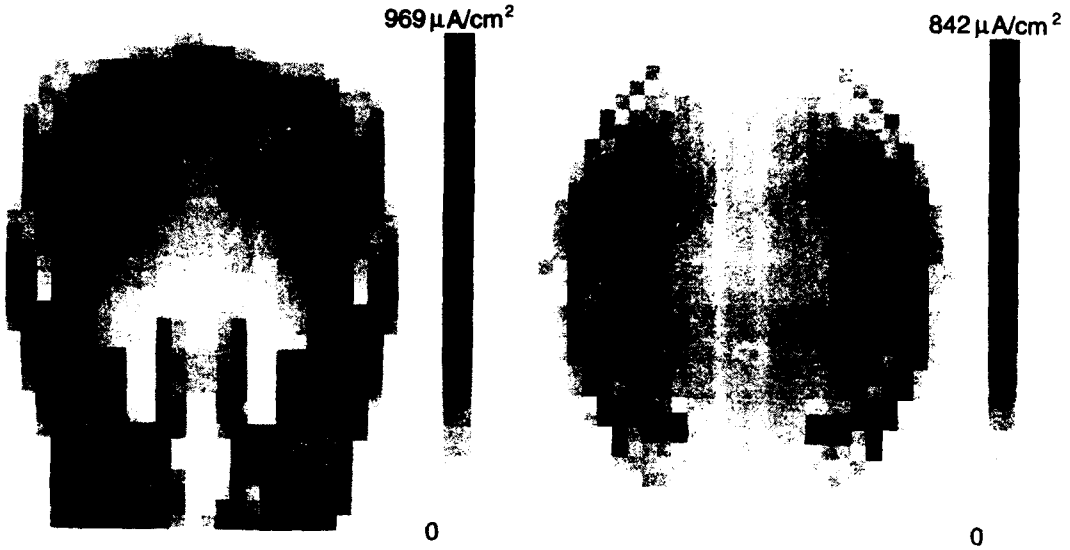

Figure 7 Spatial distribution of the current density induced in the human head on
(a) the frontal and
(b) the transverse cross-sectionpassing through the nose, obtained from the head subregion analysis using 1/4-inch man model.

Acknowledgement

This work is supported by a strategic grant from the Natural Sciences and Engineering Research Council of Canada and a grant from the U.S. National Institutes of Health through a contractual agreement with the University of California, Riverside. The authors also wish to thank Dr. O.P. Gandhi and Ms. C. Furse of the University of Utah for their generous assistance.

References

[1] G. Theriault, "Cancer risks due to exposure to electromagnetic fields", *Recent Results in Cancer Res.*, Vol.120, pp.166-180, 1990.

[2] S.F. Cleary, "In vitro studies: low frequency electromagnetic fields", *Proc. Sci. Workshop on the Health Effects of Electromagnetic Radiation on Workers*, U.S.Dept. of Health and Human Services, Cincinnati, OH, Publ. No.91-111, pp.47-89, 1991.

[3] M.A. Stuchly, "Applications of time-varying magnetic fields in medicine", *CRC Crit. Rev. Biomed. Eng.*, vol.18, pp.89-124, 1990.

[4] O.P. Gandhi and J.Y. Chen, "Numerical dosimetry at power-line frequencies using anatomically based models", *Bioelectromagn.*, Supplement No.1, pp.43-60, 1992.

[5] P.J. Dimbylow, "The calculation of induced currents and absorbed power in a realistic, heterogeneous model of the lower leg for applied electric fields from 60 Hz to 30 MHz", *Phys. Med. Biol.*, Vol.33, No.12, pp.1453-1468, 1988.

[6] P.J. Dimbylow, "Finite-difference time-domain calculations of SAR in a realistic heterogeneous model of the head for plane-wave exposure from 600 MHz to 3 GHz", *Phys. Med. Biol.*, Vol.36, No.8, pp.1075-1089, 1991.

[7] N.Orcutt and O.P. Gandhi, "A 3-D impedance method to calculate power deposition in biological bodies subjected to time varying magnetic fields, *IEEE Trans.Biomed. Eng.*, vol.BME-35, pp.577-587, 1988.

[8] W. Xi, M.A. Stuchly and O.P. Gandhi, "Induced electric currents in models of man and rodents from 60 Hz Magnetic fields", Accepted to *IEEE Trans. Biomed. Eng.*, 1994.

[9] A.C. Eycleshymer and D.M. Schoemaker, *A Cross-Section Anatomy*, New York: Appleton, 1911.

A VECTORIZED MULTIPLE PLATE SCATTERING CODE

John W. Nehrbass and Inder J. Gupta

The Ohio State University ElectroScience Laboratory
Dept. of Electrical Engineering
1320 Kinnear Road, Columbus, Ohio 43212

Abstract

A computer code named Vectorized Multiple Plate Scattering (VMPS) code has been developed at the Ohio State University ElectroScience Laboratory to compute the scattered fields from structures that can be modelled using perfectly conducting flat plates. The VMPS code uses a moment method approach to solve an electric field integral equation for the scattered fields. The code utilizes the vectorization capability of CRAY supercomputers to compute the scattered fields very efficiently. In this paper, the operation of the VMPS code is described and its vectorization efficiency is demonstrated.

I. INTRODUCTION

A computer code named Vectorized Multiple Plate Scattering (VMPS) code has been developed at The Ohio State University ElectroScience Laboratory (OSU-ESL) to compute the scattered fields from structures that can be modelled using perfectly conducting multiple polygonal flat plates. In the VMPS code, an electric field integral equation is solved using a moment method (MM) solution to compute the scattered fields. The code utilizes the vectorization capability of CRAY supercomputers and, thus, computes the scattered fields very efficiently. The MM solution used in the code is basically the same as used in the Electromagnetic Surface Patch (ESP) code [1]. However, the code has been rewritten to facilitate vectorization on a CRAY supercomputer.

In the MM solution, the equivalent currents on the various plates are approximated by piecewise sinusoidal basis functions defined over quadrilateral patches. Therefore, this code divides the various plates into quadrilateral patches. A piecewise sinusoidal function (mode) is defined over every two quadrilateral patches that share a common side. Whenever two plates have a common edge, overlap modes, as shown in Figure 1, are placed near the edge to ensure the continuity of currents. The test sources in the moment method solution are filamentary dipoles placed along the axial center of the various modes.

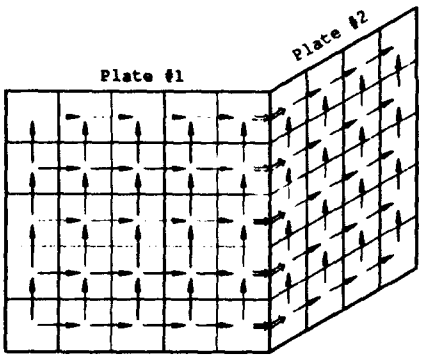

Figure 1: Quadrilateral patches on two flat plates and modal distribution. (⟶) plate modes, (⟹) overlap modes.

In this paper, the operation of the code is described and the approach used to vectorize various section of the code is discussed. The CPU time used by the code on a VAX 8550 computer, an IBM 486 personal computer and a CRAY Y-MP computer are compared. The vectorization efficiency of the code is studied by executing the code on the CRAY Y-MP computer both in scalar and vector modes. It is shown that by developing a code so that vectorization is facilitated, one can decrease the CPU time by a factor as large as 8.

II. CODE DESCRIPTION

An EM moment method code, in general, consists of the following steps.

1. Read the geometry of the structure, frequency of operation and angular regions along which the scattered fields are to be computed.
2. Set up the modal distribution.
3. Compute the impedance matrix $[Z]$.
4. Compute the excitation vector $[V]$.
5. Solve for the unknown current coefficients $[I]$.
6. Using the equivalent currents, calculate the scattered fields.
7. Write the scattered fields to a data file.

For electrically large structures (defined by more than 50 modes), Steps 3 and 5 use most of the CPU time followed by steps 4 and 6. These four steps account for more than 98% of the total CPU time. The VMPS code is, therefore, written to facilitate the vectorisation of these four steps. Since steps 1 and 7 involve input/output operations which can't be vectorised, no attempt has been made to vectorize these sections of the code. Further, existing software from the Electromagnetic Surface Patch Code [1] is used to set up the modal distribution. The approach used to vectorise steps 3 through 6 is discussed below.

Impedance Matrix

Using the MM solution of an electric field integral equation (EFIE), the elements of the impedance matrix are given by

$$Z_{mn} = -\iint_{S_n} \vec{J}_n \cdot \vec{E}_m dS_n \qquad (1)$$
$$m, n = 1, 2 \cdots N$$

where $\vec{E}_m$ is the field of the m^{th} test source, $\vec{J}_n$ is the current distribution on the n^{th} mode, N is the total number of modes, and the integration is carried over the surface defining the n^{th} mode. In the MM solution used in the code, the test sources are filamentary dipoles placed along the axial center of the various modes. Thus, a test source consists of two sinusoidal monopole filaments placed end-to-end. The radiated fields of a monopole filament with sinusoidal current distribution are known in closed form. For example, if the monopole is positioned along the z axis, as shown in Figure 2, the field at a point $P(\rho, z)$ is given by

$$\vec{E} = \frac{\eta_0}{4\pi \sinh(\gamma d)} \left[\left\{ \frac{\exp^{-\gamma R_2}}{R_2} - \cosh(\gamma d) \frac{\exp^{-\gamma R_1}}{R_1} \right\} \hat{z} + \frac{1}{\rho} \left\{ \sinh(\gamma d) \exp^{-\gamma R_1} + \cosh(\gamma d) \cos\theta_1 \exp^{-\gamma R_1} - \cos\theta_2 \exp^{-\gamma R_2} \right\} \hat{\rho} \right] \qquad (2)$$

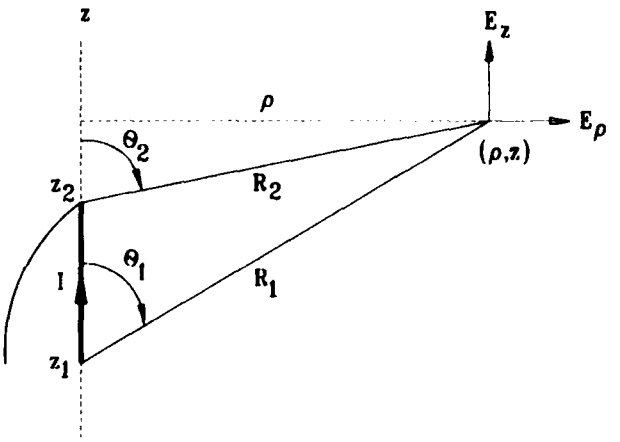

Figure 2: A filament with a sinusoidal current distribution positioned along the z axis.

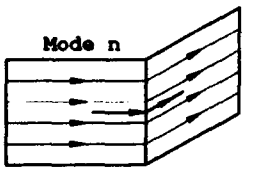

Figure 3: Mode n is defined by filamentary V-dipoles.

where η_0 is the free space intrinsic impedance, d is the length of the monopole, and γ is the complex propagation constant. For this work, γ is purely imaginary. The distances (ρ, R_1, R_2), angles (θ_1, θ_2) and unit vectors $(\hat{\rho}, \hat{z})$ are defined in Figure 2. Note that (2) does not include the field contribution from the point charge at the end of the monopole. Since two of these monopoles are placed end-to-end to form a test source, the contributions from the two point charges are cancelled. The field, $\vec{E}_m$, of the m^{th} test source is found by adding the fields of the individual monopoles. Next, numerical integration can be carried out to solve (1).

Note that when the observation point P moves closer to the filamentary dipole, the distance R_1 and R_2 will become small and the field as given in (2) will approach infinity. Thus, (2) can not be used to calculate the self impedance terms or the impedance terms for overlapping or touching modes. Let these terms be defined as near-zone terms. To compute the near zone terms, the n^{th} mode in (1) is represented by an array of filamentary V-dipoles (see Figure 3). The impedance term is then found as the weighted sum of the reaction between the test

source and these filamentary V-dipoles. To compute these reactions, the distance between the test source and each filamentary V-dipole is examined. Numerical integration is performed whenever the distance is large enough such that (2) is not singular. Otherwise Richmond's [2] closed form solution is used. The closed form solution involves complicated exponential integrals and requires more CPU time.

In the VMPS code, to facilitate vectorisation, a whole row of the impedance matrix is computed at a time rather than as individual elements. This approach increases the size of the DO loop structures, which increases the vectorisation efficiency. Note that the m^{th} row of the impedance matrix represents the reaction from the test source m to all modes. This section of the code involves the following steps.

1. Calculate the distance between the test source and the various modes.
2. Separate the near zone terms and select the number of integration points for the other terms (far zone terms).
3. Select the location of the integration points on the various modes and calculate the weights for these points.
4. Find the reaction between the field of the test source and the currents at the selected points.
5. Sum the weighted point reactions to calculate the far zone elements of the impedance matrix.
6. Compute near zone terms.

In the first step, the distances from the m^{th} test source to the various modes are calculated. These distances are used in the second step to identify the near zone terms and to determine the number of integration points for the other terms. If the distance between the test source and a mode is less than a predetermined distance, that element of the impedance matrix is computed using the near zone approach in step 6 and the number of integration points for the mode is set equal to zero. Otherwise, numerical integration is used to compute the element. The number of points used in the integration is selected based on the distance between the source and the test mode. For distances less than or equal to $\lambda/4$, 50 integration points are used. For distances between $\lambda/4$ and $\lambda/2$, 18 integration points are used. For distances between $\lambda/2$ and 2λ, 8 integration points are used, and for distances greater than 2λ, only two integration points (a single point on each quadrilateral defining the mode) are used.

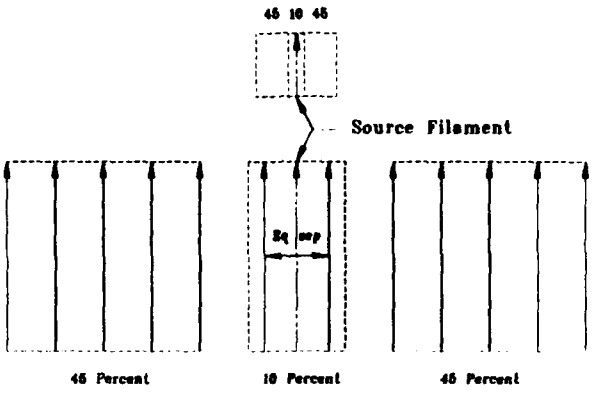

Figure 4: Filamentary monopole distribution when the source monopole lies along the center line of a quadrilateral.

Note that this step provides a map of the number of integration points for various modes.

In step 3, the locations of the integration points on the various modes are found and the integration weights for these points are defined. In step 4, the reaction between the fields of the m^{th} test source and the currents at all the integration points selected in step 3 is calculated. Note that for large structures the total number of integration points will be very large. Thus, the DO loop structure in this step has a large index. In the VMPS code, this DO loop is written to maximise vectorisation. In step 5, the point reactions associated with a mode are combined to obtain the elements of the impedance matrix.

The above five steps compute all the elements of the m^{th} row of the impedance matrix except the near zone terms. The near zone terms are computed in step 6. Again, to facilitate vectorization, all the near zone terms are calculated as a group, rather than as individual elements. The procedure used to compute the near zone terms is briefly described below.

To compute a near zone term of the impedance matrix, each quadrilateral of a mode is represented by an array of filamentary monopoles. The distribution of the filamentary monopoles depends on the location of the source monopole (remember that the test source consists of two monopoles) with respect to the quadrilateral. If the source monopole lies along the centerline of the quadrilateral, then the filamentary monopole distribution on that quadrilateral is given in Figure 4. Otherwise, the filamentary monopoles are equally spaced on the quadrilateral. Using the above approach, the filamentary monopole distribution on all the near zone modes for a given source monopole is found and the integration

weights for the various monopoles are calculated. Next, these filamentary monopoles are grouped in two sets. The first set contains all of the filaments for which the reactance can be computed using numerical integration, and the second set contains the filaments for which Richmond's closed form solution is used. The reactances for the two sets are computed in two separate DO loops. Again, the DO loops are written to facilitate vectorisation. Next, these reactances are combined to obtain the elements of the impedance matrix. It should be pointed out that Richmond's solution involves extensive computations and is very hard to vectorise.

This completes the calculation of one row of the impedance matrix. The procedure is repeated over all of the test sources to compute the whole impedance matrix.

Excitation Vector

Using the MM solution of EFIE, the elements of the excitation vector are given by

$$V_m = \iiint_{V_m} \vec{E}_i \cdot \vec{J}_m dv_m \qquad (3)$$

where $\vec{E}_i$ is the incident field, $\vec{J}_m$ is the current along the mth test source and the integration is performed over the volume of the test source. Since filamentary test sources are used in the VMPS code, (3) can be written as

$$V_m = \int_{l_m} \vec{E}_i \cdot \vec{J}_m dl_m \qquad (4)$$

where integration is carried out over both monopoles that comprise the test source m.

Let the impressed current source be located at (r_0, θ_o, ϕ_0) and separated by a large (electrically) distance from the scatterer. Then the incident field $\vec{E}_i$ can be considered as locally planar and can be written as

$$\vec{E}_i = \vec{E}_0 e^{jk\vec{r}\cdot\hat{r}_0} \qquad (5)$$

where $\vec{E}_0$ is a constant containing the polarization of the incident field, $\hat{r}_0$ is a unit vector from the coordinate origin to the source and $\vec{r}$ is a radial vector from the origin to the observation point. Substituting (5) into (4), one obtains

$$V_m = \vec{E}_0 \cdot \int_{l_m} \vec{J}_m e^{jk\vec{r}\cdot\hat{r}_0} dl_m. \qquad (6)$$

Or,

$$V_m = -\frac{4\pi j}{\omega\mu} \vec{E}_0 \cdot \vec{E}_m \qquad (7)$$

where

$$\vec{E}_m = \frac{j\omega\mu}{4\pi} \int_{l_m} \vec{J}_m e^{jk\vec{r}\cdot\hat{r}} dl_m \qquad (8)$$

is the far-zone field of the m^{th} source. The closed form expression for the far-zone fields of an electric line source with sinusoidal current distribution is known [3]. Since the test source consists of two monopoles with sinusoidal current distribution, $\vec{E}_m$ and, thus, the elements of the excitation vector are known in a closed form. In the VMPS code, all the elements of the excitation vector are calculated in a single DO loop, and this DO loop is written to facilitate vectorisation.

Current Coefficients

Once the impedance matrix and the excitation vector have been determined, it is a straight-forward task to compute the current coefficients. The current coefficients are given by the following set of linear equations.

$$[Z][I] = [V] \qquad (9)$$

where $[Z]$ is the impedance matrix, $[V]$ is the excitation vector, and $[I]$ is a vector containing the current coefficients. Most of the vector computers have very efficient routines to solve a set of simultaneous linear equations. For CRAY supercomputers, NAGLIB library routines are recommended. In the VMPS code, routines F03AHE and F03AKE are used. Routine F03AHE is used for LU decomposition, and routine F03AKE is used in the second step (back substitution).

Scattering Field Calculations

To calculate the scattered fields, the current flowing on the surface of various modes is represented by 5 filamentary V-dipoles with piecewise sinusoidal current distribution. The scattered field for each mode is then given by the weighted sum of the 5 V-dipoles representing the mode. The fields radiated by a given filamentary V-dipole can be calculated by summing the fields radiated by the two monopoles forming the dipole. As pointed out before, the closed form expression for the far-zone fields of an electric line source with sinusoidal current distribution is known. Thus, to calculate the scattered fields, one needs to compute the fields radiated by $10N$ monopoles, where N is the total number of modes. Next, all these fields can be summed to compute the total scattered fields. In the VMPS code, a single DO loop is used to calculate the fields radiated from

Table 1: CPU time (in seconds) used by the VMPS code to analyse 1 meter square plate on various computers.

Freq. (MHz)	No. of modes	VAX 8550	IBM 486 PC	CRAY Y-MP scalar mode	CRAY Y-MP vector mode
300	40	113.75	109.14	10.36	1.48
400	84	301.31	282.10	26.55	3.81
500	144	596.88	569.75	52.72	7.32
600	180	800.02	757.41	69.26	9.03
700	264	1400.18	1344.58	117.89	15.62
800	364	2275.81	2171.21	184.78	23.64
900	420	2809.23	2664.00	223.83	28.33
1000	544	4308.07	4050.88	327.86	42.10

Table 2: CPU time used to calculate the impedance matrix on a CRAY Y-MP computer.

Freq. (MHz)	CPU (seconds) Scalar Mode	CPU (seconds) Vector Mode	Improvement
300	7.30	0.96	7.60
400	19.37	2.73	7.10
500	38.52	5.29	7.28
600	49.97	6.53	7.65
700	84.18	11.48	7.33
800	128.61	17.07	7.53
900	152.46	20.05	7.60
1000	215.53	29.65	7.27

all monopoles. Again, the DO loop is written to facilitate vectorisation.

Thus, the four major steps (3–6) in the moment method code have been vectorised. The improvement in the computation speed due to this vectorisation is demonstrated in the next section.

III. CODE EFFICIENCY

The VMPS code was executed on various computers to calculate the backscattered fields from a square plate and the CPU time used by the code on these computers is listed in Table 1. The plate dimensions are 1 meter × 1 meter. The backscattered fields are calculated at different frequencies along a 45° conical cut in 1° steps (361 aspect angles). The CPU time listed in the table is the time spent in steps 3 through 6 of the computer program. The number of modes used to define the equivalent currents on the plate at various frequencies is also listed in the table. Note that, as expected, the number of modes increases with the frequency of operation, and so does the CPU time used to calculate the plate back scattered fields. For fair comparisons, only a single processor was used on the CRAY computer. Note that the code uses the maximum CPU time on VAX 8550 computer and the minimum CPU time on CRAY Y-MP computer. This is true even if the vector option of the CRAY computer is not utilised; i.e. the code is compiled with no vectorisation option (scalar mode operation). When the vectorisation option is utilised on the CRAY, the CPU time shows further improvement. At higher frequencies, the CPU times used in the vector mode of operation is only one eighth of the CPU time used in the scalar mode of operation, which is a significant improvement. In the vector mode of operation, the code uses only 42 CPU seconds to analyse the plate at 1,000 MHz, which is very efficient.

When the code was run on the VAX 8550, IBM 486 and in the CRAY scalar mode of operation, a subroutine based on Crout's method [4] was used to solve for the unknown current coefficients in step 5. In the CRAY vector mode of operation, this subroutine was replaced by NAGLIB subroutines. The *reason for using the Crout based subroutine in* the scalar mode of operation is that the NAGLIB subroutines are compiled using the vectorisation option and we did not have access to the source subroutines.

Next, to study the extent to which various sections of the code have been vectorised, the CPU time used in the various sections of the code in scalar mode and vector mode of operation are compared. Tables 2, 3, 4 and 5, respectively, compare the CPU time used to calculate the impedance matrix, excitation vector, current coefficients and the backscattered fields. Note that, as expected, all sections of the code use less CPU time in the vector mode of operation. The improvement in the CPU time used to calculate the impedance matrix is approximately a factor of 7.5; whereas, the improvement in the CPU time used to calculate the excitation vector is approximately a factor of 8.8. Similarly, the improvement in the CPU time used to calculate the scattered fields is approximately 7.8. In general, for an optimally vectorised computer code the improvement in the CPU time in the vector mode of operation is a factor of 9–10. Thus, these sections of the code have been vectorised effectively. The improvement factor for the CPU time used to calculate the current coefficients

Table 3: CPU time used to calculate the voltage vector on a CRAY Y-MP computer.

Freq. (MHz)	CPU (seconds)		Improvement
	Scalar Mode	Vector Mode	
300	0.41	0.053	7.74
400	0.86	0.11	7.82
500	1.47	0.19	7.74
600	1.84	0.21	8.76
700	2.70	0.31	8.71
800	3.72	0.42	8.86
900	4.30	0.49	8.78
1000	5.56	0.63	8.82

Table 4: CPU time used to calculate the current coefficients on a CRAY Y-MP computer.

Freq. (MHz)	CPU (seconds)		Improvement
	Scalar Mode	Vector Mode	
300	0.39	0.097	4.02
400	1.63	0.27	6.04
500	4.75	0.68	6.98
600	7.47	0.94	7.95
700	16.43	1.88	8.74
800	32.31	3.52	9.18
900	43.88	4.73	9.28
1000	76.80	7.93	9.68

Table 5: CPU time used to calculate the scattered fields on a CRAY Y-MP computer.

Freq. (MHz)	CPU (seconds)		Improvement
	Scalar Mode	Vector Mode	
300	2.19	0.30	7.30
400	4.62	0.63	7.33
500	7.91	1.11	7.13
600	9.91	1.28	7.74
700	14.51	1.87	7.76
800	20.06	2.56	7.84
900	23.11	2.99	7.73
1000	29.87	3.82	7.82

Table 6: CPU time (in seconds) used by the VMPS code and the ESP4 code on a CRAY Y-MP computer.

Freq. (MHz)	Scalar mode		Vector mode	
	ESP4	VMPS	ESP4	VMPS
300	6.48	10.36	6.24	1.48
400	16.33	26.55	15.36	3.81
500	33.58	52.72	30.39	7.32
600	49.95	69.26	40.46	9.03
700	81.09	117.89	69.19	15.62
800	134.41	184.78	110.41	23.64
900	169.71	223.83	136.87	28.33
1000	263.18	327.86	204.21	42.10

increases with an increase in the frequency of operation and reaches as high as 9.68. This improvement may be misleading in the sense that different routines have been used in the scalar mode and vector mode of operation. Remember that in the vector mode of operation NAGLIB subroutines are used; whereas, a Crout based subroutine is used in the scalar mode of operation. In any event, the CPU time in the vector mode of operation is quite small and it is clear that NAGLIB subroutines are very efficient.

Next, to demonstrate the computation efficiency of the VMPS code, its CPU times are compared with the CPU times of the ESP4 code. Both codes were executed on the CRAY computer in scalar as well as vector mode of operation using the same options. The same modal distribution was used in the two codes. Table 6 shows the CPU time used by the two codes at different frequencies. Note that in the scalar mode of operation, the ESP4 code is a little more efficient than the VMPS code. This is because the VMPS code performs more calculations and is written to calculate the impedance matrix more accurately. The ratio of the CPU times used by the two codes, however, is approaching unity at higher frequencies. In the vector mode of operation, the VMPS code is completely outperforming the ESP4 code. The VMPS code is 4–5 times faster than the ESP4 code. The ratio of the CPU time used by the ESP4 code to the CPU time used by the VMPS code increases with an increase in the frequency of operation. Thus, the VMPS code utilises the vectorisation capability of CRAY supercomputers better than the original ESP4 code.

IV. SUMMARY AND CONCLUSIONS

The operation of the VMPS code was described and the approach used to vectorise the various parts of the code was discussed. It was demonstrated that the code runs very efficiently on CRAY supercomputers. For example, to compute the back scattered fields of a square plate with 544 modes, the code used only 42.1 CPU seconds on a CRAY Y-MP machine.

For the VMPS code, the CPU time may not be the limiting factor in analysing electrically large structures. The available memory space may be the limitation. This problem can be addressed using an out-of-core matrix solver. In the future, the VMPS code will be modified to incorporate out-of-core matrix solver.

Acknowledgement

This work was supported by NASA, Langley Research Center, Hampton, VA. The authors also want to express their thanks to the Ohio Supercomputer Center for the Grant #PAS355 which was a major factor in starting this research.

REFERENCES

[1] E.H. Newman, "A User's Manual for Electromagnetic Surface Patch Code: ESP Version IV," Technical Report 716199-11, The Ohio State University ElectroScience Laboratory, Columbus, OH, August 1988.

[2] J.H. Richmond and N.H. Geary, "Mutual Impedance of Non-Planar Skew Sinusoidal Dipoles," *IEEE Trans. Antennas and Propagat.*, Vol. AP-23, pp. 412–414, May 1975.

[3] J.H. Richmond, "Radiation and Scattering by Thin-Wire Structures in the Complex Frequency Domain," Technical Report 2902-10, The Ohio State University ElectroScience Laboratory, Columbus, OH, July 1973.

[4] G. Forsythe and C.B. Moler, Computer Solution of Linear Algebraic Systems, Prentice Hall, Englewood Cliffs, NJ, 1967.

PARTIAL SURVEY OF CODES FOR HIGH FREQUENCY SCATTERING FROM FACET MODELS OF RADAR TARGETS

Michael A. Richards
Nichols Research Corporation
Shalimar, Florida 32579

ABSTRACT

In this work, four high-frequency electromagnetic scattering codes are surveyed with regard to their capabilities and limitations for the calculation of the radar cross section (RCS) of facet models of targets. The codes discussed are MISCAT, NRCPTD, McPTD, and Xpatch. All of these codes utilize the physical theory of diffraction (PTD) to approximate the field scattered from the target. A short discussion of the modeling features of each code is given and some sample numerical results are generated. It is concluded that, of the models considered here, Xpatch possesses the most comprehensive modeling features available, with no loss in accuracy over the other codes.

1.0 INTRODUCTION

Choosing a high-frequency electromagnetic scattering code to accurately describe the radar signature of a given target can be a substantial endeavor. Often, the modeller will utilize the "familiar" code even when it is not the tool best suited to the objective. Also, when there is a lack of accessible information on available codes, additional effort may be expended in modifying existing models or in developing new codes to perform a specific task. However, as users become more familiar with the available models, the need to modify existing codes and develop new models is sometimes decreased.

The purpose of this paper is to familiarize the reader with the aforementioned scattering codes. It is acknowledged that this survey is not comprehensive in that only four PTD-based computer models are considered. Other excellent models are available that utilize the PTD and/or the Geometrical Theory of Diffraction (GTD).

2.0 TARGET MODELING AND SCATTERING CODES

In this report, four active far-field electromagnetic scattering codes are discussed. These are MISCAT, McPTD, NRCPTD, and Xpatch. All of these codes are written in FORTRAN and employ the PTD to determine the scattering signature of radar targets. The PTD does not include higher order edge diffractions or creeping wave effects. These codes do not model the scattering from extended targets. The incident radiation is assumed to be a uniform plane wave with constant magnitude and polarization over the target surface, and the scattered radiation is assumed to be a spherical wave emanating from a single location. Also, these models do not currently possess the capability to comprehensively analyze rough surfaces in that no incoherent scattering pheonomena are modeled. However, the Xpatch code does have the capability to associate a user-defined reflection coefficient with the scattering surface as discussed in section 2.4. Some of the assumptions, limitations, and modeling features of these codes are discussed in the following sections.

2.1 MISCAT

The MISCAT scattering code was written by Northrop Corporation for the U.S. Army

Missile and Space Intelligence Center (MISC) [1]. The code was written for the purpose of calculating the RCS of complex airborne targets such as aircraft and missiles.

The current version of the code [2] calculates the RCS of conducting or coated conducting targets. The RCS calculation can be monostatic or bistatic, and both co-polarized and cross-polarized scattering signatures can be determined. The target geometry is modeled as a set of primitives (plates, polygonal cylinders, elliptical cylinders, and bodies specified by surface contours) and the total body RCS is obtained by coherently summing the contribution due to each geometrical primitive.

The code can be used to predict the scattering signature of convex targets. Its major limitations are in the shadowing calculation and single-bounce scattering assumption. The shadowing of a facet is calculated using only the facet normal vector. That is, the shadowing of one portion of the body by another portion is not analyzed. Another limitation of the code comes about due to the method employed to describe the target geometry. The format employed is quite general but also quite bulky and no automatic edge/wedge extraction feature is provided. (If the target under consideration can be modeled using some of the higher-order geometrical primitives, then an automatic wedge contribution calculation can be performed.) The code is quite useful for the purpose for which it was intended -- analysis of airborne targets. However, analysis of these target at aspects associated with body inlets, cavities, and other interacting surfaces can not be performed reliably.

2.2 NRCPTD

This acronym (NRCPTD) is used to signify the author's efforts at RCS prediction of complex targets [3]. At present, NRCPTD is not a single code but consists of separate modules for analyzing different contributions of the scattering process. Some of the features of these codes will now be discussed.

The physical optics (PO) currents depends upon an approximation of the geometrical optics (GO) field on the surface of the illuminated region of the target. When the body can be approximated by a perfect electric conductor (PEC), the GO field is just twice the tangential incident magnetic field since the total tangential electric field is zero on the surface of the body. To allow for the modeling of nonperfectly conducting bodies as well as RAM coated targets, we have utilized the exterior equivalent Fresnel reflection coefficients to obtain the GO surface field.

The material composition of the target can be quite general but not completely arbitrary. The target can consist of PEC components and/or conducting components coated with arbitrary dielectric layers and/or lossy dielectric components coated with dielectric layers. Transparent body components can not be treated with this code.

There exists a shadow boundary on the target which divides the illuminated region from the shadowed region. For a simple convex body, we can distinguish between the illuminated and shadowed regions by use of the body's normal vector. If the target is complex, more elaborate steps can be taken to identify the illuminated portion of the body. The method implemented in this model is approximate but still quite useful. It consists of treating each facet of the target as hidden or illuminated dependent upon whether the centroid of the facet is hidden or illuminated. Clearly, this is an approximation but one that can be used to obtain

any desired level of accuracy by adjusting the facet size. We have also retained the simpler, and computationally faster, surface normal approximation to the shadowed region as a user option.

In using the PTD to approximate the high-frequency scattering signature of a target, it is necessary to know the location and orientation of the geometrical discontinuities (wedges and edges) on the body. In this code an algorithm was implemented to extract exterior wedges and edges (wedges with zero interior angle) from a facet file. The extraction routine locates connected facets and then checks the angle between the adjoining facet normals to decide if a "true" wedge or edge is formed. The angle between the normals for which a wedge is determined is a user-defined parameter and can be set based on how finely the target is discretized.

Since the wedge extraction algorithm looks for wedges and edges when the vertices of two connected facets are the same, it is possible to construct a wedge geometry that the algorithm will not process correctly. For instance, when a wedge is formed by two facets whose vertices are offset such that the wedge does not run the full length of both facets, the wedge will not be found.

In summary, this code employs the PTD to predict the scattered field and associated RCS of complex targets. The target is modeled by a set of triangular facets. The total body contribution is obtained by summing the contribution due to each facet. The facets can be conducting or can be coated with material layers. Geometrical optics is used to approximate the surface field on the target. From the GO surface field, the equivalent currents are calculated. Integrating over the equivalent currents provides the PO approximation to the scattered field. Edge effects can be included for conducting body components. The RCS determined by the code can be monostatic or bistatic and both co-polarized and cross-polarized scattering signatures can be calculated. Angle scans and frequency sweeps can be easily performed.

2.3 McPTD

McPTD consists of a family of component computer codes for the high-frequency computation of the scattered field/RCS of complex targets [4]. The codes were written primarily by S. W. Lee at the University of Illinois and have undergone several upgrades since they were first distributed in 1990. They are currently being distributed by Dr. Lee's company, DEMACO, and by the electromagnetic code consortium (EMCC).

The codes analyze the scattering from a variety of geometrical components ranging from flat facets to numerically-defined, CAD-generated surfaces. A main routine exists for the summation of the field scattered from the different target components.

The primary limitations of the code lie in its inability to model multiple-bounce scattering mechanisms and in its shadowing capability. While the ability to perform accurate shadowing is available, the code uses an inefficient process, just as in NRCPTD. Nevertheless, McPTD is a more sophisticated modeling tool than both MISCAT and NRCPTD discussed previously.

Since the McPTD family of codes is written by the same author as the Xpatch codes to be discussed next, no numerical results generated via McPTD will be given

here. Also, McPTD is essentially a subset of the more sophisticated modeling tool, Xpatch.

2.4 Xpatch

Xpatch consists of a set of codes written primarily by S. W. Lee [5]. The codes analyze the scattering signatures of complex targets in both the frequency and time domains. Shown in Table 1 is a list of some of the capabilities of the various Xpatch modules.

Notice that Xpatch1 and Xpatch2 are frequency-domain codes while Xpatch3 and Xpatch4 are time-domain codes. Although conversion from one domain to another can be accomplished via the Fourier transform, each domain offers computational advantages. For instance, modules 3 and 4 are time-domain codes and do not easily model material parameters.

The Xpatch codes provide for a range of target modeling geometrical primitives. Modules 1 and 3 employ a triangular facet description of the target geometry in ACAD format [6]. (These ACAD facet files can be easily converted to formats applicable for input to MISCAT and NRCPTD). Modules 2 and 4 employ a numerical description of the target surface. The initial graphics exchange specification (IGES) can be used to describe target geometries to the code. Also, the code can utilize constructive solid geometry (CSG) models created with BRL-CAD [7].

The frequency-domain codes (modules 1 and 2) can model the edge diffraction contribution for conducting edges. This contribution is for a single-bounce interaction. That is, only the field originally incident on the target can produce an edge diffraction contribution. Parameter extraction for wedges and edges can be performed by a component preprocessing code.

All modules of the Xpatch family can utilize a shooting and bouncing ray (SBR) algorithm [8,9]. In this approach a dense grid of rays is shot at the target. The rays are traced throughout the target using GO and then a PO integration over the equivalent currents on the last interacting surface is performed. Perfect specularity is assumed in the ray tracing. Shadowing is automatically performed in the SBR analysis.

When using facet models generated via CAD packages, errors in the direction of the facet normal vectors is a common occurrence. Using the Xpatch codes in SBR mode eliminates the need to know the direction of the facet normal vector.

Another feature of the Xpatch code is its capability to read a set of angular and frequency dependent reflection coefficients and associate these coefficients with various facets on the target. These coefficients are then used in the ray tracing and equivalent current computation. It appears feasible to use this feature of the code to model the reduction in the coherent component of the RCS of a slightly rough target. This has application in the millimeter wave (MMW) region of the spectrum.

The documentation provided with the Xpatch codes is currently limited. No comprehensive technical description of the techniques and approximations employed is given. However, some documentation is given within the input file structure as well as in an example problem set provided with the codes. For researchers already familiar with the modeling of high-frequency electromagnetic scattering, enough

documentation is provided to enable the user to become proficient with the code.

The Xpatch codes are currently being utilized on Silicon Graphics machines. The main routines are written in FORTRAN and can be ported to other machines with minimal effort. If a PC is to be used, then a compiler is needed that can access extended memory. Some utility codes (format conversion, wedge parameter extraction, etc.) are written in C and no source code is provided.

The Xpatch codes have other features which have not been fully discussed here. For some comparisons of measured results to numerical Xpatch simulations, the reader can consult some recent literature [10].

2.5 Numerical Results

In this section some numerical results will be considered. These examples serve as a partial validation of the newer codes against the more established models and also illustrate some of the features and limitations of the codes. The frequency of the incident radiation in the following examples is taken to be 1.0 GHz in all cases and is chosen for illustration purposes. While the PTD would provide a more accurate estimate of the true RCS of the targets considered below if the frequency were increased an order of magnitude, the resulting plots would be unnecessarily dense. Hence, the lower frequency was preferred for these comparisons.

Numerical comparisons other than the ones shown below have been made. While some of these comparisons have utilized more complex and realistic geometric models, the resulting predictions are readily extrapolated from the examples given below. Please note that in making comparisons with the Xpatch codes, only results generated via Xpatch1 will be shown here. The other Xpatch modules have many interesting features and capabilities as outlined above but tend to be beyond the scope of this comparison.

2.5.1 PEC Plate

Consider the thin square plate shown in Fig. 1. It is 1.0 m on a side and is taken to be perfectly conducting. The co-polarized monostatic RCS of the plate has been calculated using the scattering codes and the results are shown in Fig. 2. The incident field is a vertically polarized plane wave. The zenith angle is $\theta = 90^\circ$ (x-y plane) and the azimuth angle is varied from 0° (broadside) to 90° (grazing).

The calculations were performed using the PTD and for reference purposes the method of PO (no edge contribution). Notice that at broadside, the RCS has a value of 21.4 dBsm and agrees with the analytical PO result of $4\pi(A_P/\lambda)^2$, where A_P is the area of the plate and λ is the wavelength of the incident radiation. Furthermore, notice that the first sidelobe is 13.2 dB down from the maximum as is typical for rectangularly-shaped scatterers and uniformly illuminated apertures. The PO result is a fairly accurate estimate for the first few sidelobes except in the prediction of the nulls. After the first few lobes, the edge starts to dominate the response and the PO approximation yields an inaccurate result. Finally, notice that for this simple target, all three PTD scattering codes agree well for all aspects considered.

2.5.2 RAM Coated Plate

In this example a coated body will be analyzed. Consider the rectangular plate

shown in Fig 3. The plate is of width 2.0 m and height 3.0 m and is coated with a broadband RAM. The coating is 1.0 cm thick with relative permittivity and permeability of $\varepsilon_r = \mu_r = 2 - j\,5$. This RAM does not exist in practice but is used for the purpose of illustration.

The PO approximation to the co-polarized (VV) monostatic RCS of the coated plate has been computed and the results are shown in Fig. 4. The zenith angle is held constant at $\theta = 90^\circ$ (x-y plane) and the azimuth angle is scanned from 0° to 90°. Shown for comparison is the PO approximation to the RCS of a PEC plate of the same size. Notice that the RAM coating significantly reduces the RCS from that of the uncoated plate. At normal incidence, the amount of reduction is seen to be 18.2 dB corresponding to the reduced Fresnel reflection coefficient. As in the previous example, the first side lobe is 13.2 dB down from the maximum and the first null occurs at an azimuth angle of $\phi = \sin^{-1}(\lambda/2w)$ where w is the width of the plate. Observe that all scattering models again produce equivalent results in this case.

2.5.3 Dihedral Corner

Consider the dihedral corner reflector shown in Fig. 5. It is of length 2.0 m in each of the x, y, and z dimensions. The co-polarized (VV) monostatic RCS of the corner has been calculated and the results are shown in Fig. 6. The zenith angle is held constant at $\theta = 90^\circ$ (x-y plane) and the azimuth angle is varied from 0° (normal to face 2) to 90° (normal to face 1). Only scattering from the interior of the corner has been considered and all edge diffraction effects have been ignored. Although edge diffraction effects can be important for scattering from the exterior corner (wedge), the single and double-bounce scattering mechanisms dominate the response of the interior corner.

Shown in Fig. 6 are the results of three different solution procedures. First, the analytical solution to the RCS is shown. This represents the combined single-bounce PO approximation and the double-bounce GO/PO approximation. Also shown in this figure is the single-bounce approximation available with any of the codes. Finally, the Xpatch code was used in SBR mode (SBR/2 BOUNCE) to approximate the RCS of the corner. In the SBR mode, 10 rays/wavelength were shot at the target and 2 bounces were allowed. Notice the results of the SBR analysis agree very well with the analytical result. Furthermore, notice that the single-bounce PO approximation is inadequate for describing the response of the interior corner over most of the aspects shown.

The Xpatch code is the only model considered that can provide an adequate description of the response of the dihedral corner. The other scattering codes considered (MISCAT, McPTD, and NRCPTD) do not attempt to analyze multiple bounce scattering. While the effect of multiple bounces is not always an important contributory mechanism, the errors introduced by neglecting them can, for some targets, be significant.

The SBR mode of the Xpatch code requires that a dense grid of rays be shot at the target. The density of the ray grid governs the accuracy of the approximation with a dense grid providing more accurate results than a coarse grid. In the previous example, the density of the grid was 100 rays per square wavelength. Shown in Fig. 7 is the RCS of the corner calculated via Xpatch in SBR mode using a grid density of 2 rays/wavelength (4 rays per square wavelength). Also shown for

comparison purposes is the analytical calculation of the RCS. Notice that the Xpatch solution is degraded somewhat from the previous example but still provides what for some cases could be an adequate approximation.

2.6 Model Survey Summary

A summary of the capabilities and limitations of the various codes discussed in this report is given in Table 2. Of the codes considered, MISCAT is currently the most trusted (for a limited set of targets) and best documented while Xpatch provides the most comprehensive modeling features. Xpatch has the capability to model multiple bounce scattering as well as shadowing. While NRCPTD and McPTD can perform global shadowing checks, they are not as efficient in this regard as the Xpatch codes.

ACKNOWLEDGEMENT

The author would like to thank Major Keith Trott (USAF) of WL/MNGS at Eglin AFB for his encouragement to write this paper and for his proofreading of an earlier version of the work. Also, the author owes John Watson of Nichols Research Corporation much thanks for providing direction to undertake this work. This work was supported through the Data Analysis and Modeling (DAAM) Program (F08635-91-C-0110) with the Armament Directorate of Wright Laboratory located at Eglin, AFB.

REFERENCES

1. T. J. Kim and H. B. Tran, Monostatic and Bistatic Radar Cross Section Analysis, Vol. 1 - The High Frequency Electromagnetic Scattering Theory, Technical Report NOR-82-215, Dec. 1982.

2. S. C. Gibson and T. J. Kim, Radar Cross Section Analysis by the Physical Theory of Diffraction, Vol. 2 - User's Manual, Technical Report NOR-89-56, Mar. 1989.

3. M. Richards, IRMA Active MMW Channel Upgrade Investigations, Technical Report NRC-TR-93-042, May 1993.

4. S. W. Lee, McPTD-2.1: A High Frequency RCS Computation Code Based on Physical Theory of Diffraction, Technical Report, DEMACO, Mar. 1992.

5. S. W. Lee, Xpatch: A High Frequency RCS Computation Code for Facet Targets and Curved Patches, Technical Report, DEMACO, Aug. 1992.

6. Advanced Computer Aided Design User's Manual-7.2, General Dynamics, Fort Worth, TX, Jan. 1991.

7. The Ballistics Research Laboratory CAD Package-3.0, Aberdeen Proving Ground, MD, 1988.

8. H. Ling, R. Chou, and S. W. Lee, "Shooting and Bouncing Rays: Calculating the RCS of an Arbitrarily Shaped Cavity," IEEE Trans. Antennas Propagat. pp. 194-205, Feb. 1989.

9. J. Bauldauf, S. W. Lee, L. Lin, S. K. Jeng, S. M. Scarborough, and C. L. Yu, "High Frequency Scattering from Trihedral Corner Reflectors and Other Benchmark Targets: SBR Versus Experiment," IEEE Trans. Antennas Propagat. pp. 1345-1351, Sept. 1991.

10. E. M. Miller, "Validation of Xpatch Radar Signature Prediction Using Flat Flat Facet Geometries," MS Thesis, Air Force Institute of Technology, Dec. 1992.

Table 1. Capabilities of Xpatch family of scattering codes.

Code / Feature	Xpatch1	Xpatch2	Xpatch3	Xpatch4
Domain	Frequency	Frequency	Time	Time
Modeling Primitives	Facet	CSG/IGES	Facet	CSG/IGES
Coatings	Yes	Yes	No	No
Edge Diffraction	Yes	Yes	No	No
Shadowing	Yes	Yes	Yes	Yes
Multiple Bounces	Yes	Yes	Yes	Yes
Uses	RCS and Range Profile	RCS and Range Profile	Range profile and SAR*	Range profile & SAR*

* Not conventional SAR but images are similar.

Table 2. Capabilities of EM scattering codes surveyed.

Feature / Code	Surface Coatings	Wedge Extraction	Wedge Effects (PEC)	Global Shadowing	Multiple Bounces
MISCAT	Yes	No	Yes	No	No
NRCPTD	Yes	Yes	Yes	Yes *	No
McPTD	Yes	Yes	Yes	Yes *	No
Xpatch	Yes	Yes	Yes	Yes	Yes

* Not handled as well as in Xpatch

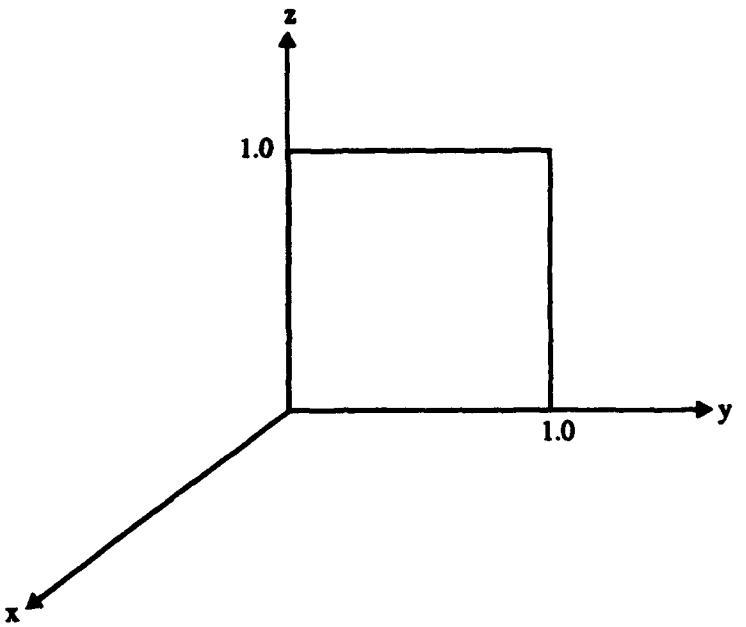

Fig. 1. Thin conducting square plate.

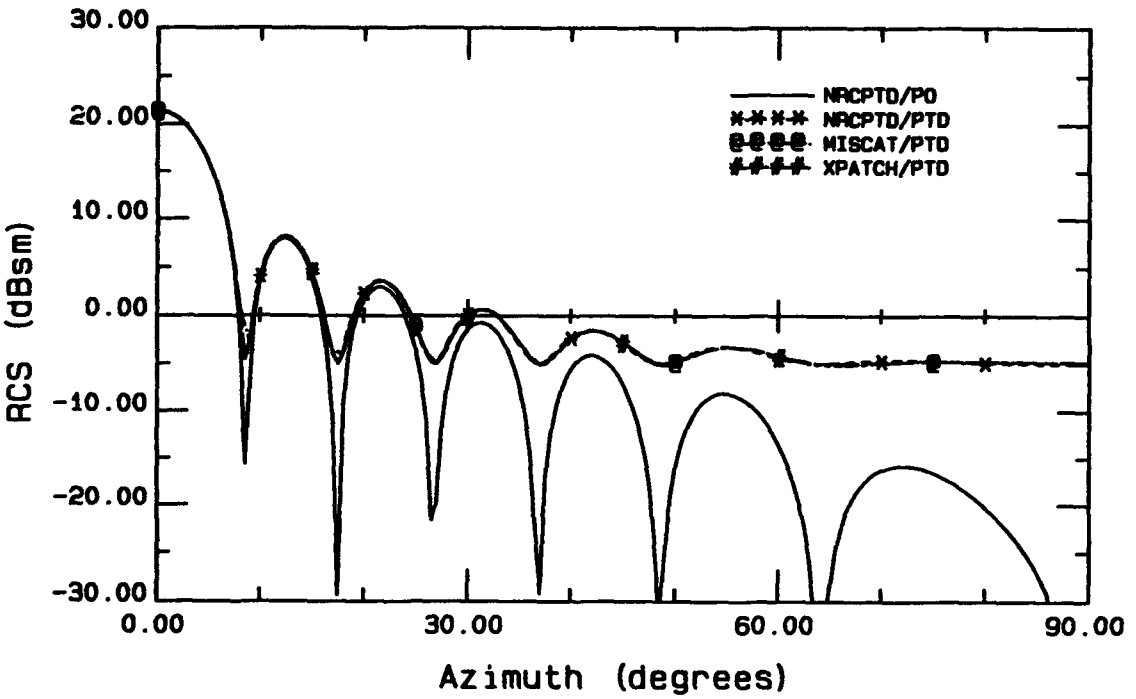

Fig. 2. Co-polarized (VV) monostatic RCS of a square (1m x 1m) conducting plate. The zenith angle is held constant at $\theta = 90^{\circ}$ and the azimuth angle is varied from 0° to 90°.

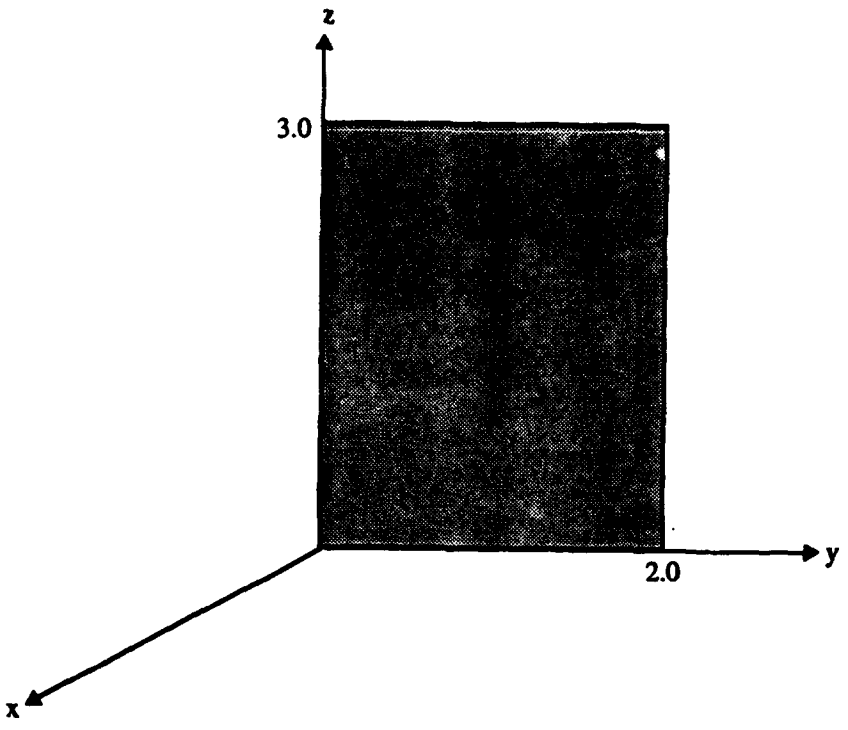

Fig. 3. Rectangular plate of height 3.0 m and width 2.0 m coated with a broadband RAM. The coating is 1.0 cm thick with dielectric properties $\hat{\epsilon}_r = \hat{\mu}_r = 2 - j\,5$.

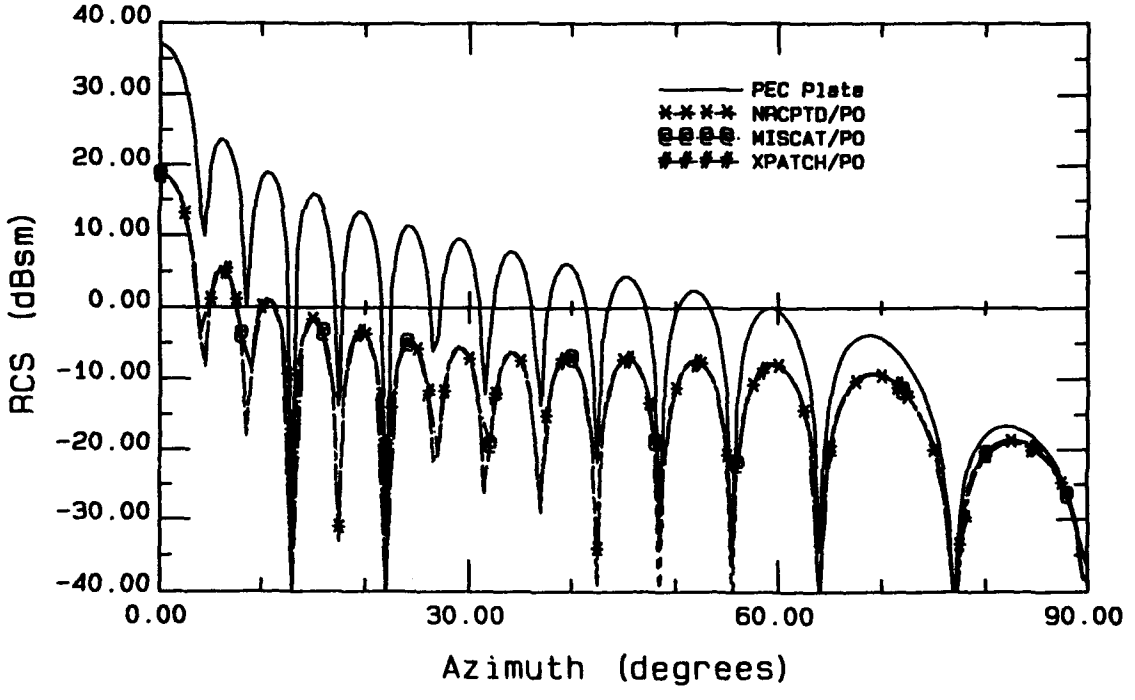

Fig. 4. PO approximation to the RCS of the RAM coated plate. Shown for comparison is the PO approximation to the RCS of a PEC plate of the same size.

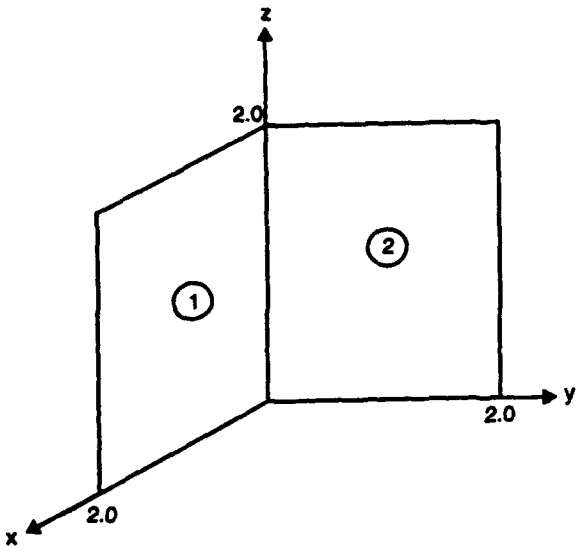

Fig. 5. Dihedral corner reflector.

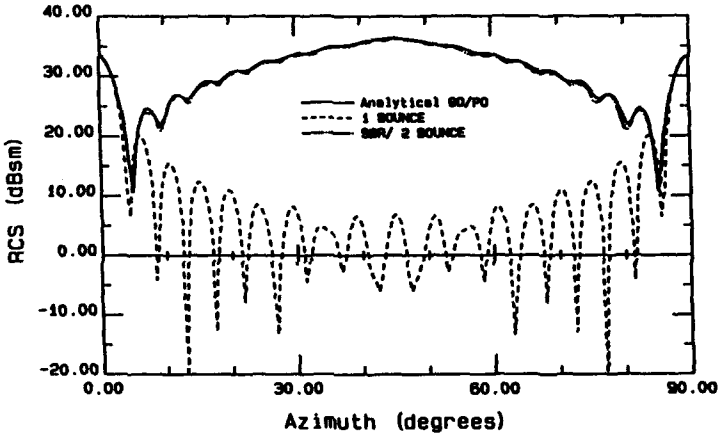

Fig. 6. Co-polarized (VV) monostatic RCS of the dihedral corner reflector as a function of azimuth angle. The analytical solution is compared to the single-bounce PO solution and a double-bounce SBR solution calculated using 10 rays/wavelength.

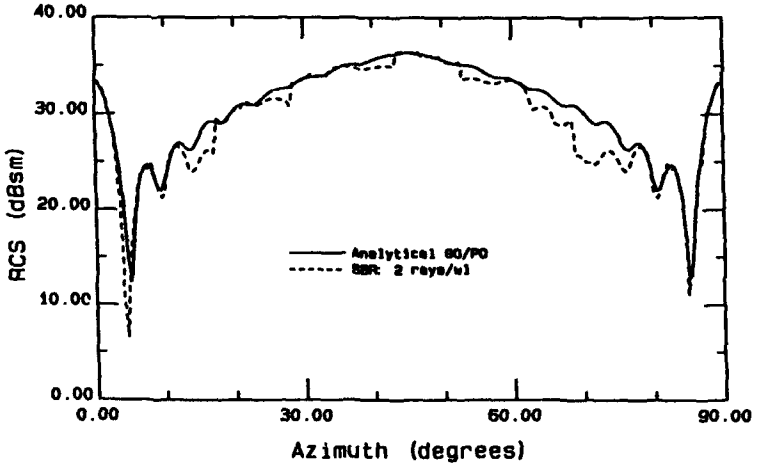

Fig. 7. Co-polarized (VV) monostatic RCS of the dihedral corner reflector obtained from an analytical solution and the SBR technique with 2 rays/wavelength.

AN EXPERIMENTAL AND THEORETICAL INVESTIGATION OF SCATTERING BY FINITE PERFECTLY CONDUCTING CYLINDERS WITH VARYING CROSS-SECTION

KRISHNA M. PASALA, PH.D.
University of Dayton
Electrical Engineering Department
Dayton, Ohio 45469-0226

CARLOS R. ORTIZ
Wright Labs
Wright Patterson AFB
Dayton, Ohio 45433-7408

ABSTRACT. ***In this paper we consider the problem of scattering from a class of three dimensional (3-D) targets which are finite cylinders but whose cross-section varies along the axis of the structure. We devise a technique wherein the solution to this 3-D problem is reduced to a sequence of two dimensional (2-D) problems. Solutions of 2-D problems are easier to obtain than the solutions of 3-D problems and further a variety of well established 2-D methods are available. This procedure results in a dramatic reduction in computational complexity and also makes the technique suitable for implementation on computers with highly parallel architectures. A number of targets with ogival and elliptical cross-sections were built and their back-scattered RCS was measured at 3, 6 and 10 GHz. Good agreement between computed and experimental results is obtained validating the technique described here.***

1. INTRODUCTION

It is frequently of interest to compute the scattering from three dimensional (3-D) targets with rather arbitrary shape. While a number of numerical techniques exist [1]-[11] to solve two dimensional (2-D) problems efficiently, relatively few techniques are available to solve the 3-D problems. Some of the methods are based on integral equations such as the surface patch code [6], [7]; others are based on solving the Maxwell's equations directly as in the FD-TD method [8], [9]. Codes that consider bodies of revolution are also available [10], [11]. Inevitably, 3-D codes demand large amounts of CPU time of powerful machines even for targets that are of moderate size. In addition to numerical techniques, high frequency techniques such as GTD, UTD or PTD [12], [13] may be used advantageously in cases where the targets are electrically large and when the requisite diffraction coefficients are available. Diffraction coefficients are not always available, however, as when the target is made of a dielectric, for instance. By combining numerical techniques with asymptotic techniques in appropriate fashion, hybrid methods [14] are realized which may be used to solve a wider class of problems.

In this paper, we are interested in computing the scattered field from a class of 3-D targets which are finite cylinders but whose cross-section may vary along the axis of the structure [15]-[17]. The technique itself is valid for targets that are made of metal, dielectric or both, though, we are only interested in perfectly conducting targets for the present. While the target is 3-D, the induced currents are determined by solving a sequence of 2-D problems. Efficient numerical techniques and codes [4], [5] are available to solve these 2-D problems. The notion of using 2-D solutions to solve 3-D problems is often used in the context of GTD, except that the solutions in this case are analytic and are based on asymptotic approximations [12]. Kumar has solved the problem of radiation from tapered dielectric rod antenna [18], by using the known solution to the underlying 2-D problem. Lai et. al. [19] have determined the scattering from straight dielectric structures by solving the underlying 2-D problem.

A number of models were fabricated. Some of these models are thin while others are bulbous. Some models have sharp edges while others are rounded. Measurements of backscattered RCS were made on these targets at 3, 6 and 10 GHZ and for both horizontal and vertical polarizations. These measured results are compared with results predicted by the theory described in this paper. Overall, excellent agreement is obtained between computed and experimental results. A salient feature of the method is the numerical efficiency. Computations are typically carried out using a PC. One of the typical cases consists of a target that is approximately $30\lambda^2$ in surface area. To compute the monostatic backscattered RCS over a range of 180 different angles of incidence, the CPU time required, on a Zenith Z386/25 PC with Weitek co-processor, is under three minutes! It may also be noted that the algorithm described here is specially suited for implementation on a parallel machine with many processors because each of the 2-D problems may be solved by a separate processor simultaneously and independent of the other 2-D problems.

2. THEORY

In this section we describe a technique to obtain the induced currents on a frustum of arbitrary cross-section illuminated by a plane wave as shown in Fig. 1. We also

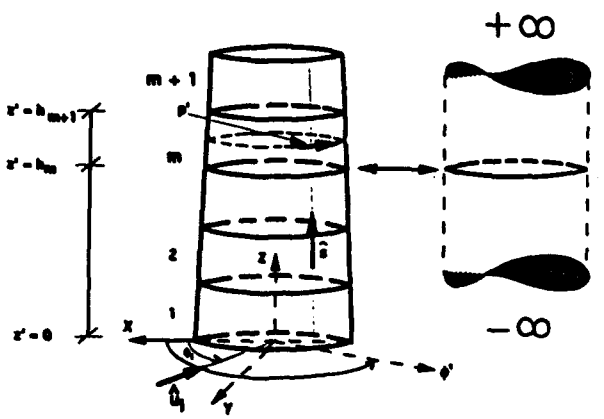

FIGURE 1. FRUSTUM OF ARBITRARY CROSS-SECTION

enumerate an efficient method to compute the field radiated by these induced currents. The frustum is divided into a number of electrically small blocks bounded by cross-sectional contours as shown in Fig. 1. Block numbered "m" is bounded by cross-sectional contours numbered "m" and "(m+1)". These contours need not be similar. The current on any contour, say the m^{th} contour, is taken to be the same as that on an infinitely long cylinder (shown with dashed line in Fig. 1) with the same cross section and subject to the same illumination. This is a 2-D problem and may be solved readily and efficiently. Thus, determining the current induced on a frustum is reduced to solving a sequence of 2-D problems. In order to determine the scattered field, we need to know the induced current at every point on the scatterer such as p' on the m^{th} block. This current is obtained, approximately, in terms of the current on the m^{th} contour. The details depend upon the polarization of the incident wave and we discuss here both the TM and TE polarizations.

2.1 TM Polarization: Induced Currents:

The electric field of the incident plane wave is parallel to the axis of the frustum and is given by,

$$\vec{E}_{inc} = E_0 \, e^{jk\rho\cos(\phi-\phi_i)} \, \hat{z} \quad . \tag{1}$$

E_0 is the amplitude of the incident field, k is the propagation constant and ϕ_i is tne angle of incidence. For an arbitrary observation point p', the current is given by,

$$\vec{J}(p') = J(\phi', z') \, \hat{s}, \quad h_m \le z' \le h_{m+1} \quad . \tag{2}$$

The unit vector $\hat{s}$ is as shown in Fig. 1. For an observation point p' that is on the m^{th} contour,

$$\vec{J}(p') = J_m(\phi') \, \hat{s}, \quad z' = h_m \quad . \tag{3}$$

For an observation point p' that is on the $(m+1)^{th}$ contour,

$$\vec{J}(p') = J_{m+1}(\phi') \, \hat{s}, \quad z' = h_{m+1} \quad . \tag{4}$$

The currents $J_m(\phi')$ and $J_{m+1}(\phi')$ are obtained by solving 2-D problems. For p' arbitrary, say on the m^{th} block ($h_m \le z' < h_{m+1}$), $J(\phi')$ remains unknown but may be approximated in terms of the known currents $J_m(\phi')$ and $J_{m+1}(\phi')$. Given that the m^{th} block is electrically small, the magnitude and phase of the current may be assumed to vary linearly between m^{th} and $(m+1)^{th}$ contours. This gives,

$$J(\phi') \approx |J_m(\phi')| \, e^{j(\psi_m + \delta\psi)} + \delta J \, e^{(\psi_m + \delta\psi)} \qquad h_m < z' < h_{m+1} \tag{5}$$

Where,

$$J_m(\phi') = |J_m(\phi')| \, e^{j\psi_m}$$

$$\delta J = \frac{\delta J_m}{\delta h_m} \left(z' - h_m \right)$$

$$\delta\psi = \frac{\delta\psi_m}{\delta h_m} \left(z' - h_m \right)$$

$$\delta J_m = |J_{m+1}| - |J_m|$$

$$\delta\psi_m = \psi_{m+1} - \psi_m$$

$$\delta h_m = h_{m+1} - h_m \tag{6}$$

In Equation (5), the change in magnitude δJ is quite small and may be neglected; however, the change in phase may not be neglected. Thus,

$$J(\phi') \approx |J_m(\phi')| \, e^{j(\psi_m + \delta\psi)} = J_m(\phi') \cdot e^{j\delta\psi} \quad . \tag{7}$$

According to Equation (7), the current on the contour through p' (refer to Fig. 1) may be taken to be the same as that on the m^{th} contour with the addition of the phase factor $e^{j\delta\psi}$. The change in phase $\delta\psi$ may be computed from Equation (6). It is highly desirable to find a closed form expression for $\delta\psi$. This may be accomplished if one assumes that $\delta\psi$ is simply the difference in the phase of the

incident field on the mth contour and the contour through p (dashed contour, Fig. 1). With this assumption, $\delta\psi$ is given by (refer to Fig. 2),

$$\delta\psi = k(\hat{u}_i \cdot \hat{\rho})\, d(z') \quad . \tag{8}$$

The vector $\hat{u}_i$ is the unit vector in the direction of propagation and is given by,

$$\hat{u}_i = -\cos\phi_i\, \hat{x} - \sin\phi_i\, \hat{y} \quad . \tag{9}$$

Also, as shown in Fig. 2,

$$\begin{aligned} d(z') &= \rho'_m(\phi') - \rho'(\phi') \\ &= (z' - h_m)\tan\gamma(\phi') \end{aligned} \tag{10}$$

and is a measure of the taper of the mth block at $\phi = \phi'$. Finally, the current is given by,

$$J(\phi') = J_m(\phi') \cdot e^{jk(\hat{u}_i \cdot \hat{\rho})\, d(z')} \quad . \tag{11}$$

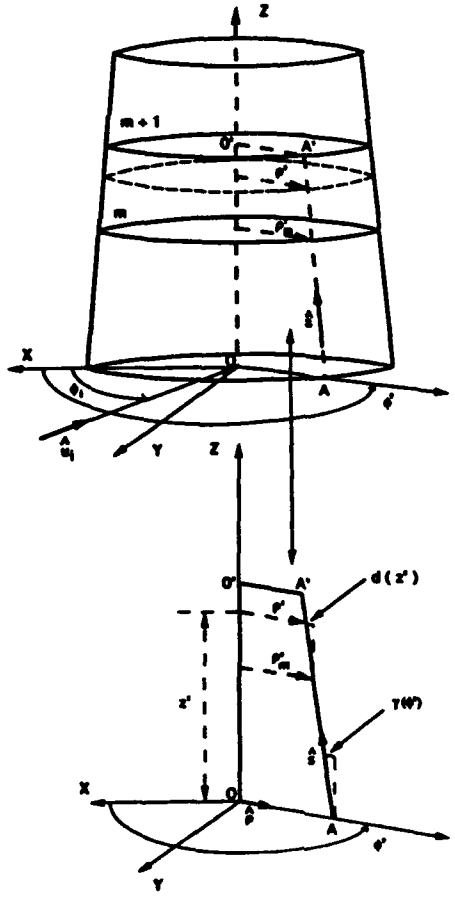

FIGURE 2. GEOMETRY FOR EVALUATING PHASE FACTOR

2.2 TM Polarization: Scattered Field:

The z-component of the scattered field from the mth block, E_{zm} is given by,

$$E_{zm} = -jk\eta \int_{\phi'=0}^{2\pi} \int_{z'=h_m}^{h_{m+1}} \left[\hat{z} \cdot \vec{J}(p')\right] \frac{e^{-jkr}}{4\pi r}\, da'$$

$$= -jk\eta \int_{\phi'=0}^{2\pi} \int_{z'=h_m}^{h_{m+1}} J_m(\phi') \sec\gamma(\phi') \tag{12}$$

$$e^{jk(\hat{u}_i \cdot \hat{\rho})(z'-h_m)\tan\gamma(\phi')} \frac{e^{-jkr}}{4\pi r}\, \rho'(\phi')\, ds'\, d\phi' \cdot$$

In the far field, making the usual far field approximations, we obtain,

$$e^{-jkr} \approx e^{-jkr_0}\, e^{jk\rho_m \cos(\phi_0 - \phi')} e^{-jk(z'-h_m)\tan\gamma(\phi')\cos(\phi_0 - \phi')} \quad . \tag{13}$$

Note that,

r = distance from the source point to the observation point,
r_0 = distance from the origin to the observation point, and
ϕ_0 = azimuthal coordinate of the observation point.

Referring to Fig. 2, we obtain,

$$\rho'(\phi') = \rho'_m - (z' - h_m)\tan\gamma(\phi') \quad . \tag{14}$$

Let,

$$c_1 = \left[\hat{u}_i \cdot \hat{\rho} - \cos(\phi_0 - \phi')\right] \tan\gamma(\phi') \tag{15}$$

and

$$F(\phi') = Sec\gamma(\varphi')\, J_m(\phi')\, e^{jk\rho_m \cos(\phi_0 - \phi')} \quad . \tag{16}$$

Now, the scattered field from the mth block may be obtained as,

$$E_{zm} = -jk\eta \frac{e^{-jkr_0}}{4\pi r_0}\, I_{TM} \tag{17}$$

where,

$$I_{TM} = \int_{\phi'=0}^{2\pi} F(\phi')\rho'_m(\phi')d\phi' \int_{z'=h_m}^{h_{m+1}} e^{jkc_1(z'-h_m)}\, dz'$$

$$- \int_{\phi'=0}^{2\pi} F(\phi') \tan\gamma(\phi')d\phi' \int_{z'=h_m}^{h_{m+1}} (z' - h_m) e^{jkc_1(z'-h_m)}\, dz' \tag{18}$$

Note that in Equation (18), variations with respect to ϕ' and

z' are separated. Further more, integrations with respect to z' may be carried out in closed form to yield,

$$I_{TM} = \int_{\phi'=0}^{2\pi} F(\phi')\rho'_m(\phi')Q_1(\phi')\,d\phi'$$

$$- \int_{\phi'=0}^{2\pi} F(\phi')\tan\gamma(\phi')\,Q_2(\phi')\,d\phi' \quad . \qquad (19)$$

Where,

$$Q_1(\phi') = \delta h_m\, e^{jkc_1\frac{\delta h_m}{2}}\, \frac{\sin\left(kc_1\frac{\delta h_m}{2}\right)}{\left(kc_1\frac{\delta h_m}{2}\right)} \qquad (20)$$

and

$$Q_2(\phi') = \frac{\delta h_m}{jkc_1}\left[e^{jkc_1\delta h_m} - e^{jkc_1\frac{\delta h_m}{2}}\, \frac{\sin\left(kc_1\frac{\delta h_m}{2}\right)}{\left(kc_1\frac{\delta h_m}{2}\right)} \right] \qquad (21)$$

Thus, to compute the scattered field from the m^{th} block, it is only necessary to carry out one numerical integration with respect to the azimuth. The scattered field from the target as a whole may be obtained by summing the field from all the blocks. The number of blocks are taken to be sufficiently large to yield a converged scattered field.

2.3 TE Polarization: Induced Currents:

For the TE polarization, the magnetic field of the incident plane wave is parallel to the axis of the cylinder and is given by,

$$\vec{H}_{inc} = H_0\, e^{jk\rho\cos(\phi-\phi_i)}\,\hat{z} \quad . \qquad (22)$$

At an observation point p' on the m^{th} block, the induced current is given by,

$$\vec{J}(p') = J_m(\phi')\, e^{jk(\hat{u}_i\cdot\hat{\rho})d(z')}\,\hat{u}_\epsilon(\phi') \quad . \qquad (23)$$

The unit vector $\hat{u}_\epsilon(\phi')$ depends upon the azimuthal coordinate of the observation and is shown in Fig. 1. All other variables of interest in Equation (23) were previously defined in section 2.1. Note that, as before, $\delta\vec{J}$ is neglected in obtaining Equation (23).

2.4 TE Polarization: Scattered Field:

Using the far field approximations, the z-component of the scattered magnetic field due to the m^{th} block, H_{zm}, may be expressed as,

$$H_{zm} = -jk\frac{e^{-jkr_0}}{4\pi r_0}\, I_{TE} \quad . \qquad (24)$$

Where,

$$I_{TE} = \int_{\phi'=0}^{2\pi} \left[\hat{r}_0 \times \hat{u}_\epsilon(\phi')\cdot\hat{u}_z\right] F(\phi')Q_1(\phi')\rho'_m(\phi')d\phi'$$

$$- \int_{\phi'=0}^{2\pi} \left[\hat{r}_0 \times \hat{u}_\epsilon(\phi')\cdot\hat{u}_z\right] F(\phi')\tan\gamma(\phi')Q_2(\phi')\,d\phi' \quad . (25)$$

The functions $F(\phi')$, $Q_1(\phi')$ and $Q_2(\phi')$ are defined in Equations (16), (20) and (21). The total scattered field may be obtained by summing up the contributions from all the blocks comprising the target.

3. EXPERIMENTAL WORK

In order to test the theory described in Section 2, a number of models which are finite cylinders with varying cross-section were built. Two basic cross-sectional shapes were adopted. These are the circular ogive and the ellipse. The ogival geometry leads to a target with edges while the elliptical cross-section is used to devise targets that simulate the behavior of rounded edges. While all the targets with ogival cross-section are chosen to be "thin" blade like targets, some elliptical targets are thin and others are bulbous. Thus, a variety of models were fabricated. Typical geometries of these models are shown in Fig. 3. These targets are completely characterized by specifying the five parameters, L_1, D_1, L_2, D_2 and H. In this study, the height, H, of all the targets is taken to be 18 cm, which is six wavelengths at 10 GHz. Different tapers are obtained by changing L_1, D_1 and L_2, D_2. It may be noted that the slant angle γ is a function of azimuth. In the case of elliptical targets, the ratio of minor to major axis, may be controlled to obtain a "thin" or "bulbous" target. Three ogival targets and four elliptical targets were built initially. However, for the sake of brevity we present here the results corresponding to three ogival cylinders and two elliptical targets. The nominal dimensions of these cylinders are listed in Table 1. The actual dimensions realized after the fabrication process are also given (in parentheses) in Table 1. It may be readily seen that there are discrepancies between the actual and nominal dimensions of the target. These discrepancies are due to the fabrication process used.

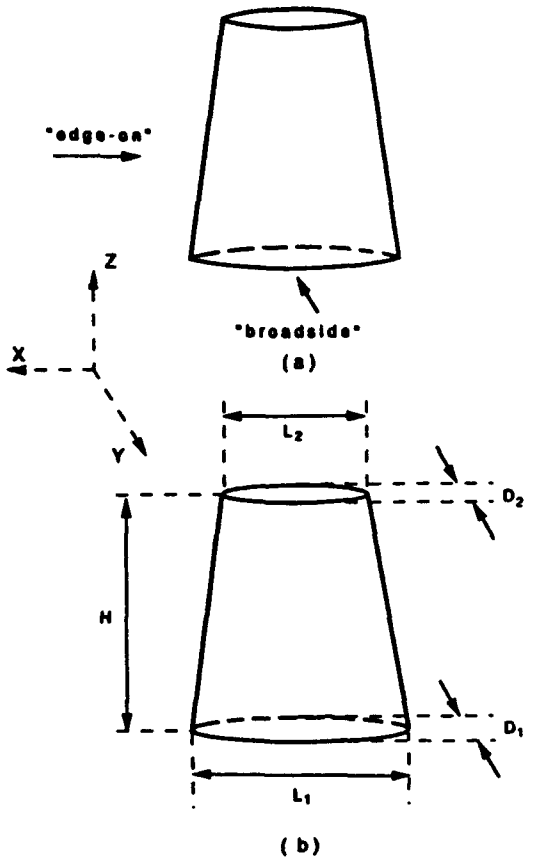

FIGURE 3. GEOMETRY OF TARGETS (a) OGIVAL CYLINDER (b) ELLIPTICAL CYLINDER

4. THEORETICAL AND EXPERIMENTAL RESULTS

The back scattered RCS of the five targets in Table-1 was measured in the Multi-Spectral Measurement facility at the Wright Patterson Air Force Base (WPAFB). These measurements were made at three different frequencies, 3,6, and 10 GHz, and also for both TE and TM polarizations. That is, a total of thirty scattering patterns were measured. Based on the theory presented here, scattering patterns were computed for each of these thirty cases. All the scattering patterns shown here are computed in the azimuthal plane because the measured patterns corresponded to this plane. However, the scattering pattern in any plane may be computed since the method determines the current on the target. The underlying 2-D problems of scattering by cylinders of arbitrary cross-section illuminated by TE and TM polarizations were solved by using the method of moments (MOM). The particular versions of the MOM and the corresponding codes are described in [4] and [5] for TE and TM polarizations respectively. The computed scattered field depends upon the number of blocks into which the target is divided. Numerical experiments are carried out to ensure the convergence of the scattered field as the number of blocks (of equal height) is increased. Indeed, good convergence is obtained and for the targets under consideration, a block size of about $\lambda/4$ or shorter appears to yield good results. All the computational results shown here are based on subdividing the target models into 24 blocks of equal height, which is a block size of $\lambda/4$ at 10 Ghz.

Table 1: Dimensions of Target Models

Model No.	Cross-Section	L1 Cm	D1 MM	L2 Cm	D2 MM	H Cm
O1	Ogive	7.5 (7.52)	6.3 (7.24)	6 (6.03)	5 (6.35)	18 (18)
O2	Ogive	8.7 (8.96)	7.5 (7.9)	6 (5.99)	5 (5.74)	18 (18.01)
O3	Ogive	9 (9.02)	7.5 (7.93)	6 (6.0)	5 (5.74)	18 (18)
E1	Ellipse	7.5 (7.48)	6.3 (6.81)	6 (5.98)	5 (5.74)	18 (18.01)
E2	Ellipse	9 (8.9)	22.5 (20.0)	6 (5.9)	15 (12.62)	18 (17.98)

We present here the results of both the theoretical and experimental work described. However, thirty scattering patterns are too many to be presented in a conventional fashion. Instead, the data has been presented in the form of five graphs, (Fig. 4 to Fig. 8) with each graph corresponding to one target. In order to accomplish this, the following conventions are used: All the targets are symmetric with respect to the "edge-on" angle of incidence and the "broad-side" angle of incidence. The edge-on angle of incidence is taken to be 0° and the broad-side angle of incidence is taken to be 90°. Hence, each of the Figs. 4-8 is divided into two parts where the region corresponding to 0°-90° corresponds to the TM polarization and the region corresponding to 90°-180° corresponds to the TE polarization. For each target and for each polarization, there are three different curves corresponding to the three frequencies. The RCS data corresponding to 6 GHz (σ_6) is plotted as is. The RCS data corresponding to 3 GHz (σ_3) is augmented by 15 dB and

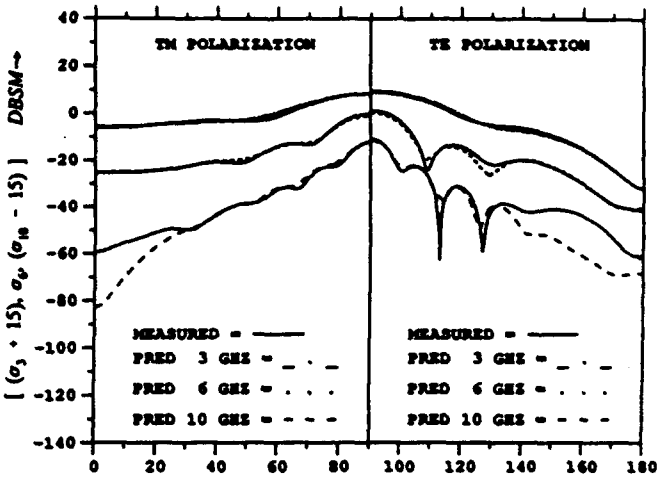

FIGURE 6. SCATTERING FROM OGIVAL CYLINDER NO. 3

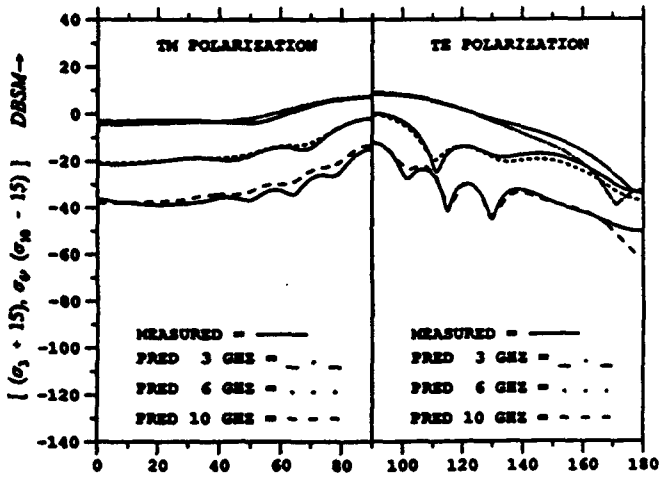

FIGURE 4. SCATTERING FROM OGIVAL CYLINDER NO. 1

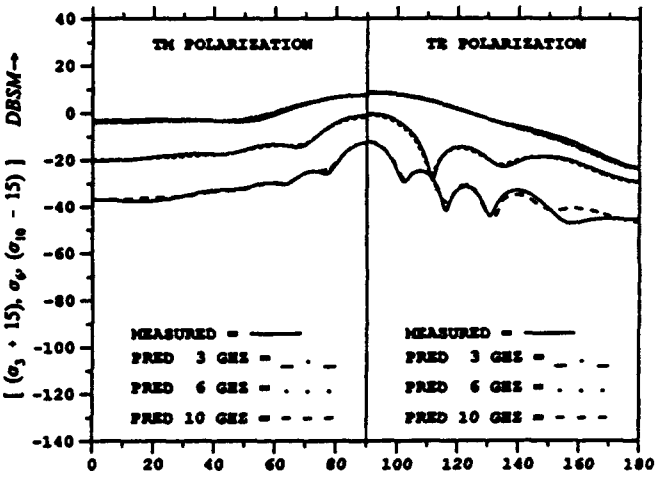

FIGURE 7. SCATTERING FROM ELLIPTICAL CYLINDER NO. 1

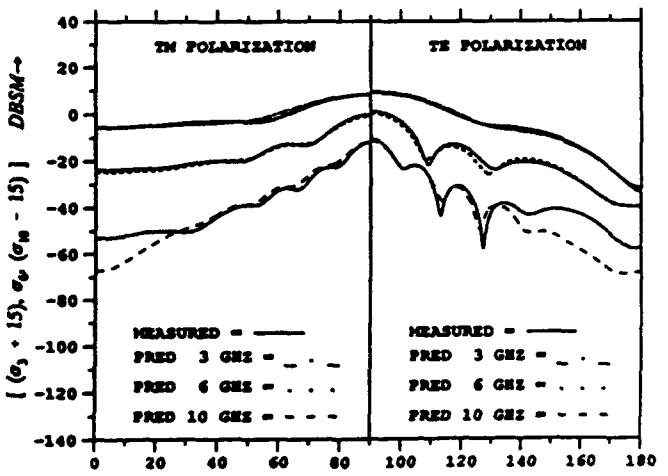

FIGURE 5. SCATTERING FROM OGIVAL CYLINDER NO. 2

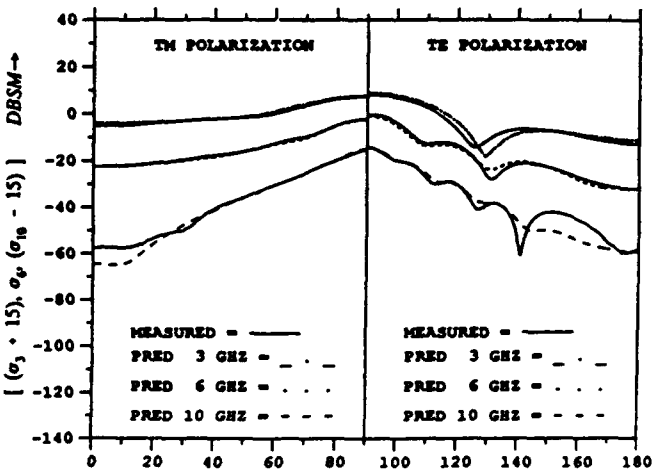

FIGURE 8. SCATTERING FROM ELLIPTICAL CYLINDER NO. 2

plotted, while the RCS data corresponding to 10 GHz (σ_{10}) is reduced by 15 dB and plotted. This procedure allows all three sets of data to be plotted on the same figure and assess the degree of agreement between the theoretical and measured data at the three frequencies simultaneously.

5. CONCLUDING REMARKS

In this paper we present an approximate but simple and computationally efficient technique to obtain the RCS of a class of 3-D targets. Scattering from any of the targets considered here may be readily computed using a PC. Not only is this technique computationally efficient, it places a minimum of demands on the memory required. It is only required to store the data necessary to compute the currents on one of the contours at a time. Once these currents have been used to compute the scattered field using Equation (19) or (26) for TM and TE polarizations respectively, these currents may be discarded and the memory cleared and used to compute scattering from the next block.

Our original intent of carrying out this investigation was to extend the use of the low frequency techniques like the method of moments into intermediate frequency region and for a class of commonly occurring 3-D targets. The technique has succeeded in doing so and appears to give useful results well into asymptotic region. It must be pointed out, though, that the technique is approximate. When the cylinders are straight the agreement is excellent. As the taper is increased and at the highest frequency, especially for edge-on angles of incidence, discrepancies occur as in Fig. 6. One possible reason is the difficulty of realizing a good edge in practice. The scattered field from the edge may be modelled by the field of a line source of travelling wave current located along the edge. Given that the length of this line source is larger than 6λ, at 10 GHz, it's scattered field has a very narrow beam and changes rapidly. A slight discrepancy in fabrication can result in tilting this pattern causing a rather large change in the measured field. Another possible reason is the breakdown of the assumption that the field of these targets is purely TE or TM, especially, for cases with the greatest taper (target-3 for instance). All of these may be a factor in the relatively large discrepancy seen in Fig. 6 for the edge-on angles of incidence.

The ansatz presented here is not limited to perfectly conducting targets, but may be readily extended to include penetrable, composite and coated targets. Investigations along these lines are discussed elsewhere [20], [21]. While we have used the MOM to solve the sequence of 2-D problems, one could equally well have used the FD-TD method or perhaps the finite elements method. Thus, the technique is quite flexible.

ACKNOWLEDGEMENT

We acknowledge the interest, help and encouragement of Dr. Gary Thiele. We gratefully acknowledge the support and encouragement of the Mission Research Corporation and Dr. Bill Kent in particular in carrying out the work reported here. The support of the Radar Branch, Avionics Mission Avionics Division, Wright Laboratory is acknowledged. The models were fabricated by the Fabrication Management Branch and the measurements were carried out at the Multi-spectrum Measurement facility at WPAFB.

REFERENCES

1. R. Mittra, *Computer Techniques for Electromagnetics*, New York, Hemisphere Publishing Co., 1987.

2. J.H.H. Wang, *Generalized Moment Methods in Electromagnetics*, New York, John Wiley & Sons, Inc., 1991.

3. J.A. Kong, *Finite Element and Finite Difference Methods in Electromagnetic Scattering*, New York, Pier 2, Elsevier Science Publishing Co., 1990.

4. D.T. Auckland, R.F. Harrington, "Moment Solution for Radiation and Scattering from Conducting Cylinders, TM Case," Syracuse University, Syracuse , New York, July 1975.

5. J.H. Richmond, "An Integral Equation Solution for TE Radiation and Scattering from Conducting Cylinders," NASA Contractor Report NASA CR-2245, April 1973.

6. S.M. Rao, D.R. Wilton, and A.W Glisson, "Electromagnetic Scattering by Surface of Arbitrary Shape," *IEEE Trans. Ant. Prop.*, Vol. AP-30, pp. 409-418, May 1982,

7. E.H. Newman and D.M. Pozar, "Electromagnetic Modeling of Composite Wire and Surface Geometries," *IEEE Trans. Ant. Prop.*, Vol. AP-26, pp. 784-789, Nov. 1978.

8. K.S. Yee, "Numerical solution of Initial Boundary Value Problems Involving Maxwell's Equations in Isotropic Media," *IEEE Trans. Ant. Prop.*, Vol. AP-14, No.3, pp. 302-307, 1966.

9. A. Taflove, K.R. Umashankar, "Review of FD-TD Numerical Modeling of Electromagnetic Wave Scattering and Radar Cross Section," *Proc. IEEE*, Vol. 77, No.5, pp. 682-699, 1989.

10. J.R. Mautz and R.F. Harrington, "Radiation and Scattering from Bodies of Revolution," App. Sci. Res., vol 20, p. 405, June 1969.

11. J.R. Mautz and R.F. Harrington, "An Improved E-field solution for a Conducting Body of Revolution," A.E.U, Band 36, p.198,1982.

12. P.H. Pathak, "Techniques for High-frequency Problems," Chapter 4 in *Antenna Handbook*, edited by Y.T. Lo and S.W. Lee, New York, Van Nostrand Reinhold Company, 1988.

13. J.B. Keller, "Geometrical Theory of Diffraction," *J. Opt. Soc. Am.*, Vol. 52, pp. 116-130, 1962.

14. G.A. Thiele, Overview of Selected Hybrid Methods in Radiating System Analysis," *Proc. IEEE*, Vol. 80, No. 1, pp. 66-78, January 1992.

15. J.M. Frederick, "Radar Signature of a Finite Ogive Cylinder," M.S.E.E. thesis, University of Dayton, Dayton, OH, August 1987.

16. C.R. Ortiz, "RCS of Arbitrary Finite Cylinders with Varying Cross-Section," M.S.E.E. Thesis, University of Dayton, Dayton, OH, April 1990.

17. K.M. Pasala, C.R. Ortiz, "Experimental and Theoretical Investigations on Scattering by Finite Cylinders with Varying Cross-section," IEEE-APS International Symposium Digest, Vol. 1, pp.180-183, Chicago, IL, July 1992.

18. A. Kumar, "Tapered Dielectric Rod Aerials," Ph.D. Thesis, Indian Ins. Sci., Bangalore, India, 1965.

19. A.K.Y. Lai, I.J. Gupta, W.D. Burnside, "Scattering by Dielectric Straps with Potential Applications as Target Support Structures," IEEE Trans. Ant. Propagat., Vol. AP-37, No.9, pp. 1164-1171, September 1989.

20. E.M. Friel, "Time and Frequency Domain Scattering by Dielectric Targets with Gently Varying Cross-Section," M.S.E.E. Thesis, University of Dayton, Dayton, OH, December 1992.

21. E.M. Friel, K.M. Pasala, "Scattering by Finite Cylindrical Dielectric Targets With Gently Varying Cross Section," IEEE-APS Symposium, Ann Arbor, MI, June 1993.

AUTOMATIC AND EFFICIENT SURFACE FDTD MESH GENERATION FOR ANALYSIS OF EM SCATTERING AND RADIATION*

Weimin Sun, Mike P. Purchine*, Jian Peng, Constantine A. Balanis, and George C. Barber**
Telecommunications Research Center, Arizona State University
Tempe, AZ 85287-7206
* Communications Semiconductor Products Division, Motorola
Phoenix, AZ 85062-2953
** JRPO/CECOM/NASA, NASA Langley Research Center
Hampton, VA 23681-0001

Abstract

The finite difference time domain (FDTD) method has found very wide applications in the analysis of electromagnetic scattering and radiation. The first and most important issue of the FDTD modeling is to decompose a computation space, containing a given geometry, into FDTD unit cells. There are a few dedicated mesh generators which could discretize the space into cells for general analysis. However, among FDTD applications, a large portion of them deal with objects structured primarily with conducting and/or thin-dielectric plates, such as a conducting sphere or cube, a cavity, an airplane, etc.. The mesh data necessary to input are those of node indices and material parameters on the object surface. Consequently geometry modeling is essentially to generate FDTD cells on the surfaces. For this purpose, a simple and effective algorithm capable of on-surface FDTD mesh generation is introduced based on a ray-tracing method. The algorithm presumes that the input geometry is described in polygons and lines which are often approximations of smooth surfaces and thin wires. In output, the algorithm decomposes automatically the polygons and lines into on-surface cells compatible with, and readable by, an FDTD solver. The algorithm has been coded in programs allowing effective and automatic generation of surface cells on various high- or low-end computer platforms.

*This work was sponsored by the Advanced Helicopter Electromagnetics (AHE) Program and NASA Grant NAG-1-1082.

1 Introduction

The finite difference time domain (FDTD) method has been demonstrated to be both powerful and versatile for modeling complex electromagnetic problems [1]. However, a complex geometry has to be discretized first to apply the method. While there are many mesh generators developed primarily for a finite element method, relatively few automatic mesh generators are dedicated to the FDTD method. Though an FDTD mesh is simpler and easier to generate, it has unique lattice-like features and needs some special consideration. Especially when the surface of a geometry cannot be represented by simple analytic formulas, an automatic mesh generator is necessary and desirable.

In most publications reporting FDTD applications, Yee's offset cube cell model [2] has been overwhelmingly used. Based on the model, a computation domain is decomposed into a lattice of cube cells in Cartesian coordinates. As shown in Figure 1, for each unit cell, the electric and magnetic field components are positioned so that not only central differences in space can be applied, but also the fundamental physical laws are naturally obeyed. Geometry modeling or mesh generation of a complex object is thus to establish an FDTD lattice of Yee's cells and provide the position and medium parameters for each cell. At the same time, the object volume is best body-fitted with unit cells.

In an FDTD lattice, cells filling non-occupied space always have medium parameters of free space; only their cell positions are important. Moreover, if a cell in the lattice is indexed by three indices which

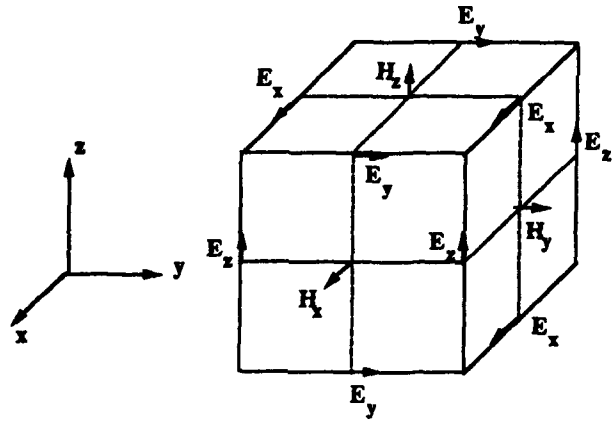

Figure 1: FDTD unit cell – Yee's model

are proportional to coordinates of the cell, its position is then determined solely by the origin and the lattice constant (cell size). The burden of geometry modeling lies in the provision of cell indices and medium parameters of cells occupying object volume. In general, the cell data are generated from a 3D volume space and need large storage space.

In a large portion of electromagnetic scattering and radiation problems a complex object is structured with shells of conducting and/or thin-dielectric materials. Now the necessary input is the indices and medium parameters of the cells distributed on the object surface. Thus it is appropriate to generate only on-surface mesh cells. Consequently, very efficient algorithms can be developed and implemented even on a very low-end personal computer.

This paper presents a program developed at Arizona State University to generate automatically three-dimensional surface FDTD meshes for complex objects. The program is based on an efficient ray-tracing method [3], and has been tested in various numerical simulations [4].

2 Algorithm Development

As a starting point, the algorithm assumes that a given surface geometry can be approximated by a cluster of polygons and lines. More accurate geometry modeling usually requires larger amount of polygons. Their mesh generation is actually to embed these polygons and lines into an FDTD lattice of Yee's cells. The word "embed" means that a polygon is approximated into stair-cased unit squares, each of which is aligned with a cell face. These squares are best fit to the original polygon. To do so, we project respectively the polygon onto three Cartesian coordinate planes. In each projection, the unit squares shaded by the projected polygon are identified. The distance of each shaded unit square to the polygon in the projection direction is evaluated and then the unit square is displaced the same distance in the projection direction. How to judiciously identify a unit square, which is covered by the projection of a polygon, is the focus of the algorithm, which can resort to a ray-tracing method and the rules set in the following sections.

Ray tracing method

Since any polygon with more than three vertices can always be tessellated into triangles, it is sufficient only to implement ray tracing on a triangle. Ray tracing is a well developed method to determine whether a ray intersects with a triangle in the 3D space. As shown in Figure 2, a ray originates from point s on the yz plane with coordinates of (0,j,k). A given triangle has three vertices represented by the three vectors o, p, and q. Its normal direction is given by

$$\mathbf{n} = (\mathbf{o}-\mathbf{p}) \times (\mathbf{q}-\mathbf{p}) \tag{1}$$

If an intersect point is represented by vector r, then vector r must satisfy

$$\mathbf{n} \cdot \mathbf{r} + c = 0 \tag{2}$$

where c is the distance of the triangle to the origin which can be obtained from $-\mathbf{n} \cdot \mathbf{p}$. In Figure 2, one can see that

$$\mathbf{r}-\mathbf{p} = \alpha(\mathbf{q}-\mathbf{p}) + \beta(\mathbf{o}-\mathbf{p}) \tag{3}$$

and the intersection distance d is given by

$$d = -(c+\mathbf{n} \cdot \mathbf{s})/\mathbf{n} \cdot \hat{d} \tag{4}$$

with $\hat{d}$ being a unit vector in the ray direction.

The sole condition which guarantees that the intersect point r is inside the triangle is [3]

$$\alpha \geq 0, \quad \beta \geq 0, \quad \textit{and } \alpha + \beta \leq 1 \tag{5}$$

Thus a ray that intersects with a triangle can be identified from the solution of α and β in (3). To

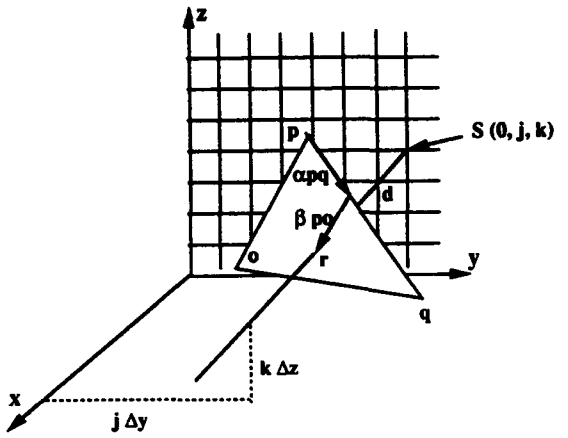

Figure 2: Illustration of a ray-trace algorithm

solve α and β from (3), only two component equations are required. By referring to Figure 2, the y and z components of (3) can be utilized as

$$r_z - p_z = \alpha(q_z - p_z) + \beta(o_z - p_z) \quad (6)$$

$$r_y - p_y = \alpha(q_y - p_y) + \beta(o_y - p_y) \quad (7)$$

All vector component coordinates in (6) and (7) are known, therefore α and β can be directly solved. Subsequently it can be determined whether the ray, originating from (0, j, k), intersects with the triangle.

Rounding off a triangle

From the established ray tracing method, it can be determined whether a ray hits a triangle, or in other words, whether the point s is covered by the projection of the triangle on the yz plane, as shown in Figure 2. To approximate a triangle by stair-cased square cell faces, we need to find all squares, which are displaced cell faces in the projection direction, covered by the projection of the triangle. However, to determine whether a unit square is covered by a triangle, some rules need to be established. The rules used in this algorithm include:

- if the center of the square is covered by the projection, then the square is displaced. Otherwise,
- if a center of one of the edges of the square is hit by the triangle, the edge (short line segment) is displaced. The edge will be used to force tangential boundary condition in the FDTD solution procedure. Otherwise,
- no squares and edges are displaced

The output of a square is different from that of a short segment. A square output will inform an FDTD solver to force boundary conditions at all four edges, while a short segment will inform the solver to force boundary conditions only at the segment.

The second problem in rounding off a triangle to FDTD cells is to round off the triangle vertices to the nearest cell nodes. It is considered necessary for the rules established above to be implemented without complication. Otherwise, more possibilities, concerning how a unit square is covered by a triangle, need to be considered in the algorithm. It should be noted that before rounding off its vertices, the triangle has to be displaced to yield a least rounding-off error. This fact is best illustrated in Figure 3 where a triangle is rounded off to unit squares and edge segments. Figure 3(a) is an original triangle. Its vertices are rounded off to nearest nodes in Figure 3(b), and applying the above rules results in an FDTD lattice compatible triangle as shown in Figure 3(c). However, if the triangle in Figure 3(a) is displaced first as shown in Figure 3(d) and then rounded off as in Figure 3(e), the resulting approximate triangle in Figure 3(f) is substantially different from that in Figure 3(c).

A complex structure consists of a cluster of polygons and lines. Any displacement should be applied to all polygons and lines. The criterion governing the displacement is to minimize the overall vertex rounding-off error. Minimization of the global vertex rounding-off error is a least square problem the solution of which could be very time consuming. When one is concerned about development of an efficient algorithm, it is only necessary to minimize the global rounding-off error in subdomains. For example, the absolute global error in rounding vertices to their nearest cell nodes can be considered in one dimension at a time and defined as

$$\epsilon_x = \min_j \sum_{i=1}^{N} |r_{ix} - d_x^j - Round[r_{ix} - d_x^j]| \quad (8)$$

where N is the total number of vertices of all polygons, r_{ix} is the x coordinate of the ith vertex, and d_x^j is a displacement in x direction which is the x-distance needed to round off the jth vertex to its nearest node. The *Round* operator in (8) rounds an

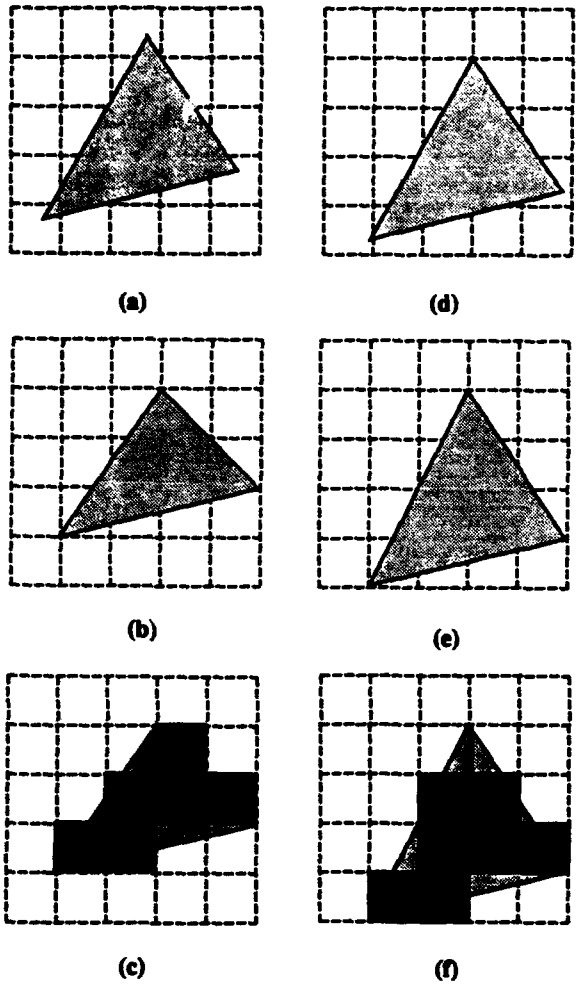

Figure 3: Algorithm illustration for rounding off a triangle. a) A triangle projected onto a coordinate plane; b) Round off the vertices of the triangle; c) Round off the triangle (in light shadow) to FDTD cell compatible squares (in dark shadow); d) Displace the triangle first; e) Then round off the vertices of the triangle; f) After that round off the triangle.

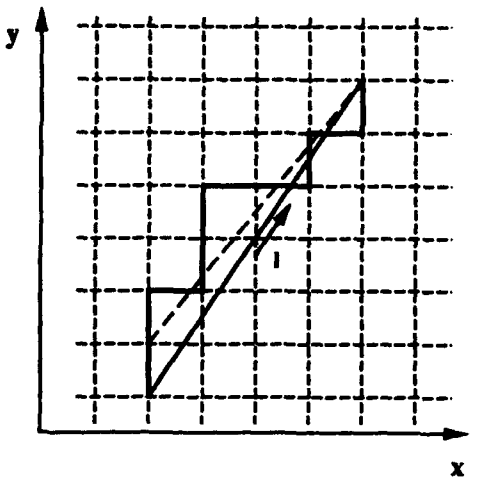

Figure 4: Digitising a line in 2D space.

non-integer number into an integer. By choosing d_x^j to be the x distance of the jth vertex to its nearest node each time with a j for N times, the minimal global error ϵ_x and thus the d_x can be identified. This procedure is then repeated for both the $\hat{y}$ direction and $\hat{z}$ direction. The resulting d_x, d_y, and d_z define the global displacement of the object.

Digitising a line

At low frequencies, thin wire antennas are very often employed. The geometry of a thin wire can be modeled by a line. For tangential boundary conditions to be applied on the wires, their representative lines have to be compatible with the FDTD lattice in which they are embedded. A line in an FDTD lattice is only allowed to run through cell edges due to the fact that electric field components in a cell are positioned at, and aligned with, cell edges.

Figure 4 illustrates the rule used to digitize a line in a two-dimensional space. A line is in the direction $\mathbf{l}$. If the inner product of $\mathbf{l}\cdot\hat{x}$ is greater than $\mathbf{l}\cdot\hat{y}$, a unit line segment in $\hat{x}$ direction is chopped off. The line is terminated at a new end. Repeating the procedure leads to a zig-zag line which is a digitized line with all its segments aligned with either the $\hat{x}$ or $\hat{y}$ direction. The same line digitizing rule has been applied to the three-dimensional space and implemented in the algorithm.

Algorithm

To summarise, the algorithm proposed for an on-surface FDTD mesh generation can be presented as:

1. Divide the surface of a given object into a cluster of polygons and use different colors to identify different media. The shape and the number of utilized polygons determine the accuracy of geometry modeling.

2. Round off the vertices of each triangle to nearest mesh nodes (represented in integer indices) with a minimal global rounding-off error respectively in $\hat{x}$, $\hat{y}$ and $\hat{z}$ directions.

3. Tessellate each polygon into triangles. If the vertices of the polygon are numbered clockwise from 1 to N, then the tessellation is done by connecting vertices i and j with

$$|\mathbf{r}_i - \mathbf{r}_j| < |\mathbf{r}_i - \mathbf{r}_k|$$

for $k, j \in (1, 2, ..., N)$ and $k, j \neq i-1, i, i+1$.

4. Project each triangle, respectively, onto three principal coordinate planes and scan the triangle by using the ray-tracing method, as shown in Figure 2. When a ray in a normal direction originates from a node and hits the triangle, the node indices i and j are collected and the distance d between the ray intersection point and the node is evaluated. Whether a ray hits the triangle can be determined via the criterion of (5).

5. The intersection distance d is rounded off to the nearest integer. The three integer indices (two from the coordinate plane and one from the distance), and the color of the intersection point are output as a surface cell or a short segment.

6. Repeat the above procedure for every triangle and every polygon.

7. Digitize a line into short FDTD cell compatible segments, and output the indices and direction of each individual segment.

3 Numerical Example

The above algorithm has been coded in both C and FORTRAN, and tested in various numerical simulations. For brevity, we only illustrate a few examples here.

The first example is a perfectly conducting cube. The edges of the cube are aligned with rectangular coordinate axes. The incident wave is in the -$\hat{z}$ direction. The geometry was originally presented in six squares as shown in Fig. 5(a). Its FDTD surface mesh is simple to generate since the FDTD cells can be naturally fitted to the cube surfaces. The bistatic RCS of the cube has been obtained via an FDTD solver, and compared with the solution by the Numerical Electromagnetics Code (NEC) [5]. In the NEC solution, the cube surface was modeled by a wire frame mesh. It is seen from Fig. 5(b) that the FDTD solution agrees very well with the NEC results on both the E-plane ($\phi = 0^0$) and the H-plane ($\phi = 90^0$).

The second example is a perfectly conducting sphere. Its geometry was originally represented as a cluster of polygons as shown in Fig. 6(a). Its FDTD surface mesh was generated and subsequently input into an FDTD solver. The bistatic RCS of the sphere has also been obtained via the FDTD method and compared in Fig. 6(b) with the exact Mie theory. The FDTD solution agrees well with the exact solution on both the E-plane ($\phi = 0^0$) and the H-plane ($\phi = 90^0$), though the stair-case approximation is not smoothly body-fitted.

Figure 7 shows the mesh generation for a scale model helicopter. The helicopter geometry was modeled in polygons, and then discretized into a surface mesh, as illustrated in Fig. 7(a). The radiation patterns of a dipole mounted at the bottom center of the helicopter fuselage have been simulated and measured at 880 MHz. The FDTD simulation was conducted with two different cell sizes ($\lambda/16$ and $\lambda/20$), and the measurements were performed at NASA Langley Research Center. The co-polarization patterns in roll and yaw planes are shown in Fig. 7(b) and 7(c), respectively. The cross-polarization pattern in yaw plane is shown in Fig. 7(d). It is sufficient to see that all of the FDTD predictions are consistent with the measurements.

4 Conclusion

Based on a ray-tracing method, an efficient surface FDTD mesh generator has been developed. The mesh generator can be used for a complex object enclosed by conducting and thin-dielectric surfaces. The high efficiency of the algorithm allows the mesh generation to be performed on a personal computer.

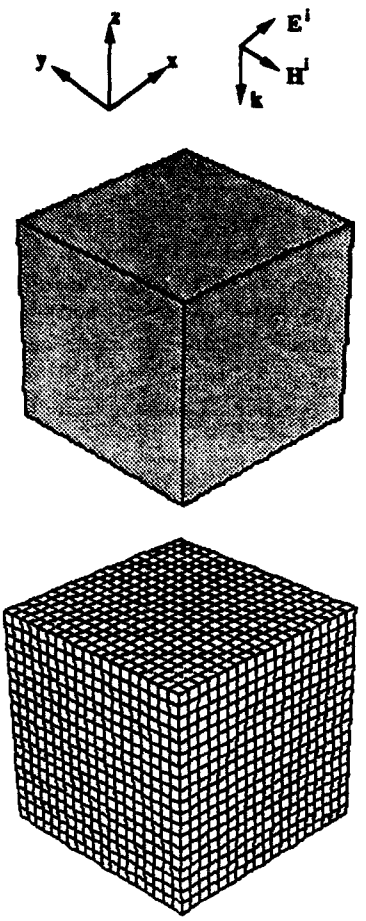

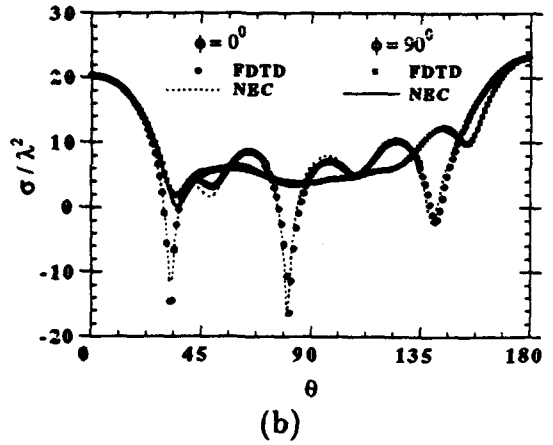

Figure 5: Mesh generation for a conducting cube and its bistatic RCS solution. (a) A cube modeled in six squares and its FDTD mesh; b) Bistatic RCS of the cube in the E-plane ($\phi = 0^0$) and the H-plane ($\phi = 90^0$).

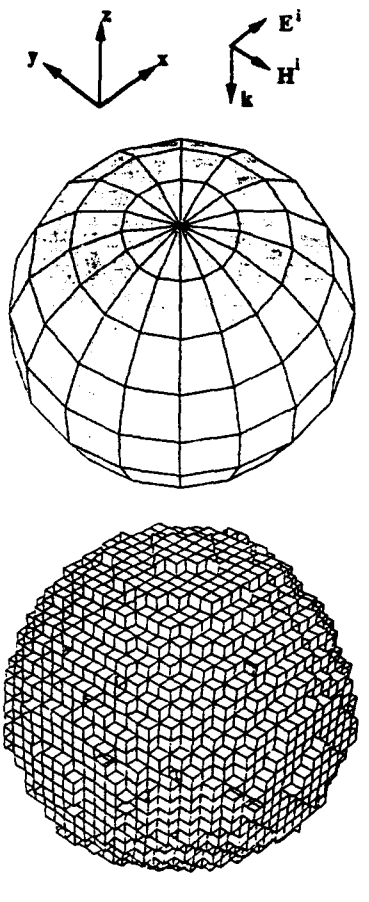

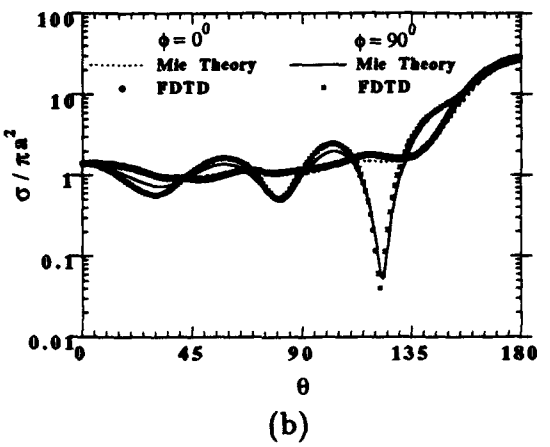

Figure 6: Mesh generation for a sphere and its bistatic RCS solution. (a) A sphere modeled in polygons and its subsequent FDTD mesh; b) Bistatic RCS of the sphere in the E-plane ($\phi = 0^0$) and the H-plane ($\phi = 90^0$).

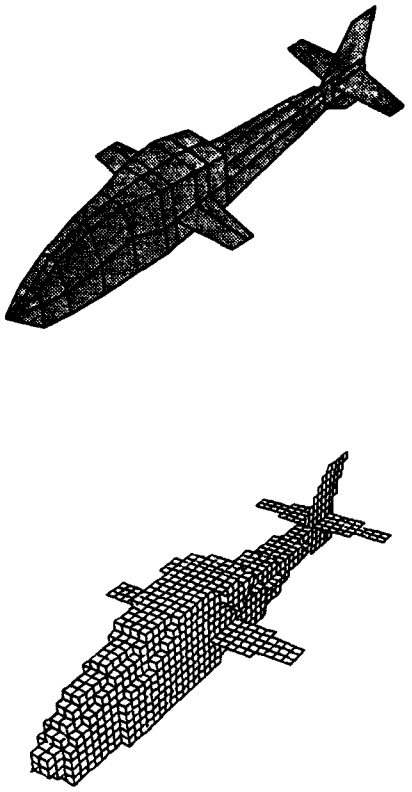

(a)

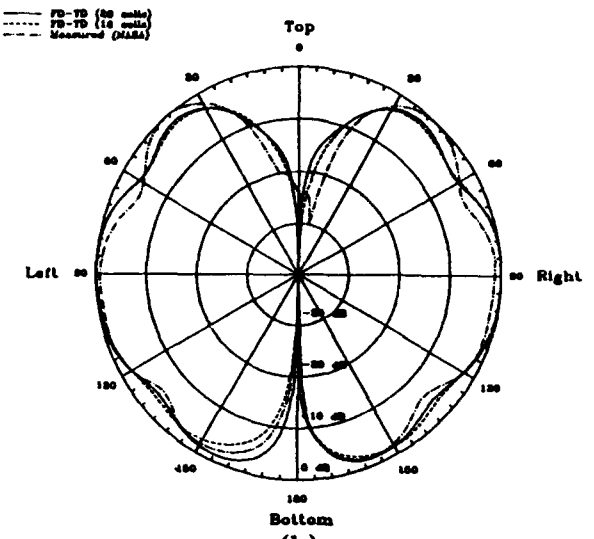

(b)

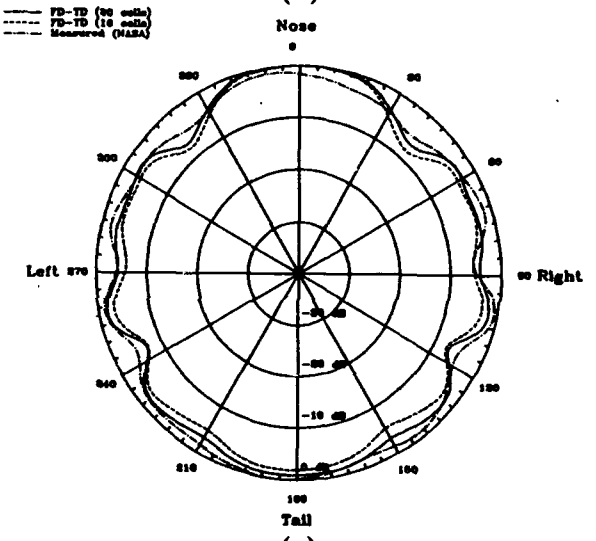

(c)

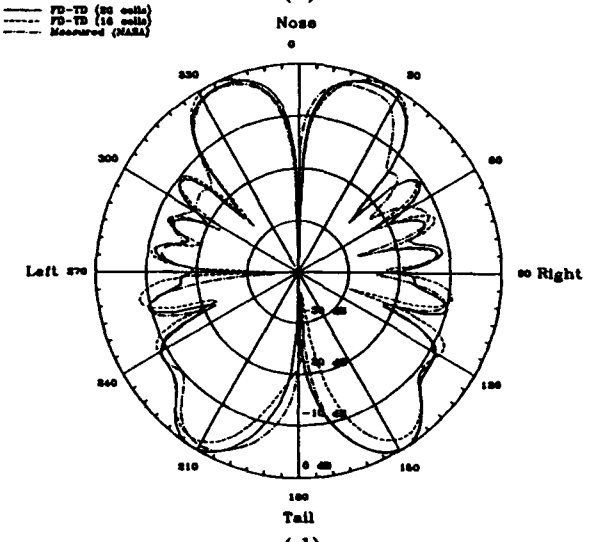

(d)

Figure 7: Mesh generation for a scale helicopter. a) The scale helicopter modeled in polygons and Its FDTD mesh; b) A dipole co-polarization radiation pattern in roll plane; c) The dipole co-polarization radiation pattern in yaw plane; d) The dipole cross-polarization radiation pattern in yaw plane.

5 References

[1] A. Taflove and K.R. Umashankar, "The finite-difference time-domain method for numerical modeling of electromagnetic wave interactions with arbitrary structures," *Finite Elements and Finite Difference Methods in Electromagnetics Scattering*, PIER 4, edited by M.A. Morgan, Elsevier, New York, pp. 287-373, 1990.

[2] K.S. Yee, "Numerical solution of initial boundary value problems involving Maxwell's equations in isotropic media," IEEE Trans., Antennas Propagat., Vol. AP-14, No. 5, pp. 302-307, May, 1966.

[3] D. Badouel,"An efficient ray-polygon intersection", *Graphics Gems II*, edited by J. Arvo, pp. 390-393, Academic Press, Boston, 1990.

[4] C.A. Balanis etc., "Advanced electromagnetic methods for helicopter applications," Annual Report, Oct. 1, 1990–Sept. 31, 1991, Advanced Helicopter electromagnetics Industrial Associates Program, Arizona State University.

[5] J. Burke and A. J. Poggio, "Numerical Electromagnetics Code (NEC)-Methods of Moments Part 1, 2, and 3," Naval Ocean Systems Center, San Diego, CA, NOSC TD 116, 1980.

1994 INSTITUTIONAL MEMBERS

THE AEROSPACE CORPORATION PO Box 92957 Los Angeles, CA 90245-2957	ANDREW CORPORATION 10500 W 153rd Street Orland Park, IL 60462	ARC, INC 8201 Corporate Dr. Ste 3550 Landover, MD 20785
ASELSAN INC. LIBRARY PO Box 101 Yenimahalle Ankara, TURKEY 06172	ATOMIC WEAPONS ESTAB UK Building E3, Awe Aldermaston Reading, Berkshire, UK RG7 4PR	AVITRONICS PO Box 8492 Hennopsmeer, S AFRICA 0046
BNR EUROPE LTD London Road Harlow, Essex, UK CM17 9NA	BRITISH LIBRARY Boston SPA Harlow, Essex, UK CM17 9NA	CSELT-RADIO Via Guglielmo Reiss Romoli 274 Turin, ITALY 10148
CSIRO, CENTER FOR ADV TECH PO Box 883 Kenmore, Qld, AUSTRALIA 4069	AEA TECH/CULHAM LAB UK Atomic Energy Authority Abingdon, Oxford, UK OX14 3DB	DEFENSE RESEARCH ESTAB. 3701 Carling Ave. Ottowa, Ont. CANADA K1A OK2
D L R OBERPFAFFENHOFEN Zentralbibliothek Wessling/Obb, GERMANY 8031	D S T O SALISBURY LIBRARY Box 1500 Salisbury, SA, AUSTRALIA 5108	DYNETICS, INCORPORATED PO Drawer B Huntsville, AL 35814-5050
ENGINEERING DEVELOPMENT EST. Private Bag 12 Ascot Vale, Victoria, AUSTRALIA 3032	FGAN/FHP Neuenahrer Strabe 20 D-5307 Wachtberg-Werthoven, GERMANY	HARRIS CORPORATION LIBRARY PO Box 37 Melbourne, FL 32902-9739
HARRIS CORPORATION 1680 University Avenue Rochester, NY 14610-9983	HKUST LIBRARY Clear Water Bay Road Kowloon, Hong Kong	HOKKAIDO DAIGAKU Nishi 8, Kita 13 Sapporo, JAPAN 060
HUGHES RESEARCH LIBRARY 3011 Malibu Canyon Road Malibu, CA 90255-4797	HUNTING ENGINEERING LTD Redding Wood Amphill, Bedford, UK MK45 2HD	IABG Einsteinstrasse 20 Ottobrunn, GERMANY D-85521
IIT RESEARCH INST. LIBRARY 185 Admiral Cochrane Dr. Annapolis, MD 21401-7347	IPS RADIO & SPACE SERV. LIBRARY PO Box 5606 W Chatswood NSW, AUSTRALIA 2057	KATHREIN-WERKE KG Postbox 260 Rosenheim 2, GERMANY D-8200
LINDA HALL LIBRARY 5109 Cherry Street Kansas City, MO 64110	LITTON ELECTRON DEVICES LIBRARY 960 Industrial Road San Carlos, CA 94404	LOCKHEED MISSILES AND SPACE 3251 Hanover Street Palo Alto, CA 94304
M/A COM INCORPORATED 100 Chelsford St. Lowell, MA 01851	MARITELERADAR/BIBLIOTECA Viale Italia 72 Livorno 72, ITALY	MATRA DEFENSE 37 Av. Louis Breguet BP1 Velizy, Cedex, FRANCE 78146
MISSISSIPPI STATE UNIV LIBRARY PO Box 5408 Mississippi State, MS 39762	MITRE CORPORATION LIBRARY 202 Burlington Road Bedford, MA 01730	MOTOROLA INCORPORATED 1301 E Algonquin Road Schamburg, IL 60196
MPB TECHNOLOGIES INC. 151 Hymus Blvd. Pointe-Claire, Que, CANADA H9R 1E9	NAVAL RESEARCH LAB. 4555 Overlook Avenue SW Washington, DC 20375-5336	NORWEGIAN TELECOM RES. PO Box 83 Kjeller, NORWAY N-2007
OCEAN APPLIED RESEARCH CORP. 10447 Roselle Street San Diego, CA 92121	OFFICE OF RESEARCH PO Box 15183 Arlington, VA 22215-0183	PENNSYLVANIA STATE UNIV Pattee Library University Park, PA 16802

1994 INSTITUTIONAL MEMBERS (Cont.)

QUEEN MARY & WESTFLD COLLEGE Mile End Road London, UK E1 4NS	RADIO FREQUENCY SYSTEMS Box 191 Croydon, Vic, AUSTRALIA 3136	ROCKWELL 855 35th St. NE Cedar Rapids, IA 52498
SAAB-SCANIA AB Tusta 5 Linkoping, SWEDEN S-58188	SERCO SERVICES Cheeseman's Lane Hambrook, W Sussex, UK	STG NATIONAL LUCHT-EM Ruimtevvart Lab. A Fokkerweg 2 Amsterdam, NETHERLANDS 1059
SWETS SUBSCRIPTION SERVICE 440 Creamery Way Suite A Exton, PA 19341	SYRACUSE RESEARCH CORPORATION Merrill Lane Syracuse, NY 13210-4080	TASC LIBRARY 55 Walkers Brook Drive Reading, MA 01887
TECHNICAL RESEARCH CENTRE Telecom Lab/Otakaari 7B Espoo, FINLAND SF-01250	TECHNION-ISRAEL INST OF TECH Faculty of Electrical Engineering Technion City, ISRAEL 32000	TELECOM AUSTRALIA 770 Blackburn Road Clayton, Victoria, AUSTRALIA 3168
THE MOTOR INDUSTRY Watling Street Nuneaton, Warwicks, UK	THORN EMI ELECTRONICS Wookey Hole Rd. Wells, Somerset, UK 13A5 1AA	UNIV. OF CENTRAL FLORIDA LIB. PO Box 162440 Orlando, FL 32816
UNIVERSITAT DER BUNDESWEHR Werner Heisenberg Weg 39 Neubiberg, GERMANY W-8014	VISTA RESEARCH INC. 100 View St, #202, Box 998 Mountain View, CA 94042	FANFIELD LIMITED Sproughton House Sproughton, Ipswich Suffolk, UK IP8 3AW

AUTHOR'S KIT FOR THE ACES JOURNAL

Information concerning the types of articles considered for publication by the ACES Journal are normally printed on the two back cover pages of the Journal. Papers submitted for consideration for publication may be in 12 point font size (or acceptable equivalent) and may be in one and a half or double line spacing for the convenience of the reviewers. It is requested that intending author(s) for the Journal send four copies of their article to the Editor-in-Chief of the Journal. Some additional information applicable to final camera-ready copies is also provided on the back pages of the Journal. However, in response to many enquiries from prospective authors it has been decided, for archival purposes, to publish copies of the material sent to authors whose papers have been accepted for publication in the Journal. The kit comprises the following:

1) ACES Copyright forms (these are regularly published in the Journal)
2) Page charge policy
3) A note concerning the preferred font sizes and lay-out for camera-ready Journal articles,
4) Specific requirements for camera-ready copies, and
5) Style requirements for Journal articles. The kit is subject to revision from time to time. Please note that these requirements apply only to the final camera-ready copy. It is important to note that once a paper has been accepted for publication, it will not be turned down because the author(s) is/are unable to meet the requirements for the preferred font sizes or lay-out. Where necessary, every effort is made to assist authors to produce acceptable camera-ready copy.

Duncan C. Baker
Editor-in-Chief, ACES Journal
EE Department, Univ of Pretoria
0002 Pretoria, South Africa.

16 May 1994

ACES JOURNAL PAGE CHARGE POLICY

EXCESSIVE LENGTH PAGE CHARGE POLICY: A mandatory EXCESSIVE LENGTH charge of $75.00 per page is required for each paper **longer than twelve (12) printed pages where any author is an ACES member**, or **eight (8) printed pages where no author is a member of ACES**. If the author(s) will not agree to pay the mandatory EXCESSIVE LENGTH page charges, the author(s) will be required to reduce the final manuscript to twelve pages or less when any author is an ACES member, eight pages or less when no author is a member of ACES, including all figures and illustrations, before the paper will be published. The **ACES Journal** Editor-in-Chief may, at his discretion, waive the page limit for one paper per issue.

VOLUNTARY PAGE CHARGE POLICY: After a manuscript has been accepted for publication, the company or institution *designated by the first author* will be requested to pay a charge of $75 per printed page to partially cover the cost of publication. **Page charges for the first twelve (12) pages where any author is an ACES member, or first eight (8) pages where no author is a member of ACES, are not obligatory** nor is their payment a prerequisite for publication. EXCESSIVE LENGTH PAGE CHARGES (see separate policy statement) apply to papers longer than twelve (12) pages when any author is an ACES member, or eight (8) pages when no author is an ACES member, and are mandatory. Authors with questions about ACES page charge policies should contact the **ACES Journal** Editor-in-Chief directly.

PRIORITY COURTESY GUIDELINE: The **ACES Journal** is subject to printed page limitations, by issue, set annually by the ACES Executive Committee. The available pages for a given issue, therefore, may be less than the total pages of accepted papers; whenever this occurs, (i) **members of ACES and (ii) those non-members who agree to pay Voluntary Page Charges for their full paper (all pages)** will be given priority for early publication. Publication of accepted papers from other non-members, in such circumstances, will be deferred to the first subsequent issue with available pages.

last revision 21 March 1994
approved Pubs. Comm. 3/21/94
W. Perry Wheless, Jr.
ACES Editor-in-Chief

PREFERRED FONT SIZES AND LAY-OUT FOR CAMERA-READY *ACES JOURNAL* ARTICLES

Duncan C Baker, *ACES Journal* Editor-in-Chief

ABSTRACT. This brief discussion for intending ACES Journal authors deals with the vexing question of fonts, point sizes and lay-out. It represents a first attempt at optimising the use of available printed pages in the ACES Journal to the benefit of all members and authors. The ultimate objective is to be able to publish more worthy papers in the allocated number of pages without affecting the actual length (word count) of the papers themselves. This should eventually lead to faster turnaround time, cost savings and/or a regular quarterly Journal. The guidelines proposed are just that - only guidelines. No author's work will be turned down because he/she is unable to adhere to the proposed formats.

1 INTRODUCTION

Desktop publishing has become a reality for many authors. There are a large number of word processing packages and printers such as laser or inkjet printers available. These make it possible for an author to produce a high quality camera-ready copy with minimal effort. In this brief discussion proposals are motivated for a number of preferred presentation formats for papers to be published in the *ACES Journal*. The pages saved in this way will be utilised to the benefit of *ACES* members and authors. More worthy papers can be published on the same number of printed pages and the *Journal* can more readily achieve its longterm objective of becoming at least a quarterly publication.

It is emphasised that, while the preferred formats will result in substantial savings of printed pages without shortening the actual text of a paper, **no author will be discriminated against because he or she does not have access to modern word processing and/or desktop publishing facilities.**

2 READABILITY AND LEGIBILITY

2.1 Introduction

Readability and legibility are sometimes considered to be synonymous. Of course, they are not. Legibility is the quality of a typeface that makes it possible to read it, whereas readability is the characteristic of a body of type which makes it comfortable to read. The ensuing discussion is based on information available in texts on printing [1,2,3].

Readability is affected ultimately by no less than 9 factors. These are:

(a) typeface, or font
(b) size of type, or point size
(c) length of line (and words per line)
(d) leading, or space between words
(e) page pattern (including margins)
(f) contrast of type of paper (including colour)
(g) texture of paper
(h) typographic relationships (heads, folios, etc), and
(i) suitability of content.

2.2 Point size

This document was produced using Wordperfect 5.1 along with an HP LaserJet 4P printer. It was originally printed on A4 (European standard) paper but with the margins and page length set to conform to US standard size. The margin width was set at 20 mm (about 3/4 inch), the column width at 85 mm (about 3 3/8 inches) and the inter-column space at 6 mm (about 1/4 inch). A variety of fonts in different point sizes were available for use with the printer. There are 72 points per inch. Unless otherwise stated this document was prepared in Times Roman (TR) font with proportional spacing and the following point sizes. The title and author lines are in TR 12 point. The body of the text is in TR 10 point.

By way of comparison this specific sentence is printed in TR 12 point.

In books intended for people over 60, the point size should not be smaller than 11 point. For adults with normal eyesight the "apparently larger" 10 point typefaces are adequate (some typefaces are more "open" than others). For reference, note that most hardcover books are set in 11 point, while paperbacks with their enormous popularity are set in 10 or 9 point, and sometimes even 8 point. As can be seen from this sentence set in 8 point TR, this point size is not nearly as comfortable to read as the 9 or 10 point sizes.

2.3 Pitch

Pitch refers to the spacing of words.

Courier font with 10 characters per inch (cpi), as used in this sentence, certainly tends to spread the document. Contrast the

previous sentence with this one in Times Roman 12 point with proportional spacing. This sentence, on the other hand, is prepared in Prestige Elite with 12 characters per inch.

2.4 Serifs and sans-serif

Serifs refer to the little finishing strokes at the ends of letters in the typeface or font. These are in turn related to the "certainty of deciphering", and thus the legibility. They help to differentiate individual letters.

It is important to note the following

(a) sans-serif type (that without the serifs) such as the Helvetica 10 point used in this sentence, is intrinsically less legible than seriffed type,

(b) well-designed Roman upper or lower case seriffed type is easier to read than any of its variants, e.g. *italic,* **bold,** CAPITALS, or various expanded or condensed versions, and

(c) words should be set closer to each other (about as far apart as the width of the letter 'i'); and there should be more space between the lines than between the words.

3 RECOMMENDATIONS

While this has by no means been a comprehensive study of the vexing question of the ideal font type, point size and lay-out, some clear recommendations can be made. These recommendations must be seen against the background of trying to achieve maximum advantage in order to stretch the available printed page allocation to allow more worthy papers to be published. Another consideration is of course the desirable long term objective of producing at least a quarterly issue of the *ACES Journal.*

The recommendations are thus that provision should be made for at least three paper presentation formats with the following order of preference:

(a) Double column presentation with a 10 point seriffed type of font and proportional spacing; the heading should be in 12 or 14 point size. Margins and column width have been discussed elsewhere in these notes.

(b) Paste-ups with the body of the text in 14 point seriffed font, which after linear reduction to 71% becomes the equivalent of 10 point. The heading should be in about 18 point size, which reduces to about 13 point. Consideration should be given to providing the heading in suitably sized font in a space left at the top of the document for those authors lacking suitable facilities.

(c) For those who cannot accommodate either of the above formats, a 10 or 12 point seriffed font with proportional spacing is suggested. If proportional spacing is not available, suitable fonts with 10 or 12 characters per inch are suggested. The smaller font sizes should be given preference.

For comparison, the length of this note in different font styles is as follows:

Times Roman 12 point - 3 pages and about 1 inch of script,
Courier 10 cpi - 3 pages and about 2 inches of script,
Prestige Elite 12 cpi - 2 pages and about 7 inches of script, and
Helvetica 12 point - 3 pages and about 1 inch of script

It is important to reiterate that no author will be deprived of the possibility of publishing in the *ACES Journal* because of a lack of suitable typing and/or word processing facilities occasioned by adherence to the more stringent guidelines. The above guidelines are proposed in the face of continuing pressure for optimum usage of the available printed pages for the various issues. If an author is unable to meet the suggested criteria, every effort will be made to assist him or her to produce an acceptable camera-ready copy.

4 REFERENCES

[1] M. Lee, 'Bookmaking: The Illustrated Guide to Design/Production/Editing', R.R. Bowker Company, New York, 1979. ISBN 0-8352-1097-9.

[2] R. McLean, The Thames and Hudson Manual of Typography', Thames and Hudson, London, 1980. ISBN 0-500-68022-1.

[3] H. Williamson, 'Methods of Book Design', Yale University Press, New Haven and London, 1983. ISBN 0-300-02663-3.

<Revised - April 1994>

APPLIED COMPUTATIONAL ELECTROMAGNETICS SOCIETY JOURNAL

REQUIREMENTS FOR CAMERA-READY COPY FOR *ACES JOURNAL* ARTICLES

Congratulations! Your paper has been accepted for publication in the *ACES Journal.*

In order that we may publish your paper promptly, please prepare your final, camera-ready copy in accordance with the following instructions:

1. PRESENTATION FORMAT

Many authors have access to word processing facilities and laser-printers. This enables the preparation of high quality camera-ready copy. Where possible authors should capitalize on this capability to produce a camera-ready copy in the equivalent of Times Roman 10 point type face with proportional spacing such as that used in the body of these notes.

If the reduced font size is used, a double column presentation is preferred to go with it. An oversize paste-up (140% linear enlargement of a normal US standard sheet) using double columns and 14 point font is also acceptable, although a larger font will have to be used for the Title. The oversize sheets are photo-reduced by 71% linear dimension to provide standard size copy with the equivalent of 10 point font size if 14 point was originally used.

The use of these two options considerably reduces the number of printed pages compared to the normal font size of approximately 12 points by as much as a third. The resultant advantages for members and authors include more worthy papers per issue and faster turnaround time.

Where an author is not able to produce an original camera-ready copy in the reduced font size of 10 points, he/she may use the normal font size of approximately 12 points. Proportional spacing is preferred, but not mandatory.

Single line spacing is preferred. Where the use of subscripts and superscripts influences the readability of a document, one and a half spacing is recommended above or below the line so affected. Double spacing should only be used in the same way when one and a half spacing is not possible.

No author will have his/her work rejected after it has been accepted for publication because of an inability to meet the more stringent requirements in terms of font size and lay-out for camera-ready copy.
The Board of Directors has imposed an excess pages levy on papers greater than a pre-determined length. For more information see the page titled 'Excess Length Page Charge Policy'.

2. TYPES OF PAPER FOR THE DOCUMENT

Special materials such as mats, other special forms, India Ink, and glossy prints ARE GENERALLY NOT REQUIRED. Any plain white paper may be used. Note, however, the possible exception of oversized paper referred to in paragraph 1.

3. MARGINS

All top and bottom margins should be approximately 1 inch (2.54 cm), based on US standard page sizes of 8.5 in x 11.0 in. The side margins may not be less than 0.75 in (2.0 cm) or more than 1 in (2.54 cm). The approximate area of the text itself is then 6.5 in x 9.0 to 7 in x 9 in. The slightly larger area is recommended for double column use. In this case the space between the columns should be approximately 0.25 in (0.6 cm).

You must maintain this approximate area, even if you are using a different page size (other than 8.5 in x 11.0 in) such as the European standard A4 page.

4. THINGS TO AVOID

The following are to be avoided in the original camera-ready copy:

a. Faded or broken lines on figures - especially graph grids (use either a "good" grid or else no grid);

b. White streaks in text or figures, especially along fold lines. Do NOT fold your final, camera-ready manuscript when you mail it. Stiffen the envelope with a sheet of cardboard the same size as the paper itself;

c. Captions, coordinates, labels, or other text too small to read - especially in super- and subscripts, tables and on figures;

d. Blurred, smeared, smudged, or other low-contrast areas;

e. Spotty or smeared typeface;

f. Sloppy equations, or other sloppy handwriting or corrections;

g. Large numbers of streaks or dots resulting from poor quality photocopying, especially on figures;

h. Figures which are misaligned or not centered (see below); and

i. More than one layer of tape on top of any printing (see below).

Final Reminders

We have noticed that many "camera-ready" submissions are just that -- very clean and sharp original documents. Equally often, however, we receive non-original photocopies of original typed or laser-printed pages. These submissions are only on occasion clean and sharp. A majority of them suffer from non-optimal copy machine conditions. Dirty glass, streaky toner, and jittery light sources or print tables all contribute to low quality in the final printed pages.

We must adhere to our policy on what is acceptable in order to maintain quality standards. Your paper is at risk if you submit other than original typed or laser-printed pages. We will return any and all originals which you require. **If an article's print quality is poor, we will not publish it until it meets our camera-ready copy requirements.**

WE REPEAT - Do NOT fold final submissions! Use full-size envelopes with cardboard stiffeners.

5. FIGURES

Original figures -- even paste-ups -- are preferred. These original figures will be returned upon request. Do NOT send "nth generation" photocopies.

6. LAY-OUT OF PASTE-UP FIGURES AND CAPTIONS

Additional requirements and suggestions for lay-out of paste-up figures and captions are:

a. Line up all figures and captions parallel to the edges of the paper. (The use of a T-square and drafting table is recommended.)

b. Position (centre) small figures on a page to obtain an eye pleasing layout. Do NOT run all figures to one margin limit if this means that the remaining margins are large, such that the page lay-out is unbalanced.

c. The use of glue-stick or other transparent adhesive is acceptable. However, do NOT use more than one layer of "Frosty cellophane" tape - such as Scotch Magic Tape in the green box - on top of any printing. (By the time we photograph through two layers of frosty tape, the image fuzzes out, and two or more layers mean that we have to dissect the page and re-do it. In addition, we suggest that you use Scotch Removable Magic Tape, which is packaged in a blue box, instead of frosty tape. We find that the Removable Magic Tape simplifies re-positioning, is acceptable optically, and is otherwise convenient.)

d. We will gladly do the lay-out of your pages if you will provide the original to-be-pasted figures on captions, together with your instructions as **to how you want the pages to look**. However, if you choose to lay-out your own figures in final camera-ready form, then place the captions directly on the figures and NOT on a separate page.

To maintain our rapid turnaround policy and our quality standards, it is important that we do NOT waste time re-constructing unsatisfactory lay-outs.

7. OPTIONAL SUBMISSION OF PAPERS ON DISKETTE

You MAY submit an extra copy of your paper on diskette, in addition to the original camera-ready copy. **This is NOT A REQUIREMENT**, but it will enable us to correct typographical and other errors which might otherwise delay publication of your paper. If you choose to submit a diskette, send it to the Managing Editor, together with the original camera-ready copy. For further information regarding acceptable word processors, contact the Managing Editor.

IN SUMMARY - each page must be neat, legible, and photo-offset reproducible. This is most easily achieved if the document submitted is the original print copy and not a photocopy. If you have additional questions concerning this, please contact the Managing Editor, Dr. RW Adler, at:

Naval Postgraduate School, Phone: 408-656-2352
EC/AB Dept. Code EC/AB Fax: 408-656-2955 or
833 Dyer Road, Room 437 408-649-0300
Monterey, CA 93943-5121
USA e-mail5541304@mcimail.com

<Revised - April 1994>

APPLIED COMPUTATIONAL ELECTROMAGNETICS SOCIETY JOURNAL

STYLE REQUIREMENTS FOR *ACES JOURNAL* ARTICLES

The *ACES Journal* is flexible, within reason, in regard to style. However, certain requirements are in effect:

1. The paper title should NOT be placed on a separate page. The title, author(s), abstract, and (space permitting) beginning of the paper itself should all be on the first page. The title, author(s), and author affiliations should be centered (centre-justified) on the first page.

2. An abstract is REQUIRED. The abstract should reflect the content of the paper and should be usable by technical abstracting and indexing services. If applicable, the computer codes and computational techniques (for example, moment method, finite difference time domain, transmission line method, finite element, or modal expansion) discussed in the paper should be stated in the abstract.

3. Either British English or American English spellings may be used, provided that each word is spelled consistently throughout the paper.

4. Any commonly-accepted format for referencing is permitted, provided that internal consistency of format is maintained. As a guideline for authors who have no other preference, we recommend that references be given by author(s) name and year in the body of the paper (with alphabetical listing of all references at the end of the paper). We prefer that names of journals, monographs, and similar publications be in boldface italic font or boldface font (or underlined if these fonts are not available). In addition, we prefer that names of papers and articles be in quotation marks.

5. Internal consistency shall also be maintained for other elements of style, such as equation numbering. As a guideline for authors who have no other preference, we suggest that equation numbers be placed in parentheses at the right column margin.

6. The intent and meaning of all text must be clear. For authors who are NOT masters of the English language, the ACES Editorial Staff will provide assistance with grammar (subject to clarity of intent and meaning).

7. It is RECOMMENDED that figures and tables be placed within the paper, and as close to the relevant text as possible -- especially if the paper is long. However, this is NOT A REQUIREMENT.

8. To economize on space, a section or subsection should NOT begin on a new page if this will result in several lines of unused space on the previous page. (If the previous page has only enough space to accommodate the section or subsection title, in part or in total, then the section or subsection may begin on a new page.)

9. For similar reasons, we prefer that lines be single-spaced (no blank lines between lines of text). However, double spacing should be used for equations, section headings, and section sub-headings, to place a blank line between adjacent lines of text. In addition, double spacing between paragraphs is recommended. If the use of single spacing will "crowd" subscripts and superscripts so that readability is difficult, then one and a half line spacing should be used if possible, to place a blank half-line between adjacent lines of text. Use double spacing only if necessary to maintain readability and one and a half line spacing is not available.

<Revised - April 1994>

COLOR PRINTING COSTS FOR THE ACES JOURNAL AND NEWSLETTER

1. Color Printing of ACES publications is a process involving four separate passes through a printing press with different ink colors; black, magenta (a red), yellow and cyan (a blue).

2. Originals that are in the "Final Form" (all colors present in the correct mix) must be prepared for the press as "Color Seps", meaning that four copies of the page must be prepared by a photographic "color separation" process, producing a black, a magenta, a yellow and a cyan page. These four color seps represent the four passes through the press. ACES' cost of preparing a set of color seps for various size images are:

3"X 4"	$ 65
4"X 6"	$ 80
5"X 8"	$ 95
7"X 9"	$100
9"X11"	$160

3. Additional printing costs, above the standard cost for black and white pages, are:

up to	4 pages	$250/ea.
	8 pages	$160/ea.
	12 pages	$180/ea.
	16 pages	$150/ea.

(The reason for the price variation is that a sheet of paper that is run through the press contains four pages on one side and four pages on the other side. Thus, 12 pages of color is priced at the cost of running one sheet through the color passes on one side (four pages) and running a second sheet through the color passes on both sides (8 more pages).

4. Since the costs for 8 pages are based on the front and back sides of a page in color, the *LAYOUT* of the publication with regard to where in the issue the color pages will be placed is critical. It *IS* possible that eight pages back-to-back will require two partial sheets at a higher cost than for a single sheet, depending on the publication layout sequence of pages.

5. It may be possible to provide a rough estimate of the cost of color pages, but an accurate prediction will require knowledge months before press-time, of nearly all of the papers to be published in a given issue and of the sequence of the papers within the publication, a very unlikely scenario.

6. There is a possibility of the binder folks adding color pages that have been preprinted and provided by the author, but the logistics of knowing exactly which page numbers to have printed on the color pages before the publication goes to press are very difficult to set up. Thus author-provided color page drop-ins are also a very unlikely scenario.

For further clarification, contact Richard W. Adler. Managing Editor, ACES Publications.

THE APPLIED COMPUTATIONAL ELECTROMAGNETIC SOCIETY

1995 CALL FOR PAPERS 1995

The 11th Annual Review of Progress in Applied Computational Electromagnetics

March 20-24, 1995

Naval Postgraduate School, Monterey, California

Share your knowledge and expertise with your colleagues

The Annual **ACES** Symposium is an ideal opportunity to participate in a large gathering of **EM** analysis enthusiasts. The purpose of the Symposium is to bring analysts together to share information and experience about the practical application of **EM** analysis using computational methods. The symposium offerings include technical presentations, demonstrations, vendor booths and short courses. All aspects of electromagnetic computational analysis are represented. Contact Ray Luebbers for details.

TECHNICAL PROGRAM CHAIRMAN
Ray Luebbers
Department of Electrical Engineering
Pennsylvania State University
University Park, PA 16802
Phone: (814) 865-2362
FAX: (814) 865-7065
Email: lu4@psuvm.psu.edu

SYMPOSIUM ADMINISTRATOR
Richard W. Adler
ECE Dept./Code ECAB
Naval Postgraduate School
833 Dyer Rd. Room 437
Monterey, CA 93943-5121
Phone: (408) 646-1111
FAX: (408) 649-0300
Email: 554-1304@mcimail.com

PUBLICATION CHAIRMAN
Richard K. Gordon
EE Dept. Univ. of Mississippi
Anderson Hall, Box 41
University, MS 38677
Phone: (601) 232-5388
FAX: (601) 232-7231
Email: eegordon@vm.cc.olemiss.edu

PUBLICITY CHAIRMAN
Paul M. Goggans
EE Dept. Univ. of Mississippi
Anderson Hall, Box 1
University, MS 38677
Phone: (601) 232-5954
FAX: (601) 232-7231
Email: eepmg@cotton.vislab.olemiss.edu

1995 ACES Symposium

Sponsored by:	ACES, NCCOSC, NPS, DOE/LLNL
In cooperation with:	The IEEE Antennas and Propagation Society, the IEEE Electromagnetic Compatibility Society and USNC/URSI

THE APPLIED COMPUTATIONAL ELECTROMAGNETIC SOCIETY

CALL FOR PAPERS

The 11th Annual Review of Progress
in Applied Computational Electromagnetics

Papers may address general issues in applied computational electromagnetics, or may focus on specific applications, techniques, codes, or computational issues of potential interest to the Applied Computational Electromagnetics Society membership. Areas and topics include:

- Code validation
- Code performance analysis
- Computational studies of basic physics
- Examples of practical code application
- New codes, algorithms, code enhancements, and code fixes
- Computer hardware issues
- Partial list of applications:

antennas	wave propagation
radar imaging	radar cross section
shielding	bioelectromagnetics
EMP, EMI/EMC	visualization
dielectric & magnetic materials	inverse scattering
microwave components	**MMIC** technology
fiberoptics	remote sensing & geophysics
communications systems	propagation through plasmas
eddy currents	*non-destructive evaluation*

- Partial list of techniques:

frequency-domain & time-domain techniques	
integral equation & differential equation techniques	
finite differences & finite element techniques	
diffraction theories	physical optics
modal expansions	perturbation methods
hybrid methods	moment methods

INSTRUCTIONS FOR AUTHORS AND TIMETABLE

For both summary and final paper, please supply the following data for the principal author: name, address, Email address, FAX, and phone numbers for both work and home.

October 3, 1994:	Submission deadline. Submit four copies of a 300-500 word summary to the Technical Program Chairman.
November 18, 1994:	Authors notified of acceptance.
December 23, 1994:	Submission deadline for camera-ready copy. The papers should not be more than 8 pages long including figures.

Registration fee per person for the Symposium will be approximately $235 for ACES members and $260 for non-ACES members. The exact fee will be announced later.

SHORT COURSE

Short courses will be offered in conjunction with Symposium covering numerical techniques, computational methods, surveys of EM analysis and code usage instruction. It is anticipated that short courses will be conducted principally on Monday March 20 and Friday March 24. Fee for a short course is expected to be approximately $90 per person for a half-day course and $140 for a full-day course, if booked before March 3, 1995. Full details of 1995 Symposium will be available by November 1994.

EXHIBITS

Vendor booths and demonstrations will feature commercial products, computer hardware and software demonstrations, and small company capabilities.

For information regarding ACES or to become a member in the Applied Computational Electromagnetics Society, contact Dr. Richard W. Adler, ECE Department, Code ECAB, Naval Postgraduate School, 833 Dyer Rd, Rm 437, Monterey, CA. 93943-5121, telephone (408) 646-1111, Fax: (408) 649-0300, E-mail:554-1304@mcimail.com. You can subscribe to the Journal and become a member of ACES by completing and returning the form below.

ACES MEMBERSHIP / SUBSCRIPTION FORM

Please print

LAST NAME	FIRST NAME	MIDDLE INITIAL

COMPANY/ORGANIZATION/UNIVERSITY	DEPARTMENT/MAIL STATION

PLEASE LIST THE ADDRESS YOU WANT USED FOR PUBLICATIONS!

MAILING ADDRESS

CITY	STATE/PROVINCE	COUNTRY	ZIP CODE

TELEPHONE	FAX

E-MAIL ADDRESS — E-MAIL ADDRESS CAN BE INCLUDED IN ACES DATABASE ( ) YES ( ) NO

PERMISSION IS GRANTED TO HAVE MY NAME PLACED ON MAILING LISTS WHICH MAY BE SOLD ( ) YES ( ) NO

CURRENT MEMBERSHIP PRICES ARE VALID THROUGH 31 MARCH 1995
PRICES ARE SUBJECT TO CHANGE EACH 1 APRIL, *EXCEPT* FOR STUDENTS

AREA	INDIVIDUAL SURFACE MAIL	INDIVIDUAL AIRMAIL	ORGANIZATION (AIRMAIL ONLY)
U.S. & CANADA	( ) $65	( ) $65	( ) $115
MEXICO, CENTRAL & SOUTH AMERICA	( ) $68	( ) $70	( ) $115
EUROPE, FORMER USSR TURKEY, SCANDINAVIA	( ) $68	( ) $78	( ) $115
ASIA, AFRICA, MIDDLE EAST & PACIFIC RIM	( ) $68	( ) $85	( ) $115

FULL-TIME STUDENT RATE IS $25 FOR ALL COUNTRIES

METHOD FOR NON-U.S. PAYMENT: (1) **INTERNATIONAL MONEY ORDER**, DRAWN IN U.S. DOLLARS. (2) **TRAVELER'S CHECKS** IN U.S. DOLLARS, (3) **BANK CHECKS**, ONLY IF THEY ARE DRAWN ON A U.S. BANK & SHOW A U.S. BANK ADDRESS; THEY MUST ALSO CONTAIN A SERIES OF (9) DIGIT ROUTING NUMBERS (WHICH ARE PUT ON THE CHECK WHEN IT IS ORIGINATED). WITHOUT THESE NUMBERS, ACES MUST RETURN YOUR CHECK. June 1994

MAKE PAYMENT PAYABLE TO: "ACES"	SEND TO: RICHARD W. ADLER, EXECUTIVE OFFICER, (ADDRESS ABOVE)

ADVERTISING RATES

	FEE	PRINTED SIZE
Full page	$200.	7.5" x 10.0"
1/2 page	$100.	7.5" x 4.7" or 3.5" x 10.0"
1/4 page	$ 50	3.5" x 4.7"

All ads must be camera ready copy.

Ad deadlines are same as Newsletter copy deadlines.

Place ads with Paul Elliot, Newsletter Editor, ARCO, 1250 24th St. NW, Suite 850, Washington, D.C. 20037 USA. The editor reserves the right to reject ads.

ACES JOURNAL AND NEWSLETTER COPY INFORMATION

ISSUE	COPY DEADLINE
March	January 25
July	May 25
November	September 25

ACES COPYRIGHT FORM

This form is intended for original, previously unpublished manuscripts submitted to ACES periodicals and conference publications. The signed form, appropriately completed, MUST ACCOMPANY any paper in order to be published by ACES. PLEASE READ REVERSE SIDE OF THIS FORM FOR FURTHER DETAILS.

TITLE OF PAPER:

AUTHORS(S)

PUBLICATION TITLE/DATE:

RETURN FORM TO:
Dr. Richard W. Adler
Naval Postgraduate School
Code EC/AB
Monterey, CA 93943

PART A - COPYRIGHT TRANSFER FORM

(NOTE: Company or other forms may not be substituted for this form. U.S. Government employees whose work is not subject to copyright may so certify by signing Part B below. Authors whose work is subject to Crown Copyright may sign Part C overleaf).

The undersigned, desiring to publish the above paper in a publication of ACES, hereby transfer their copyrights in the above paper to The Applied Computational Electromagnetics Society (ACES). The undersigned hereby represents and warrants that the paper is original and that he/she is the author of the paper or otherwise has the power and authority to make and execute this assignment.

Returned Rights: In return for these rights, ACES hereby grants to the above authors, and the employers for whom the work was performed, royalty-free permission to:

1. Retain all proprietary rights other than copyright, such as patent rights.
2. Reuse all or portions of the above paper in other works.
3. Reproduce, or have reproduced, the above paper for the author's personal use or for internal company use provided that (a) the source and ACES copyright are indicated, (b) the copies are not used in a way that implies ACES endorsement of a product or service of an employer, and (c) the copies per se are not offered for sale.
4. Make limited distribution of all or portions of the above paper prior to publication.
5. In the case of work performed under U.S. Government contract, ACES grants the U.S. Government royalty-free permission to reproduce all or portions of the above paper, and to authorize others to do so, for U.S. Government purposes only.

ACES Obligations: In exercising its rights under copyright, ACES will make all reasonable efforts to act in the interests of the authors and employers as well as in its own interest. In particular, ACES REQUIRES that:

1. The consent of the first-named author be sought as a condition in granting re-publication permission to others.
2. The consent of the undersigned employer be obtained as a condition in granting permission to others to reuse all or portions of the paper for promotion or marketing purposes.

In the event the above paper is not accepted and published by ACES or is withdrawn by the author(s) before acceptance by ACES, this agreement becomes null and void.

AUTHORIZED SIGNATURE — TITLE (IF NOT AUTHOR)

EMPLOYER FOR WHOM WORK WAS PERFORMED — DATE FORM SIGNED

PART B - U.S. GOVERNMENT EMPLOYEE CERTIFICATION

(NOTE: If your work was performed under Government contract but you are not a Government employee, sign transfer form above and see item 5 under Returned Rights).

This certifies that all authors of the above paper are employees of the U.S. Government and performed this work as part of their employment and that the paper is therefore not subject to U.S. copyright protection.

AUTHORIZED SIGNATURE — TITLE (IF NOT AUTHOR)

NAME OF GOVERNMENT ORGANIZATION — DATE FORM SIGNED

PART C - CROWN COPYRIGHT

(Note: ACES recognizes and will honor Crown Copyright as it does U.S. Copyright. It is understood that, in asserting Crown Copyright, ACES in no way diminishes its rights as publisher. Sign only if *ALL* authors are subject to Crown Copyright.

This certifies that all authors of the above Paper are subject to Crown Copyright. (Appropriate documentation and instructions regarding form of Crown Copyright notice may be attached).

AUTHORIZED SIGNATURE — TITLE OF SIGNEE

NAME OF GOVERNMENT BRANCH — DATE FORM SIGNED

Information to Authors

ACES POLICY

ACES distributes its technical publications throughout the world, and it may be necessary to translate and abstract its publications, and articles contained therein, for inclusion in various compendiums and similar publications, etc. When an article is submitted for publication by ACES, acceptance of the article implies that ACES has the rights to do all of the things it normally does with such an article.

In connection with its publishing activities, it is the policy of ACES to own the copyrights in its technical publications, and to the contributions contained therein, in order to protect the interests of ACES, its authors and their employers, and at the same time to facilitate the appropriate re-use of this material by others.

The new United States copyright law requires that the transfer of copyrights in each contribution from the author to ACES be confirmed in writing. It is therefore necessary that you execute either Part A-Copyright Transfer Form or Part B-U.S. Government Employee Certification or Part C-Crown Copyright on this sheet and return it to the Managing Editor (or person who supplied this sheet) as promptly as possible.

CLEARANCE OF PAPERS

ACES must of necessity assume that materials presented at its meetings or submitted to its publications is properly available for general dissemination to the audiences these activities are organized to serve. It is the responsibility of the authors, not ACES, to determine whether disclosure of their material requires the prior consent of other parties and if so, to obtain it. Furthermore, ACES must assume that, if an author uses within his/her article previously published and/or copyrighted material that permission has been obtained for such use and that any required credit lines, copyright notices, etc. are duly noted.

AUTHOR/COMPANY RIGHTS

If you are employed and you prepared your paper as a part of your job, the rights to your paper initially rest with your employer. In that case, when you sign the copyright form, we assume you are authorized to do so by your employer and that your employer has consented to all of the terms and conditions of this form. If not, it should be signed by someone so authorized.

NOTE RE RETURNED RIGHTS: Just as ACES now requires a signed copyright transfer form in order to do "business as usual", it is the intent of this form to return rights to the author and employer so that they too may do "business as usual". If further clarification is required, please contact: The Managing Editor, R.W. Adler, Naval Postgraduate School, Code EC/AB, Monterey, CA, 93943, USA (408)646-2352.

Please note that, although authors are permitted to re-use all or portions of their ACES copyrighted material in other works, this does not include granting third party requests for reprinting, republishing, or other types of re-use.

JOINT AUTHORSHIP

For jointly authored papers, only one signature is required, but we assume all authors have been advised and have consented to the terms of this form.

U.S. GOVERNMENT EMPLOYEES

Authors who are U.S. Government employees are not required to sign the Copyright Transfer Form (Part A), but any co-authors outside the Government are.

Part B of the form is to be used instead of Part A only if all authors are U.S. Government employees and prepared the paper as part of their job.

NOTE RE GOVERNMENT CONTRACT WORK: Authors whose work was performed under a U.S Government contract but who are not Government employees are required to sign Part A-Copyright Transfer Form. However, item 5 of the form returns reproduction rights to the U.S. Government when required, even though ACES copyright policy is in effect with respect to the reuse of material by the general public.

June 1994

CALL FOR PAPERS

THE APPLIED COMPUTATIONAL ELECTROMAGNETICS SOCIETY ANNOUNCES A SPECIAL ISSUE OF THE ACES JOURNAL ON:

ADVANCES IN THE APPLICATION OF THE METHOD OF MOMENTS TO ELECTROMAGNETIC RADIATION AND SCATTERING PROBLEMS

The Applied Computational Electromagnetics Society is pleased to announce the publication of a 1995 Special Issue of the ACES Journal on the use of the Method of Moments in the evaluation of electromagnetic radiation and scattering problems. The objectives of this special issue are: (1) to provide the computational electromagnetics community with an assessment of the current capabilities and uses of the Method of Moments for electromagnetics problems from the low-frequency to the high-frequency regimes and (2) to provide information on recent advances that may extend range of applicability and usefulness of the Method of Moments. Prospective authors are encouraged to submit papers of archival value that address these objectives and other suggested topics listed below.

SUGGESTED TOPICS

- Modeling Guidelines for Complex Geometries
- Accuracy Assessment and Improvement
- Special Formulations: Low Frequency/High Frequency
- Hybrid Method of Moment Approaches
- New Integral Equation Formulations
- Parallelization of Moment Method Codes
- Novel Equivalence Principle Applications for the Method of Moments
- Fast Matrix Computation/Solution Techniques
- Large-Scale Problems

DEADLINE FOR PAPERS IS MARCH 31, 1995

Send papers and inquiries to:

A.W. Glisson and A.A.Kishk
Special Guest Editors
Department of Electrical Engineering
University of Mississippi
University, MS 38677

Tel: (601) 232-5353
FAX: (601) 232-7231
E-mail: eeallen@vm.cc.olemiss.edu

APPLIED COMPUTATIONAL ELECTROMAGNETICS SOCIETY JOURNAL

INFORMATION FOR AUTHORS

PUBLICATION CRITERIA

Each paper is required to manifest some relation to applied computational electromagnetics. **Papers may address general issues in applied computational electromagnetics, or they may focus on specific applications, techniques, codes, or computational issues.** While the following list is not exhaustive, each paper will generally relate to at least one of these areas:

1. **Code validation.** This is done using internal checks or experimental, analytical or other computational data. Measured data of potential utility to code validation efforts will also be considered for publication.

2. **Code performance analysis.** This usually involves identification of numerical accuracy or other limitations, solution convergence, numerical and physical modeling error, and parameter tradeoffs. However, it is also permissible to address issues such as ease-of-use, set-up time, run time, special outputs, or other special features.

3. **Computational studies of basic physics.** This involves using a code, algorithm, or computational technique to simulate reality in such a way that better or new physical insight or understanding is achieved.

4. **New computational techniques,** or new applications for existing computational techniques or codes.

5. **"Tricks of the trade"** in selecting and applying codes and techniques.

6. **New codes, algorithms, code enhancement, and code fixes.** This category is self-explanatory but includes significant changes to existing codes, such as applicability extensions, algorithm optimization, problem correction, limitation removal, or other performance improvement. NOTE: CODE (OR ALGORITHM) CAPABILITY DESCRIPTIONS ARE NOT ACCEPTABLE, UNLESS THEY CONTAIN SUFFICIENT TECHNICAL MATERIAL TO JUSTIFY CONSIDERATION.

7. **Code input/output issues.** This normally involves innovations in input (such as input geometry standardization, automatic mesh generation, or computer-aided design) or in output (whether it be tabular, graphical, statistical, Fourier-transformed, or otherwise signal-processed). Material dealing with input/output database management, output interpretation, or other input/output issues will also be considered for publication.

8. **Computer hardware issues.** This is the category for analysis of hardware capabilities and limitations in meeting various types of electromagnetics computational requirements. Vector and parallel computational techniques and implementation are of particular interest.

Applications of interest include, but are not limited to, antennas (and their electromagnetic environments), networks, static fields, radar cross section, shielding, radiation hazards, biological effects, electromagnetic pulse (EMP), electromagnetic interference (EMI), electromagnetic compatibility (EMC), power transmission, charge transport, dielectric and magnetic materials, microwave components, MMIC technology, remote sensing and geophysics, communications systems, fiber optics, plasmas, particle accelerators, generators and motors, electromagnetic wave propagation, non-destructive evaluation, eddy currents, and inverse scattering.

Techniques of interest include frequency-domain and time-domain techniques, integral equation and differential equation techniques, diffraction theories, physical optics, moment methods, finite differences and finite element techniques, modal expansions, perturbation methods, and hybrid methods. This list is not exhaustive.

A unique feature of the Journal is the publication of unsuccessful efforts in applied computational electromagnetics. Publication of such material provides a means to discuss problem areas in electromagnetic modeling. Material representing an unsuccessful application or negative results in computational electromagnetics will be considered for publication only if a reasonable expectation of success (and a reasonable effort) are reflected. Moreover, such material must represent a problem area of potential interest to the ACES membership.

EDITORIAL REVIEW

In order to ensure an appropriate level of quality control, papers are refereed. They are reviewed both for technical correctness and for adherence to the listed guidelines regarding information content. Authors should submit the initial manuscript in draft form so that any suggested changes can be made before the photo-ready copy is prepared.

<continued on next page>

STYLE FOR CAMERA-READY COPY

The ACES Journal is flexible, within reason, in regard to style. However, certain requirements are in effect:

1. The paper title should NOT be placed on a separate page. The title, author(s), abstract, and (space permitting) beginning of the paper itself should all be on the first page. The title, author(s), and author affiliations should be centered (center-justified) on the first page.

2. An abstract is REQUIRED. The abstract should state the computer codes, computational techniques, and applications discussed in the paper (as applicable) and should otherwise be usable by technical abstracting and indexing services.

3. Either British English or American English spellings may be used, provided that each word is spelled consistently throughout the paper.

4. Any commonly-accepted format for referencing is permitted, provided that internal consistency of format is maintained. As a guideline for authors who have no other preference, we recommend that references be given by author(s) name and year in the body of the paper (with alphabetical listing of all references at the end of the paper). Titles of Journals, monographs, and similar publications should be in boldface or italic font or should be underlined. Titles of papers or articles should be in quotation marks.

5. Internal consistency shall also be maintained for other elements of style, such as equation numbering. As a guideline for authors who have no other preference, we suggest that equation numbers be placed in parentheses at the right column margin.

6. The intent and meaning of all text must be clear. For authors who are NOT masters of the English language, the ACES Editorial Staff will provide assistance with grammar (subject to clarity of intent and meaning).

7. Unused space should be minimized. Sections and subsections should not normally begin on a new page.

MATERIAL, SUBMITTAL FORMAT AND PROCEDURE

Only camera-ready original copies are accepted for publication, although authors may submit other copies for publication review. The term "camera-ready" means that the material is neat, legible, and reproducible. The preferred font style is Times Roman 10 point (or equivalent) such as that used in this text. A double column format similar to that used here is preferred. **No author's work will be turned down once it has been accepted because of an inability to meet the requirements concerning fonts and format.** Full details are sent to the author(s) with the letter of acceptance.

There is NO requirement for India ink or for special paper; any plain white paper may be used. However, faded lines on figures and white streaks along fold lines should be avoided. Original figures - even paste-ups - are preferred over "nth-generation" photocopies. These original figures will be returned if you so request.

While ACES reserves the right to re-type any submitted material, this is not generally done.

Four copies of all submissions should be sent to the Editor-in-Chief. Each submission should be accompanied by a covering letter. The letter should include the name, address, and telephone of at least one of the authors.

PUBLICATION CHARGES

ACES members are allowed 12 pages per paper without charge; non-members are allowed 8 pages without charge. Mandatory page charges of $75 a page apply to all pages in excess of 12 for members or 8 for non-members. Voluntary page charges are requested for the free (12 or 8) pages, but are NOT mandatory or required for publication. A priority courtesy guideline, which favors members, applied to paper backlogs. Full details are available from the Editor-in-Chief.

COPYRIGHTS AND RELEASES

Each primary author must sign a copyright form and obtain a release from his/her organization vesting the copyright with ACES. Forms will be provided by ACES. Both the author and his/her organization are allowed to use the copyrighted material freely for their own private purposes.

Permission is granted to quote short passa[illegible]d reproduce figures and tables from an ACES Journal is[illegible]provided the source is cited. Copies of ACES Journal articles may be made in accordance with usage permitted by Sections 107 or 108 of the U.S. Copyright Law. This consent does not extend to other kinds of copying, such as for general distribution, for advertising or promotional purposes, for creating new collective works, or for resale. The reproduction of multiple copies and the use of articles or extracts for commercial purposes require the consent of the author and specific permission from ACES. Institutional members are allowed to copy any ACES Journal issue for their internal distribution only.